A SEMI-EMPIRICAL FORMULATION FOR DETERMINATION OF RAIN ATTENUATION ON TERRESTRIAL RADIO LINKS

By

Odedina Modupe Olubunmi

UNIVERSITY OF KWAZULU-NATAL

A Thesis Submitted in Fulfillment of the Academic Requirements for the Degree of Doctor of Philosophy in the School of Electrical, Electronic and Computer Engineering, University of KwaZulu-Natal

November 2010

A Semi-Empirical Formulation for Determination of Rain Attenuation on Terrestrial Radio Links

SUBMITTED BY

Modupe Olubunmi Odedina

IN FULLFILMENT OF THE DEGREE OF

Doctor of Philosophy in Electronic Engineering from the University of KwaZulu-Natal

DATE OF SUBMISSION

2010

SUPERVISED BY

Professor T. J. Afullo

Preface

The research presented in this thesis was done by Mrs. Modupe Olubunmi Odedina, under the supervision of Professor Thomas J. Afullo in the School of Electrical, Electronic and Computer Engineering at the University of KwaZulu-Natal, Durban, South Africa. This work has been partially supported by Alcatel-Lucent and Telkom South Africa through the Centre of Excellence programme in the school.

Certain aspects of this thesis have been presented and published by the author at various fora: the Southern Africa Telecommunication Networks and Applications Conference (SATNAC) in 2007, 2008, and 2009 in Mauritius, Eastern Cape and Swaziland respectively; the North American Radio Science Meeting (URSI), Ottawa, Canada in 2007; IEEE AFRICON Conference, Namibia in 2007; the XXIX General Assembly of the International Union of Radio Science (URSI) in Chicago, USA in 2008; and the 6th IASTED Conference on Antennas, Radar and Wave Propagation at Banff, Alberta, Canada in 2009. Part of this thesis has also been published in Radio Science journal (American Geophysical Union journal) in October 2007 and another in the same journal in January, 2010

The whole thesis, unless specifically indicated to the contrary in the text, is the author's original work, and has not been submitted in part, or in whole to any other University.

Acknowledgements

I give all the glory to the Almighty God who, through His infinite mercies, has given me strength and grace to complete this work.

The unrelenting effort of my supervisor Prof. T.J. Afullo is highly appreciated. His patience, professionalism and unique approach to research have been really helpful and vital to the completion of this thesis. I will forever be grateful for having worked under his supervision.

I express my profound gratitude to the Head of School of Electrical, Electronic and Computer Engineering, Prof. S.H. Mneney and other staff members for creating a friendly and conducive atmosphere to do the research. I would also like to thank Mr. Bruce Harrison, the LAN manager and the entire administrative staff, especially Mrs. Bev Bennet for her help and support during the research period.

I would like to express my appreciation to my postgraduate colleagues, most especially Mr. Pius Owolawi, Mr. Olutayo oyerinde, Mr. Gbolahan Aiyetoro and Mr. Chrispin Mulangu for their friendship, and valuable inputs during the course of this research work. My appreciation also goes to Dr. Langa Khumalo for proofreading this thesis.

Special thanks must go to my dear husband, colleague, and a very long-time-friend Mr. Kemi Odedina for his understanding and unwavering commitment to my academic life. Finally I will like to give kudos to my little lovely son Master Leke Odedina for his patience, love and enduring acts all through the period of my study.

Abstract

Advances in today's fast growing communication systems have resulted in congestion in the lower frequency bands and the need for higher capacity broadband services. This has made it inevitable for service providers to migrate to higher frequency bands so as to accommodate the ever increasing demands on radio communication systems. However, the reliability of such systems at these frequency bands tend to be severely degraded due to some natural atmospheric phenomena of which rain is the dominant factor. This is not to say that other factors have become unimportant; however, if attenuation by rain is so severe that a radio link is unavailable for use, then other factors become secondary. Therefore, it is paramount to establish a model capable of predicting the behaviour of these systems in the presence of rain.

This study employs a semi-empirical approach for the formulation of rain attenuation models using the knowledge of rain rate, raindrop size distribution, and a signal level measurement recorded at 19.5 GHz on a horizontally polarized terrestrial radio link. The semi-empirical approach was developed by considering the scattering effect of an electromagnetic wave propagating through a medium containing raindrops. The complex forward scattering amplitudes for the raindrops are determined for all raindrop sizes at different frequencies, utilizing the Mie scattering theory on spherical dielectric raindrops. From these scattering amplitudes, the extinction cross-sections for the spherical raindrops are calculated. Applying the power-law regression to the real part of the calculated extinction cross-section, power-law coefficients are determined at different frequencies. The power-law model generated from the extinction cross-section is integrated over different raindrop-size distribution models to formulate theoretical rain attenuation models.

The developed rain attenuation models are used with $R_{0.01}$ rain rate statistics determined for four locations in different rain climatic zones in South Africa to calculate the specific rain attenuation. From a horizontally polarized 6.73 km terrestrial line-of-sight link in Durban, South Africa,

experimental rain attenuation measurements were recorded at 19.5 GHz. These rain attenuation measurements are compared with the results obtained from the developed attenuation models with the same propagation parameters to establish the most appropriate attenuation models that describe the behaviour of radio link performance in the presence of rain. For the purpose of validating the results, it is compared with the ITU-R rain attenuation model. This study also considers the characteristics and variations associated with rain attenuation for terrestrial communication systems. This is achieved by utilizing the ITU-R power-law rain attenuation model on 5-year rain rate data obtained from the four different climatic rain zones in South Africa to estimate the cumulative distributions of rain attenuation. From the raindrop size and 1-minute rain rate measurement recorded in Durban with a distrometer over six months, rain events over the six months are classified into drizzle, widespread, shower and thunderstorm rain types and the mean rain rate statistics determined for each class of rain. Drop-size distribution for all the rain types is estimated.

This research has shown a statistical analysis of rain fade data and proposed an empirical rain attenuation model for South Africa localities. This work has also drawn out theoretical rain attenuation prediction models based on the assumption that the shapes of raindrops are spherical. The results predicted from these theoretical attenuation models have shown that it is not the raindrop shapes that determine the attenuation due to rain, but the raindrop size distribution and the rain rate content in the drops. This thesis also provides a good interpretation of cumulative rain attenuation distribution on seasonal and monthly basis. From these distributions, appropriate figures of fade margin are derived for various percentages of link availability in South Africa.

Table of Contents

List of Figures

List of Tables

Chapter One

Introduction

1.1 Introduction

The enormous demands on radio communication systems in recent times have put a lot of pressure on scientists, radio engineers and communication system designers to develop microwave systems operating at higher frequency bands. The main reason for this is to decongest the lower frequency bands, and to have access to high capacity communication channels to accommodate the ever-increasing demands of consumers. However, the reliability of these systems in the higher frequency bands may be severely impaired by some natural atmospheric phenomena such as cloud, fog, atmospheric gases, rain drops, snowflakes, ice crystals, and hail [*Crane,* 2003; *Hall et al.,* 2003]. Of these, rain is the main problem at certain radio frequencies and has to be appropriately accounted for to make the systems work satisfactorily [*Freeman*, 1997; *Asen et al.*, 2003]. For temperate climates, frequencies higher than about 10 GHz become significantly attenuated in rain, while in the tropical and equatorial climates, it can be as low as 7 GHz because of the occurrence of higher rain rates and larger raindrops than in the temperate regions [*Moupfouma et al.,* 1982*; Moupfouma*, 1984].

Rain attenuation can be described empirically through link measurements, or predicted from point rainfall rate, drop-size distribution and other relevant parameters along the radio paths [*Ajayi et al.,* 1996; *Myers,* 1999]. Several models ranging from empirical to theoretical have been proposed for the prediction of rain attenuation by several authors, like, *Medhurst* [1964], *Oguchi,* [1973],

Lin [1975; 1977], *Rogers and Olsen* [1976], *Uzunoglu et al.* [1977], *Olsen et al,* [1978], *Crane* [1980;1996], *Garcia-Lopez and Peiro* [1983], *Moupfouma* [1984; 1997, 2009], *Lin et al.* [2002], *Mätzler* [2002b], *ITU-R 838-3* [2005], *ITU-R 530-12* [2007], *da Silva Mello et al.*[2007] etc. Most of the attenuation models are based on the accuracy of the cumulative distribution of rain rate at a point [*Moupfouma,* 1984; 2009].

Many authors have based their models on the concept of equivalent path averaged or integrated rain rate along the propagation path length [Lin, 1975; *Crane,* 1980; 1996] which is obtained by multiplying the point rain rate for the time percentage of interest by a reduction factor [*Moupfouma,* 1984]. Other authors have used the concept of effective path length or effective rainfall rate [*Garcia-Lopez and Peiro,* 1983; *Moupfouma,* 1984; 2009; *ITU-R 530-12,* 2007; *Perez Garcia and da Silva Mello,* 2004; *da Silva Mello et al.,* 2007]. Others like *Oguchi* [1973], *Rogers and Olsen* [1976], *Uzunoglu et al.* [1977], *Olsen et al.* [1978], *Mätzler* [2002b] have based their attenuation models on the theoretical microphysical structure of rain. These latter authors have concentrated their efforts on the scattering electromagnetic waves by raindrops and the distribution of raindrops.

All these models are intended for the estimation of rain attenuation, especially in situations where adequate or direct measurements are not available. But because of the complex and the random nature involved in the physical process of rain, it is quite challenging to find a model which is simple and at the same time sufficiently precise to predict the behaviour of radio waves propagating through rain [*Medeiros Filho et al.,* 1986]. Nevertheless, there is a particular need for accurate propagation predictions, because over-prediction of a propagation effect can result in costly over-design of a system whereas, on the other hand, under-prediction can result in a system that is unreliable [*Olsen,* 1999].

This research employs a semi-empirical approach for the modeling and prediction of rain attenuation along a terrestrial radio link. This is achieved by utilizing 5-year rain rate data recorded in 12 different geographical locations in South Africa between the years 2000-2004, and one-year signal level measurement and its corresponding 1-minute rain rate recorded along a horizontally polarized 6.73 km path length at an operating frequency of 19.5 GHz in 2004. The approach in this work also looks into the theoretical formulation of rain attenuation models in which the raindrop size distribution and the scattering effect of electromagnetic waves by raindrops are studied. Furthermore, the characteristics and the variations associated with rain

attenuation in different climatic rain zones in South Africa are studied. Finally, an estimate of the raindrop-size distribution model for different rain classes are determined from six months distrometer measurement recorded in Durban, South Africa.

1.2 Motivation

The ever increasing demands for fast, reliable and flexible broadband communication over wireless (or radio) systems in recent times, has led to the use of higher frequency bands especially in the Ku-bands and above. The utilization of these higher frequency bands provides a number of important benefits; it relieves the congestion in the lower frequency bands; it exploits the larger bandwidths available at higher frequencies so as to accommodate the high demands for broadband services. As attractive and reliable as these frequency bands could be for system operators and radio engineers to implement their technologies, the systems can be easily degraded by some natural atmospheric phenomena [*Asen, et al.,* 2003], of which rain is the principal factor and needs to be appropriately quantified so as to enhance reliable communication [*Freeman,* 1997; *Myers, 1999; Asen, et al.,* 2003].

The effect of rain on radio propagation systems starts to become a major problem at frequencies as low as 7 GHz in areas of heavy rainfall especially in the tropics and equatorial climates; and about 10 GHz in the temperate climates [*Moupfouma et al.,* 1982*; Moupfouma,* 1984; *Green,* 2004]. This is not to assume that other factors such as crosstalk or inter-system interference have become irrelevant; but in a situation where the effect of rain is so severe that a radio link no longer functions, then other factors can be considered as secondary [*Green,* 2004]. The effects of atmospheric ice, cloud or fog are much less when compared to liquid rain [*Freeman,* 1997; *Green,* 2004]. Rain being a natural phenomenon which displays a high degree of spatial and temporal variation along propagation paths from location-to-location, year-to year, season-to-season, and even on monthly basis, causes rain induced attenuation, which is a dominant fading mechanism for higher frequency propagation paths [*Ajayi et al.,* 1996; *Crane,* 1996; *Myers,* 1999].

This means a solid database of propagation measurements should be made as early as possible in the intended geographical area of operations. Attempts have been made by the ITU-R *837* and later by *Crane* [1980; 1996] to classify the globe into climatic rain zones so as to extend existing

propagation data to a wider range of situations. The attenuation results from these models suffer a huge setback when applied to the tropics and equatorial climates. This is because most of the measurements in the databases have been recorded in the Northern Hemisphere's temperate zones [*Green,* 2004]. Much evidence suggests that in the tropical and equatorial zones, the factors that make important contributions to propagation degradation can be quite different from the measurements recorded in the temperate zones [*Green,* 2004]. As stated by *Maagt et al.,* [1993] "*the present ITU-R path attenuation prediction procedure for rain is not as accurate in the tropical climates as it has been found in the temperate."* Hence, this has prompted huge research in the tropical and equatorial climates.

South Africa, which is located in the sub-tropical region of the world [1], possesses some climatic characteristics that at one point, is similar to that of the temperate, and at the other point, similar to that of the tropical climates. This is due to the variation of the climatic conditions of South Africa which ranges from mediterranean in the south-western corner of the country, to temperate in the interior plateau, subtropical in the coastal (with the rain possessing some tropical features in the summer season such as: violent convection storms accompanied by thunder, lightning, sudden squalls and often hail), and a small area in the northwest with a desert climate [2]. Though not much work has been done in South Africa and its environs (sub-tropical); but *Seeber* [1985a; 1985b] proposes a rain rate model based on Southern Africa extreme rain rate data and also classifies South Africa into twelve different climatic rain zones using the Köppen system. *Fashuyi* [2006] and *Fashuyi et al.,* [2006] also determine three additional rain climatic zones (M, P and Q to that of the ITU-R classification of C, D, E, K, and N) for South Africa using a 5-years rain rate data recorded in twelve different geographical locations in South Africa. In 2007, *Owolawi and Afullo* [2007] determined an empirical rain rate distribution model, the seasonal cumulative distribution of rain rate, and the worst month statistics for eight different geographical locations in South Africa [*Owolawi and Afullo,* 2007].

From the above findings, it can be observed that the rainfall in South Africa is very variable in from one geographical location to another, which prompts a great need to establish a model that will be able to predict the effect of this rain on terrestrial line-of-sight links. To be able to tackle this rain-induced propagation effect on terrestrial radio links, a semi-empirical approach is adopted in this study to formulate a rain-induced attenuation model. This is a semi-empirical approach in the sense that it employs a theoretical and an experimental method to estimate the rain-induced attenuation on a terrestrial line of sight link. This is obtained by using the size

distribution and electromagnetic scattering properties of the raindrops. The dielectric properties of the liquid water (raindrop) which is a function of temperature and the propagating frequency of the wave is a key item that is needed here.

This research also employs direct signal level measurements recorded at 19.5 GHz on a horizontally polarized 6.73 km path length in the coastal climatic region of South Africa, Durban, KwaZulu-Natal to develop a rain attenuation model for South Africa and its environs. Also the research determines seasonal and monthly attenuation distributions for four different geographical locations situated in four different climatic rain zones in South Africa. Estimates of raindrop size distribution for different rain types (drizzle, widespread, shower and thunderstorm) are developed from the raindrop size and 1-minute rain rate measurements recorded in Durban with a distrometer for six months.

1.3 Thesis Overview

This thesis is divided into seven chapters. It is aimed at formulating rain attenuation models that will be able to predict the behaviour of radio communication systems in the presence of rain for different geographical locations around the world; investigating the variational patterns associated with the distributions of rain attenuation for different geographical locations situated in different climatic rain zones in South Africa; and to estimate the raindrop size distribution models for the different classes of rain, in South Africa.

Chapter one is an introduction to the research work. The areas covered are: motivation for the study; the thesis overview; the original contributions of the work and the list of publications. Chapter two deals with various propagation phenomena that can affect the transmission of radio wave signals (or electromagnetic waves) on terrestrial communication systems. It also looks into the microphysical structures and properties of raindrops which have led to the study of raindrop size distributions. Specific rain attenuation which is a fundamental quantity in the calculation of rain attenuation statistics is also introduced. The dependence of the specific attenuation models on the scattering properties, drop-size distributions and rain rate statistics is also mentioned. The types of rain, as related to precipitation effects on terrestrial radio links are briefly mentioned.

Chapter three consists of a detailed description of different rain attenuation investigations that have been carried out in different parts of the world. This descriptive part of the thesis is intended

to present a general overview of some terrestrial rain attenuation models that have been proposed experimentally or theoretically by different authors. Rain rate statistics which can also be in the form of rain rate cumulative distribution is discussed, being the starting point of all rain attenuation prediction models [*Crane,* 1996; *COST 255,* 2002; *Moupfouma,* 2009]. Propagation measurements done in different climatic regions which has led to the formulation of rain attenuation model is mentioned; and the validity of these rain attenuation models from one climatic region to another is investigated.

In Chapter four, the signal level measurements recorded at 19.5 GHz over a horizontally polarized 6.73 km terrestrial radio link path for one year, and the 1-minute point rainfall rate recorded concurrently along the path in Durban, South Africa, are utilized to develop empirical rain attenuation models. The monthly rain attenuation models which depict the month-to-month attenuation variability along the path are predicted and analyzed statistically. Also, the rain attenuation models for the entire year are developed for the minimum, average and maximum attenuation values. These models are compared with different established rain attenuation models which have been formulated from available local propagation data in different parts across the globe for the purpose of cross- referencing the results and reflecting the suitability of developed model to other parts of the world. This chapter also looks into the non-rain faded signal level, the average clear-air attenuation for each month in the year and the propagation phenomena contributing to these effects. The time series for received signal levels and the rain attenuation for different features of rain rates (light, moderate, and heavy rains) are also analysed in this chapter.

Chapter five gives a theoretical approach for the calculation of rain attenuation along a terrestrial communication radio link based on the assumption that the raindrops are of a spherical shape. The scattering amplitudes of the spherical raindrops are computed for a wide range of frequencies, and the extinction cross-section calculated. The extinction cross-section calculated at different frequencies for the spherical raindrop sizes are modeled with a power law relation. The power law models generated from the extinction cross-section are integrated over different established raindrop-size distribution models to formulate the rain attenuation models. These models are utilized to compute the specific rain attenuation for four locations situated in different rain climatic zones in South Africa. For the purpose of validating these theoretical attenuation models, the models are compared with the experimental signal level measurement recorded in Durban at 19.5 GHz. And for the purpose of cross referencing, the theoretical models are compared with the ITU-R rain attenuation model and other theoretical rain attenuation models.

Also, this chapter presents brief introduction to raindrop size distribution estimates for different rain types employing the raindrop size measurements recorded in Durban with a distrometer over a period of six months. Longer period of these measurements may be needed in Durban and other geographical locations in South Africa to establish the raindrop size distribution models for this environment.

Chapter six gives a descriptive analysis of the variation and characteristics associated with rain attenuation distributions in South Africa. The chapter looks into the seasonal statistics of rain attenuation in different climatic rain zones in South Africa. This is obtained by utilizing a 5-year locally observed point rainfall data in each zone to estimate the seasonal distributions of rain attenuation for different seasons in each climatic rain zone. From these seasonal distributions, appropriate figures for fade margins are derived, which gives the percentage of time for which a certain attenuation level is exceeded for different seasons in each location. This Chapter also analyses distribution of the attenuation on a monthly basis. From which the monthly fade margin figures are also derived.

Chapter seven presents the summaries drawn from the study and concludes the thesis. Future extensions of the work done in the thesis are also presented.

1.4 Original Contributions

As the title of this thesis implies, *"A Semi-empirical Formulation for Determination of Rain Attenuation on Terrestrial Radio links,"* all the chapters in this thesis have aimed at making significant and original contributions to this topic. Below are the summary of the significant contributions in this work:

- Proposition of empirical monthly rain attenuation models that depict the month-to-month variability of rain attenuation along a terrestrial radio link of 6.73 km path length operating at 19.5 GHz frequency. Development of rain attenuation model along the terrestrial link for the entire year. But due to the varying rain intensity with same signal level strength recorded along the terrestrial path, rain attenuation bounds are proposed. These attenuation bounds depict the maximum, average, and minimum rain attenuation values per rain rate recorded for the entire year along the terrestrial path.

- Formulation of theoretical rain attenuation models for the prediction of specific rain attenuation and rain attenuation on terrestrial radio links from the scattering properties of raindrop and different established raindrop size distribution models. This is achieved by utilizing the Mie scattering theory for dielectric spheres on the raindrops, and some mathematical integration. The findings from these models show that the shape of the raindrop is not a predominant factor for the prediction of rain attenuation but the size of the drops as well as the rainfall rate content of the drop. Preliminary study of raindrop size distribution for different rain types in Durban has also been investigated

- Development of seasonal and monthly rain attenuation distributions from a 5-year locally observed point rainfall data collected in different climatic rain zones in South Africa. From these distributions, fade margins figures are derived on a monthly and seasonal basis at different percentages of time. The rain attenuation distributions analysed in this work is a very valuable tool for System designers and Radio engineers.

1.5 Publications in Journal and Conference Proceedings

Listed here are parts of the materials in this thesis that have been published.

1. **M.O. Fashuyi** and T.J. Afullo, "Modeling of Attenuation Due to Rain at 19.5 GHz for Line-of Sight Radio Systems in South Africa," *In Proceedings of the North American Radio Science Meeting, (URSI 2007),* Ottawa, ON, Canada, ISBN 978-0-9738425-2-4, July 22-26, 2007

2. **M.O. Odedina** and T.J. Afullo, "Rain Attenuation Prediction on Terrestrial Paths in South Africa Using Existing Attenuation Models,*" In IEEE AFRICON 2007 Conference*, ISBN: 0-7803-8606-X, Namibia, September 26-28 2007.

3. **M.O. Odedina** and T.J. Afullo, "Modeling of Rain Attenuation for Terrestrial LOS Radio Systems in South Africa," *In Proceedings of the Southern Africa Telecommunications Networks Applications conference (SATNAC 2007),* Mauritius, ISBN 978-0-620-39351-5, September 9-13 2007

4. **M.O. Fashuyi** and T.J. Afullo, "Rain Attenuation Prediction and Modeling for LOS Links on Terrestrial Paths in South Africa," *Radio Science, Vol. 42* RS5006, October 2007

5. **M.O. Odedina** and T.J. Afullo, "Seasonal Variation of Rain Attenuation on Radio Propagation Paths in South Africa," *In the Proceedings of the XXIX General Assembly of the International Union of Radio Science (URSIGA 2008),* Chicago, Illinois, USA, August 7-15 2008

6. **M.O. Odedina** and T.J. Afullo, "Characteristics of Seasonal Attenuation and Fading for Line-of-Sight Links in South Africa," *Southern Africa Telecommunications Networks Applications conference (SATNAC 2008)* , Wild Coast Eastern Cape South Africa, ISBN 978-0-620-41696-2, 7-10 September 2008

7. **M.O. Odedina** and T.J. Afullo, "Characterization of Rain Attenuation and Its Application to Terrestrial Communication Systems in South Africa," *In the 6th IASTED Conference on Antennas, Radar and Wave Propagation* Banff, Alberta, Canada, ISBN: 978-0-88986-795 -6, July 6-8 , 2009

8. **M.O. Odedina** and T.J. Afullo, "Analytical Modeling of Rain Attenuation and Its Application to Terrestrial LOS Links," *In the Proceedings of the Southern Africa Telecommunications Networks Applications conference (SATNAC 2009),* Swaziland, August 31st -2nd September 2009

9. **M.O. Odedina** and T.J. Afullo, "Determination of Rain Attenuation from Electromagnetic Scattering by Spherical Raindrops: Theory and Experiment" *Radio Science, doi:10.1029/2009RS004192,* January, 2010

Chapter Two

Propagation Effects and Characterization of Rain

2.1 Introduction

There are some basic parameters that affect the propagation of electromagnetic waves in the atmosphere. Some of them are forms of water which appear in the atmosphere in diverse forms, commonly referred to by the term hydrometeors. Hydrometeors include various particles in the atmosphere such as cloud, fog, rain drops, snow, hail and water vapour. Of these, rain, hail and snow are generally referred to as precipitation, and liquid precipitation is referred to as rain [*Crane, 1996; Hall,* 1996]. The atmospheric gases are also part of the parameters that hinders the effective transmission of electromagnetic waves in the atmosphere. The effects that the atmospheric gases and hydrometeors have on radio communication systems are dependent on the system frequency and type of particles present along the radio path [*Hall,* 1996]. For frequencies below 3 GHz, path attenuation due to atmospheric gases, clouds, and rain is small and sometimes neglected, whereas for terrestrial paths, the relatively large vertical antenna beamwidths in use at these frequencies invite problems due to multipath propagation [*Crane,* 2003]. At frequencies greater than 3 GHz, scattering from hydrometeors may cause considerable interference between radio communication systems. At frequencies above 30 GHz, narrow beamwidth antennas may prevent multipath, but path attenuation due to rain will be important [*Crane,* 2003]. In clear air, the refractive, obstacle and vegetation effects may also contribute to the problems affecting the effective propagation of electromagnetic waves.

2.2 Refractive Effects

In clear-air, the radio refractive index[1] for electromagnetic wave propagating through the lower atmosphere (troposphere) is slightly greater than unity (typically about 1.0003). The way in which the index of refraction varies with height has immense effect on radio wave propagation at frequencies greater than 30 MHz. Above 30 MHz the wavelength is comparable to distance over which variations of atmospheric refractive index occur in the troposphere. These variations are due to changes of temperature, pressure and humidity [*Hall,* 1996]. The refractive index of the troposphere generally decreases with height. This leads to slight downward refraction of radio rays, which can be very important for radio communication at VHF, UHF and SHF (See Appendix A-1: nomenclature for frequency bands).

Radio refractivity, N is used to magnify the change in index of refraction from unity (free space or vacuum). According to ITU-R 453 [*ITU-R,* 2003] for the usual frequency range, the atmospheric refractive index, n, may be written as :

$$n = 1 + N \times 10^{-6}, \tag{2.1}$$

where N, is the refractivity and is given by:

$$N = \frac{77.6}{T}\left(p + \frac{4810e}{T}\right) \tag{2.2}$$

where p is the atmospheric pressure (in hPa), e is water vapour pressure (in hPa) and T is the absolute temperature (in K) [*Freeman,* 1997; *Salema,* 2003].

Over a large horizontal area, the refractive index decreases with height, and this may lead to partial reflection of radio energy. Both ducting and partial reflection mechanisms may cause multipath interference on line-of-sight. On line-of-sight paths, these refractive index fluctuations may cause significant scintillation (rapid fading), for longer line-of-sight path or higher frequency [*Hall,* 1996].

[1] A measure of the ability of a medium to bend electromagnetic waves

2.3 Obstacle Effects

Obstacles such as buildings, trees, earth mounds and hills may attenuate the electromagnetic waves depending on the wavelength considered. If the attenuation through the obstacles is high enough, the obstacle will diffract the wave over or around the obstruction [*Crane*, 2003]. Such obstacles can also cause reflection (and multipath), scattering and absorption. The elements of building structures such as walls, floors and roofs, are generally constructed from several different materials, each with its own dielectric and conductivity properties [*Goldhirsh et al*, 1998; *ITU-R 679*, 1999] which may uniquely affect the transmission of electromagnetic waves. The electromagnetic waves are scattered by, reflected from, and transmitted through, buildings.

Windows and doors in buildings have transmission properties that are different from surrounding walls. The calculation of the scattered fields is complex. Measurements have been made to characterize the scattering properties of "typical" building [*Goldhirsh et al*, 1998; *Crane*, 2003]. In a built-up area, the obstacle effects results in a wide variation in electromagnetic field strength [*Hall*, 1996].

A single propagation path between a transmitting antenna and a receiving antenna is a clear line-of-sight path if no obstruction occurs within the first few Fresnel zones about the path. Fresnel zones are enclosed within equiphase ellipsoids enclosing path as seen in Fig. 2-1 [*Crane*, 2003]. The quantitative specifics on the size of the first Fresnel zone are explained in chapter four (Fig. 4-2)

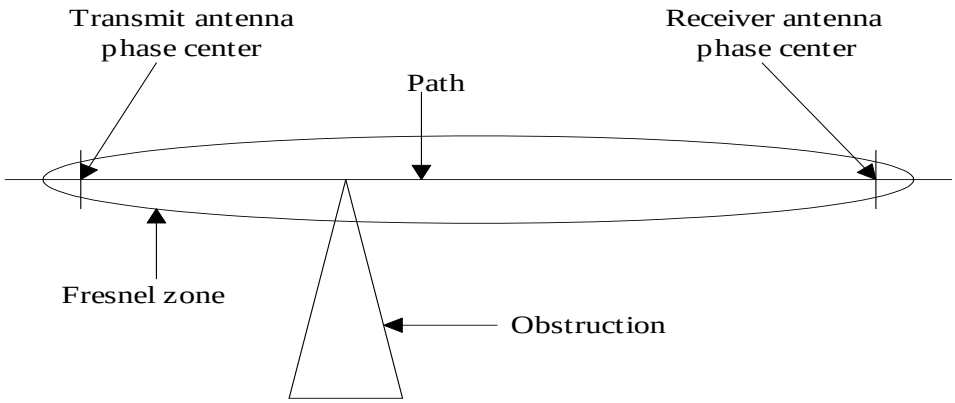

Fig. 2- 1: The Fresnel zone

2.4 Vegetation Effects

The interaction of leaves and branches of individual trees along radio propagation paths tend to scatter the electromagnetic waves [*Crane,* 2003]. This, otherwise known as foliage losses may be a limiting propagation impairment in some cases [*Marcus et al.,* 2005]. Measurements have shown differences in the path loss through forest with season and, at higher frequencies, with the amount of water in and on the leaves [*Burrows,* 1966; *CCIR,* 1986; *Cost 235,* 1996; *Al-Nuaimi,* 1998]. Foliage loss along a propagation path also depends on the number and species of trees along the path (i.e. the foliage depth), and the height and orientation of the propagation path through the leaves [*Crane,* 2003]. An empirical relationship was developed by the in CCIR Report 236-2 [*CCIR,* 1986], (now the ITU-R) from measurements carried out mainly at UHF to predict the foliage loss. For the case where the foliage depth $d < 400\ \mathrm{m}$, the loss is given by [*CCIR Rpt 236-2,* 1986]:

$$L_{ITU-R}(dB) = 0.2 f^{0.3} d^{0.6} \tag{2.3}$$

where f is the frequency in MHz, and d is the depth of the foliage in meters and applies for $d < 400\ \mathrm{m}$.

The COST 235 model was also developed based on measurements made in millimeter wave frequencies (9.6 –57.6 GHz) through a small foliage depth of $d < 200\ \mathrm{m}$ over two seasons, when the trees are in-leaf and out-of-leaf and are given by [*COST 235,* 1996]:

$$L_{COST}(dB) = \begin{cases} 26.6 f^{-0.2} d^{0.5} & \text{out-of-leaf} \\ 15.6 f^{-0.009} d^{0.26} & \text{in-leaf} \end{cases} \tag{2.4}$$

where f is the frequency in MHz, and d is the depth of the trees (or foliage) in meters. Both relationships, (i.e. the ITU-R and the COST models) are commonly used for frequencies in the range of 200 MHz to 95 GHz [*Marcus et al.,* 2005; *Meng et al.,* 2009].

From the above empirical relationship, it can be deduced that the vegetation induced loss along radio propagation paths can be represented by this expression:

$$L_{foliage}(dB) = Af^{B}d^{C} \tag{2.5}$$

where $A, B,$ and C are parameters which can be determined empirically depending on the type of foliage, propagating frequency and the distance [*Meng et al.,* 2009].

2.5 Atmospheric Gases Effects

The propagation of electromagnetic waves along the earth's surface through a clear atmosphere is subject to attenuation due to absorption by oxygen and water vapour [*Hogg,* 1968]. These effects are greater at certain frequencies, coinciding with the mechanical resonant frequencies of gas molecules [*Marcus et al.,* 2005]. Other gases such as N_2O, SO_2, O_3, NO_2 and NH_3 display resonant lines as well, but because of their low density in the atmosphere, they have negligible effect on propagation [*Freeman,* 1997]. Fig. 2-2 below shows the specific attenuation due to oxygen and water vapour as a function of frequency. Calculations of this figure are at 7.5 g/m^3 water vapour density and 20^{O}C temperature [*Crane,* 1996]. A single water vapour (H_2O) absorption lines occurs at 22.235 GHz and a complex of oxygen (O_2) lines is between 30 – 70 GHz frequency bands [*Crane,* 1996].

For current technology, the important absorption peaks occur at 24 and 60 GHz [*Marcus et al.,* 2005]. The frequency regions between the absorption lines or complexes of lines are called atmospheric windows [*Crane,* 1996]. The spectral regions between the absorption peaks provide windows where propagation can more readily occur. The transmission windows are at 35, 94, 140 and 220 GHz [*Marcus et al.,* 2005]. As the windows become congested from the deployment of a large number of systems, designers are forced to migrate to higher and higher frequencies. At frequencies above 100 GHz, the absorption line structure become more complex with significantly stronger water vapour lines occurring at 183, 325, and 380 GHz [*Liebe,* 1989].

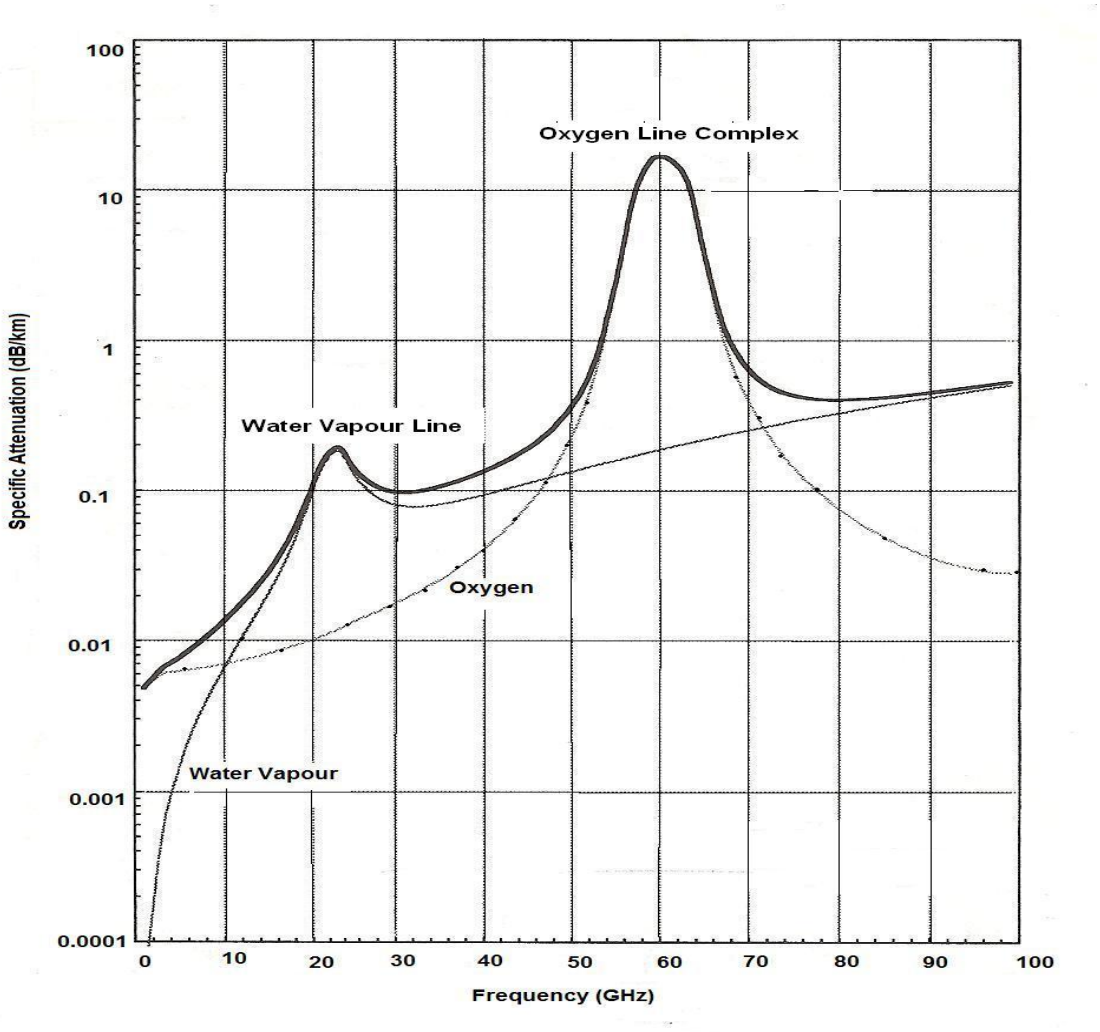

Fig. 2- 2: Specific attenuation caused by oxygen and water vapour at sea level [Crane, 1996]

2.6 Rain Effects

Rain has long been recognized as one of the principal causes of attenuation on electromagnetic wave propagation paths through the lower atmosphere [*Hogg*, 1968; *Crane*, 1980]. Scattering from raindrops may produce significant path attenuation at frequencies just above 10 GHz in most temperate climates and as low as 7 GHz in tropical and equatorial climates due to larger raindrops in the later [*Moupfouma*, 1984; *Crane*, 2003]. Fig. 2-3 shows the variation of specific attenuation with frequency with rain rates 1, 10 and 100 mm/h calculated for spherical raindrops at 0^{O}C and *Laws and Parsons* [1943] drop-size distribution.

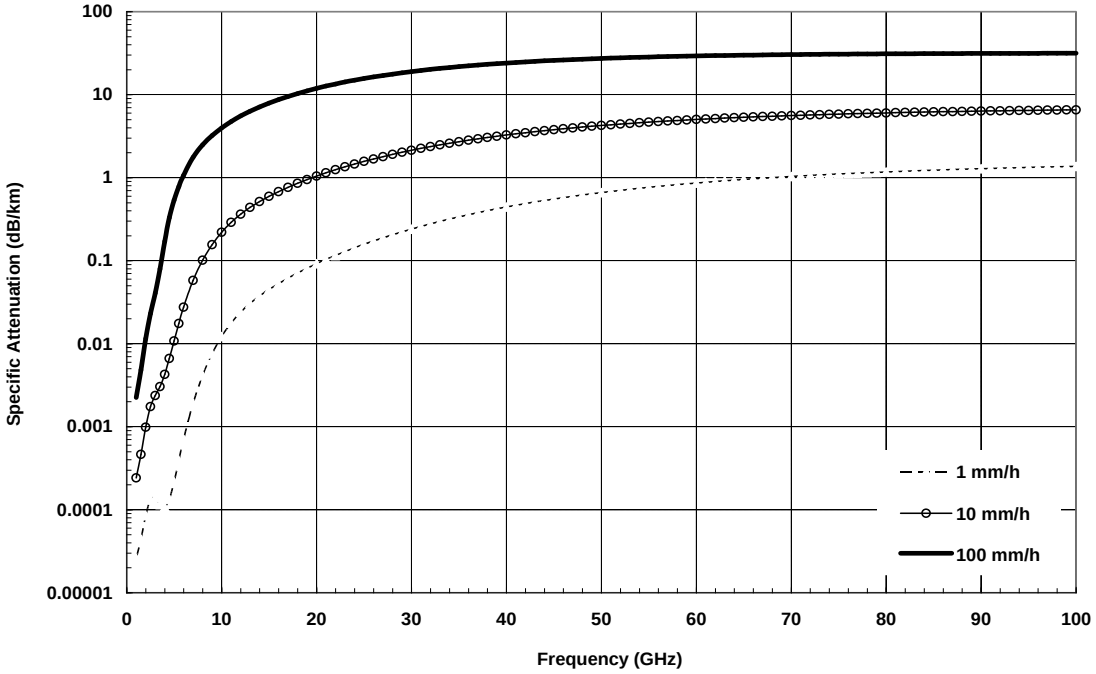

Fig. 2- 3: Specific attenuation caused by rain

In contrast to absorption by atmospheric gases, the attenuation produced by rain increases nearly monotonically with frequency throughout the 1-100 GHz range. The specific attenuation values reach a maximum and then slowly decrease as frequency continues to increase. This is due to the fact that raindrops which give large attenuation fail to follow the electric field alternations which are very fast at higher frequencies [*Mondal et al.*, 1999].

At 100 mm/h, the maximum attenuation occurs at about 40 GHz. At lower rain rates the maximum attenuation is reached at frequencies above 100 GHz [*Crane*, 1996]. In the range 1-100 GHz, no frequency window regions occur. Fortunately it does not rain all time and the occurrence of 100 mm/h rain rate is very uncommon [*Crane*, 1996]. The lower the frequency, the better the system designs. An increase in the rain factor reduces the communication signal availability.

2.7 Fog and Clouds Effects

Fog particles are supersaturated air in which some of the water has precipitated to form water droplets whose sizes are less than 0.1 mm in diameter [*Altshuler,* 1984]. Cloud particles are

defined by a size small enough to move very slowly relative to the air surrounding them. Fog particles are considered to be the same as cloud particles, the difference being that fogs are clouds in contact with the ground [*Crane,* 1996]. Scattering by the very small liquid water droplets that make up liquid water fogs near the earth's surface and liquid water clouds higher in the atmosphere can produce significant attenuation at the higher frequencies. Clouds in the most active parts of mid-latitude thunderstorms may have liquid water content in excess of 5 g/m^3. The liquid water heights in the atmosphere can range from 0 km above ground (fog) to 6 km above ground in the strong updrafts in convective clouds [*Crane,* 2003].

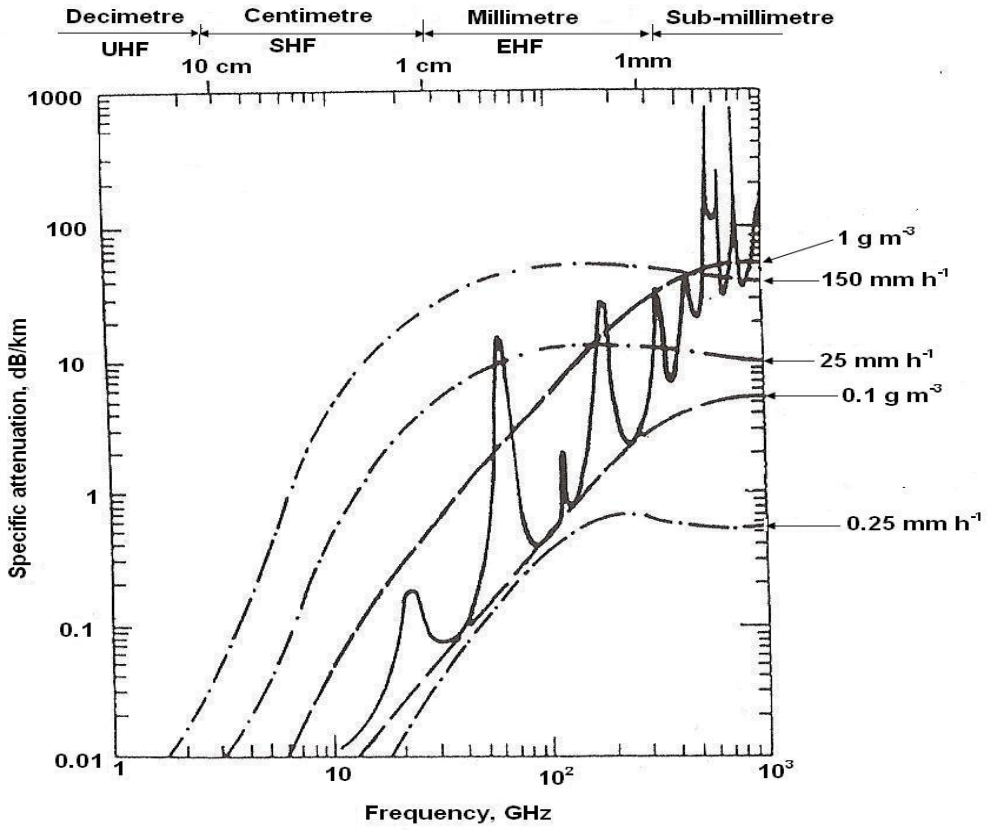

Fig. 2- 4: Comparison of specific attenuation due to gaseous constituents, fog and rain [Hall, 1996]

Key:

Gaseous attenuation assuming 1013 mb, 20^{O}C, 7.5 g/m^3

Fog attenuation for water contents shown at 20^{O}C

Rain attenuation for rates shown

Fig. 2-4 shows the comparison of specific attenuation due to gaseous constituents, fog, and three levels of rainfall rate which correspond to light drizzle, moderate rain and very intense rain [*Hall*, 1996]. The fog attenuation increases monotonically with frequency through the UHF, SHF, and EHF frequency bands as seen from Fig. 2-4. For frequencies lower than 10 GHz, cloud (fog) attenuation can be ignored. At a frequency of 30 GHz, cloud (fog) attenuations may approach 3 to 4 dB. At a frequency of 120 GHz, this result approaches 30 to 40 dB [*Crane*, 2003].

2.8 Loss in Free Space

In order to define the loss between the transmitting and receiving antenna separated by a particular distance we assume that the transmission medium between the transmitter and receiver is a vacuum. The antenna at each end of the link is assumed to be isotropic, so that we can say a point source is an isotropic source[2] [*Freeman*, 1997]. Let the total power in watts radiated by the source be P_T. The envelope containing the radiation around the source can be considered to be an expanding sphere of radius r. The net power flow through the surface of a sphere at its center point is also P_T, therefore, it follows that the power flow per unit area through any portion of the sphere's surface is given by [*Freeman*, 1997] :

$$P_{av} = \frac{P_T}{4\pi r^2} \tag{2.6}$$

For an isotropic antenna, the effective area A_R, located on the surface of the sphere is $\lambda^2/4\pi$, where λ is the wavelength of the incident radiation field. From equation (2.6) it then follows that an isotropic antenna situated in a radiation field with a power density of P_{av} will deliver into its load, a power P_R given by:

$$P_R = P_T\left(\frac{\lambda}{4\pi r}\right)^2 \tag{2.7}$$

The transmission loss between transmit and receive antennas is defined as:

[2] An isotropic source radiates uniformly in all directions (i.e. has a gain of 1 or 0 dB). [*Freeman*, 1997]

$$L_{FSL}(dB) = 10\log\frac{P_T}{P_R} \tag{2.8}$$

Combining equations (2.7) and (2.8), the loss in free space can be given as:

$$L_{FSL}(dB) = 20\log\left(\frac{4\pi r}{\lambda}\right) \tag{2.9}$$

Equation (2.9) can be restated in a more useful form:

$$L_{FSL}(dB) = 32.45 + 20\log r_{km} + 20\log F_{MHz} \tag{2.10}$$

where r_{km} is the distance, in kilometers, between transmit and receive antennas, and F_{MHz} is the frequency of the emitted radio field in megahertz [*Freeman,* 1997].

2.9 Scattering of Electromagnetic Waves by Raindrops

When an electromagnetic wave propagates through a medium containing raindrops, part of its energy is absorbed by the raindrops and dissipated as heat, and the remainder is scattered in all directions [*Hogg*, 1968; *Medeiros Filho et al.,* 1986; *Cermak et al.,* 2005]. This scattered part introduces unwanted or interfering signals into the communication receiver that may mask the desired signal [*Crane*, 1996], thereby causing attenuation (reduction of signal strength or power). Fig. 2-5 shows the scattering and the absorption effect of radio wave when it is incident on a rain-filled medium. At wavelengths long compared with the drop-size, absorption will be greater; while at shorter wavelengths, scattering will be predominant [*Hogg,* 1968; *Ajayi,* 1989]. How scattered or absorbed the electromagnetic wave can be depends on the raindrop size, shape and the materials of which the raindrop is made up of [*Bohren, et al.,* 2004]. The attenuation experienced by a radio wave crossing a rainy medium is given by the sum of the individual contributions of the drops that constitute the medium. Since rainfall consists of drops of various dimensions, the specific attenuation is calculated by integrating each raindrop contribution [*Hogg,* 1968; *Ajayi et al,* 1996; *Sadiku,* 2000].

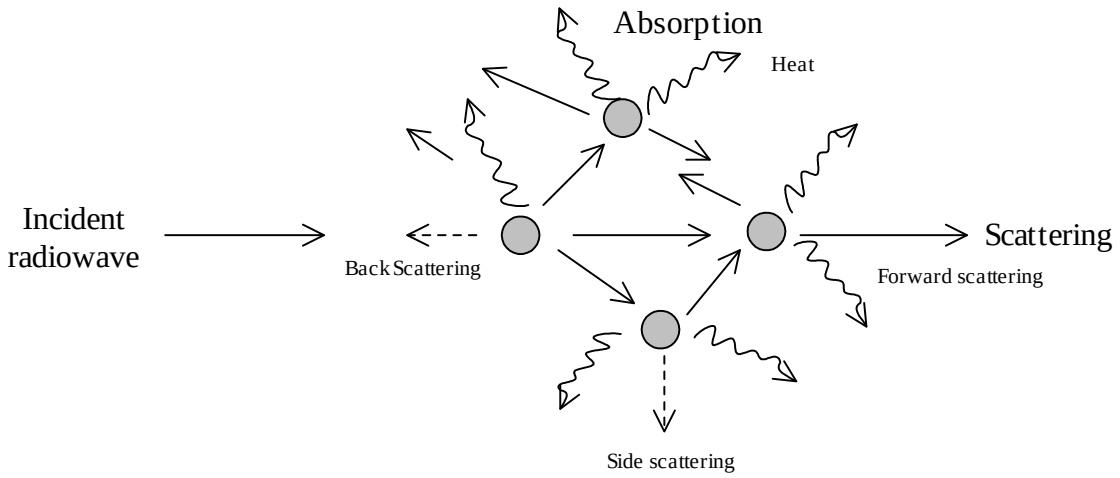

Fig. 2- 5: Interaction of an incident radio wave in a rain-filled medium

2.9.1 Propagation Phenomena in Raindrops

Basically, an electromagnetic wave can propagate through the following media [*Sadiku,* 2007]:

i. Free space ($\sigma = 0, \varepsilon = \varepsilon_0, \mu = \mu_0$)
ii. Lossless dielectrics ($\sigma = 0, \varepsilon = \varepsilon_r \varepsilon_0, \mu = \mu_0 \mu_r$, or $\sigma \ll \omega\varepsilon$)
iii. Lossy dielectrics ($\sigma \neq 0, \varepsilon = \varepsilon_r \varepsilon_0, \mu = \mu_0 \mu_r$)
iv. Good Conductors ($\sigma = \infty, \varepsilon = \varepsilon_0, \mu = \mu_0 \mu_r$ or $\sigma \gg \omega\varepsilon$)

where σ is the conductivity, ε_0 and μ_0 are the free space permittivity and permeability respectively, ε_r and μ_r are the relative permittivity and permeability of the medium and ω is the angular frequency of the wave.

From the study of these four media, it is observed that the attenuation constant γ in free space and lossless dielectric is equal to zero [*Sadiku,* 2007]. Therefore, if a material is made up of these two media, no attenuation effects will be recorded. Lossy dielectrics can be regarded as a partially conducting medium with attenuation constant $\gamma \approx \frac{\sigma}{2}\sqrt{\frac{\mu}{\varepsilon}}$. Therefore, in this type of medium some significant attenuation effects will be noticed if an electromagnetic wave propagates through it [*Sadiku,* 2007]. For a good conductor which has conductivity $\sigma \approx \infty$, its

attenuation constant α is equal to the phase constant β which is equal to $\sqrt{\pi f \mu \sigma}$ [*Pozar,* 1988; *Sadiku,* 2007].

From the above description, raindrop can be assumed to be made up of either lossy dielectric or a good conductor, because both dielectrics possess an attenuating factor, which means an electromagnetic wave loses its power as its propagates through the medium. Checking for the conductivity of these dielectrics, a medium is regarded as a good conductor if $\sigma \gg \omega\varepsilon$ or the loss tangent, $\frac{\sigma}{\omega\varepsilon} \gg 1$. Estimating the conductivity of rain (water) drops, taking the operating frequency f to be 10 GHz, relative permittivity ε_r of water (distilled) is 81; conductivity σ is 10^{-4} s/m and ε_0 is $\frac{10^{-9}}{36\pi}$ F/m [*Sadiku,* 2007]. Therefore,

$$\frac{\sigma}{\omega\varepsilon} = \frac{10^{-4}}{\left(2\times\pi\times10^{9}\right)\left(\frac{10^{-9}}{36\pi}\times 81\right)} = 2.2\times10^{-5} \qquad (2.11)$$

Since $2.2\times10^{-5} \ll 1$, then raindrop can not be regarded as a good conductor but as a lossy dielectric.

2.9.2 Size and Shapes of Raindrops

The knowledge of drop shape and their variation with drop size is essential for the calculation of scattering and extinction cross-sections in the formulation of rain attenuation. Rain consists of drops of various sizes which vary from the smallest drops comparable to those found in clouds to relatively large drops [*Hogg,* 1968; *Medeiros Filho et al.,* 1986]. The size of raindrop diameter ranges from about 0.1 mm to 7.0 mm [*Cermak et al.,* 2005]. Raindrops larger than about 7.0 mm may be hydro-dynamically unstable and so break up very easily due to the influence of surface tension and aerodynamic forces around the drop as they fall to the ground [*Pruppacher and Beard,* 1970]. This effect tends to distort the shape of the raindrop from its original normal spherical shape. This is more pronounced on larger raindrop diameters because of the free fall nature of rain which assumes a flattened shape at the bottom and rounded on the top [*Pruppacher and Pitter,* 1971]. With this effect, the shape of the raindrop is said to be oblate spheroid [*Medeiros Filho et al.,* 1986].

It has been observed that raindrops with small diameter $D \leq 0.3\,\text{mm}$ have no measurable distortion from the primitive spherical shape [*Pruppacher and Beard,* 1970]. The study by *Pruppacher and Pitter* [1971], further shows that for drop diameter $D > 4.0\,\text{mm}$, a concave depression begins to form at the center of the flattened base [*Pruppacher and Pitter*, 1971], and the flattening base of drop becoming more pronounced as the drop sizes increases [*Beard and Chuang*, 1987]. The spherical raindrop constitutes a first-order approximation of raindrop shape and a higher order approximation consists of modeling the raindrops as oblate spheroids [*Medeiros Filho et al.,* 1986]. The oblate spheroid has a horizontal principal axis and its symmetry axis is close to the vertical. An electromagnetic wave passing through it will experience higher attenuation along its horizontal axis than along the vertical axis [*Ajewole et al*, 1997; *Myers*, 1999]. In all, the shape of the raindrop does not alter the volume of the liquid water content present, hence the definition of the equivolumetric sphere or spheroid [*Ajewole*, 1997].

Therefore, calculations used in this study to develop rain attenuation models employ the equivolumetric or effective diameter D or effective radius $\bar{a}$, and can be simply referred to as drop diameter or radius, where $\bar{a} = (1/2)D$. The attenuation calculation has been observed to improve with increasing frequency as the smaller raindrops are those that contribute most to the attenuation in the higher frequency range [*Medeiros Filho et al.,* 1986]. This has been verified in the dual-polarised radar measurements reported by *Hall* [1981] and later by *Moupfouma et al.* [1990], who explains that at high microwave frequencies, the attenuation is greatly influenced by the mean and small raindrops, which are more numerous than large raindrops.

2.10 Specific Rain Attenuation

Specific rain attenuation A (dB/km) or attenuation per unit distance is a fundamental quantity in the calculation of rain attenuation statistics [*Olsen et al.,* 1978]. The specific rain attenuation at any point in space depends upon the rain rate at that point through the properties characterizing the rain such as shape, size, orientation, temperature, size distribution of the rain drop [*Uzunoglu et al,* 1977] and the properties of the incident electromagnetic wave (such as the frequency, polarization and the direction of propagation) at that point [*Crane*, 1996]. The specific rain attenuation has been estimated theoretically by employing a uniformly random distribution of raindrops modeled as water spheres based on the Mie scattering theory [*Mie,* 1908] by various authors: *Medhurst* [1965], C*rane* [1971, 1974], *Rogers et al* [1976], *Mätzler* [2002a; 2003] or

more complex shapes which makes it to be modeled as oblate spheroids [*Olsen*, 1978; *Medeiros Filho et al.*, 1986]. And in the latter case, the scattering solution is more complex and has been studied by *Oguchi* [1973], *Morrison and Cross* [1974], *Uzunoglu et al.,* [1977], *Holt et al.,* [1978], etc.

Besides the shape of the rain drops, the specific rain attenuation, A, depends on the forward scattered electromagnetic wave (and its effects are influenced by the water temperature, the refractive index of water and the radio link operating frequency) from which the extinction cross-section is calculated; as well as the distribution of the raindrops [*Ajayi et al.,* 1996]. Then A is given by:

$$A = 4.343 \int_0^\infty Q_t(D) N(D) dD \qquad \text{dB/km} \tag{2.12}$$

where $Q_t(D)$ is the extinction cross-section, $N(D)$ is the raindrop size distribution, and $N(D)dD$ is the number density of raindrops with equivalent diameter D in the interval dD [*Ajayi et al.,* 1996].

$Q_t(D)$ can be determined theoretically from either Rayleigh approximations for small rain drop radii compared to the wavelength of the scattered electromagnetic wave (frequencies between 1 and 3 GHz) or from the Mie scattering theory which is valid for spherical drops of various sizes for frequencies above 3 GHz [*Ajayi et al.,* 1996; *Cox et al,* 2002]. $Q_t(D)$ is a function of drop-size diameter, wavelength and complex refractive index m of the water drops [*Ajayi et al.,* 1996].

The specific rain attenuation A has been found to be empirically related to the rainfall rate through a power law equation which is an alternative way of calculating rain attenuation [*Olsen et al*, 1978; *Zhang et al.,* 1999]:

$$A(dB/km) = kR^{\alpha} \tag{2.13}$$

where the power law parameters k and α are functions of frequency, rain temperature and polarization of the wave, and R is the rain rate (mm/h) [*Olsen et al,* 1978] .

Fedi [1979] and *Maggiori* [1981] calculated the values of k and α for frequency range 1 to 400 GHz for drops with assumed shape of oblate spheroids at 20^{O}C using the *Laws and Parsons* [1943] raindrop size distribution, *Gun and Kinzer* [1949] terminal velocity and the complex refractive index according to the model of *Ray* [1972]. Because of the simplicity of the power law relation, it has subsequently been used by several authors, system designers and also been adopted by the Radio Communication study group of the International Telecommunication Union as a standard [*ITU-R 838-3,* 2005]. The ITU-R 838-3 determined the power law values for k and α as a function of frequency in the range of 1 to 1000 GHz (See Appendix A-2); these were developed from curve fitting of the scattering calculations. The values of k and α have been tested and found to be reasonably accurate for the prediction of specific rain attenuation for frequencies up to 55 GHz [*Zhang et al.,* 1999].

To find the values of the power law parameters k and α for both horizontal and vertical polarization for frequency f which lies in between discrete frequencies in [*ITU-R 838-3,* 2005], logarithmic interpolations are used for f and k, and linear interpolation for α. If k_1, k_2, α_1, and α_2 are the values at frequencies f_1 and f_2 to be interpolated in order to have the power law parameters values at frequency *f*, then [*Ajayi et al.,* 1996]:

$$k(f) = \log^{-1}\left\{\log\frac{k_2}{k_1}\times\left[\frac{\log(f/f_1)}{\log(f_2/f_1)}\right]+\log k_1\right\}$$
$$\alpha(f) = \left\{\left[\alpha_1-\alpha_2\right]\times\left[\frac{\log(f/f_1)}{\log(f_2/f_1)}\right]+\alpha_1\right\} \qquad (2.14)$$

2.11 Rainfall Rate

Rainfall rate (or rain rate) can be expressed as the rate at which water reaches the ground or the rate of accumulation of water per unit time [*Ajewole,* 1997]. The contribution of a drop of water of mass M_i to the rain rate R is given as [*Battan,* 1973]:

$$R = M_i(\mu_v - \mu_u) \qquad (2.15)$$

where μ_v is the terminal velocity of the rain drop, and μ_u is the updraft rate of the rain drop

To compute the rain rate from a unit volume of air, R value should be integrated over all the drops in the volume. But when all the particles are of the same size, the rain rate can be written as:

$$R = \frac{4}{3}\pi\rho a^3 N(\mu_v - \mu_u) \tag{2.16}$$

where N is the concentration of particles of density ρ.

In a general case where rain consists of drops of various sizes, rain rate from a unit volume of air can be written as:

$$R = \frac{4}{3}\pi\rho\int_{a=0}^{a=\infty} a^3 N(a)v(a)da \tag{2.17}$$

where $v(a)$ is the terminal velocity of the raindrop radius a, $N(a)da$ is the number of drops of radius between a and $a + da$ per unit volume [*Battan,* 1973]. Equation (2.17) must be divided by density of water $\rho = 1gcm^{-3}$ so that the unit of rain rate R will remain as length/time.

In a more recent notation, equation (2.17) can be expressed as [*Medeiros Filho et al.,* 1986; *Ajayi et al.,* 1996]:

$$R = 6\pi \times 10^{-4}\int_0^{\infty} D^3 N(D)v(D)dD \qquad \text{mm/h} \tag{2.18}$$

Equation (2.18) gives the relationship between rainfall rate and raindrop size, where $v(D)$ is the terminal velocity of the raindrops in ms^{-1} tabulated by *Kerr* [1951], D is the diameter of the raindrop in mm, and $N(D)$ is the drop-size distribution in $mm^{-1}m^{-3}$.

2.12 Raindrop Size Distributions

A realistic rainfall rate consists of drops of various sizes (rather than identical drops) [*Hogg,* 1968; *Sadiku,* 2001]. Due to the complexity involved in the physical formation of rainfall, and its

spatial and temporal variability, it is therefore quite challenging to find a model that is simple and at the same time relatively precise to describe the distribution of raindrop [*Rogers et al.,* 1976; *Medeiros Filho et al.,* 1986]. However, the need to know the raindrop size distribution governing a given rain intensity is paramount, the reason being that it is one of the major parameters required for the modeling and calculation of rain attenuation. A raindrop size distribution is commonly represented by the function $N(D)$, the number concentration of raindrops with diameter D in a given volume of air. Many researchers have proposed different methods to determine raindrop size distribution in different climatic regions. What follows is a brief description of some methods that have been employed to describe the distribution of raindrop sizes.

The first direct measurement of raindrop sizes is dated back to as early as 1895 in Germany by Weisner. The raindrop size measurements were undertaken by exposing sheets of filter paper dusted with water soluble-dye to rain for a brief time interval. The impact of the sheet with raindrop created a spot marked permanently by the dye. A known empirical relation was then utilized to convert the size of the spots on the filter paper into the size of the actual raindrops. However, there are some inconsistencies in this method due to the occurrence of larger raindrops which splatter upon impact filter paper; and this makes it difficult to determine their exact size [cited in *Laws and Parsons,* 1943].

Another common method was the flour method proposed by *Laws and Parsons* [1943] for several rain types in Washington DC. In this method, a pan containing fine flour was exposed to rain for few seconds. After a while, each raindrop forms a dry, hard pellet. A known relationship between the size or mass of the dried pellets and the size of the raindrops are used. *Laws and Parsons* employed this method for different types of rain. The *Laws and Parsons* [1943] distribution has been found to be a good representation of the mean drop-size distribution especially in the continental temperate regions. This method is currently adopted by the ITU-R for the calculation of rain attenuation [*Ajayi and Olsen,* 1985; *Adimula et al.,* 1996; *Ajayi,* 1996]. *Marshall and Palmer* [1948] showed that their measurements recorded in Ottawa and that of *Law and Parsons* [1943] can be modeled using negative exponential relation to describe the drop-size distribution [*Green,* 2004].

2.12.1 Negative Exponential Drop-size Distribution

Distributions which describe the raindrop size variations in terms of analytical expression were first proposed by *Marshall and Palmer* [1948] and later by *Joss et al.,* [1968] for different types of rain. The functional form of the negative exponential raindrop size distribution can be expressed [*Marshall and Palmer,* 1948] as:

$$N(D) = N_0 \exp(-\Lambda D) \quad \text{and}$$
$$\Lambda = \alpha \mathrm{R}^{-\beta} \tag{2.19}$$

where $N(D)$ in $\mathrm{mm}^{-1}\mathrm{m}^{-3}$ is the number of drops with diameters in mm from D to $D + dD$ per unit volume of space, N_0 in $\mathrm{mm}^{-1}\mathrm{m}^{-3}$ is the number of drops with diameter 0 (corresponds to the lowest diameter of 0.36 mm in the distrometer RD-80) on the exponential approximation (or the intercept parameter) and Λ in mm^{-1} is the exponential fitting coefficient (or the slope) which tends to increase with rain rate, R is the rain rate in $\mathrm{mmh}^{-1,}$ and α and β are the power law coefficients for the slope Λ parameter [*Marshall and Palmer,* 1948; *Konwar,* 2006].

From the measurements of *Marshall and Palmer* [1948], it was found that $N_0 = 8000\,\mathrm{mm}^{-1}\mathrm{m}^{-3}$ and $\Lambda = 4.1R^{-0.21}$ for all rain types. The *Marshall and Palmer* [1948] distribution is particularly close to the *Law and Parsons* [1943] distribution so much so that researchers regard it to be most applicable to widespread rain especially in the continental temperate regions [*Rogers,* 1976; *Fang et al.,* 1982].

In 1968, *Joss et al.,* measured raindrop size distribution with a distrometer in Locarno, Switzerland, and observed that the distribution of the drops varies considerably with different rain types. They classified rainfall into three types; drizzle, widespread and thunderstorm. The drizzle drop distribution is associated with very light widespread rains which mostly consist of small drops with maximum rain rate of about 2.5 mm h^{-1}. On the other hand, the thunderstorm distribution describes drop-size distribution for convective rains with relatively high concentration of large drops [*Joss et al.,* 1968]. The values for N_0 and Λ for drizzle, widespread and thunderstorm types of rain are shown in Table 2-1 below.

Table 2- 1: Joss et al., values for N_0 and Λ for different rain types [Joss et al., 1968]

TYPE OF RAIN	N_0	Λ
Drizzle	30,000	$5.7R^{-0.21}$
Widespread	8000	$4.1R^{-0.21}$
Thunderstorm	1,400	$3.0R^{-0.21}$

The negative exponential drop-size distribution has been the most tested and reasonably well verified distribution to describe most drop-size spectra fairly well. This is because of its parameters (N_0 and Λ) which can easily be modified depending on the rain rate intensity or rain type [*Rogers et al.,* 1976]. In addition to this, the work of *Srivatava* [1967] and *Young* [1975] have highlighted the theoretical support for this distribution. Many authors have preferred the 2-parameter exponential distribution (N_0 and Λ), for its simplicity, and non-restriction to the N_0 value [*Feingold et al.,* 1986]. The sudden increase or decrease in the value of N_0 can be explained as the transitions from one rain type to another. Thus, time variations in raindrop size distributions are usually expressed as N_0 jumps [*Waldvogel,* 1974]

Though this distribution can be very attractive for its simplicity, it fails to fit observed instantaneous spectra (sampling time 1 minute or less) with reasonable accuracy and generally tends to exaggerate the number of both the smallest and the largest drops [*Waldvogel,* 1974; *Joss and Gori,* 1978; *Ajayi and Olsen,* 1985]. Drop size distributions tend to be exponential only when the sampling time is sufficiently long [*Joss and Gori,* 1978]. The 2-parameter negative exponential distribution has its limitations as mentioned, but the inherent assumption is that raindrop size distributions are exponential [*Feingold et al.,* 1986].

2.12.2 Gamma Drop-size Distribution

The gamma drop-size distribution was proposed so as to achieve a drop-size distribution with functions showing improved flexibility than the negative exponential distribution [*Feingold et al.,* 1986]. This distribution is generally referred to as a modified negative exponential distribution (or modified gamma distribution), in contrast to the negative exponential; it tends to correct the exponential increase of the raindrop number density when diameter $D \Rightarrow 0$ [*Ajewole,* 1997]. Numerous authors like *Diermendjian* [1969], *Takeuchi* [1978], *Ulbrich* [1983], *Willis* [1984] have expressed the gamma distribution as a 3-parameter equation given as:

$$N(D) = N_0 D^{\mu} \exp(-\Lambda D) \tag{2.20}$$

with μ, N_0, and Λ being the three parameters. Where the exponent μ defines the shape or curvature parameter of the distribution which can either have negative or positive value, Λ is the slope parameter of the distribution in mm^{-1}, N_0 is the number of raindrops in $m^{-3}mm^{-1}$, μ is dimensionless [*Konwar, et al,* 2006], and D is the drop diameter in mm. Deviations from the exponential distribution are expressed in terms of the curvature parameter μ. If $\mu = 0$, the distribution reduces to an exponential distribution [*Feingold et al.,* 1986].

de Wolf [2001] gave the coefficients for the gamma distribution fit to the measurements of *Laws and Parsons* [1943]. The parameters are given as:

$$\begin{aligned} N_0 &= 1.98 \times 10^4 \ \text{m}^{-3}\text{mm}^{-1-\mu} \\ \mu &= 2.93, \text{ and} \\ \Lambda &= 5.38 R^{0.186} \ \text{mm}^{-1} \end{aligned} \tag{2.21}$$

For a given rain rate R in mm h^{-1}, the complete gamma function can be expressed as [*Maitra,* 2000; *Tseng et al.,* 2005]:

$$N(D) = N_0 \left\{ \frac{\Lambda^{\mu+1}}{\Gamma(\mu+1)} D^{\mu} \exp(-\Lambda D) \right\} \tag{2.22}$$

where mean $\bar{x} = \mu + 1/\Lambda$ and the variance $\sigma^2 = \mu + 1/\Lambda^2$ and $\Gamma(n+1)$ is the complete gamma function [*Maitra et al.* 2005] .

When drop-size spectra are dominated by large number of small to medium sized rain drops, with very few larger drops, the three parameters μ, N_0 and Λ are large values. On the other hand, if the drop spectra are dominated by larger number of large drops, the three parameters give smaller values [*Tokay and Short,* 1996]. Table 2-2 below shows an example of gamma raindrop size distribution parameter values for different rain rate as categorized by *Tokay and Short* [1996] in Kapingamarangi Atoll (~1.00^{O}N, 154.8^{O}E). *Ulbrich and Atlas* [1984] have further shown that

there is an improved accuracy in the drop-size distribution if drop spectra are described with gamma distribution. The gamma distribution can be viewed as a reasonable choice to approximate observed drop spectra for a given rain rate [*Tokay and Short,* 1996].

Table 2- 2: The gamma raindrop size distribution parameters for different rain rate [Tokay and Short, 1996].

Rain rate category	Rain rate (mm/h)	Raindrop Spectra	N_0 ($m^{-3}mm^{-1}$)	Λ (mm^{-1})	μ
Very light	$R<1$	3009	5.29×10^3	4.7	1.7
Light	$1\le R<2$	1246	1.31×10^4	4.7	2.3
Moderate	$2\le R<5$	1715	2.41×10^4	4.7	2.9
Heavy	$5\le R<10$	901	8.01×10^4	5.2	3.9
Very heavy	$10\le R<20$	392	3.32×10^5	6.3	6.1
Extreme	$R\ge20$	342	4.26×10^5	6.8	8.9

2.12.3 Lognormal Drop-size Distribution

Due to the shortcomings of the negative exponential and the gamma raindrop size distributions especially when applied to tropical and equatorial rain climates, a number of investigators such as *Levin* [1971] *Bradley and stow* [1974], *Markowitz* [1976], *Harden et al.*, [1978], *Ajayi and Olsen* [1985], *Feingold and Levin* 1986], *Zainal et al.,* [1993] *Adimula and Ajayi* [1996] have studied the lognormal distribution to describe the drop-size spectra. They observed that the lognormal distribution is suitable for a broad range of applications and that it reflects the behaviour of small raindrops and facilitate interpretation of the physical process that controls the shape of the drop-size spectra [*Cerro et al.,* 1997; *Konwar et al.,* 2006]. A general form of the lognormal distribution is given by:

$$N(D)=\frac{N_T}{(2\pi)^{0.5}\sigma_g D}\left\{\exp-\left[\frac{1}{2}\frac{\ln(D)-\mu_g}{\sigma_g}\right]^2\right\} \qquad (2.23)$$

where N_T, σ_g and μ_g are the three parameters describing the characteristics of the drop spectra.

The lognormal distribution has a distinct advantage, in the sense that, if the number of drops per unit volume per unit size is lognormally distributed, then the parameters (N_T, σ_g and μ_g) will be linearly related to the moments of the drop-size distribution [*Feingold et al.,* 1986; *Timothy et al.,* 2002]. Furthermore, the three parameters of the lognormal distribution have direct physical meaning; N_T (m^{-3}) is the total number of drops per unit volume, μ_g (mm) is the geometric mean of the drop diameters (or mean size diameter), and σ_g is the standard geometric deviation (the standard deviation of the log of drop diameters) which is a measure of the breadth of the spectrum [*Feingold et al.,* 1986; *Cerro et al.,* 1997].

The 3-parameter lognormal drop-size distribution can also be expressed in relation to rain rate as [*Ajayi and Olsen* 1985]:

$$\begin{aligned} N_t &= A_o R^{b_o} \\ \mu_g &= A_{\mu g} + B_{\mu g} \times \ln R \\ \sigma_g^2 &= A_{\sigma g} + B_{\sigma g} \times \ln R \end{aligned} \qquad (2.24)$$

with parameters $A_0, b_0, A_{\mu g}, B_{\mu g}, A_{\sigma g}$ and $B_{\sigma g}$ depending on the geographical location of interest

Table 2-3 below gives the summary of coefficients for various lognormal distributions for different rain types in different climatic regions. *Ajayi and Olsen* [1985] observes that the *Marshall-Palmer* [1948] and *Law-Parsons* [1943] drop-size distribution over-estimates the number of the drops in the small diameter regions in Ile-Ife, Nigeria, which is in contrast with the results from temperate region. *Moupfouma and Tiffon* [1982] also confirm this limitation by using an inversion method on the attenuation measured at a number of frequencies to obtain the drop-size distribution. Similar conclusions have been made in most tropical climates such as Brazil [*Massambani, et al.,* 1990; *Maciel and Assis,*1990], Malaysia [*Zainal et al.,* 1993], Singapore [*Yeo et al.,* 1993; *Li et al.,* 1995; *Zhou et al.,* 2000], and India [*Maitra,* 2004; *Konwar et al.,* 2006].

Due to the drop-size distribution variation for different types of rain, *Adimula and Ajayi* [1996] classified the drop-size distributions measurement conducted in three different locations in Nigeria; Calabar, Zaria and Ile–Ife for three years into drizzle, widespread, shower and thunderstorm rain types [*Adimula and Ajayi*, 1996]. The results showed that the negative exponential distributions provided a better fit to the drizzle rain type in Calabar and Zaria; while the Ile – Ife data was well fitted with the lognormal drop-size distributions. The other rain types

Table 2- 3: Summaries of the lognormal raindrop size distribution coefficients for different rain types

Lognormal distributions	**Type of rain**	N_T	μ_g	σ_g^2
Ajayi and Olsen [1985]	Tropical rains	$108R^{0.363}$	$-0.195+0.199\ln R$	$0.137-0.013\ln R$
Adimula and Ajayi [1996], Nigeria data	Showers	$137R^{0.370}$	$-0.414+0.234\ln R$	$0.223-0.034\ln R$
	Thunderstorms	$63R^{0.491}$	$-0.178+0.195\ln R$	$0.209-0.030\ln R$
	Widespread	$229R^{0.086}$	$-0.339+0.159\ln R$	$0.103+0.051\ln R$
	Drizzle	$718R^{0.399}$	$-0.505+0.128\ln R$	$0.038-0.013\ln R$
Barclay et al., [1978], Miami, Melbourne and Australian data	Showers $12.5 \le R \le 50$ mm/h	$46R^{0.55}$	$-0.451+0.264\ln R$	$0.409-0.076\ln R$
	Thunderstorms $50 < R < 200$ mm/h	$8.8R^{1.0}$	$0.567+0.0\ln R$	$0.099+0.0\ln R$
Harden et al [1978], Slough data	0.25 mm/h	502	-0.81	0.020
	1.25 mm/h	281	-0.35	0.118
	2.50 mm/h	200	-0.15	0.160
	5.0 mm/h	139	+0.05	0.213
	12.50 mm/h	114	+0.31	0.259
	25.0 mm/h	103	+0.51	0.301
	50.0 mm/h	123	+0.71	0.341

were well modeled by the lognormal distribution in all the stations. Hence, the authors combined the results to obtain expression for drizzle, widespread, shower and thunderstorm rain types. These drop-size distributions can be very useful in investigating the variations of propagation parameters due to variations in drop-size distribution especially in the tropics.

The difference between exponential and lognormal distributions is not so important for meteorological studies. Both forms of approximation fit measurement results equally well for raindrops with drop diameter $D \ge 1$mm, which is the range of validity of most measurements [*Fang and Chen*, 1982]. The exponential distributions are preferred by most meteorologists because of their simplicity. However, for microwave modeling, an accurate account of raindrops with small diameters is as important as for large drops [*Fang and Chen*, 1982].

2.12.4 Weibull Drop-Size Distribution

The Weibull drop-size distribution is another form of three parameter distribution that was proposed to estimate raindrop size spectra. This distribution can be expressed as [*Sekine at al.*, 1987; *Jiang et al.*, 1997]:

$$N(D) = N_0 \frac{c}{b}\left(\frac{D}{b}\right)^{c-1} \exp\left[-\left(\frac{D}{b}\right)^{c}\right] \tag{2.25}$$

where D (mm) is the diameter of the drop, N_0 (m^{-3}) is the total number of drops, c and b are the rain dependent parameters. *Sekine et al.,* [1985] defined the three parameters $N_0 = 1000$ m^{-3}, $c = 0.95R^{0.14}$ and $b = 0.26R^{0.44}$ mm, with R as the rain rate in mm/h for drizzle, widespread and shower rain types.

It is important to note that a single drop-size distribution may not be adequate to describe the physical reality of raindrop size spectra in all regions of the world. This reason has demanded the need for drop-size distributions in different geographical regions. Though the ITU-R recommends the *Laws-Parsons* [1948] approximations, which have been given a functional form in the negative exponential distribution of Marshall-Palmer [*Green,* 2004], however, its tendency to overestimate propagation parameters makes its use less attractive in most regions outside the continental temperate regions [*Ajayi and Olsen,* 1996]. The lognormal drop-size distributions, which have proved to be more efficient in the tropical and equatorial climates by many investigators, can as well be limited to the ability of the distrometer to measure accurately the small diameter raindrops in heavy rains [*Tokay and Short,* 1996; *Konwar et al.,* 2006]. These are known to be major contributors to attenuation at millimeter wavelengths [*Hall,* 1981; *Moupfouma et al.,* 1990]. Also, the distrometer is assumed to work under an ideal terminal velocity, and this can be altered due to the occurrence of updrafts and downdrafts on the raindrops. Nevertheless, alternative drop-size distributions have been developed to minimize the large disparities from the negative exponential distributions results in the tropical and equatorial climates [*Ajewole,* 1997].

2.13 Types of Rain

Rain is known to be very complex to describe and classify due to its variability in space, time and occurrence frequency [*Matricciani et al.,* 2000; *Ajayi, et al.,* 1996]. Meteorologists have classified rain into two categories: stratiform and convective rain [*Ajayi, et al.,* 1996; *Green,* 2004]. Basically, the rain types observed over the globe are a combination of these two categories of rain, which are very important for radio propagation [*Matricciani et al.,* 2000; *Tokay and Short,* 1996]. Stratiform rains falls from nimbostratus clouds [*Houze,* 1993] which by definition are stably stratified [3]. They are formed from small ice particles in the upper tropospheric layers, which join together to form bigger nuclei as they fall. As these growing nuclei pass through the so-called melting layer they become unstable and turn into raindrops that fall down to the earth surface [*Ajayi et al.,* 1996; *Green,* 2004]. Raindrop growth in a stratiform cloud is slow, so its rain consists of small drops. This normally results in light rain and drizzle [4].

On the other hand, the convective rains fall from cumulonimbus clouds which are generally formed from below the 0^{O}C isotherm [*Ajayi, et al.,* 1996; *Tokay and Short,* 1996]. They are stirred up by strong movement of air masses caused by tropospheric pressure differences. In this process, water drops are formed and they grow in size until they are precipitated by gravity [*Houze,* 1993; *Green,* 2004]. It falls as showers with rapidly changing intensity with large drops. Convective rain falls over a certain area for a relatively short time, as convective clouds have limited horizontal extent. Convective rainfalls are heavier, more intense, and of shorter duration than the stratiform rains [5]. They are also characterized by sharper spatial and temporal intensity gradients than stratiform rain [3].

From these two categories of rain, rain has further being classified into drizzle, widespread, thunderstorm and shower rain types [*Joss et al,* 1968; *Fang and Chen* 1982; *Adimula and Ajayi,* 1996] for efficient propagation prediction and modeling. The effect of drizzle rain is not so pronounced in radio communications at centimeter wavelengths, since drizzle rain rate is generally much less than 5 mm/h [*Fang and Chen,* 1982], which then produces negligible attenuation. The widespread type has a higher rain rate than that of the drizzle of which the distributions are commonly represented by the negative exponential distribution of *Marshall-Palmer* [1948] and *Joss et al.,* [1968]. These two rain types; drizzle and widespread can be classified under the stratiform rain because of their nature, characteristics, size of their drops and

rain rate. The stratiform rain is characterized by approximately steady rain rate having $R \leq 10$ mm/h and with higher values of D_0 (mm) (mass of the weighted mean diameter) [*Atlas et al.,* 1999]. In the work of *Matricciani et al.,* [2000] and *Konwar, et al.,* [2006], rain events are classified to be convective and stratiform with 10 mm/h rain rate being the boundary between stratiform and convective rain.

The shower rain type is created from cumuliform clouds which are characterized by sudden beginning and ending, and by rapid change of intensity [*Ruffner and Blair,* 1979]. Based on data given by *Mueller and Simms* [1966] and *Barclay* [1975], *Fang and Cheng* [1982] ranged the shower rain rate between 20 – 25 mm/h, and the shower distribution does not contain raindrops diameter larger than 5 mm. The thunderstorm type of rain is a local rain storm formed by a cumulonimbus cloud. These rain types are always accompanied by lightning and thunder [*Ruffner and Blair,* 1979]. Thunderstorm rains are observed to have much higher proportion of raindrops with larger diameters than the widespread and drizzle rain type. In the work of *Fang and Cheng* [1982], the thunderstorm distributions are compared at rain rates range of 25 – 50 mm/h. The thunderstorm and shower rain type can be categorized under the convective class of rain because of their characteristics, nature, drop diameter and rain rate.

2.14 Characteristics of Rain in Tropical and Temperate Climate

The characteristics of rain in the tropics differ appreciably from those in the temperate climates. It has been observed that the empirical relationships obtained in the temperate regions may not be very suitable for propagation predictions in the tropical climates [*Ajayi et al.,* 1996; Green 2004]. Rainfalls in the tropics are largely convective and are characterized by high precipitation rates, which occur over limited extensions with short duration. On the other hand, the temperate climate rain falls from stratiform cloud. The temperate climates are characterized with widespread rain which can extend over a longer propagation path with lower rain rates of up to 25 mm/h and small embedded showers, and duration exceeding one hour [*Ajayi,* 1989; *Salema,* 2003].

Experiments over the eastern tropical Atlantic, northern Australia, and the western equatorial Pacific have shown that almost all convection rain occurs in association with stratiform rain [*Houze,* 1997]. When the convective cloud decays, it becomes stratiform and, the rain extends

over wider areas with smaller intensities. Stratiform rain generally occurs more frequently in the tropics, yet convective rainfall accounts for most (~70%) of the cumulative rainfall, because its intensity is so much higher [3]

Generally, tropical regions possess two climatic seasons; wet and dry season. The wet season are characterized with high rain rates and the dry season with rain total of about 50 mm which occur for about two months [*Green,* 2004]. The equatorial climates which possess similar characteristics with that of the tropics in terms of their formation and drop sizes, have no dry season and all the months have a mean precipitation values of at least 60 mm. Equatorial climates have no pronounced summer or winter, it is wet and hot throughout the year and rainfall is heavy and falls in the afternoon on an almost daily basis. The equatorial climates exhibit only very small temperature variation both within the day and throughout the year [*Green*, 2004; [6]].

2.14.1 South Africa Climate and Seasonal Variability

South Africa is located on latitude 29^{o}00'S and longitude 24^{o}00'E in the most southern tip of the African continent [7]. With this positioning on the globe, South Africa can be classified as a sub-tropical region, because the subtropics include all parts of the world just outside 23.4°N and 23.4°S latitude [8]. South Africa borders other countries like Botswana and Zimbabwe in the central north, Mozambique in north-east, Namibia in north-west. Swaziland and Lesotho are embedded in the country (see Fig. 2-6 below) [9]. South Africa is climatically moderated by its surrounding oceans; the Atlantic ocean in the western part and the Indian ocean in the eastern part. The cold Benguela current pushes northwards from the Antarctic along the Atlantic coastline up to the west coast, and a much warmer stream, the Agulhas current also moves southwards from the Indian Ocean. The eastern seas' steady evaporation provides generous rainfall while the Benguela current retains its moisture to cause desert conditions in the west [*South Africa year book,* 2006; [2]].

Rainfall is highly seasonal over most of southern Africa. South Africa can be classified into four seasons: summer which occurs in mid-October to mid-February; autumn which is in mid-February to April; winter occurs in May to July; and spring which occurs in August to mid-October. These seasons have varying temperatures ranging from -2^{o}C in the winter to 36^{o}C in the summer [2]. Rainfall over the interior northern regions of South Africa follows an annual cycle

Fig. 2- 6: Map of South Africa

and is almost entirely a summer phenomenon [*Tyson*, 1986]. South Africa has an average annual precipitation of 502 mm, as against a world mean of 857 mm. Twenty-one per cent of the country receives less than 200 mm annually, 48 per cent between 200 and 600 mm, while 31 per cent records a total above 600 mm [*South Africa year book*, 2006]. The 400 mm rainfall line divides the country into a wet and a dry western half.

The moist Indian Ocean air masses, which are the chief source of rain over most of the country, gradually lose their moisture as they move towards the western interior. The rainfall distribution pattern in South Africa is also influenced by the orographic[3] effect. The coastal plain has abundant low stratus cloud and fog, particularly during the summer. At night fog tends to advance on to the coastal plain to a depth of 30 – 50 km, withdrawing again as the land heats up during the day [*South Africa year book*, 2006].

[3] Caused mostly by the forced uplift of air over high grounds [*Ajayi*, 1989]

The winter rainfall region is a relatively small area along the Cape West and South West Coast and has a rainfall regime of the Mediterranean type with a conspicuous winter maxima. The rain is often long lasting and not very intense, except along the mountains, where the orographic effect may induce heavy showers. Snow occurs on the mountains four to six times during winter, but it usually melts within a few days. Hail and thunderstorm are both rare [*South Africa year book*, 2006]. The summer rainfall region covers most of the rest of the country, with common light orographic rains along the windward slopes of the eastern escarpment. Over most of the summer months, violent convection storms accompanied by thunder, lightning, sudden squalls and often hail are associated with the rainfall [2].

Between the winter and summer rainfall regions lies a transitional area, where rain comes in all seasons, that is, neither in winter nor in summer, but in autumn and spring. This transitional area can be divided into two sub-regions: a southern coastal strip with annual total of 375 to 875 mm, and a drier inland corridor behind the coastal ranges with an annual total of 50 to 250 mm [*Brasseur et al.*, 1999]. In general, the climatic conditions in South Africa ranges from mediterranean in the south-western corner of the country to temperate in the interior plateau, subtropical in the northeast, and a small area in the northwest with a desert climate. Most rainfall in South Africa normally comes in the summer and autumn months. The spring and winter months are drier months; with the exception of Western Cape (Cape Town), because of its location and mediterranean nature of climate gets most of its rain in winter [[10];*Odedina and Afullo*, 2008].

It can be seen that rainfall in South Africa is highly variable and unpredictable throughout the country. Large fluctuations around the mean annual figure are the rule rather than exception. Like other countries in similar latitudes, South Africa, is periodically afflicted by severe and prolonged droughts. However, the droughts often end with in severe floods especially during summer [*South Africa year book*, 2006]. *Tyson et al*., [1976] observed that over the period of 1910-1972, much of the summer rainfall area of South Africa experienced a quasi 20-year oscillation rainfall [*Tyson et al.*, 1976]. This rainfall spectrum shows a clear peak at about twenty years as well as peaks in 2-3 and 3-4 years bands [*Fashuyi*, 2006; *Fashuyi et al.*, 2006].

2.15 Chapter Summary

This chapter has given the general introduction and the basic ideas needed for this research work. Different propagation phenomena that can affect effective transmission of electromagnetive waves along radio propagation links are discussed. This chapter has also looked into the microphysical structures and properties of raindrops which have led to the study of raindrop size distributions. The specific rain attenuation which is a fundamental quantity in the calculation of rain attenuation statistics is also studied. "Rain" being the key word in the context of this work has been studied for different climates around the world and its influence on terrestrial radio links has been reviewed. South African climatic conditions and its seasonal characteristics has also been the subject of study in this chapter.

The next chapter focuses on the various attenuation models that have been proposed by different authors in different parts of the world.

Chapter Three

Rain Attenuation on Terrestrial Links

3.1 Introduction

Rain attenuation can be obtained directly from link measurements or from the knowledge of point rain rate, raindrop size distribution or other relevant propagation parameters along the radio path [*Ajayi et al*., 1996; *Myers,* 1999]. Also, it can be obtained indirectly by understanding the interaction between an individual raindrop particle and the propagating electromagnetic wave. This is achieved by calculating the electromagnetic scattering properties of the raindrops – knowing the size and the dielectric properties of the water (rain) drop. The dielectric properties of the raindrop which is represented by the complex refractive index of water is dependent on the drop temperature and the operating frequency of the radio link [*Oguchi,* 1973; *Uzunoglu et al.,* 1997; *Moupfouma,* 1997; *Mätzler,* 2002a].

Since propagation experiments are done only in few places around the world and for a limited number of frequencies, their results can not be directly applied to all sites. This is due to the different features and climatic conditions associated with each region around the world, which directly influence the rain in a particular environment. Therefore, several attenuation models have been developed based on the physical facts and available propagation data in a particular geographical region. The main focus of this chapter is to review the rain attenuation work (empirical and theoretical) that has been done in different parts of the world. Point rain rate and

cumulative distribution of rain rate which is the starting point of rain attenuation prediction models [*COST 255,* 2002] will also be mentioned.

3.2 ITU-R Study Group

The International Telecommunication Union – Radiocommunication (ITU-R) study group have developed point rain-rate distributions models for the prediction of cumulative distributions of rain attenuation on terrestrial line-of-sight links since early 1970's (CCIR 1974)[*Olsen,* 1999]. This was done so as to provide information needed for the prediction of rain attenuation for all locations on the globe especially for regions without adequate rain data [*Ajayi et al.,* 1996]. This model initially divide the whole globe into fifteen discrete rain zones by using median cumulative distribution of rain rate for the rain climatic region. From here, the rain rate exceeded for different percentages of time are determined for the fifteen climatic rain zones ranging from A – Q (see Appendix B-1 and B-2 [*ITU-R 837-1*, 1994]).

Due to the discrete nature of the zonal approach in the ITU-R rain climatic zone and its inherent lack of precision to some degree in some climatic rain zones in their initial classification, other attempts have been made to predict point rain rate distributions at specific points within a region [*Olsen,* 1999]. Some of these approaches have used measured rain rate distributions for as many locations in a region as possible, and then fitted into contour maps for particular parameters of the distribution. The contour maps produced by this approach have been regularly revised and updated by the radiocommmunication study groups of the ITU (see Appendix B-3). More recently, the ITU-R [*ITU-R 837-4,* 2007] has produced the revised version of this recommendation which adds a new method for the conversion of rainfall rate statistics from 10-, 20-, 30-minutes integration times to 1-minute integration time.

The 1-minute integration time rain rate has been the recommended time rain rate for the calculation of long-term statistics of rain attenuation [*Crane,* 1996; *ITU-R 530-12,* 2007]. This is because rainfall rate measured with high resolution rain gauge, 1- minute or 2-minute resolution – resolves the small but significant rain rate which is needed for the prediction of rain attenuation values. Gauges with longer averaging times will miss the peak-rain-rate values. Therefore for the prediction of rain attenuation on terrestrial links, a 1-minute accumulation or averaging time is a reasonable compromise.

Equation (3.1) shows the relationship to convert rainfall rate statistics of 10-, 20-, 30-minutes integration times to 1-minute integration time [*ITU-R 837-4,* 2007]:

$$R_1(p) = a[R_\tau(p)]^b \qquad \text{mm/h} \qquad (3.1)$$

where $R_1(p)$ and $R_\tau(p)$ are the rainfall rates with 1-minute and τ-minute integration time exceeded with equal probability $(p\%)$, and a and b are the regression coefficients. The values of coefficients a and b for 5-, 10-, 20-, and 30-minute integration times are given in Table 3-1 below. These values have been obtained from long-term measurements of point rainfall rate at 14 sites in Korea, China, and Brazil in the range of 0.01% to 0.1% of time [*Revised ITU-R 837-4*, 2007].

Table 3- 1: a and b values for various integration times [Revised ITU-R 837-4, 2007]

τ (minutes)	a	b
5	0.986	1.038
10	0.919	1.088
20	0.680	1.189
30	0.564	1.288

3.2.1 ITU-R Terrestrial Rain Attenuation Model

The ITU-R [*ITU-R 530-12,* 2007] also gives a step-by-step technique for estimating long-term statistics of rain attenuation on terrestrial line-of-sight systems. The steps are as follows:

Step 1: Obtain the rain rate $R_{0.01}$ exceeded for 0.01% of the time with an integration time of 1-minute.

Step 2: Compute the specific attenuation, γ_R (dB/km) for the rainfall rate at the frequency and polarization of the transmission. *ITU-R P.838* provides a method for achieving this using the power-law relationship stated in equation (2.13) and the power law values shown in Appendix A-2.

Having obtained the specific attenuation corresponding to the reference rainfall rate, the path attenuation needs to be estimated. At this point, it is necessary to recognize that, because of the

spatial inhomogeneity present in rain, it is unlikely that a point rainfall rate will extend uniformly over the length of the transmission path, unless this is very short [*Hall*, 1996; *Asen et al.* 2003]. The longer the path, the less likely it is that rain will extend uniformly over the full length of the path; hence therefore an effective path length, d_{eff}, is introduced to incorporate this effect [*Hall*, 1996]. This leads to the next step.

Step 3: Compute the effective path length, d_{eff} of the link by multiplying the actual path length *d* of the link by a distance factor *r*.

$$d_{eff} = rd \tag{3.2}$$

An estimate of this factor is given by:

$$r = \frac{1}{1 + d / d_0} \tag{3.3}$$

where quantity d_0 is a rainfall-rate-dependent factor introduced to reflect the fact that the greater the intensity of rainfall in a storm, the smaller the physical dimensions of the storm. It is given by [*Hall*, 1996; *ITU-R 537*, 2007] as:

$$d_0 = 35e^{-0.015}R_{0.01} \tag{3.4}$$

for $R_{0.01} \leq$ 100 mm/h. When $R_{0.01}$ > 100 mm/h, 100 mm/h is use in place of $R_{0.01}$, as this limits the effects of the reduction factor with increasing rainfall rate [*Forknall et al.*, 2008].

Then, finally, the path attenuation exceeded for 0.01% of time is obtained from:

$$A_{0.01} = \gamma_R d_{eff} = \gamma_R rd \qquad \text{dB} \tag{3.5}$$

If attenuation statistics are required for other time percentages, for radio links located in latitudes equal to or greater than 30^O north or south, it can be obtained from:

$$A_p = A_{0.01} \times 0.12 p^{-(0.546+0.043 \log_{10} p)} \tag{3.6}$$

and for radio links located in latitude below 30^O north or south, the attenuation exceeded for other time percentages is given as:

$$A_p = A_{0.01} \times 0.07 p^{-(0.855+0.139 \log_{10} p)} \tag{3.7}$$

where p is the required time percentage, in the range $0.001\% \leq p \leq 1\%$ [*Hall,* 1996: *ITU-R 530-12,* 2007]. The prediction steps outlined above is considered to be valid in all parts of the world – at least for frequencies up to 40 GHz and path lengths up to 60 km [*ITU-R 530-12,* 2007].

3.3 Rain Attenuation Research in North America

The work of *Segal* [1979; 1980] in Canada significantly influenced the ITU-R zonal models approach. This is because of the sufficiently large database of short integration time rain rate data in Canada. Due to the shortcomings of the zonal approach mentioned in section 3.2 above, *Segal* [1980] employed contour maps of two parameters of rain rate distribution based on the data for 47 locations within Canada and United States.

The work of Crane has also considerably influenced the zonal models of the ITU-R. He has extensively used data in the United States, although a lesser extent in other parts of the world to develop a global rain-rate climatic model [C*rane,* 1980; 1996]. This model can be employed to estimate rain attenuation especially for areas where local rain data is scarce. The Crane global rain rate model classified the globe into eight regions labeled A through H going from dry to wet for each latitude band from the pole to the equator [*Crane,* 1980; 1996]. Description of the Crane's global rain rate climatic model is shown in Appendix B-4. By 1982, a significant amount of new data was published for Canada by *Segal* [1979]. The climatic map was then revised by addition of two new sub-regions, B1 and B2; then an adjustment of the contour region boundaries near the U.S. – Canadian border was made.

For the relevance of 1-minute integration time rain rate in the calculation of rain attenuation, *Segal* [1986]developed empirical conversion factors suitable for converting 5- and 10- minute rain-rate data based on the rain rate measurements recorded in 45 locations within Canada to the 1-minute recommended rain rate statistics. *Segal* [1986] defines the conversion factor, $\rho_\tau(P)$, for converting rain having an integration time of τ minutes to equivalent 1-minute statistics [*Segal,* 1986]:

$$\rho_\tau(P) = R_1(P) / R_\tau(P) \tag{3.8}$$

where R_1 and R_τ are the rainfall rates exceeded with equal probability P, for the two integration times. $\rho_\tau\ (P)$ is also given by the power law:

$$\rho_\tau(P) = a.P^b \tag{3.9}$$

over the range $0.001\% \le P \le 0.03\%$, where a and b are constants

3.3.1 Olsen et al. Specific Rain Attenuation Model

Olsen et al. [1978] found the specific rain attenuation to be related to rain rate through a power law relation, given as $\gamma = kR^\alpha$. This empirical power law relation between the specific attenuation γ and the rain rate R is often used in the calculation of rain attenuation statistics because of its simplicity. However, the values of the frequency dependent parameters k and α are available only for limited number of frequencies. Furthermore, these values were obtained experimentally and may contain errors due to limitations in the experimental techniques employed.

Olsen et al. [1978] presented a more general theoretical relation between γ and R and confirmed that the approximation is a good one except in the low frequency and optical limits. In their work, values for k and α is presented for frequency range from 1 to 1000 GHz. These values were determined by applying the logarithmic regression to Mie scattering calculations. The power law coefficients k and α, can not be easily represented over several frequency ranges, therefore, four power law relationships for both k and α, each valid over a narrow frequency segment, were established for entire frequency range from 1 to 1000 GHz. The four power law relationship for the values of k and α are given by *Olsen et al.* [1978] as:

$$\begin{aligned}
k &= 6.39\times10^{-5}(f)^{2.03} && \text{for } f < 2.9\,GHz \\
k &= 4.21\times10^{-5}(f)^{2.42} && \text{for } 2.9\,GHz \le f \le 54\,GHz \\
k &= 4.09\times10^{-2}(f)^{0.699} && \text{for } 54\,GHz \le f \le 180\,GHz \\
k &= 3.38(f)^{-0.151} && \text{for } f > 180\,GHz
\end{aligned} \tag{3.10}$$

and;

$$\begin{aligned}
\alpha &= 0.851(f)^{0.158} && \text{for } f < 8.5\,GHz \\
\alpha &= 1.41(f)^{-0.0779} && \text{for } 8.5\,GHz \le f \le 25\,GHz \\
\alpha &= 2.63(f)^{-0.272} && \text{for } 25\,GHz \le f \le 164\,GHz \\
\alpha &= 0.616(f)^{0.0126} && \text{for } f > 164\,GHz
\end{aligned} \tag{3.11}$$

where f is in GHz. The power law relationship is adopted by the ITU-R for the calculation of rain attenuation [*Olsen et al.* 1978].

3.3.2 The Crane Attenuation Models

The Crane attenuation models were developed in the late 1970s and 1980s to provide a statistical relationship between rain rate model predictions and path attenuation predictions for use on either earth-space links or terrestrial paths [*Crane,* 1996]. There are three versions of the Crane models. The Global Crane model was developed in 1980 [*Crane,* 1980]. The second is the initial version of the two-component model that employs a closed form version of the cumulative distribution of rain rate and assumes an estimate of the effective spatial correlation function for rain [*Crane,* 1982]. The final, revised version of the two-component model was introduced in 1989. This was designed to give an improvement over the spatial correlation assumptions and statistical variations of rain within a cell [*Crane and Shieh,* 1989; *Crane,* 1996].

3.3.2.1 Global (Crane) Attenuation Model

Rain is characteristically inhomogeneous in the horizontal plane, and a statistical model is required to provide an estimate of the effect of the homogeneity on the estimation of attenuation [*Crane,* 1980; 1996]. The attenuation model proposed by Crane was based on the kR^{α} rain attenuation model, for attenuation on a horizontal or terrestrial (or path-integrated) link. This is summarized below [*Crane,* 1980; 1996]:

$$A_T(R,D) = kR^{\alpha}\left(\frac{e^{y\delta(R)}-1}{y} + \frac{e^{zD}-e^{y\delta(R)}}{z}e^{\alpha B}\right) \qquad \delta(R) < D < 22.5\ km \tag{3.12}$$

$$A_T(R,D) = kR^{\alpha}\left(\frac{e^{y\delta(R)}-1}{y}\right) \qquad 0 < D < \delta(R)\ km \tag{3.13}$$

where;

A_T = horizontal path attenuation (dB)

R = rain rate (mm/h)

D = path length (km)

kR^{α} = specific attenuation (dB/km)

and the remaining coefficients are the empirical constants of the piecewise exponential model along the horizontal path length and is represented as:

$$B = \ln(b) = 0.83 - 0.17\ln(R) \tag{3.14}$$

$$c = 0.026 - 0.03\ln(R) \tag{3.15}$$

$$\delta(R) = 3.8 - 0.6\ln(R) \tag{3.16}$$

$$u = \frac{B}{\delta(R)} + c \tag{3.17}$$

$$y = \alpha u \tag{3.18}$$

$$z = \alpha c \tag{3.19}$$

For paths longer than 22.5 km, the attenuation is calculated for a 22.5 km path, and the resulting attenuation is multiplied by a factor of $D/22.5$ km. This model provides a prediction of the attenuation or path integrated rain rate given the equiprobable value of rain rate [*Crane,* 1996].

3.3.3 Lin Attenuation Model

The Lin attenuation model [*Lin,* 1977] is also used to estimate for rain attenuation along propagation path length, and because of this simplicity, the attenuation is very easy to compute. The model can be described by;

$$A_{\tau} = kR^{\alpha} LK_r(R,L) \tag{3.20}$$

where k and α are the specific attenuation power law parameters; L is the propagation path length in km, and $K_r(R,L)$ is the path reduction factor. This is introduced so as to accommodate the effect of the non-homogeneity of rain along radio propagation paths as stated in section (3.2.1). Lin established that the relationship between rain attenuation and propagation path length is non-linear from the attenuation data collected at 11 GHz in Palmetto, Georgia, USA. Therefore Lin proposed the reduction factor coefficient to be;

$$K_r(R,L) = \frac{1}{1 + L\,\dfrac{R - 6.2}{2636}} \tag{3.21}$$

provided rain rate $R > 10$ mm/h.

This model has been verified for the calculation of rain attenuation at different percentages of time at different locations referred to by Lin [*Lin,* 1977] as "city A", "city B", etc.

3.4 Rain Attenuation Research in Europe

In Europe, *Watson et al*. [1987] mapped rain rate exceeded for 0.1% and 0.01% of an average year based on data for 400 locations in Europe. This approach has been excellent in providing estimates of high quality rain rates, and has been used to update the ITU-R rain zones in Europe [*Cost 255,* 2002]. *Watson et al.* [1981] also considered the conversion factor C_R and C_e for rain gauge integration times in the range of 10 second to 60 minute, where:

$$\begin{aligned} C_e(R) &= e_T / e_\tau \\ C_R(t) &= R_T / R_\tau \end{aligned} \tag{3.22}$$

and where C_e refers to the ratio of the exceedance (with the same probability P) for a given rain rate R measured using gauges with integration times T and τ; $C_R(t)$ refers to the ratio of rain rates exceeded for a given percentage of time t as measured by rain gauges with integration times T and τ. Here, $C_R(t)$ depends on the percentage of time considered [*Watson et al.*, 1981].

3.4.1 Garcia and Peiro Attenuation Model

Garcia-Lopez and Peiro [1983] presented a simple rain attenuation prediction technique for terrestrial radio links based on the concept of path reduction coefficient. The attenuation prediction model is also based on the power relationship given for a point rain rate R_{it} measured with an integration time *it* for a given percentage of time p(%) is stated as [*Garcia-Lopez and Peiro*, 1983]:

$$A(p\%) = kR_{it}^{\alpha} LK_{rc} \tag{3.23}$$

where the parameters k and α are the power law coefficients, L is the path length, and K_{rc} the reduction coefficient that depends on the spatial structure of rain and integration time.

Garcia-Lopez and Peiro [1983] gave their reduction K_{rc} to be:

$$K_{rc} = \frac{1}{a + \left[L\left(bR_{it} + cL + d\right)/e \right]} \tag{3.24}$$

with parameters a, b, c, d and e depending on the rain rate integration time. The coefficients of these parameters also depend on the geographical area since the spatial structure of rain can be different in different geographical areas [*Rogers,* 1981]. This makes this prediction model to be applicable to most sites around the globe

Garcia-Lopez and Peiro [1983] obtained the coefficients for equation (3.24) for Europe with an integration time rain rate $it \le 1$, and is given as:

$$K_{rc} = \frac{1}{0.98 + \left[L\left(40.2R_{it} + 3L + 200\right)/28200 \right]} \tag{3.25}$$

This has been tested over 21 European radio links reported by the CCIR in *Report 338* and it has been observed to predict the attenuation fairly well. This model has also been tested in the USA and Japan, but with different path reduction coefficients, since these coefficients are geographically dependent [*Garcia-Lopez and Peiro,* 1983].

Garcia-Lopez et al. [1988], provided two sets of coefficients for a, b, c, d and e. One set for worldwide use (which is adopted by the temperate climates) and the other for Australia. The coefficients for Australia is also adopted for tropical climatic condition ($a = 0.72, b = 7.6, c = -4.75, d = 2408,$ and $e = 10,000$) [*Garcia-Lopez,* 1989] for the prediction of rain attenuation.

3 .5 Rain Attenuation Research in South America

In Brazil, *de Miranda et al.* [1998b] presented the statistical modeling of the cumulative probability distribution function of rain rate in various sites in Brazil. The sites used in their work provide a wide view of rainfall behaviour in Brazil. The sites are located in the cities of are Belem, Manaus, Recife, Rio de Janeiro, and Sao Paulo. The location of the sites span over 22 degrees of latitude and represented two types of equatorial and three types of tropical climates. Their results indicate that the ITU-R expectations for the rainfall rate distribution in climates P and N tend to overestimate the measured values for the sites studied [*de Miranda et al.* 1998b]. *Migliora et al.* [1990] also confirmed eleven different rain climatic zones in Brazil as against the two climatic zones P and N allocated by the ITU-R. *Mello Silva et al.* [1990] gave the conversion factors for converting 5-minutes rain rate to a 1-minute integration time rain rate at various probability levels for 5 locations in Brazil.

Assis and Dias [1998] presented a modified ITU-R rain attenuation model for low latitude areas, for terrestrial paths, based on the fact that rain attenuation prediction model currently adopted by ITU-R appears to be inadequate for most tropical regions [*Green,* 2004]. *Assis* [1992] suggested that the empirical expression used for scaling the rain rate exceeded for 0.01% of an average year $(R_{0.01})$ to other percentages of time may cause an overestimation of the predicted rain attenuation in the range from 0.01 to 0.001%. Therefore, *Assis and Dias* [1998] proposed a modified scaling expression to solve this problem based on 15 years experimental data from Brazil and India. In 2002, *da Costa and Assis* presented an empirical solution based on a given rain cell model to develop a path length factor. This is a very important parameter when deriving a rain attenuation model due to the non-uniformity of rain along propagation paths.

3.5.1 CETUC Rain Attenuation Model

Perez Garcia and da Silva Mello [2004] developed an attenuation model for terrestrial radio links using data from measurements in tropical climates, in Brazil, together with data from temperate climates. This model aimed at improving the ITU-R and other rain attenuation models developed in the temperate climates. The CETUC rain attenuation model uses complete point rainfall rate cumulative probability distribution as input data to calculate the attenuation distribution, in an equiprobability basis [*Perez Garcia and da Silva Mello,* 2004]. This model is developed with the assumption that the in-homogeneity of rain along a propagation path length can be modeled by an

equivalent uniform rain cell with a rain rate that is dependent on the length of the terrestrial link. The attenuation model is given as:

$$A_r = \gamma_s r.L \tag{3.26}$$

where A_r is the rain attenuation along a terrestrial link in dB, γ_s is the specific attenuation in (dB/km), r is the reduction factor, L is the actual path length link (km).

The reduction factor is given as;

$$r = 3.445L^{-0.164}R_p^{(-0.369+0.115/L)} \tag{3.27}$$

where R_p is the rainfall rate at the percentage of time of interest, p [*Perez Garcia and da Silva Mello* 2004].

3.5.2 New CETUC Rain Attenuation Model

In 2007, *da Silva Mello et al.* proposed an improved semi-empirical method for the prediction of rain attenuation along terrestrial line-of-sight links. This method uses full rain rate distribution from 74 year data set from 64 links at 34 sites in 15 countries [*da Silva Mello et al.*, 2007] to predict the attenuation distribution. This model tends to avoid extrapolations functions which are dependent on the percentage of time of interest as used in the previous CETUC model and the ITU-R model. This model also assumes an equivalent cell of uniform rainfall rate (which is the basis of the ITU-R method [*Ajayi et al.*, 1996; *Cost 255*, 2002]) and actual length d_0 to model for the non-uniformity of rain along propagation path length. Fig. 3-1 below shows the description of an equivalent rain cell. The effective path length d_{eff} is given as the average length $\langle L \rangle$ of the intersection between the cell and the path.

Therefore, the effective path length is given by:

$$d_{eff} = \langle L \rangle = \frac{1}{d_0 + d} \int_{-d_0}^{d} L(x)dx = r \cdot d = \frac{1}{1 + d/d_0} \cdot d \tag{3.28}$$

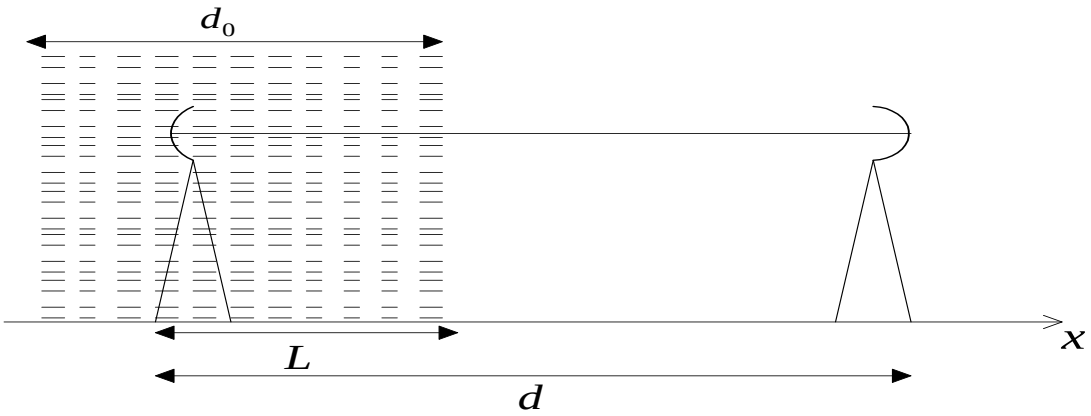

Fig. 3- 1: Equivalent rain cell [da Silva Mello et al., 2007]

The effective path length d_{eff} is always smaller than the actual path length d_0, as seen from equation (3.28), which thus leads to path reduction factor r to be given as:

$$r = \frac{d_{eff}}{d_0} \tag{3.29}$$

The cumulative distribution of rain attenuation is obtained from the distribution of rain rate along a terrestrial link by:

$$A_p = \gamma \cdot d_{eff} = k\left[R_{eff}\left(R_p, d\right)\right]^{\alpha}\left(\frac{d}{1 + d/d_0\left(R_p\right)}\right) \tag{2.30}$$

where:

γ is the specific attenuation (dB/km),

R_{eff} is the effective rain rate, as a function of R_p and d ,

R_p is the point rainfall rate exceeded at $p\%$ of time,

A_p is the rain attenuation exceeded at $p\%$ of time

k and α are the specific attenuation parameters given by ITU-R [*ITU-R 838*, 2005]

The empirical expression for the effective rainfall rate is represented by:

$$R_{eff} = 1.763R^{0.753+0.197/d} \tag{3.31}$$

and the equivalent cell diameter d_0 is given by a power law expression;

$$d_0 = 119R^{-0.244} \tag{3.32}$$

Using equations (3.31) and (3.32), the rain attenuation distribution along terrestrial paths can be predicted by [*da Silva Mello et al.*, 2007]:

$$A(P) = k \cdot \left[1.763 \cdot R_p^{0.753+0.197/d}\right]^{\alpha} \cdot \frac{d}{1 + d \Big/ \left(119 \cdot R_p^{-0.244}\right)} \tag{3.33}$$

3.6 Rain attenuation Research in Asia

In Indian, *Sarkar et al.* [1992] produced a reference data manual for rain rate distributions over the Indian sub-continent, making use of the heavy rainfall data of 5-minutes and 15- minutes available at 35 different geographical regions in Indian, using the fast response rain gauge. The rapid response rain gauges measure rain rate with 10-seconds integration time in Delhi, Shillong, Calcutta, Bombay and Tirupati. They produced the cumulative distributions of rainfall rate for different integration times from 10-seconds to 1-hour for 17 different stations in India.

In China, *Zhang and Hu* [1995] obtained contours of rainfall rate exceeded for 0.01% and 0.0% of the time based on data from several convectional meteorological stations all over China. From measurements made in 3 different locations – (Xinxiang, Nanjing and Guangzhou), *Zhang and Hu* [1995] expressed the conversion factor of rain rate statistics for 10-minutes to 1- minute based on the Segal conversion factor in equation (3.9).

In Indonesia, *Suryana et al.* [2005] presented a 2-year experimental result which indicates that the measured rainfall rate exceeded at 0.01% of the time is quite different from the ITU-R estimations. The ITU-R has classified most of the Indonesian cities to be of P climatic rain zone, whereas the cities fall in the Q climatic rain zone, and N climatic rain zone [*Juy et al.*, 1990,

Widodo, 2005]. Based on rain rate measurements in Indonesia, *Suryana et al.* [2005] developed a new prediction model of $R_{0.01}$ value for Indonesia cities.

The rain attenuation measurements conducted in Japan by *Manabe et al.* [1987] at four different frequencies; 50.4, 81.8, 140.7, and 254.5 GHz on 0.81 km terrestrial line-of-sight link has shown that, for the Japanese climate, the results from the ITU-R rain attenuation model underestimate the rain attenuation at frequencies above 80 GHz. It was further concluded that the higher the propagating frequency the more appreciable is deviation of the ITU-R model to the Japanese climate [*Manabe et al.*, 1987].

In Singapore, *Yeo et al.* [1993] presented a two-year measurement of rain rate and rain attenuation from a vertically polarized 21.225 microwave link. From their measurements a modified version of the ITU-R model for the cumulative percentage time of which the specific attenuation level is exceeded was proposed. This is given as:

$$A_p / A_{0.01} = 0.12\, p^{-(0.74+0.14\log p)} \tag{3.34}$$

where $A_{0.01}$ is the path attenuation for 0.01% of time. Also from the measurements, a new negative exponential distribution model with coefficients different from that of *Marshall –Palmer* [1948] was used to calculate the specific rain attenuation in terms of equation (2.12). With drop intensity N related to drop diameter D and rain rate R, the drop–size distribution function was obtained. This is given by [*Yeo et al.*, 1993] as:

$$N(D) = 0.333 \exp\left[-45.2 R^{-0.103} D\right] \quad (\text{cm}^{-4}) \tag{3.35}$$

In 1995, *Li et al.* also calculated the specific rain attenuation from the *Marshall-Palmer* [1948] drop-size distribution at different operating frequencies from the local rainfall data in Singapore. These results were compared with the ITU-R predicted specific attenuation for moderate climatic region. It was observed that the *Marshall-Palmer* [1948] drop-size distribution gave a fairly good fit for prediction of specific rain attenuation in moderate climatic region in Singapore where the mean drop-spectrum ranges from 1-50 mm/h [*Li et al.*, 1995].

Two microwave links operating at two different frequencies; 15 and 38 GHz was added to the 21.225 GHz experimental set up. The experimental results from these set-ups showed that the

ITU-R attenuation model cannot be used in the attenuation prediction for tropical Singapore. This is because it was observed that the measured specific attenuation in Singapore tropical environment was twice those predicted by the ITU-R model [*Li et al.,* 1995]. Later in 2000, Zhou et al. [*Zhou et al.,* 2000] presented the cumulative distributions of rainfall rate, cumulative distributions of rain attenuation, the relationship between specific attenuation and rain rate, and frequency scaling formulae from the experimental results of the 15, 21.225, and 38.6 GHz radio links set up in Singapore. Comparing their results with the ITU-R, it was concluded that the ITU-R underestimates the rainfall rate and propagation characteristics in Singapore.

Tseng et al. [2005] studied rain attenuation in northern Taiwan from a two-year raindrop size distribution measurements recorded along a vertically polarized 28.35 GHz terrestrial path. The drop-size distribution measurements were analyzed for different seasons over a 1-minute rain rates, and a relationship between drop-size distributions and the rain rates were established. Regression fit was performed to match the data to known distributions, and it was observed that the gamma distribution (see equation 2.22) gave the best description for the data regardless of the seasons, except for light rain rate, where lognormal distribution looks fitted. The three parameters coefficients for the gamma distribution for the seasons are obtained and these are used to develop a semi-empirical rain attenuation model. The attenuation results from this model are then compared with the measured data of the 28.35 GHz terrestrial link and the results from Crane and ITU-R attenuation model. It was concluded that both the ITU-R and the Crane model either underestimate or overestimate the rain attenuation for each season [*Tseng, et al.* 2005].

3.7 Rain attenuation Research in Australia

The most notable work in Australia is the work by *Flavin* [1980; 1981; 1982; 1996] which is mostly adapted for satellite radio communication systems between frequencies of 5-60 GHz. The important aspects of his model are the use of entire rainfall rate distributions and the dependence of the rainfall rate on vertical path reduction factor (for satellite radio links), and its applicability to tropical climates. But *Flavin* [1981] examined 6-minute and 1-minute cumulative distributions of rain rate for four locations in Europe, three in the United States, one in Canada and five in Australia; he obtained a power law relationship for the conversion of 6-minutes rain rate to 1-minute integration recommended for the estimation of rain attenuation on radio communication links. The relationship is as follows [*Flavin*, 1981]:

$$R_1 = 0.990 R_6^{1.054} \tag{3.36}$$

where R_1 is the 1 minute rain rate, R_6 the equiprobable 6 minutes rain rate value.

3.8 Rain Attenuation Research in Africa

During the two years of Joint Radiometric Campaign in Africa, *McCarthy et al.* in 1994, presented the cumulative distribution of rain rate obtained in Doula (Cameroun), Ile-Ife (Nigeria), and Nairobi (Kenya) [*Ajayi et al.,* 1996]. The highest rain accumulation was recorded in Doula, but has a convective factor which was lower than that of Ile-Ife; this made the rain rate exceeded for 0.01% of the year comparable at Doula and Ile-Ife. The cumulative distributions of rainfall rate in Doula and Nairobi show that the rain climate is not well described by the ITU-R predictive distributions. *Ajayi and Ezekpo* [1988] used the *Rice-Holmberg* [1973] technique to predict short integration time (1-minute) rainfall rate from long term precipitation data from thirty-seven stations in Nigeria over a period of thirty years. More recently, *Ojo et al*. [2008], developed rain rate maps for Nigeria at 0.01 and 0.1% exceedance value using rain rate models developed for tropical zones on the thirty years rain measurements made from the coast to the arid region of Nigeria [*Ojo et al.,* 2008] .

In the conversion of rain rates to recommended 1-minute integration time rain rate, *Ajayi and Ofoche* [1983] also found that a power law relationship exists between equiprobable rain rates collected in Ile-Ife between September 1979 and December 1981. The power law relationship is given by [*Ajayi and Ofoche,* 1983] as:

$$R_\tau = a R_T^b \tag{3.37}$$

where R is the rain rate, τ is the integration time at which the rain rate is required, and T is the integration time at which the rain rate is available. Table 3-2 below gives the power law coefficients a and b required to convert 2-, 5-, 10-, and 20-minutes rain rates to 1-minute integration time as determined by Ajayi and Ofoche.

Table 3- 2: Coefficients for $R_\tau = aR_T^b$, for τ = 1minute [Ajayi and Ofoche, 1983]

Integration time T (Min)	Value of coefficient	
	a	b
2	0.872	1.055
5	0.991	1.098
10	1.797	1.016
20	4.311	0.853

In South Africa, *Seeber* [1985a: 1985b] proposes a rain rate model based on Southern Africa extreme rain rate data and classified South Africa into twelve different climatic rain zones using the Köppen classification system [see Appendix B-5 and B-6]. In 2006, *Fashuyi et al.* presented the cumulative distributions of rain rate for twelve different geographical locations in South Africa based on a 5-year rain fall data recorded by the South African Weather Services (SAWS). The rainfall data which was recorded for 1-hour integration times were converted to 1-minute integration time by using the *Segal* [1986] and *Ajayi* and *Ofoche* [1983] approaches together with 1-minute rain rate recorded in Durban. From these approaches, a simple power law fit was also generated for converting the 1-hour rain rate to 1-minute integration time, and this is given as:

$$R_{1\min} = 9.228R_{60\min}^{0.8207} \quad \text{(South Africa)} \tag{3.38}$$

The power law coefficients are a =9.228 and b =0.8207, and $R_{1\min}$ and R_{1hr} are the rain rates at 1-minute and 1-hour integration time respectively [*Fashuyi.* 2006; *Fashuyi et al.*, 2006].

From the cumulative distribution of the converted 1-minute rain rate, rain rate exceeded at 1, 0.3, 0.1, 0.03, and 0.01% percentages of time (see Table 3-3 below) are determined [*Fashuyi et al.*, 2006]. From these distributions, four new climatic rain zones are determined, namely; N, M, P, and Q. This means that an additional three climatic rain zones, M, P, and Q are added to the original C, D, E, K and N climatic rain zones designated by the ITU-R 837 (see Appendix B-1 and B-2) [*Fashuyi*, 2006; *Fashuyi et al.*, 2006]. Table 3-4 below shows the determined rain zone classification and their climatic regions. In 2007, *Owolawi and Afullo* determine an empirical rain rate distribution model, and the worst month statistics for eight different geographical locations in South Africa [*Owolawi and Afullo,* 2007].

Table 3- 3: Rain rate exceeded (mm/h) for the 12 selected geographical locations in South Africa [Fashuyi, 2006; Fashuyi et al., 2006].

Percentage of time (%)	Lady smith	Durban	Richards Bay	Cape Town	Vryheid	Bloem-fontein
1.0	16.29	18.93	28.79	12.17	6.07	14.95
0.3	35.7	41.25	57.03	25.2	21.49	34.58
0.1	62.07	68.98	91.65	37.95	41.25	56.01
0.03	95.32	108.75	143	57.03	77.65	89.92
0.01	120.11	138.83	182.66	78.60	98.93	122.7
Percentage of time (%)	**Pretoria**	**East London**	**Ulundi**	**Brandvlei**	**Newcastle**	**Pietermari-tzburg**
1.0	14.95	18.93	14.95	2.46	12.17	18.93
0.3	35.71	36.83	34.58	9.22	31.14	43.43
0.1	61.07	61.07	67.02	25.19	63.07	79.55
0.03	98.03	90.74	112.27	42.33	105.2	113.15
0.01	114.90	125.27	157.01	67.02	130.39	152.92

Table 3- 4: Determined rain zone classification and climatic region classification [Fashuyi et al., 2006; Odedina and Afullo, 2007]

Locations	Climatic region [SAWS]	Geographical coordinates		Determined climatic rain zone [*Fashuyi et al.*,2006]
		Latitude South	Longitude East	
Cape Town	Mediterranean	29°.97'	30°.95'	**N**
Vryheid	Inland Temperate	28°.78'	32°.02'	
Brandvlei	Desert	33°.97'	18°.60'	**M**
Durban	Coastal Savannah	30°.47'	20°.48'	**P**
Richards Bay	Coastal Savannah	33°.03'	27°.83'	
Pietermaritzburg	Inland Savannah	28°.57'	29°.77'	
Ulundi	Inland Savannah	27°.77'	29°.98'	
Newcastle	Inland Temperate	27°.78'	30°.80'	
Bloemfontein	Steppe	25°.73'	28°.18'	
East London	Savannah	29°.10'	26°.30'	**Q**
Ladysmith	Inland Temperate	28°.30'	31°.42'	
Pretoria	Temperate	29°.63'	30°.40'	

3.8.1 Moupfouma Attenuation Model

The Moupfouma rain attenuation model for terrestrial link is grouped under the African attenuation scenario because of the extension of the experimental data utilized in formulating the model to Africa, which is uncommon in most the models discussed above. *Moupfouma* used experimental data obtained in 30 different terrestrial radio links operating in the frequency range of 7-38 GHz band range with path length ranging from 1.3 to 58 km located in Africa, Japan, United States and Europe [*Moupfouma,* 1984]. He proposed an empirical model for predicting rain-induced attenuation on terrestrial paths from the knowledge of 1-minute rain rate recorded in the considered geographical area and the corresponding percentages of time P during which these rain rate was exceeded.

Using well-known fitting procedures, his work was found to be in agreement with prediction method proposed by the International Radio Consultative Committee (CCIR) now ITU-R. The rain induced attenuation on a line-of-sight path can then be expressed as:

$$\gamma(dB) = kR^{\alpha} L_{eff} \tag{3.39}$$

with;

$$L_{eff} = rl \tag{3.40}$$

where l(km) is the actual path length, L_{eff} the effective path length and r a reduction factor coefficient having the well-known form:

$$r = \frac{1}{1 + Cl^{m}} \tag{3.41}$$

The attenuation $\gamma(dB)$ and the 1-minute rain rate R (mm/h) are calculated for the same time percentage, k and α are the power law regression coefficients which depends on frequency and polarization.

To derive C and m in equation (3.41), experimental data obtained from the terrestrial radio links were used. It was found that C depends on probability level P (percent) of interest for which data

are available, and *m* depends on the radio link path length and its frequency. The resultant formula for the path length reduction factor is given by:

$$r = \frac{1}{1 + 0.03\left(\frac{P}{0.01}\right)^{-\beta} l^{m}} \tag{3.42}$$

where

$$m(F,l) = 1 + \Psi(f)\log_e l \tag{3.43a}$$

$$\Psi(F) = 1.4 \times 10^{-4} f^{1.76} \tag{3.43b}$$

Hence, *f(GHz)* is the frequency, the β coefficient is given as a result of a best fit by:

$$\left.\begin{array}{lll} for & l < 50km & \\ & \beta = 0.45 & for\ 0.001 \le P(percent) \le 0.01 \\ & \beta = 0.6 & for\ 0.01 \le P(percent) \le 0.1 \\ for & l \ge 50km & \\ & \beta = 0.36 & for\ 0.001 \le P(percent) \le 0.01 \\ & \beta = 0.6 & for\ 0.01 \le P(percent) \le 0.1 \end{array}\right\} \tag{3.44}$$

The effective path length incorporates the effect of the spatial inhomogeneity in rain along radio paths [*Moupfouma*, 1984].

3.8.2 New Moupfouma Attenuation Model

The new rain attenuation model proposed by *Moupfouma* [2009] for rain attenuation prediction also employed the power law empirical relationship proposed by *Olsen et al.* [1978]. The model is based on rain rate exceeded for 0.01% of the time, $R_{0.01}$ (mm/h). This is because it has been established that rain rate data at $R_{0.01}$ and measures with a 1-minute integration time is less variable and more accurate than the rain rates with highest or lowest time percentages [*Moupfouma*, 1987].

Therefore, provided the rain rate $R_{0.01}$ (mm/h) exceeded for 0.01% of the time is available (maybe locally or from the ITU-R data base [*ITU-R 837*, 2007]), the specific rain attenuation on the

microwave link can be given as:

$$\gamma_{R_{0.01}} = kR_{0.01}^{\alpha} \tag{3.46}$$

with k and α as parameters governed by radio links operating frequency and polarization.

During rain events, convective rain cells are often alternated with stratiform rain cells and this leads to variation of the rain cell height [*Matricciani and Pawlina-Bonati*, 2000]. This non-uniformity of rain structure on radio propagation paths leads to the use of equivalent propagation path length, L_{eq} on which the rain structure is assumed to be uniform, rather than the actual path length [*Moupfouma*, 2009].

Therefore the attenuation exceeded at 0.01% of the time $A_{0.01}$ along a terrestrial line-of-sight link is given as:

$$\gamma_{0.01} = kR_{0.01}^{\alpha} \times L_{eq} \tag{3.47}$$

To determine the equivalent path length L_{eq}, an adjustment factor δ that accommodates the effect of the non-uniformity of rain along the radio paths is defined as:

$$L_{eq} = \delta \times L \tag{3.48}$$

Knowing the rain rate exceeded at 0.01% of the time, the adjustment factor δ is given as:

$$\delta(R_{0.01}, L) = \exp\left[\frac{-R_{0.01}}{1+\xi(L)\times R_{0.01}}\right] \tag{3.49}$$

Substituting equation 3.49 into 3.48, the equivalent path length, L_{eq} becomes:

$$L_{eq}(R_{0.01}, L) = L \times \exp\left[\frac{-R_{0.01}}{1+\xi(L)\times R_{0.01}}\right] \tag{3.50}$$

The above equivalent path length is dependent on two main parameters namely: the actual path length of the terrestrial link, and the rain rate observed for 0.01% of the time on the radio link.

From equation (3.50), the parameter $\xi(L)$, when $R_{0.01} \Rightarrow +0$, is

$$L_{eq}(R_{0.01}, L) \approx L \tag{3.51a}$$

which means when it stops raining on terrestrial radio link, the equivalent path length equals the actual terrestrial radio link path. On the other hand, when $R_{0.01} \Rightarrow +\infty$, then,

$$L_{eq}(R_{0.01}, L) = L \times \exp\left(\frac{1}{\xi}\right) \begin{cases} > L & \text{when } \xi(L) < 0 \\ & \text{or} \\ \leq L & \text{when } \xi(L) > 0 \end{cases} \tag{3.51b}$$

In equation (3.51b), $\xi(L) < 0$ parameter governs very high rain rates (convective rains), that may cover the entire terrestrial actual path length and over, and $\xi(L) > 0$ governs convective rains that may just cover less than the actual path length of the terrestrial link [*Moupfouma*, 2009]. The parameter $\xi(L)$ is determined by the magnitudes of the actual terrestrial path lengths of about 34 terrestrial radio links in Africa, Europe, Japan, and United States. Therefore, for terrestrial radio link of propagation length L, such that $L \leq 7$ km, then,

$$\xi(L) = -100 \tag{3.52a}$$

and for terrestrial path longer than 7 km, $L > 7$ km, then,

$$\xi(L) = \left[\frac{44.2}{L}\right]^{0.78} \tag{3.52b}$$

Finally, rain attenuation for terrestrial line-of-sight link can be predicted with the following expressions [*Moupfouma*, 2009]:

$$\gamma_{0.01} = kR_{0.01}^{\alpha} \times L \times \exp\left[\frac{-R_{0.01}}{1+\xi(L)\times R_{0.01}}\right] \quad \text{with} \quad \xi(L) = -100 \qquad (3.53a)$$

for any terrestrial link of length $L \leq 7$ km, and,

$$\gamma_{0.01} = kR_{0.01}^{\alpha} \times L \times \exp\left[\frac{-R_{0.01}}{1+\xi(L)\times R_{0.01}}\right] \quad \text{with} \quad \xi(L) = \left[\frac{44.2}{L}\right]^{0.78} \qquad (3.53b)$$

whenever propagation path length $L > 7$ km.

This model predicts attenuation governed by a rain rate at a given percentage of time for line-of-sight SHF and EHF radio communication links [*Moupfouma*, 2009].

3.9 Theoretical Models for Rain Specific Attenuation Prediction

Having discussed some of the empirical rain attenuation models that exist in different parts of the world, so as to investigate the effect of local propagation data in each region, rain attenuation models that best describe the behaviour of rain each region was developed. This section discusses the theoretical prediction models for rain specific attenuation. These theoretical models are formulated based on the interaction of an individual raindrop with the propagating electromagnetic wave [*Green,* 2004]. The first theoretical investigations of rain attenuation were carried out by *Ryde and Ryde* [1944] during World War II. Their calculations were based on Mie scattering [*Mie*, 1908] and absorption of electromagnetic energy by a dielectric sphere, and on the measurements of *Laws and Parsons* [1943] for average drop-size distribution in rain [*Sander,* 1975].

The interaction between raindrop and the propagating electromagnetic wave constitutes a scattering problem [*Medeiros Filho et al.,* 1986]. To calculate the electromagnetic scattering properties of the raindrops, the dielectric properties of the rain (water) drop, the shape, and the size of the raindrop must be known [*Uzunoglu et al.,* 1977; *Green,* 2004]. Raindrops which can be considered as a homogeneous, but lossy dielectric (see equation 2.11) can be described by a

complex refractive index m [*Cermak et al.,* 2005]. The complex refractive index $m(f,T)$ is a function of frequency (operating frequency of the radio link) and temperature (temperature of the raindrop) and is related to dielectric permittivity $\varepsilon(f,T)$ by;

$$m(f,T) = \sqrt{\varepsilon(f,T)} \tag{3.54}$$

Most researchers have used the old dielectric data given by *Ray* [1972], to describe the refractive index of water, while some have adopted a newer and a more accurate model namely, the dielectric function of *Liebe et al.* [1991], covering a frequency range of 1-1000 GHz to compute for the theoretical rain attenuation. This theoretical rain attenuation method which was initially developed by *Ryde and Ryde* [1944] has formed the basis of most subsequent work [*Medhurst,* 1965; *Medeiros Filho et al.,* 1986].

3.9.1 Oguchi's Method

In 1973, Oguchi calculated rain specific attenuation for frequencies 19.3 and 34.5 GHz based on the assumption that the raindrop is of oblate spheroidal shape and the incident electromagnetic wave is normal to the drop axis [*Oguchi,* 1973]. In his work, he computed the forward and the backward scattering intensities of the oblate spheroidal raindrops at both frequencies and considered polarizations parallel and perpendicular to the drop axis. The scattering properties were computed for 13 sizes of deformed raindrops (due to the free fall nature of the drop, it assumed a flattened shape at the bottom and rounded on the top [*Pruppacher and Pitter*, 1971]) which were assumed to be of oblate spheroidal shapes. The relationship between deformation and drop-size are described with a linear relation given as [*Oguchi,* 1973]:

$$S = -(0.41/4.5)R + 1 \tag{3.55}$$

where S is the ratio of the minor to the major axis, and R is the effective drop radius in mm, meaning the radius of the sphere with volume equal to that of the oblate spheroid drop [*Oguchi,* 1960; 1964]. The complex refractive indices of the water drop (rain drop) are computed from the Debye formula at 20^{O}C with constants given by *Saxton and Lane* [1952] for the two frequencies (19.3 and 34.5 GHz).

Consider electromagnetic plane wave incident on the oblate raindrop, to be given as:

$$E^i = \hat{e}\exp(-ik_0 r\hat{K}_1 \cdot \hat{K}_2) \tag{3.56}$$

with the far-field scattered wave is given as:

$$E^s = f(\hat{K}_1 \cdot \hat{K}_2)r^{-1}\exp(-k_0 r) \tag{3.57}$$

where $\hat{e}$ is a unit vector specifying the polarization state of the incident field, $\hat{K}_1$ is a unit vector in the direction of the incident field, $\hat{K}_2$ is a unit vector in the direction of the scattered field, r is the distance from the origin to the observation point, k_0 is the free space propagation constant, and $f(\hat{K}_1 \cdot \hat{K}_2)$ is the function denoting the scattering amplitude [*Oguchi,* 1973].

The scattering amplitudes for the drops are determined numerically by using three different approximates techniques namely, point-matching technique, spheroidal function expansions, and perturbation method. The forward scattering intensities are then utilized to determine the effective propagation constants of a rain-filled medium, from which the attenuation for parallel and perpendicular polarizations are calculated for different rain rates [*Oguchi,* 1973]. The effective propagation constants $k^{v,h}$ for a rain-filled medium for both vertically and horizontally polarized incident waves have been given by *Van de Hulst* [1957] as:

$$k^{v,h} = k_0 + \left(2\pi/k_0\right)\int f^{v,h}\left(\hat{K}_1 \cdot \hat{K}_1\right)n(R)dR \tag{3.58}$$

where $n(R)dR$ is the drop-size distribution function, and $f^{v,h}\left(\hat{K}_1 \cdot \hat{K}_1\right)$ is the forward scattering amplitudes for both vertical and horizontal scattered fields. Hence the specific attenuation for the spheroidal drops on a radio link can be calculated from:

$$\gamma^{v,h} = 8.686 \times \mathrm{Im}\left(k^{v,h}, L\right) \qquad \text{(dB)} \tag{3.59}$$

where Im denotes the imaginary part of the propagation constant determined from the imaginary part of the forward scattering amplitudes, and L is the propagation path length in km [*Oguchi*, 1973].

3.9.2 Morrison and Cross Method

Morrison and Cross [1974] presented numerical and analytical results for scattering by oblate spheroidal raindrops for frequencies 4, 11, 18.1 and 30 GHz, which is then used to calculate the specific rain attenuation. Two polarizations of the incident wave are considered. Firstly, the electric field parallel to the plane containing the axis of symmetry of the raindrop and the direction of propagation of the incident wave and this is denoted by I . Secondly, the electric field is perpendicular to this plane and is denoted by II . In terrestrial radio links, the angle between the direction of propagation and the axis of symmetry is represented by $\alpha = 90^o$ and other values corresponds to satellite links [*Morrison and Cross*, 1974].

The scattering by oblate spheroidal raindrops, has the ratio of the minor to the major axis depending linearly on the radius $\bar{a}$ of the equivolumetric spherical raindrop, given as:

$$a/b = (1 - \bar{a}), \tag{3.60}$$

where $\bar{a} = \left(a^2 b\right)^{1/3}$ cm is the equivolumetric radius which is similar to that given by *Oguchi* [1973].

The complex forward scattering amplitudes in the far field region for the two polarizations are designated by $S_I(0)$ and $S_{II}(0)$. The scattering amplitudes are determined numerically by point matching technique, first-order perturbation approximation, and the least square method for 14 sizes of the oblate spheroidal raindrops at the four frequencies (4, 11, 18.1 and 30 GHz) [*Morrison and Cross*, 1974]. The complex refractive indices of the raindrop at 20^{O}C are obtained by *Ray* [1972]. The total (extinction) cross sections Q_t^I and Q_t^{II} are given in terms of the real part of the forward scattering amplitude, and are given as:

$$Q_t^I = \frac{4\pi}{k_0^2} \operatorname{Re} S_I(0); \qquad Q_t^{II} = \frac{4\pi}{k_0^2} \operatorname{Re} S_{II}(0) \tag{3.61}$$

where $k_0 = 2\pi f/c$ is the free space wave number, f and c is the frequency and velocity of the wave. These scattering results were summed over the drop-size distribution to calculate the differential attenuation in radio communication systems [*Morrison and Cross*, 1974].

3.9.3 Uzunoglu et al. Method

The Uzunoglu et al. method for the calculation of specific rain attenuation utilized the solution of electromagnetic scattering from oblate spheroidal raindrops from the Fredholm integral equation presented in the work of *Holt et al.* [1978]. This mathematical solution has been applied to calculate the scattering amplitudes for oblate spheroidal drops for six different frequencies; 4, 6, 11, 14, 20, and 30 GHz [*Uzunoglu et al.*, 1977]. The scattered electric field in the far field region is denoted as:

$$E_s \simeq f(k_s)\frac{\exp(ik_0 r)}{r} \tag{3.62}$$

where $f(k_s)$ is the scattering amplitude calculated from the Fredholm integral method [*Holt et al.*, 1978] using the refractive indices of water at 20^{O}C from *Ray* [1972] for the six frequencies and oblate spheroidal drops with semi-minor axis b and semi-major axis a as given in equation (3.60).

The scattering amplitudes in the vertical and horizontal polarization are denoted by $f_{V,H}(\theta,\alpha,\bar{a})$. The scattering amplitude in the same direction as the incident wave at observation angles, $\theta = 0,$ corresponds to forward scattering; while $\theta = \pi$ corresponds to the backward scattering. These scattering amplitudes are given for extreme incidence angles of $\alpha = 90^o$ (which corresponds to terrestrial radio links) and 0^0 for range of drop-sizes for all the considered frequencies, and $\bar{a}$ is the effective radius of the drop [*Uzunoglu et al.*, 1977]. From the scattering amplitudes, the propagation constants $K_{V,H}$ given by *Van de Hulst* [1957] are written, using the *Uzunoglu et al.* [1977] notations:

$$K_{V,H} = k_0 + \frac{2\pi}{k_0}\int_0^{+\infty} f_{V,H}(0,\alpha,\bar{a})n(\bar{a})d\bar{a} \tag{3.63}$$

where k_0 is the free space wave number, and $n(\bar{a})d\bar{a}$ is the number of drops per unit volume having radius in the region $\bar{a}, \bar{a}+d\bar{a}$. From this equation, it has verified that provided the density of scatterers per unit volume is small in a rain-filled medium and the following inequality holds [*Uzunoglu et al.* 1977; *Uzunoglu and Evans,* 1978]:

$$\left.\begin{aligned} &\left|\frac{2\pi}{k_0^2}\int_0^{+\infty} f_{V,H}\left(0,\alpha,\bar{a}\right)n(\bar{a})d\bar{a}\right| \ll 1 \\ &\left|1+\frac{2\pi}{k_0^2}\int_0^{+\infty} f_{V,H}\left(0,\alpha,\bar{a}\right)n(\bar{a})d\bar{a}\right| \gg \left|\frac{2\pi}{k_0^2}\int_0^{+\infty} f_{V,H}\left(0,\alpha,\bar{a}\right)n(\bar{a})d\bar{a}\right| \end{aligned}\right\} \tag{3.64}$$

then multiple scattering effects are negligible. This have been verified for high rainfall rates, for example, rain rate of 150 mm/h; the mean distance b between drops is $b \simeq 10$ cm, therefore for heavy rainfall at frequencies greater than 10 GHz, $k_0 b \geq 21$. And from analysis of two spherical scatterer or raindrops, it can be observed that for $k_0 b > 10$, the interactions between the scatterers are negligible. This has been confirmed for all likely rain rates for frequencies of up to 30 GHz [*Uzunoglu et al.* 1977; *Uzunoglu and Evans,* 1978]. The propagation constants $K_{V,H}$ are then utilized to calculate the attenuation for oblate spheroidal drops.

3.9.4 Moupfouma Theoretical Specific Attenuation Model

Moupfouma [1997] developed theoretical attenuation models for the calculation of specific rain attenuation based on the fundamental works of *Oguchi* [1973], *Morrison and Cross* [1974], and *Uzunoglu et al.* [1977]. In his work, he utilized the oblate spheroidal scattering amplitudes calculated by these earlier works as his basic parameters to formulate the rain attenuation model: the imaginary and real parts of the scattering amplitudes were plotted against the raindrop equivolumetric radius by using *the Morrison and Cross* [1974] results at 18.1 GHz with 90^{O} incidence angle. From these plots, it was observed that the imaginary part of the scattering amplitudes can be well modeled with a power law relationship, but the real part of the scattering amplitudes cannot be described with such a power law relation. This was extended to Oguchi's and Uzunoglu et al's oblate spheroidal drops scattering amplitudes at several incidence angles. It also turns out that the imaginary part of the forward scattering amplitude can be related to the equivolumetric raindrop radius by a power law, given by [*Moupfouma,* 1997]:

$$\text{Im } f_{v,h} = (\phi = 0^o, \theta, \bar{a}, \lambda) = \eta_{v,h} \bar{a}^{\rho_{v,h}} \tag{3.65}$$

where $\text{Im } f_{v,h}$ is the imaginary part of the oblate spheroid forward scattering amplitude for horizontal and vertical polarizations, $\phi = 0^o$ signifies the forward scattering direction of the wave, θ is the angle of the incident wave which is 90^{O} (for terrestrial links), $\bar{a}$ is the equivolumetric radius, λ is the wavelength, η and ρ are the modeled power law coefficients.

Moupfouma [1997] used *Uzunoglu et al.* [1977] calculated forward scattering amplitudes for oblate spheroidal drops for frequencies ranging from 4 to 30 GHz with the refractive index of water at 20^{O}C given by *Ray* [1972]. This was used to determine the analytical relationships which described the power law relationship for the same range of frequencies; these were given for the vertical and horizontal polarization as [*Moupfouma,* 1997]:

$$4\,\text{GHz} \le f \le 30\,\text{GHz}$$

$$\rho_v = 4.88 - \frac{f(GHz)}{f_0} \tag{3.66a}$$

$$\rho_h = 5.05 - \frac{f(GHz)}{f_0} \tag{3.66b}$$

$$\rho_0 = 5 - 0.885 \times \frac{f(GHz)}{f_0} \tag{3.66c}$$

with $f_0 = 20\,\text{GHz}$;

And:

$$\eta_v = -15.6 + \frac{94.1}{\lambda(cm)} \tag{3.67a}$$

$$\eta_h = -24.85 + \frac{159.6}{\lambda(cm)} \tag{3.67b}$$

$$\eta_0 = -38.15 + \frac{205.3}{\lambda(cm)} \tag{3.67c}$$

These values are integrated over different drop-size distribution to calculate the specific attenuation, and this can be written as:

$$\gamma = \int_0^{+\infty} \eta_{v,h} \bar{a}^{\rho_{v,h}} \times n(\bar{a}) d\bar{a} \qquad (3.68)$$

where $n(\bar{a})d\bar{a}$ is the drop size distribution. This method enables one to calculate the specific rain attenuation within this frequency range without interpolation, once the raindrop size distribution governing a locality is known [*Moupfouma,* 1997].

3.10 Validity of Rain Attenuation models for different Climatic Regions

From the above discussions, it can be deduced that all the rain attenuation prediction models basically need information about the rain rate statistics or the raindrop size distribution governing a particular climatic region. The rain rate statistics can either be in the form of point rain rate data or cumulative distributions, so that rain rate exceeded at different percentages of time can be determined. As explained above (section 3.2), the International Telecommunication Union-Radio Communication research group (ITU-R), has come up with a global climatic map which shows the rain rates exceeded for 0.01% of the time for all the climatic rain zones in the world. With these, geographical locations with no rain rate data can use the global climatic map of the ITU-R to estimate the rain attenuation for the particular location considered.

However, the ITU-R prediction models have instigated a lot of questions from researchers around the world, especially those from the high rainfall rate regions like the tropical and equatorial climates. Most of these researchers observed that when the attenuation results from the ITU-R model are compared with the actual local rain attenuation measurements, there is always a measure of discrepancy between the two results. And these have been traced down to the raindrop size distribution employed by the ITU-R to develop the rain attenuation model [*Yeo et al.,* 1993]. The ITU-R has adopted the Laws-Parsons drop-size distribution model [*Yeo et al.,* 1993, *Adimula and Ajayi,* 1996; *Ajayi et al.,* 1996] which has taken a functional form of the negative exponential distribution of Marshall-Palmer [*Green,* 2004]. *Yeo et al.* [1993] have stated that the Law-Parson drop-size distribution is not a representative of weather outside Europe and North America continents.

These problems have made many researchers in tropical and equatorial climates like Nigeria [*Adimula and Ajayi*, 1996; *Ajewole et al.*, 1999b], Brazil [*Maciel and Assis*, 1990; *Massmbani et al.*, 1990], Singapore [*Yeo et al.*, 1993; *Li et al.*, 1994a, 1994b, 1995; *Zhou et al.*, 2000], Malaysia [*Zainal et al.*, 1993], Indonesia [*Maagt et al.*, 1993; *Suryana et al.* 2005], India [*Maitra*, 2004], and others to initiate propagation studies in their geographical locations. And from their experimental works, the deficiencies of the Marshall-Palmer drop-size distribution model are confirmed for convective thunderstorm rains which are usually common in the tropical and equatorial climates [*Ajayi and Olsen*, 1985]. *Awang and Din et al*. [2004] made a comparative study for rain drop distribution in some tropical climates, namely Malaysia, Singapore, Nigeria and Brazil. This was achieved by using the lognormal drop-size distributions coefficients determined from their local measurements in Nigeria [*Ajayi and Olsen*, 1985], Brazil, [Maciel *and Assis*; 1990], Singapore [*Ong and Shan*; 1997], and Malaysia [*Tharek and Din*; 1992]. The drop-size distribution is shown in Fig. 3-2 below.

From Fig. 3-2, it can be seen that even for the same lognormal drop-size distribution, each geographical location has its own drop-size distribution function. This can be used to accurately

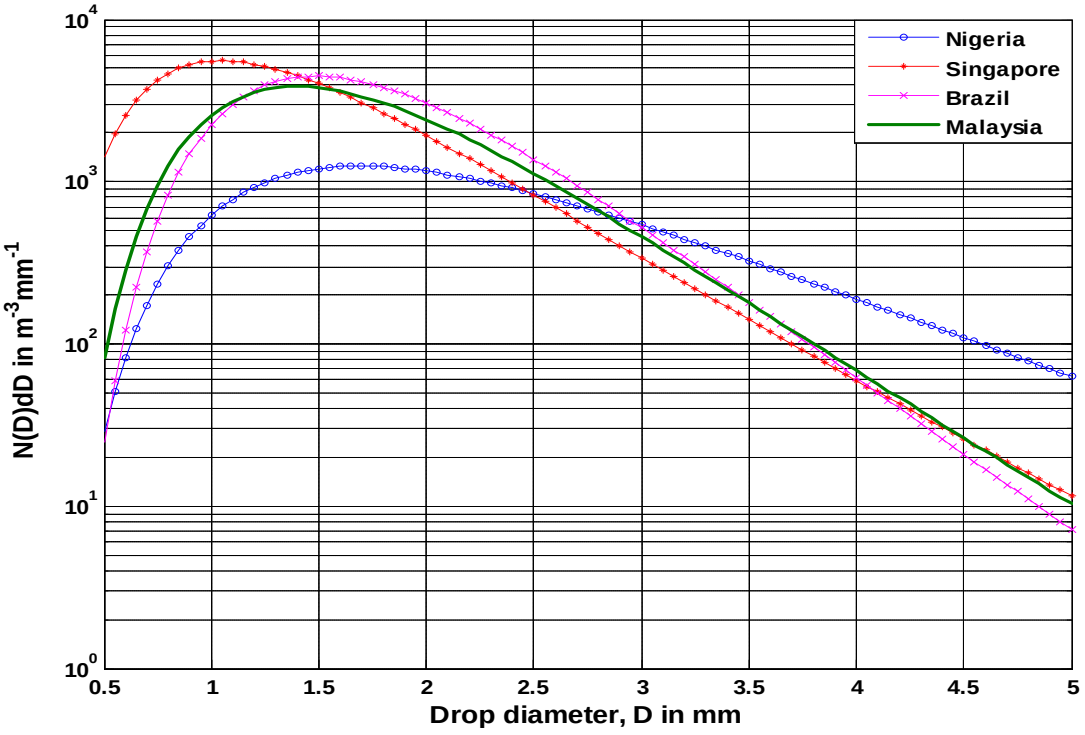

Fig. 3- 2: Comparison models of the raindrop size distribution for Nigeria, Singapore, Brazil and Malaysia at rainfall rate of 100 mm/h

predict the rain attenuation for the particular geographical location. Therefore, the validity of one attenuation prediction model in a geographical location, may not accurately predict the attenuation in other geographical location. Some authors have attempted to adjust the *Marshall-Palmer* [1948] drop-size distribution parameters so as to give a closed agreement with the measured local data in their environment [*Yeo et al.,* 1993; *Li et al.,* 1994b], but caution needs to be taken for any inconsistencies that may affect adjustment of parameters [*Green,* 2004].

All in all, for a rain attenuation model to accurately predict rain attenuation along a terrestrial radio link, an accurate prediction of the rain rate statistics, and the drop-size distribution, must be readily available for the particular climatic rain zone in which the prediction is to be made. It should also be noted that for path attenuation, the effective path length of the terrestrial link should also be considered to accommodate the non-uniformity of rain along radio paths. That is why the rain attenuation model predicted in one climatic region may not be adequate or valid for the other climatic region. Many studies have been carried out in temperate and tropical climates, but little has been reported about sub-tropical climates, in which South Africa falls; hence, this work seeks to fill that void.

3.11 Chapter Summary

The nature of rain which resulted in different hydro-meteorological zones across the world has instigated the development different rain attenuation models across the continent so as to estimate the effect of rain on radio signals. This chapter has given a general overview of these attenuation models in different parts of the world. This overview has covered empirical rain attenuation model in terms of specific rain attenuation and path attenuation along a terrestrial link. Also, the theoretical attenuation models which incorporate the scattering effects of raindrop by electromagnetic wave and raindrop size distribution have also been studied for the specific attenuation predictions. Rain rate statistics and the conversion of rain rate to the recommended 1-minute integration time for a reasonable prediction of rain attenuation was also mentioned.

The next chapter aims at utilizing a one year signal level measurement recorded at 19.5 GHz over a 6.73 km terrestrial path length, with a 1-minute rain rate recorded concurrently along the link in Durban to develop an empirical rain attenuation model.

Chapter Four

Rain Attenuation Prediction and Modeling from Propagation Measurements

4.1 Introduction

As mentioned in the previous chapter, attenuation due to rain can be described empirically from link measurements or from the knowledge of point rain rates, raindrop size distribution or other relevant propagation parameters along the radio path [*Ajayi et al*., 1996; *Myers*, 1999]. Point rainfalls are characteristically known never to be uniform along propagation path length [*Green*, 2004]. They display significant spatial and temporal variation along a horizontal path, and needs to be incorporated into attenuation models for effective propagation prediction [*Crane*, 1996]. Most attenuation models developed using point rain rate empirical distribution functions or path attenuation empirical distribution functions have used the concept of equivalent path-averaged or integrated rain rate along the propagation path length to combat these spatial effects [*Moupfouma* 1984; *Crane*, 1996]. And some attenuation models have used the concept of effective path length which is obtained by multiplying the point rain rate for the time percentage of interest with a reduction factor [*Moupfouma* 1984; *ITU-R 530*, 2007].

The aim of this chapter is to propose rain attenuation model from the signal level measurements recorded from a 19.5 GHz horizontally polarized 6.73 km terrestrial radio link set up in Durban for a period of one year by *Naicker and Mneney* in 2004. Along this propagation path length, a 1-

minute rain rate and other propagation parameters (clear air) such as temperature and relative humidity were also recorded.

From these measurements, monthly attenuation prediction models were proposed for the rainy months in the year, as well with models describing measured minimum, average and the maximum attenuation bounds for the terrestrial link. These attenuation bounds which mean the attenuation values for each rain rate along the path are then compared with other established rain attenuation models to reflect the suitability of each model on the measured attenuation bounds.

4.2 Description of the Terrestrial Link Setup

The terrestrial line-of-sight link was established between the Howard College and the Westville campuses of the University of KwaZulu-Natal, Durban in 2004 by *Naicker and Mneney* to monitor signal attenuation due to Rain. The system for monitoring the attenuation due to rain was installed at 19.5 GHz terrestrial link between the two campuses of University of KwaZulu-Natal. A block diagram of the system is provided in Fig. 4-1 below. The transmitter antenna was installed 178 m above sea level, on the roof of the Science building at Westville campus. The receiver antenna was setup on the Electrical Engineering building in Howard College campus, 145 above sea level [*Naicker and Mneney*, 2006; *Naicker* 2006].

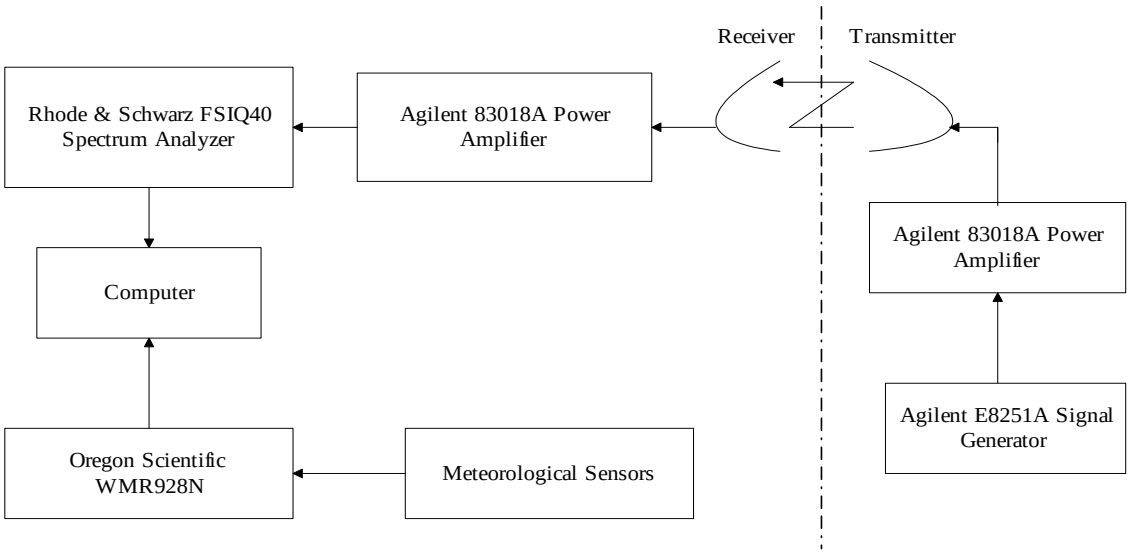

Fig. 4- 1: Block diagram of the of the monitoring System [*Naicker and Mneney,* 2004]

A valuline ® WR42/R220 parabolic antennae of diameter 0.6 m are used at both the receiving and the transmitting stations. The antennae can operate within the 17.7 – 19.7 GHz and 21.2 – 23.6 GHz bands and provide a gain of 38.6 dBi and a 3 dB beamwidth of 1.9^{O} at 19.5 GHz [*Naicker and Mneney,* 2006; *Naicker* 2006]. These parabolic antennae are protected by a weatherproof material known as radome[4]. The radome prevents ice and freezing rain from accumulating directly onto the metal surface of the antenna [11].

The cabling of the terrestrial link consists of FSJ1-50A super-flexible coaxial cable which produces an attenuation of 22 dB per 100 m. An agilent E8251A signal generator is used at the transmitting station to provide the source signal which can operate between 250 KHz – 20 GHz. This is used with an agilent 83018A microwave system amplifier which can operate from 0.5 GHz – 25 GHz and provide a gain of up to 27 dB [12]. This setup produces unmodulated continuous wave signals operating at a frequency of 19. 5 GHz.

At the receiver, another agilent 83018A power amplifier is used to give additional gain before feeding the signal into the Rhodes & Schwarz FS1Q40 spectrum analyzer. The signal strength is logged every second or minute onto a computer. The calculated expected noise power in the receiver when no signal is transmitted lies between –80.5 to –80.2 dBm. This defines the noise floor. The noise floor is determined from:

i. The noise temperature of the antenna T_A of 206^{o}K (with an estimated efficiency of 63.4%, equivalent background temperature of 150^{o}K [*Pozar,* 1988], and a maximum physical temperature of 303^{o}K);
ii. The transmission line noise temperature of 97.4^{o}K (with an attenuation of 22 dB per 100 m);
iii. 83018A Agilent amplifier (with a gain of 27 dB, and noise figure of about 9.5 dB at 19.5 GHz [12]) with noise temperature of 2398.5^{o}K;

Therefore resulting in total receiver noise temperature of 3470.4^{o}K, or a noise power of –80.2 dBm [*Pozar,* 1988]. At the lower temperature of 283^{O}K, the noise power is –80.5 dBm. In the measurements, this noise value varied from –79.5 dBm to –82 dBm [*Fashuyi and Afullo,* 2007].

[4] A radome allows a relatively unattenuated electromagnetic signal between an antenna inside the radome and outside the equipment [11]

The weather conditions were also logged using Oregon Scientific WMR928N wireless professional weather station to record the rain rate, outdoor temperature, relative outdoor humidity, outdoor dew point temperature, outdoor pressure, wind speed and wind direction. The rain rate was monitored every minute and the rainfall depth over each minute of interval for a period of one year was recorded [*Naicker and Mneney,* 2006; *Naicker* 2006]. More details on the link setup at the receiver and the transmitter end can be seen in *Naicker* [2006].

4.2.1 Path Profile

The terrestrial link has a path length of 6.73 km and passes over both hilly and the suburban terrain of Durban. The azimuth angle at the Westville transmitter station is 30.980^{O} and that of the Howard College receiver station is 30.943^{O}. Fig. 4-2 shows the digital elevation map of the propagation path, and Fig. 4-3 is the aerial map of the link showing the distance between the two stations. The terrestrial path is nearly horizontal, with a slight inclination of 0.3^{O} at the receiver. Fig. 4-4 gives the path clearance of the line-of-sight link from the first Fresnel ellipsoid. A k-factor or effective radius factor is used to examine the path clearance of the worst case of ray bending on line-of-sight link.

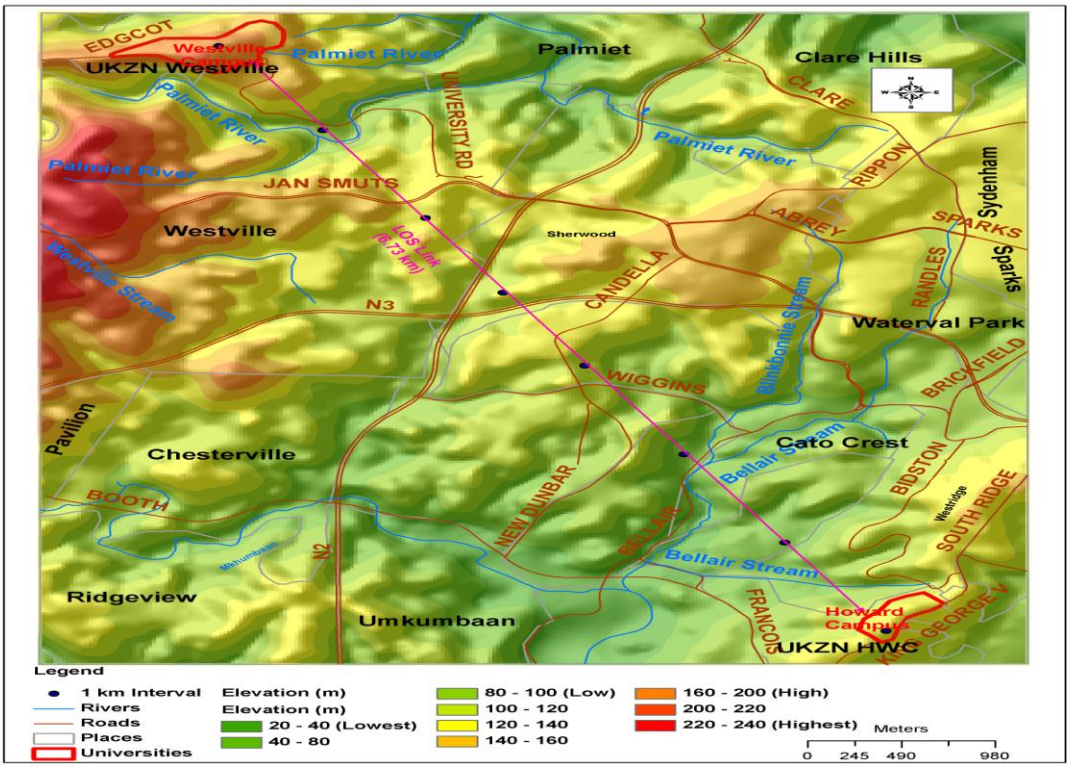

Fig. 4- 2: Digital elevation map for the 6.73 km terrestrial link between the two stations

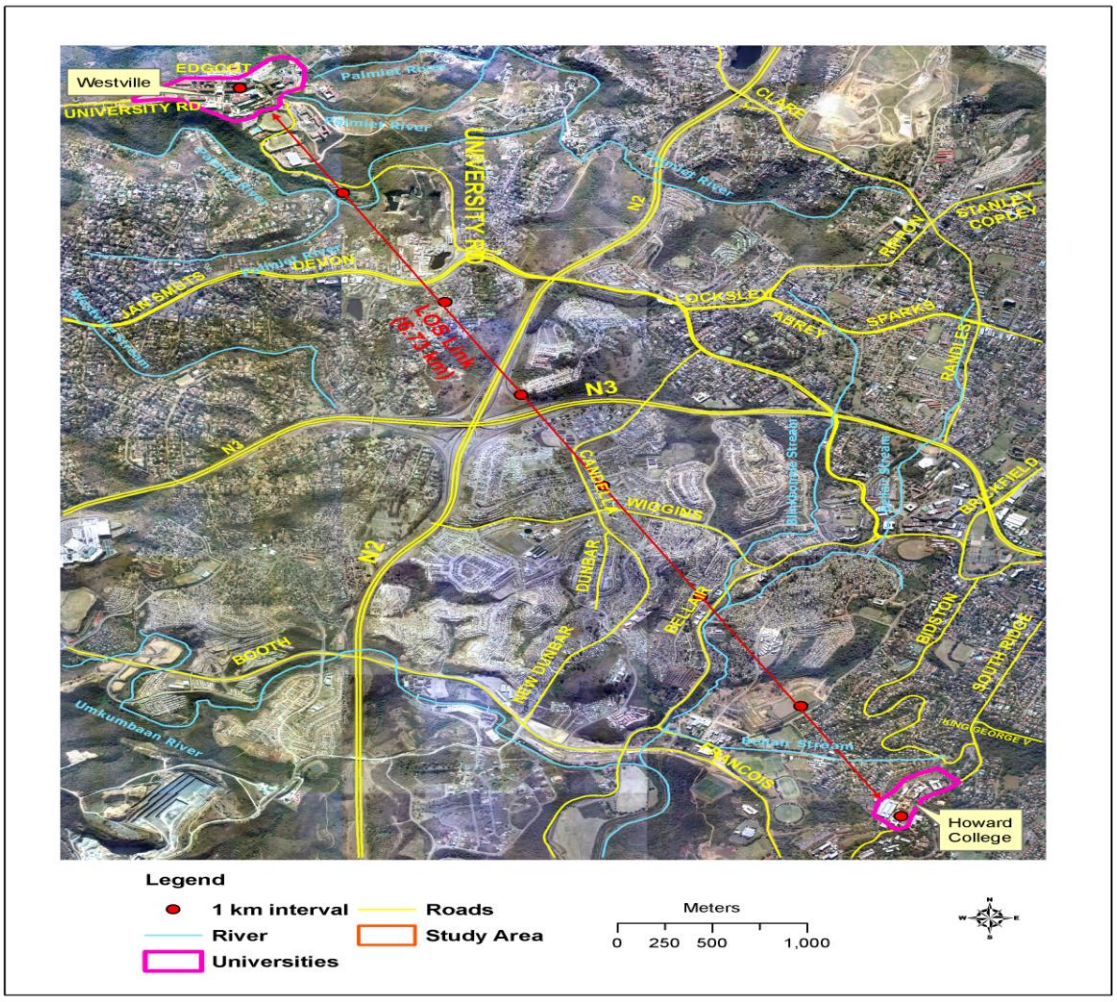

Fig. 4- 3: An aerial photograph of the 6.73 km line-of sight terrestrial link

Fresnel ellipsoids can be used to estimate the diffraction and reflections along radio propagation paths. The radius of the first Fresnel ellipsoid is given by:

$$F_1 = 17.3\sqrt{\frac{d_1 d_2}{fd}} \tag{4.1}$$

where F_1 denotes the radius of the first Fresnel ellipsoid in m, f is the frequency in GHz, d is the total path length in km and d_1 and d_2 are the distances from either stations in km.

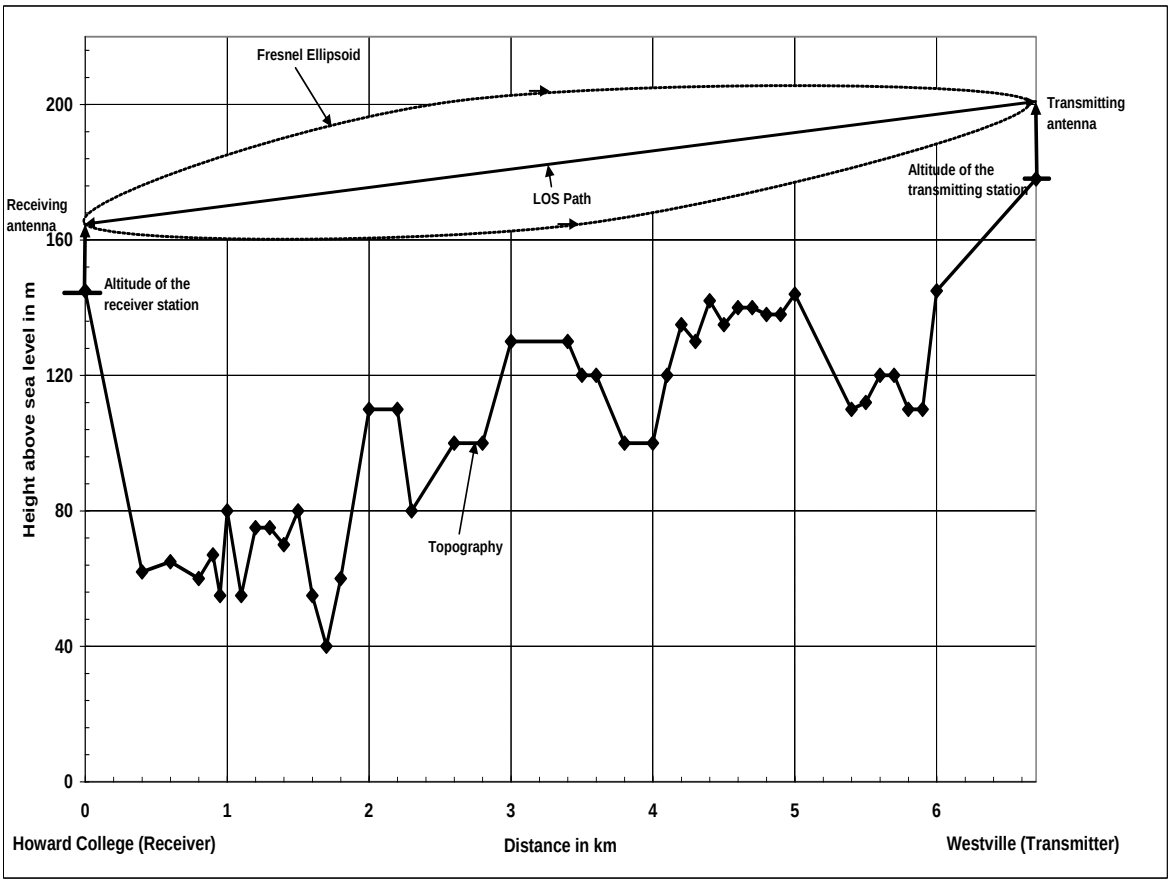

Fig. 4- 4: Path profile for the 6.73 km terrestrial line-of-sight link from Howard College campus to Westville campus [Naicker and Mneney, 2006; Fashuyi et al., 2007]

4.3 The Link Calculation and Data analysis

The terrestrial link parameters are summarized in Table 4-1 below. From the altitude data in Table 4-1, the transmitting antenna is 178+24=202 m above sea level. Similarly, the receiver station is 145+20=165 m above sea level. Also from the link parameters, the received signal level (RSL) was determined using a transmitting power of 100 mW (20 dBm) so as to have an idea of the power level that will be received at the receiver end of the link in clear air.

Calculating for the power received P_r we have:

$$\begin{aligned} P_r &= P_t - FSL + G_{rant} + G_{tant} - Losses \\ &= 20\,dBm - 135\,dB + 38.6\,dBi + 38.6\,dBi - 2.2\,dB - 1\,dB \\ &= -41\,dBm \end{aligned} \tag{4.2}$$

Table 4- 1: Terrestrial link parameters [Naicker, 2006]

Parameter	Description
Path Length	6.73 km
Height of transmitting antenna above the ground	24 m
Altitude of transmitter station above sea level	178m
Height of receiving antenna above the ground	20m
Altitude of receiver station above sea level	145m
Carrier frequency	19.5 GHz
Bandwidth under investigation	200 MHz
Transmitting power	10-100 mW
Transmitting/receiver antenna gain	38.6 dBi
Transmitting /receiver antenna beamwidth[5]	1.9 degrees
Free space loss	135 dB
Total cabling and connection losses	≈ 2.2dB
Clear air attenuation	≈ 1 dB
Receiver bandwidth	100 kHz-1 GHz

where:

P_t = Power transmitted (taken as 100mW=20dBm)

FSL = Free space loss

G_{rant} = Receive antenna gain

$G_{\tan t}$ = Transmit antenna gain

Thus, the expected power received P_r at the receiver end of the terrestrial link when a transmitting power of 100 mW is utilized between Howard College and Westville campuses should be – 41 dBm when there is no rain to cause any rain attenuation, no losses due to fog and water vapour, no multipath fading, and no diffraction fading. However, due to the other possible sources of loss, the actual received signal levels may fall below this ideal value. Example of this effect is shown in Fig 4-5 below. This figure shows the time series for clear-air signal level for a chosen day (March 15, 2004) at 19.5 GHz along the terrestrial path.

It can be seen from this figure that the received signals fluctuates between -41 and -43 dBm with an average value of -41.98 dBm for this particular day, despite the fact that there are no rains on this day to induce any rain attenuation. That means, there are excess free space loss signals on this particular day, as -41 dBm is the expected received signals on a clear-air day. The

[5] The beamwidth of an antenna is the angle enclosing the main lobe or twice the angle between the boresight direction and a reference power on the main lobe of the antenna pattern [*Pozar*, 1988].

fluctuations of signals in this figure (Fig. 4-5) may not be due to scintillation because at frequencies below 40 GHz, the scintillation fading effect on the overall fading distribution along terrestrial paths is not significant [*ITU-R 530-12*, 2007]. Several clear-air factors may contribute to this effect such as fog, water vapour, oxygen, multipath, etc.

The clear air attenuation is determined for this day by simply subtracting the actual clear-air signal level at each time for this particular day from the expected signal level of -41 dBm. Fig. 4-6 below shows the clear-air attenuation over 24 hours on 15th March, 2004. From the figure (Fig. 4-6), the clear-air attenuation varies between 1-2 dB. With this effect, the received signals for clear-air days for the period of the measurement campaign (February – December 2004) were averaged over each month to determine the clear-air signal level of which is referred to in this context as the non-rain faded average. Thus, the average clear air attenuation for each month is determined.

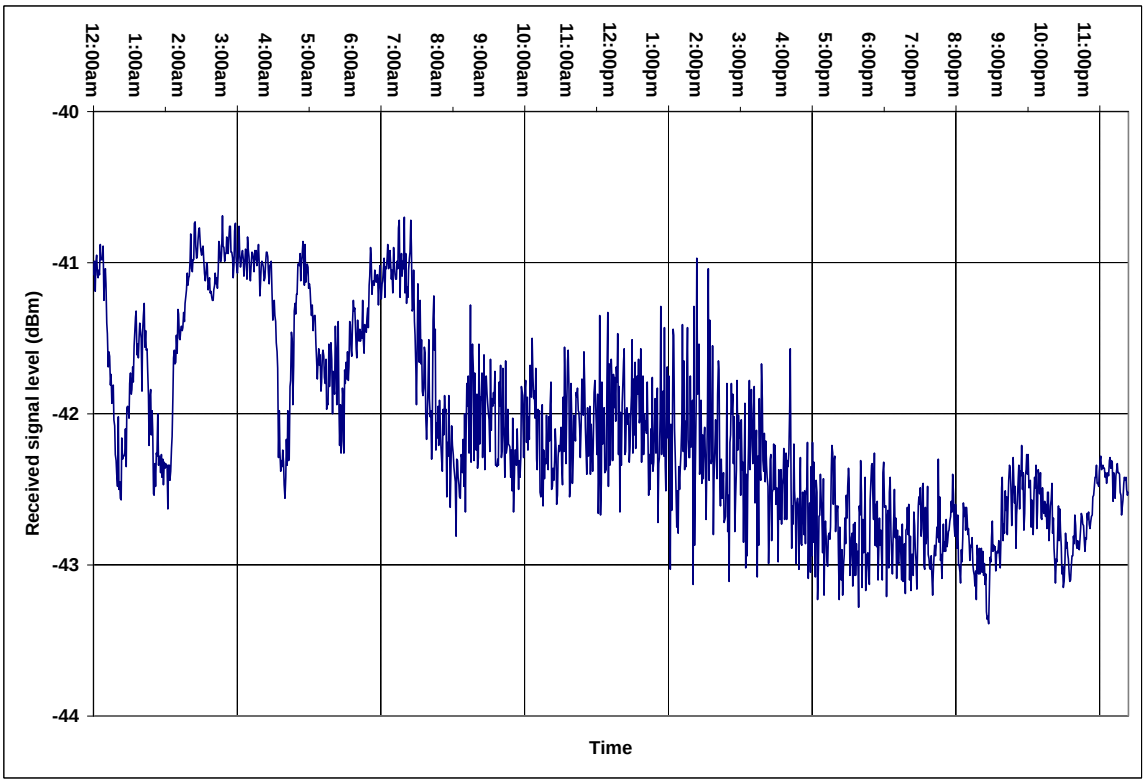

Fig. 4- 5: Clear-air signal level over 24 hours, 15th March, 2004

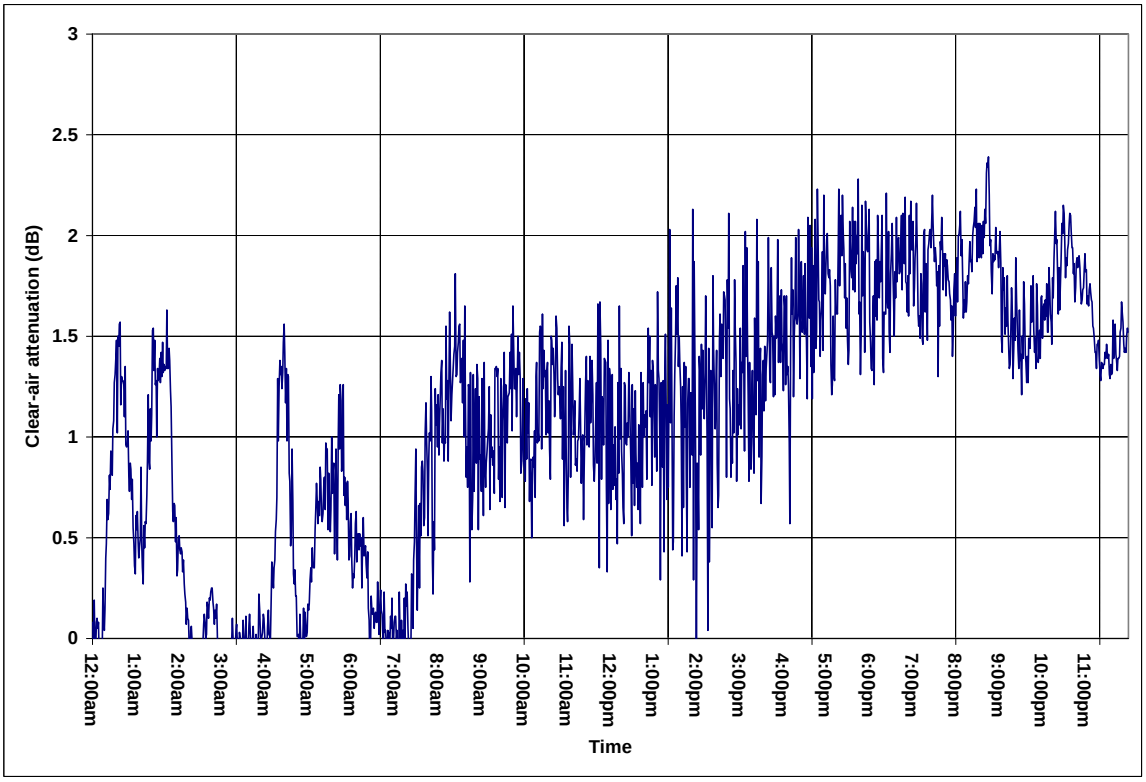

Fig. 4- 6: Clear-air attenuation over 24 hours, 15th March, 2004

4.4 Non-rain Faded Signal Level Measurements

The signal level measurement and its corresponding 1-minute rain rate statistics were recorded along the 6.73 km link at 19.5 GHz over a period of ten calendar months in Durban for the year 2004: February, March, April, May, June, August, September, October, November and December. These data was sorted, analyzed and the mean and median signal level for the non-rainy days for each month was determined. This we refer to as the non-rain faded signal and can be called the monthly mean or median received clear-air signal level observed at a given instant .This is shown in Fig. 4-7a below. Since there is little or no significant difference in the mean or median monthly non-rain faded signal level values, the mean monthly clear-air signal level was adopted in this work. With this, the mean clear-air attenuation known as the average excess attenuation (dB) above free space loss on clear air days in each of the month is determined by discounting the average received clear-air signal level for each month from the expected signal level of -41 dBm along the link. This is shown in Fig. 4-7b below.

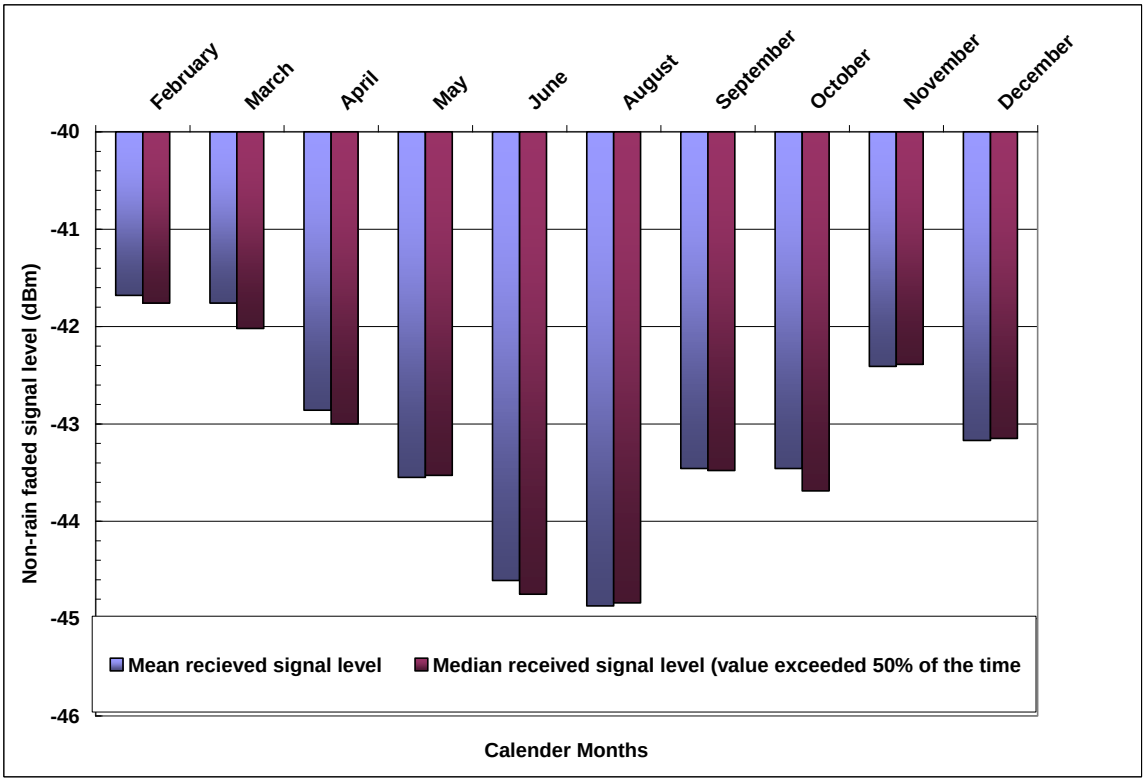

Fig. 4- 7a: Monthly mean and median received signal level in clear-air for 10 months in 2004

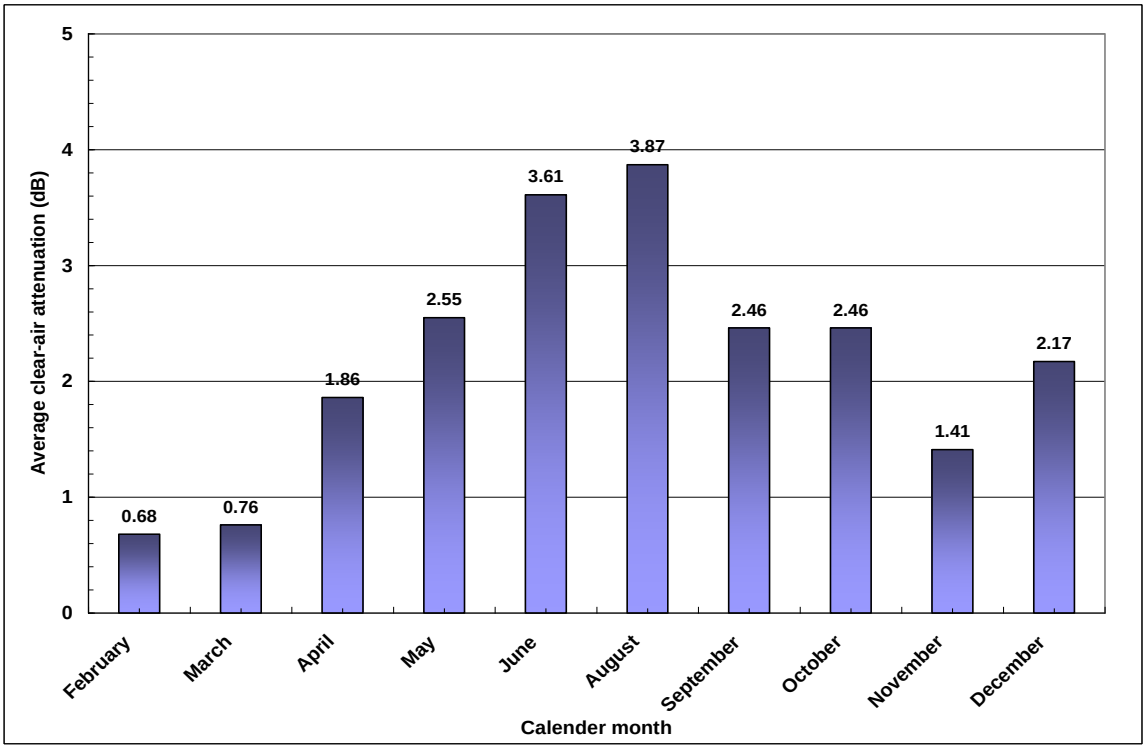

Fig. 4-7b: Mean excess attenuation (dB) above free space loss on clear-air days for 10 months in 2004

From Fig. 4-7b, the average clear-air attenuation fluctuates between 0.68 dB to 3.87 dB for the entire measurement period. With the month of August recording the highest excess attenuation (dB) above free space loss on clear air days and February with the lowest. With these values, the actual rain attenuation values in each of the month can be determined. From Fig. 4-7a, the non-rain faded average for February and March is – 41.68 dBm and – 41.76 dBm respectively while that of April is – 42.86 dBm which tends to be lower than that of the other two months and relatively lower than the expected received signal level. For the months of May, June, and August which is normally referred to as the winter months in South Africa [13]; [*South Africa year book*, 2006] a very low non-rain faded average values of – 43.55 dBm, – 44.61 dBm, and – 44.87 dBm are recorded respectively.

It should be noted at this point that the noise floor of the receiver has been calculated to be between –80.5 to –80.2 dBm, but in the measurements, this noise value varied from –79.5 dBm to –82 dBm (as stated in section 4.2). This has been adequately catered for during the sorting and the processing of the non-rain-faded received signal level in each of the month.

Several factors contributed to this clear air attenuation. Taking into considerations some factors discussed in the second chapter of this thesis, and Durban being a location that has a rugged and hilly terrain, the excess free space loss recorded especially in the winter months where there no significant rains might have arise due to k-factor fading. The value of the k used in the design of the terrestrial link is 1.33, while the median value of k-factor for Durban is 1.21, with a value of k = 0.5, exceeded 99.9% of the time [*Odedina and Afullo*, 2005; 2006]. The "worst" month for k-factor fading is February (with value of $k \approx 0.2$ exceeded 99.9% of the month); while the month of August has k-factor value exceeded 99.9 % of the time of 0.9. Note also that the median value of k for August is 1.27 as opposed to the 1.21 for February [*Odedina and Afullo*, 2006]. Thus, this type of fading may contribute 1-1.5 dB over the path (see clearance of the first Fresnel zone, Fig. 4-4), and results in *Odedina and Afullo*, [2005], and *Odedina and Afullo*, [2006]).

Water vapour effect is another contributor to the measured non-rain faded signal levels. The highest contribution to the water vapour effects occur in the summer months with an average pressure of about 25.76 mb (see Table 4-2). This gave an average attenuation of about 0.34 dB/km, or 2.2 dB over the 6.7 km path. On the other hand in winter, the average water vapour pressure is about 12.37 mb (see Table 4-2), resulting in attenuation of about 0.13 dB/km, and 0.9 dB over the 6.7 km path [*Ajayi et al*, 1996]. Thus, water vapour attenuation contributes about 1

dB in winter and 2.2 dB in summer. There are some intervening rivers along the propagation path (see Fig 4-2 and 4-3) which may cause some little reflections of the radio signals along the path, thus, the multipath fading may be limited to below 1 dB.

Also, due to the coastal nature of Durban, as well as the industries, fog attenuation is also a contributor. From the climatic characteristics of South Africa discussed in Chapter two of this thesis, the east coast of South Africa are said to have abundant low stratus cloud and fog [*South Africa year book*, 2006]. Durban, lying along the eastern coastal side of South Africa has the tendency of being influenced by this fog and low stratus cloud which in turn can affect any signal level even when there are no rains. At the operating frequency of the link of 19.5 GHz, an average attenuation of 0.1 dB/km is expected, resulting in a value of 0.7 dB along the propagation path (see Fig. 2-4) [*Hall et al.*, 1996]. This thus accounts for the attenuation during non-rainy days.

Table 4- 2: Average water vapour recorded for Durban in 2004 at 19.5 GHz

Months	Average water vapour (mb)
February	25.57
March	23.29
April	23.67
May	15.93
June	11.71
July	11.62
August	15.87
September	19.14
October	21.76
November	22.45
December	29.26
Average	**20.03 mb**

4.5 Analysis of Rainy Days Data and Its Rain Attenuation

This section gives information on the number of rainy days and their durations for the rainy months during the experimental period. There were rains in the month of February, March, April, September, October, November, and December. No rains were recorded in the winter months; May, June and July in 2004 during the experimental period. This section also shows the measured rain rate time series over selected rainy days featuring light, moderate and heavy rains. Consequently, the time series of the received signal levels (i.e. total attenuation) and the rain attenuation for each of the selected rainy days are highlighted in this section.

4.5.1 Rainy Days and Durations during the Experimental Period

An Oregon rain gauge (RGR 382) was installed at the receiver and transmitter throughout the experimental period to measure amount of rainfall and the 1-minute rain rate. The rain gauge collector has a diameter measuring 4 inches (101.6mm), and stands 5.75 inches high (146.05mm) rain accumulation. The gauge contains a collecting bucket that tips after accumulation of 1mm of rainfall. The measuring accuracy of the bucket with rain rate of 0 - 15mm per hour is +/- 10 % while above 15mm per hour is +/-15%. The gauge functioned for a period of one-year [*Naicker***,** 2006]. During this period, rain rate $\geq$ 1 mm/h were recorded over 7 months. Table 4-3 below shows the number of rainy day and durations in each month. From the table, March is the month that has the highest number of rainy days and duration with September having just one rainy day (25^{th} September).

Table 4- 3: Rainy days and durations along the 6.73 km terrestrial link for the rainy months

Months	Dates/Days	Duration (minutes)
February	21, 23, 26, 27, 29 (5 days)	1074
March	1,2,3,,11,12, 23, 24 (7 days)	1633
April	7, 8, 26 (3 days)	479
September	25 (1 day)	302
October	18, 21, 22, 23, 25 (5 days)	1356
November	11, 23, 27, 30 (4 days)	1097
December	6, 7, 8, 23, 24, 27 (6 days)	871

4.5.2 Time Series of the Experimental Data for Rainy days

This sub-section gives examples of the time series for various rainy days showing low, moderate and high rainy days. The received signal levels (dBm) for these rainy days are also shown. The total attenuation (dB) is extracted from the received signal by discounting the free space loss of -41 dBm from the received signal. The total attenuation incorporates the clear air effects and the effect of the rain rate recorded along the terrestrial link. The rain attenuation (dB) along the terrestrial path in each of the observed day is determined by deducting average clear air attenuation in the month (see Fig. 4-7b) from the total attenuation (dB).

Fig. 4-8 shows a high rainy day time series with a maximum rain rate of 79 mm/h in this particular day (September 25, 2004). The total received signal shown in Fig. 4-9 incorporates the free space loss, rain losses, and other clear air effects. Therefore, subtracting the free space loss of -41 dBm and the clear-air attenuation of 2.46 dB calculated from the non-rain faded average for the month September (as shown in Fig. 4-7b) from the total received signal for this chosen day in September, the rain attenuation along the terrestrial path is determined. The rain attenuation time series is shown in Fig. 4-10. For this day (September 21), the highest rain rate of 79 mm/h has a rain attenuation of about 25.42 dB as shown in Fig. 4-10.

Fig. 4-11 below shows another example of a high rainy day which occurred on 21st of October with the highest rain rate of 73 mm/h occurring at around 8:00 pm. The rain occurred between 7:45 pm – 11: 00 pm as shown in Fig. 4-11. The average non-rain faded signal level estimated for this month was -43.46 dBm, i.e. an average clear-air attenuation of 2.46 dB is expected along the path for the month of October. Subtracting the free space loss of -41 dBm and the average clear-air attenuation from the actual received signal level (as shown in Fig. 4-12), the rain attenuation for this particular day in October can be estimated. Fig. 4-13 shows the time series for the rain attenuation for high rainy day in October. This day has a high rain rate of 73 mm/h with corresponding rain attenuation of 21.57 dB.

Fig. 4-14 shows an example of a moderate rainy day in Durban which occurred on 29th February, 2004. The rain started around 4:40 pm and ends around 10: 00 pm getting to its climax around 5:00pm with a rain rate of 37 mm/h. The time series for the rainy day is shown in Fig. 4-14 below. Following this figure is the time series for the total received signal level for this day (Fig. 4-15). Fig. 4-16 shows the rain attenuation for the moderate rainy day, after which the free space loss of -41 dBm and the average clear air attenuation of about 0.68 dB for the February has been deducted from the actual received signal level.

Fig. 4-17 above shows the time series for a low rainy day. This occurred on the 27th of November, 2004. The rain rate ranges between 1 – 6 mm/ h and getting to its peak around 5: 48 pm with a rain rate of 6 mm/h. Fig 4-18 also shows the total received signal for this particular rainy day with the lowest value of -51.85 dBm which is induced by the 6 mm/h. The rain attenuation was extracted from the time series of the received signal level by subtracting the free space loss of -41 dBm and the average clear-air attenuation of -1.41dB determined from the non-rain faded average for the month of November. The highest attenuation for this low rainy day is 8.46 dB.

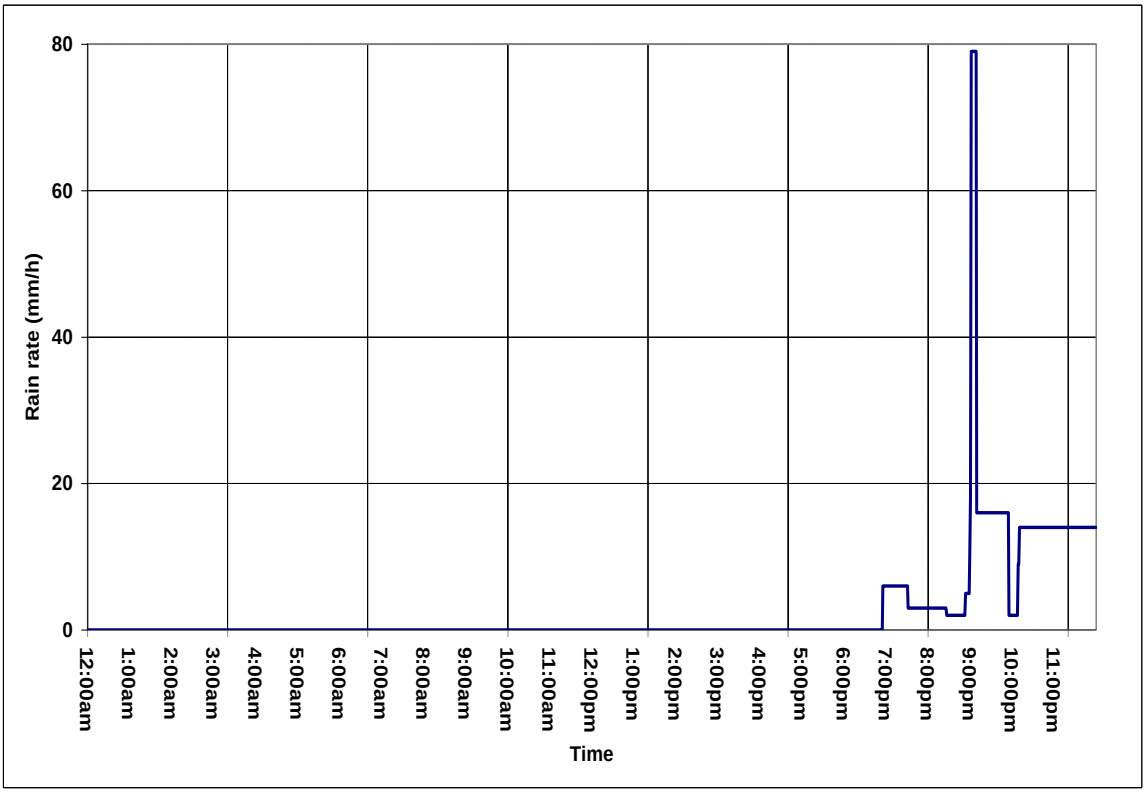

Fig. 4- 8: Time series for a high rainy day, September 25, 2004

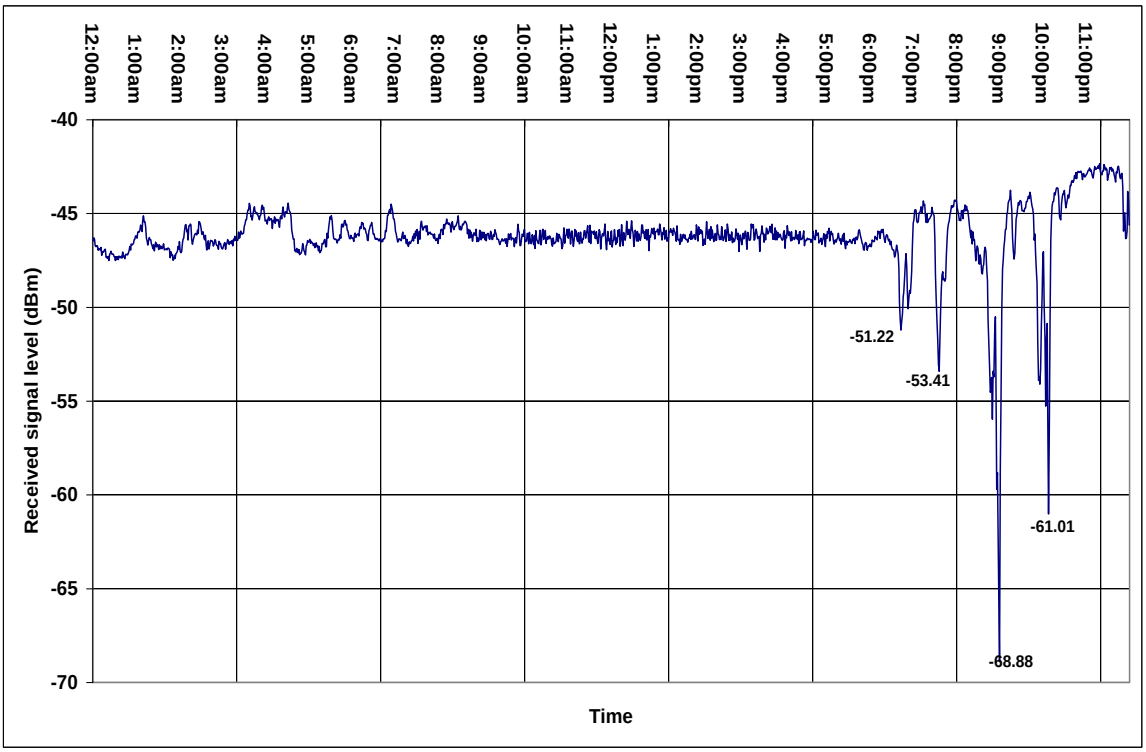

Fig. 4- 9: The received signal time series for a high rainy day, September 25, 2004

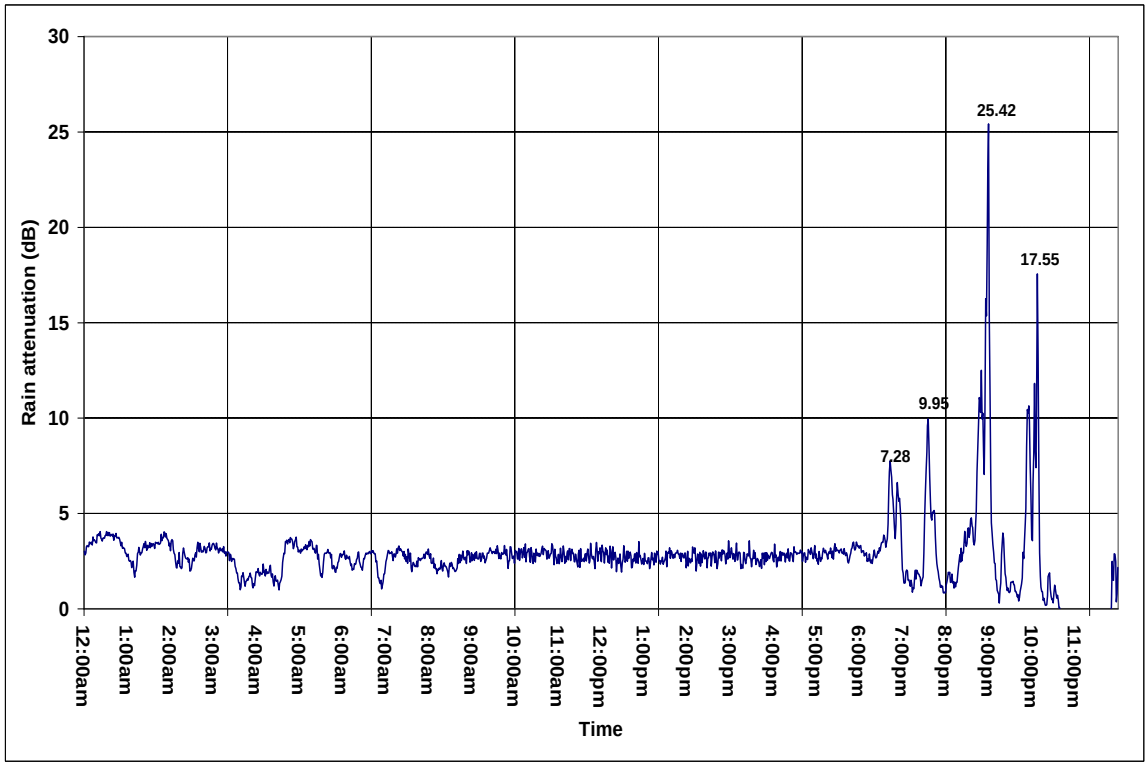

Fig. 4- 10: The rain attenuation time series for a high rainy day, September 25, 2004

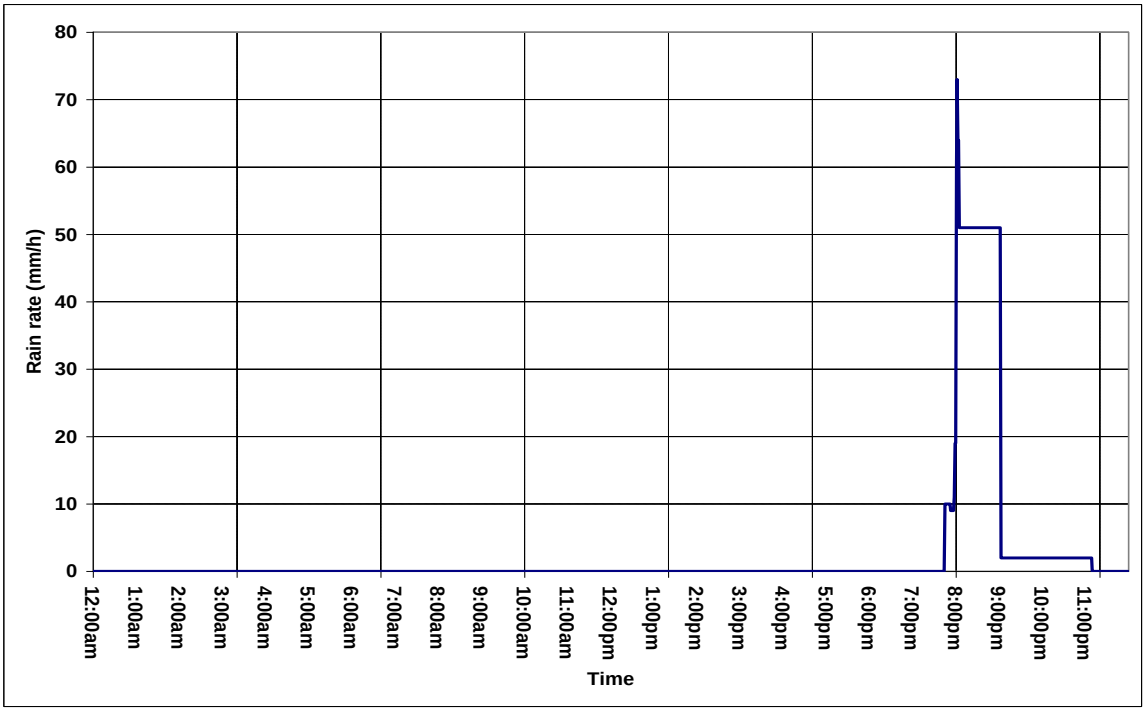

Fig. 4- 11: Time series for a high rainy day, October 21, 2004

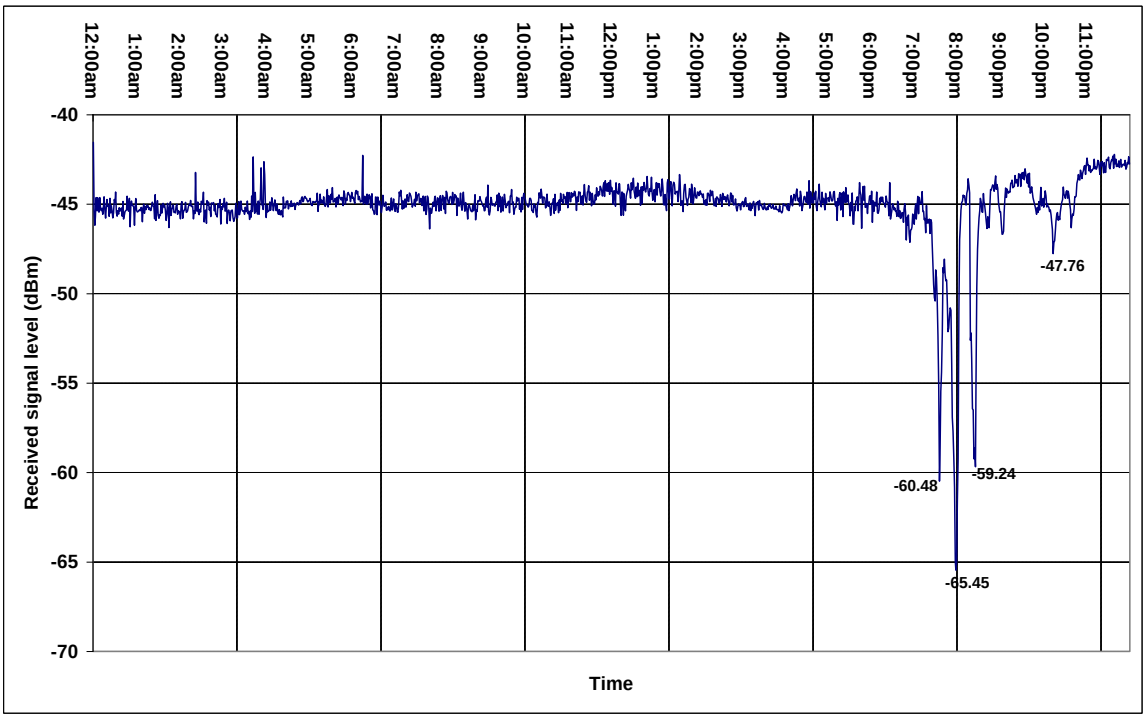

Fig. 4- 12: The received signal time series for a high rainy day, October 21, 2004

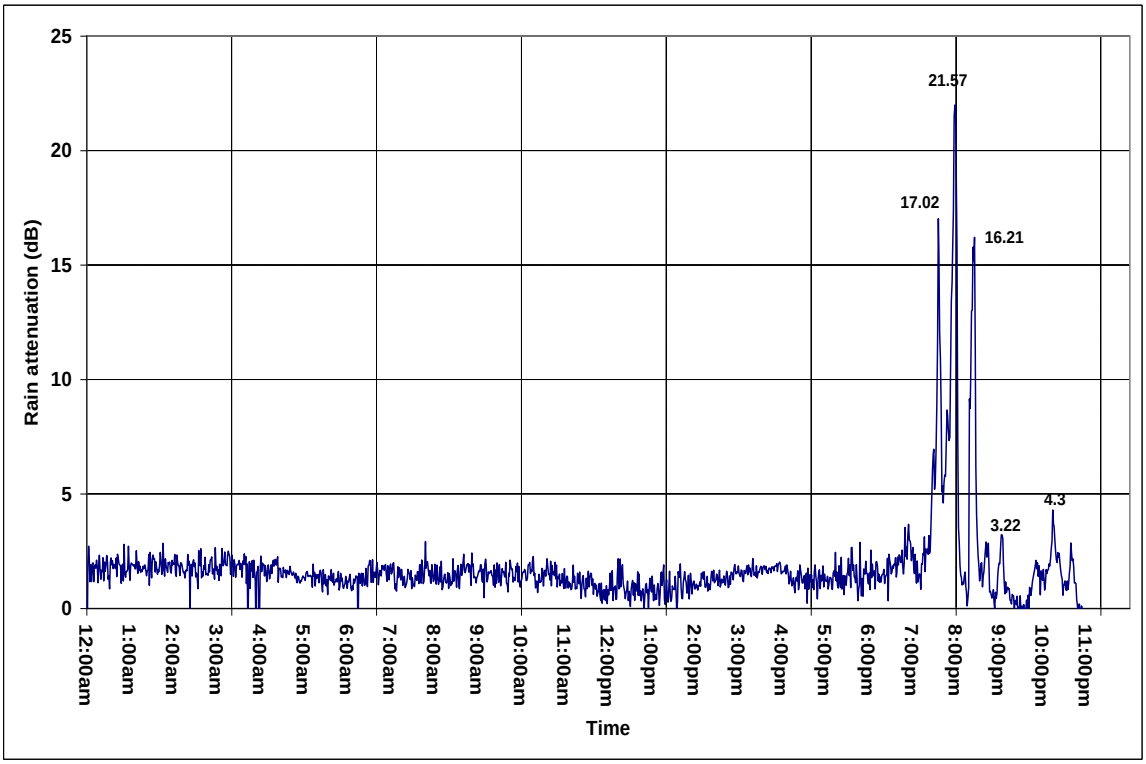

Fig. 4- 13: The rain attenuation time series for a high rainy day, October 21, 2004

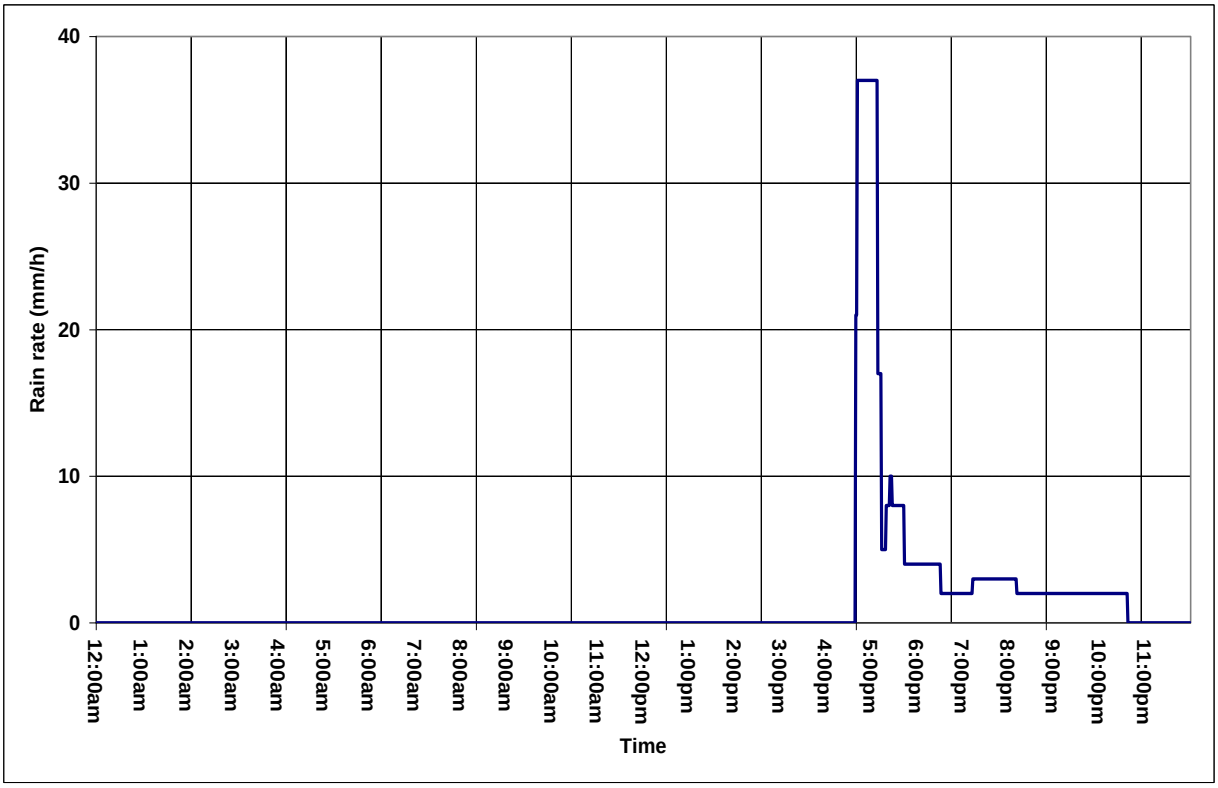

Fig. 4- 14: Time series for a moderate rainy day, February 29, 2004

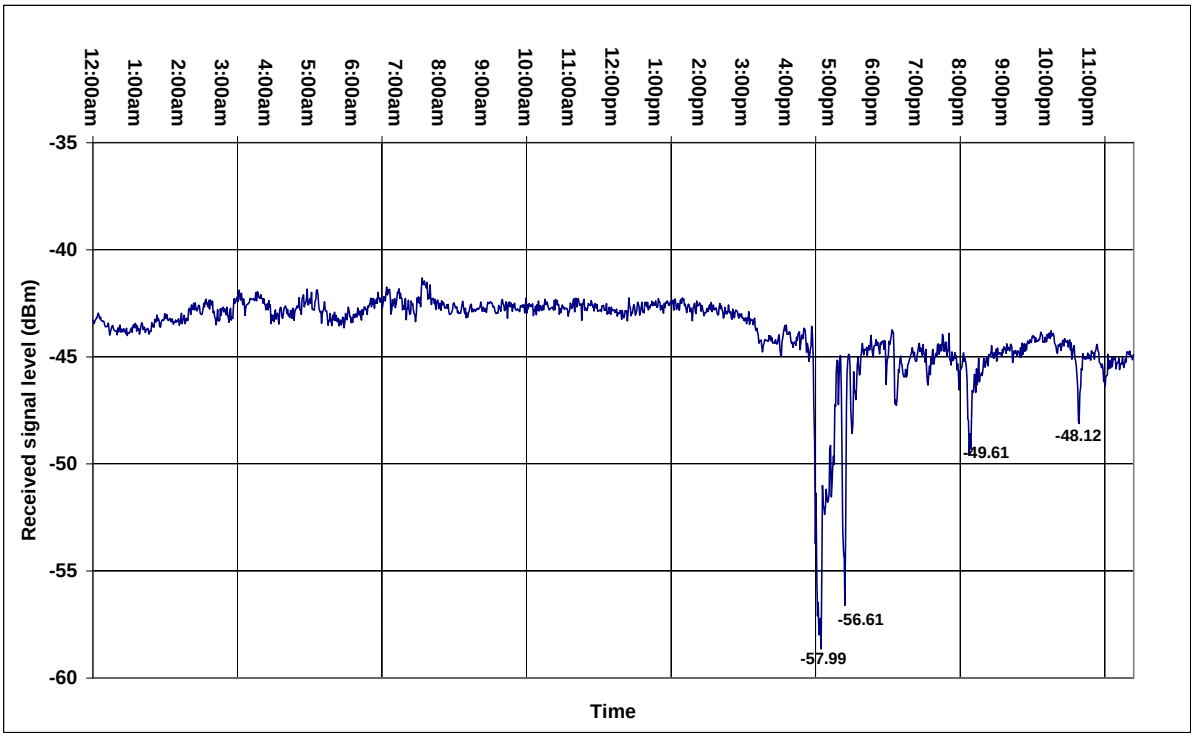

Fig. 4- 15: The received signal time series for a moderate rainy day, February 29, 2004

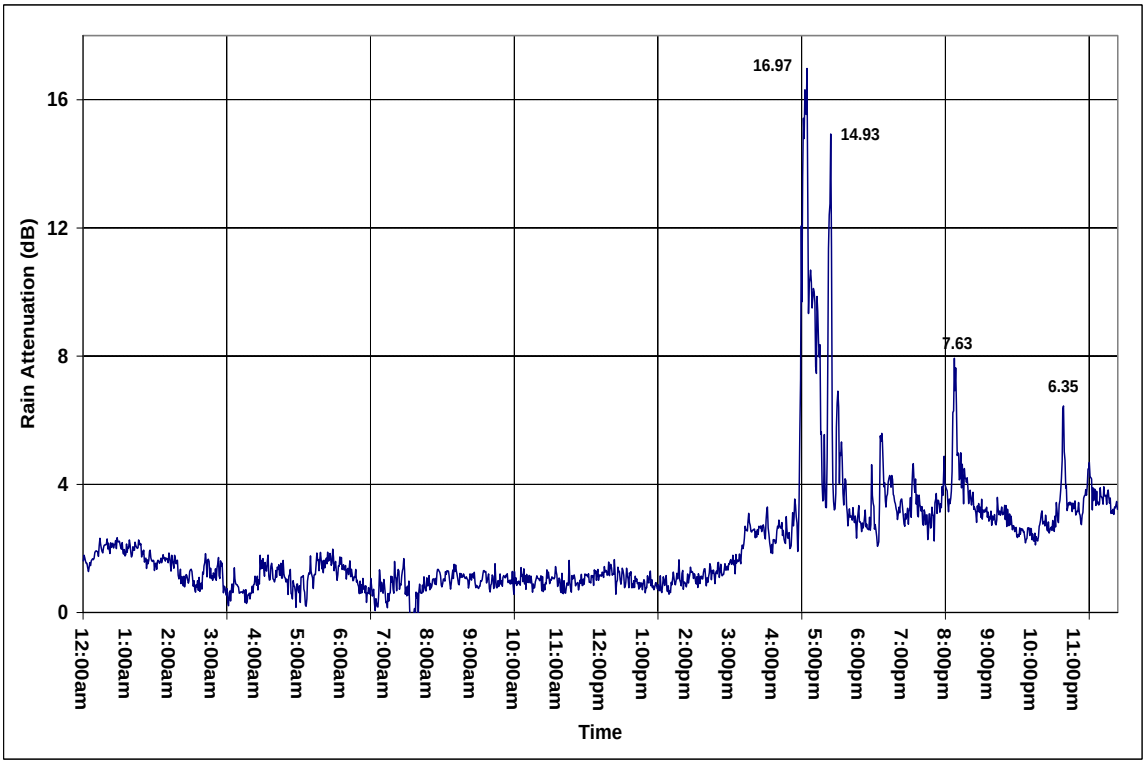

Fig. 4- 16: The rain attenuation time series for a moderate rainy day, February 29, 2004

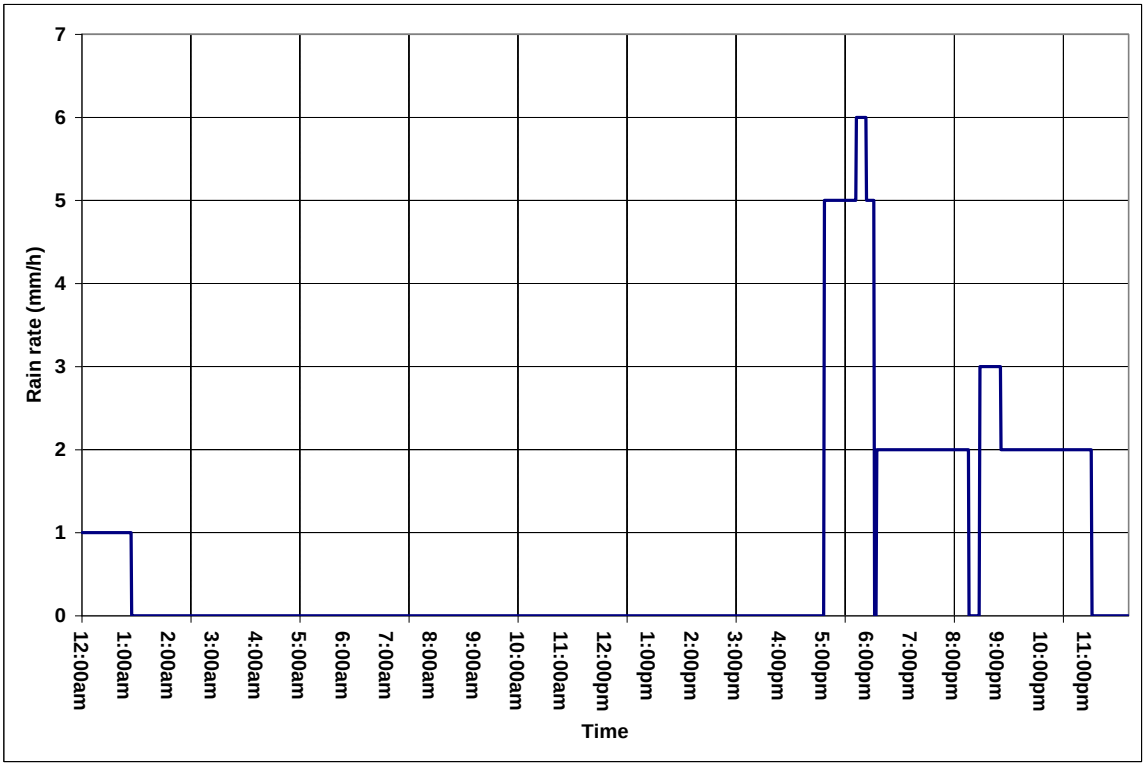

Fig. 4- 17: Time series for a low rainy day, November 27, 2004

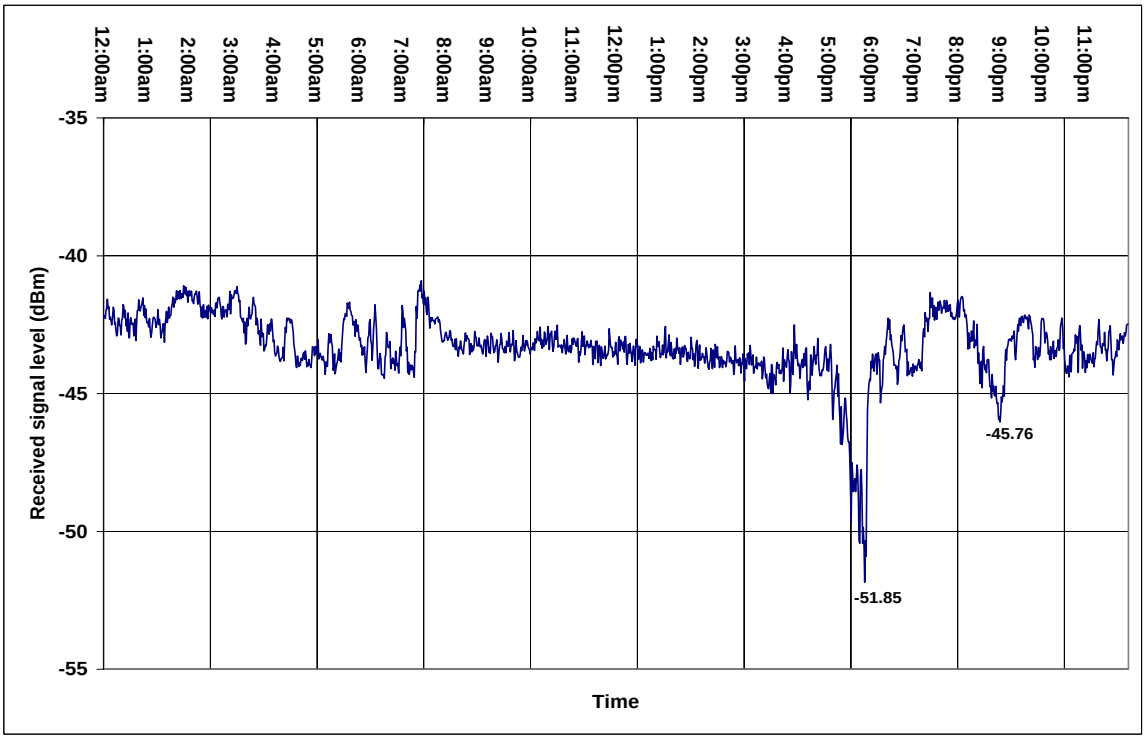

Fig. 4- 18: The received signal time series for a low rainy day, November 27, 2004

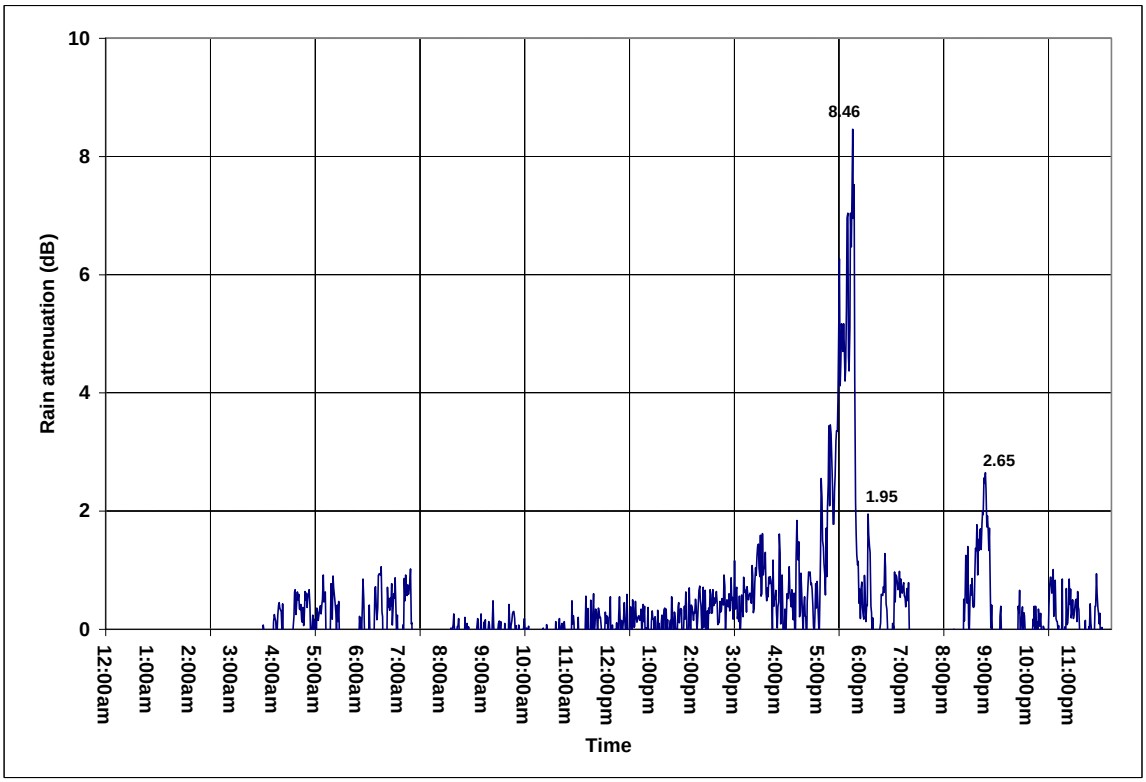

Fig. 4- 19: The rain attenuation time series for a low rainy day, November 27, 2004

4.6 Analysis of Monthly Rain Attenuation Prediction Models

Having determined the non-rain faded average for the 10-month experimental period in the year 2004, which have been utilized to calculate the average clear-air attenuation for each month. Also, rainy days data chosen for some specific days featuring light, moderate and high rains have been analyzed to quantify the effect of each nature of rain on the received signal between the radio paths. This has been used to determine rain attenuation for each of this day. With this, the monthly rain induced attenuation can be modeled for days that had rains within the experimental year, 2004. This is done for the months of February, March, April, September, October, November and December.

The rain attenuation for each of this month is determined based on the actual received signal recorded for the month. From the recorded propagation data, it was observed that the received signals for each 1-minute point rain rate varies, even though they may be of the same rain rate values. To overcome this problem, the signal levels for each of the rain rate are sorted and grouped in such a way that a 5 mm/h or a 10 mm/h, etc point rain rate has all its signal level values for the rain duration in each month for each rain rate. These signal levels are then averaged to determine the actual signal level for the 1-minute point rain rate. An example of this illustration is shown in Table 4-4 below.

From this table, a 1 mm/h rain rate will have an average received signal of about -43.15 dBm; 3 mm/h rain rate will have -45.93 dBm; 10 mm/h, an average received of -49.43 dBm; etc. These averaged received signal levels calculated for each point rain rate in each month is utilized to calculate the rain attenuation for each of the point rain rate along the 6.73 km propagation path: having incorporated the average clear-air effect for each month. Thus, rain attenuation is determined for each rainy month. The monthly attenuation statistics shows the monthly variability associated with rain attenuation along terrestrial path.

The rain attenuation values determined from the measured signal levels along the 6.73 km terrestrial path are plotted for varying rain rates in each month. Different estimations models are used on the data plots. Adequate empirical model describing the statistical data points based on the values of the regression coefficient is chosen to obtain an analytical fit for the measurement data. The equations and the regression coefficients which show the measure of the accuracy the

Table 4- 4: Illustration of received signal levels (dBm) grouped under different point rain rate (mm/h) values (sample data)

Rain rate	1mm/h	3 mm/h	5 mm/h	10 mm/h	15 mm/h	20 mm/h	30 mm/h
Received Signal Levels (dBm)	-43.31	-47.27	-49.16	-51.5	-53.74	-50.24	-64.68
	-43.87	-47.04	-48.38	-50.26	-50.37	-57.15	-63.88
	-43.67	-46.34	-49.22	-49.57	-59.29	-59	-63.43
	-43.68	-45.6	-49.19	-52.02	-51.03	-58.3	-66.19
	-43.51	-45.73	-48.92	-50.36	-50.8	-58.12	-65.18
	-42.41	-45.16	-48.73	-49.08	-51.44	-68.42	-63.34
	-43.37	-44.97	-47.83	-48.06	-58.61	-60.47	-62.01
	-42.98	-45.3	-48.26	-47.61	-57.22	-59.99	-63.23
	-43.09	-45.37	-48.45	-46.91	-50.65	-58.61	-60.65
	-42.76	-45.75	-47.51	-47.03	-52.13	-51.5	-65.46
	-43.08	-45.87	-47.18	-49.69	-51.93	-50.26	-60.91
	-42.75	-45.95	-48.53	-50.51	-51.26	-50.24	-58.43
	-42.53	-46.78	-48.63	-49.99	-50.8	-50.15	-59.05
Average signal level (dBm)	**-43.15**	**-45.93**	**-48.46**	**-49.43**	**-53.02**	**-56.34**	**-62.80**

models are also displayed on the graphs showing the monthly rain attenuation. Statistically, a good regression coefficient $\Re$ ranges between 0.95 and 1($0.95 \leq \Re \leq 1$). But 0.94 can be acceptable. A regression coefficient of 0.88 may means either the model is not adequate enough or there are no enough data points on the curve. Fig. 4-20 – 4-25 below shows the experimental attenuation values for each month and their estimation models.

Fig 4-20 below shows the rain attenuation plots for February in Durban. The figure shows the experimental rain attenuation values ranges between 2.53 dB to 16. 93 dB for rain rate value between 1 mm/h and 42 mm/h. Exponential, polynomial (3^{rd} order) and power analytical fits are used to model the experimental attenuation data points. The regression coefficients from these fits are 0.94, 0.98, and 0.72 respectively. This implies that either the exponential or the polynomial fit can be adopted to give an empirical model for the experimental rain attenuation in the month of February. For the month of March (Fig. 4-21), the exponential, polynomial, and the power analytical fit were also used to define the experimental attenuation data points. The regression coefficients for these are 0.82, 0.97, and 0.96 respectively. This means that the polynomial and the power analytical fit can be used to model for the experimental attenuation values that range between 0.69 dB and 6.41 dB with rain rate range of 1 mm/h and 16 mm/h for the month of March.

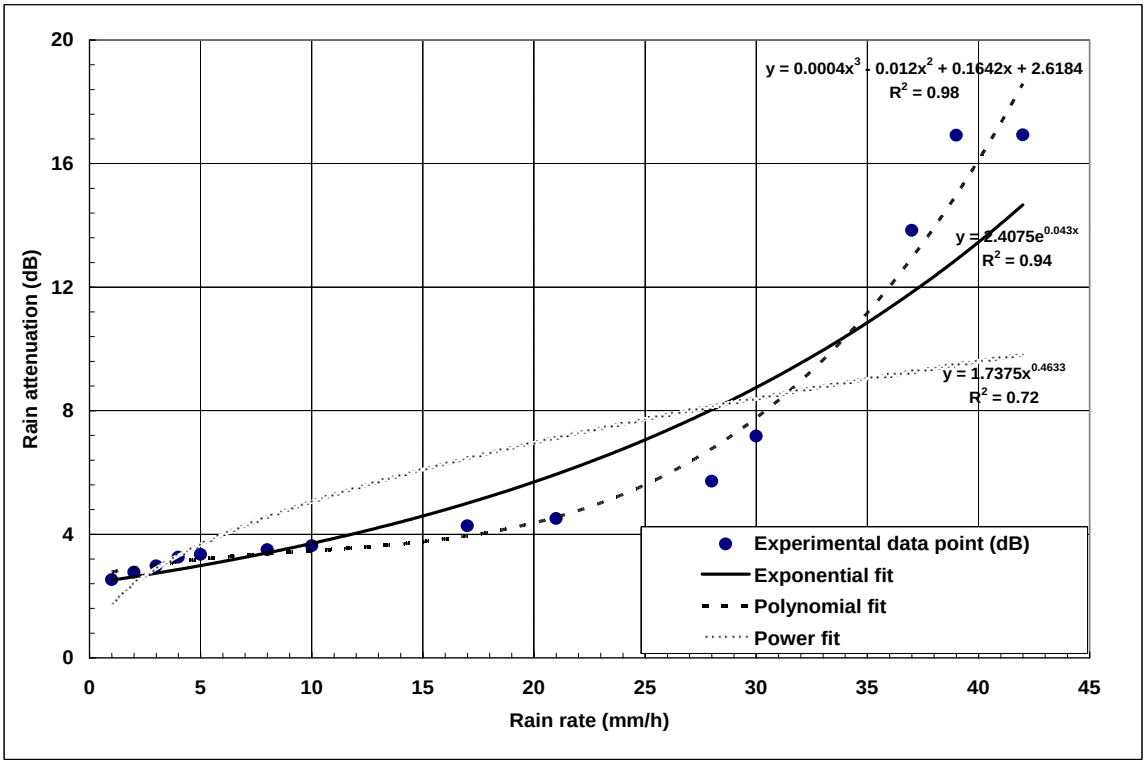

Fig. 4- 20: Rain attenuation for Durban in February: Measurement and estimated models along the 6.73 km at 19.5 GHz

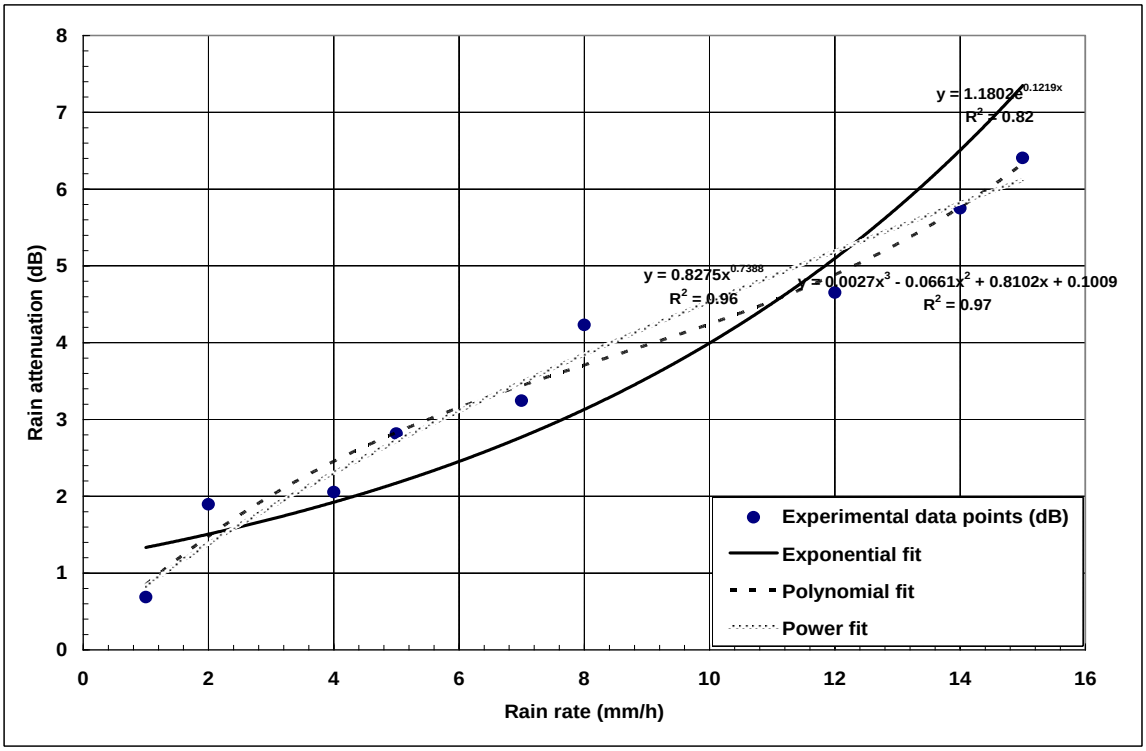

Fig. 4- 21: Rain attenuation for Durban in March: Measurement and estimated models along the 6.73 km at 19.5 GHz

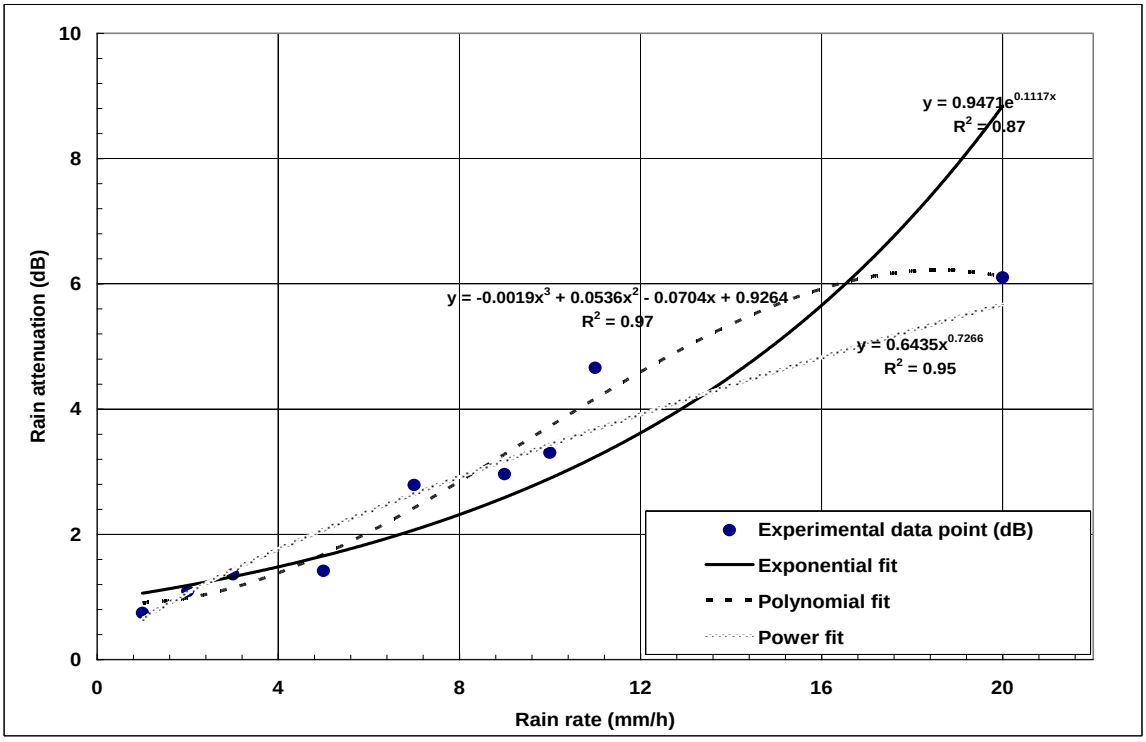

Fig. 4- 22: Rain attenuation for Durban in April: Measurement and estimated models along the 6.73 km at 19.5 GHz

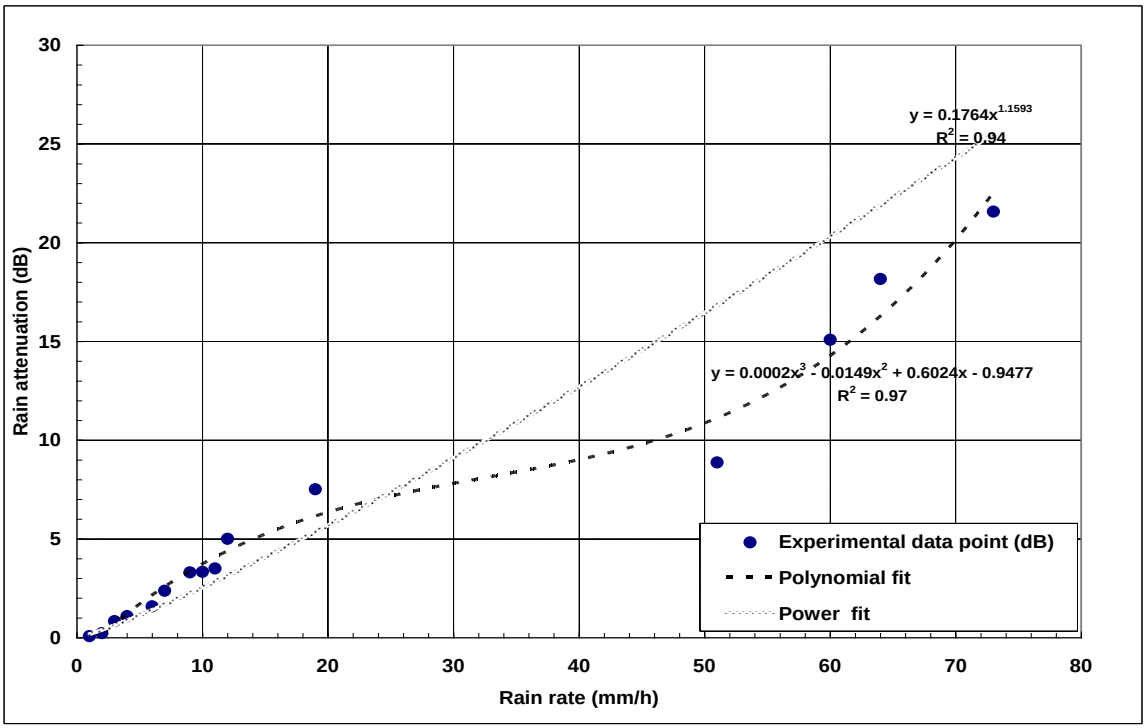

Fig. 4- 23: Rain attenuation for Durban in October: Measurement and estimated models along the 6.73 km at 19.5 GHz

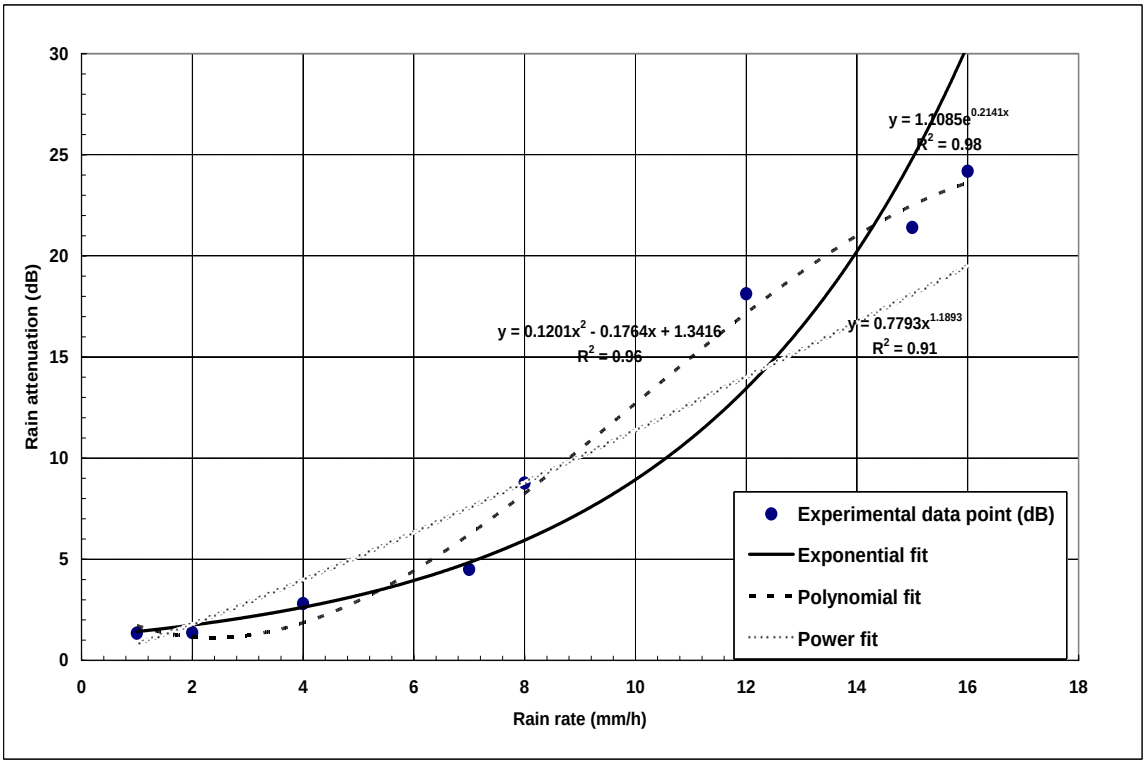

Fig. 4- 24: Rain attenuation for Durban in November: Measurement and estimated models along the 6.73 km at 19.5 GHz

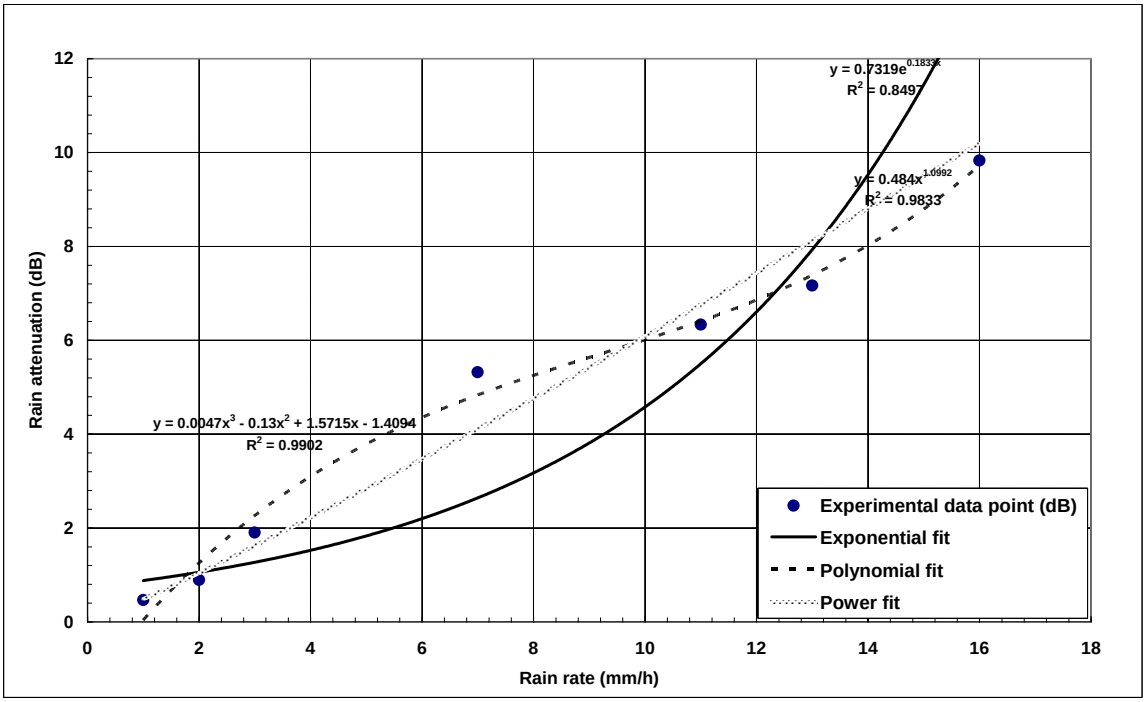

Fig. 4- 25: Rain attenuation for Durban in December: Measurement and estimated models along the 6.73 km at 19.5 GHz

Fig. 4-22 above shows the attenuation plots for the month of April. The experimental rain attenuation ranges from 0.75 dB to 6.10 dB for rain rate values that ranges from 1 mm/h to 20 mm/h along the terrestrial path for the month. The exponential, polynomial, and power fit has a regression coefficient of 0.87, 0.97, and 0.95 respectively. This also implies that the polynomial and the power fit can be used to model the experimental rain attenuation data points in the month of April. No rains were recorded in the month of May, June, July, and August; hence there is no rain attenuation for these months. For the month of September, there is only one rainy day (as seen in Table 4-3). Therefore, rain attenuation data points are too few to develop a model for the month of September.

Fig. 4-23 shows the rain attenuation plot for the month of October. The rain rate for this month ranges from 1mm/h to 79 mm/h with a maximum rain attenuation of 21.57 dB. The polynomial and the power models are used to define the experimental rain attenuation data points for this month. The exponential fit or the logarithmic fit predicts a far too high attenuation values. The regression coefficients for the polynomial and the power fit are 0.97 and 0.94 respectively for the month of October. In November (Fig. 4-24), the rain rate values range from 1 mm/h to 19 mm/h. The exponential, polynomial, and power analytical fit gave a regression coefficient of 0.98, 0.96, and 0.91 respectively. Thus, the exponential and the polynomial fit can be used to define the attenuation data points for this month.

Fig. 4-25 shows the experimental rain attenuation and the analytical fits for the month of December. The exponential, polynomial, and the power fit gave a regression coefficient of 0.85, 0.99 and 0.98 respectively. The rain rate in this month ranging from 1 mm/h to 16 mm/h resulted in a rain attenuation range of 0.46 dB and 9.83 dB along the path. It is observed from these figures (Fig. 4-20-4.25) that each month predicts its own attenuation values despite the fact that it may be of the same rain rate values. These effects can be as a result of the clear air effects in the month (which can be high or low). A high clear air effect can reduce the rain attenuation, and vice versa. The nature of the rain, in the sense that, at a given rain rate (e.g. 10 mm/h), the raindrop size distribution is bimodal (has two distinct peaks). This implies that there are two different rain types that give this rain rate (widespread and shower), in which case, they give different values of attenuation. The climatic effect on the rain rate data can also influence the rain attenuation values.

For example, the month of November gave a rain attenuation of 24.18 dB for a rain rate of 19 mm/h and October gave a 21.57 dB rain attenuation value for a79 mm/h rain rate. On seasonal

basis, October usually marks the beginning of the rainy season in Durban which is always very windy. Therefore, rains in this month normally comes with a lot of wind and thunder lightning. This wind blows the rains from having direct contact with the receiver, therefore altering the signal reception that might have resulted from the rain rate. Also, since the receiver is not well shielded against lightning effects, then the electromagnetic interferences generated by the thunder lightning degrades the signal at the reception.

With all these effects, a lower received signal may be received even at high rain rates. For November, the wind and the lightning effects on the rains and the received signals would have reduced. Since heavy rains are expected in the month November, being a summer month, a 19 mm/h (which can have two different rain types) downpour during a rain event can generate a high signal level which consequently will affect the rain attenuation.

4.6.1 Statistical Analysis of the Monthly Attenuation Models

Having defined the monthly rain attenuation with different fits, and the regression coefficients determined for each of the curve in the month, these curves are further analysed and tested to determine a suitable empirical model to define the data points. This is achieved by using chi-square, χ^2 statistic and the root mean square (rms) percentage error. The χ^2 statistic is used to determine the error bounds between models and measurements and the rms percentage error to determine the measure of the error (in percentage) between the model and the measurement [*Downie and Heath*, 1965].

These two statistical tools are employed with two curves that gave the best description of the experimental rain attenuation data points in Fig 4-20 - 4-25 above to determine the best-fit model that describe the measured rain attenuation for each month . The chi- square statistic is used to validate the acceptance or rejection of the null hypothesis of a model or relation [*Downie and Heath*, 1965]. According to *Freedman et al.* [1978], the χ^2 statistic is given as:

$$\chi^2 = \sum_{i=1}^{N} \frac{\left(X_{mea,i} - X_{pre,i} \right)^2}{X_{pre,i}} \tag{4.3}$$

where X_{mea} is the rain attenuation values from the 6.73 km line-of-sight link at 19.5 GHz , X_{pre} is the predicted values from the analytical curves, N is the number of measured or predicted points ranging from $i = 1, 2...N$ in this context. The rms percentage error is given as:

$$\Delta_{rms} = \sqrt{\frac{1}{N}\sum_{i=1}^{N}\left[\frac{100\left(A_{m,i} - A_{p,i}\right)}{A_{m,i}}\right]^2} \quad (\%) \qquad (4.4)$$

where there are N data points, and $A_{m,i}$ and $A_{p,i}$, are the i^{th} pair of measured and predicted values.

In a chi-square statistic problem, the degrees of freedom $(N-1)$ for the number of measurements recorded in each month must be determined so that the threshold values for the chi-square test at each level of confidence or significance level can be analysed. For this work, the chi-square test will be determined at a threshold value of 1% level of confidence for the months observed. Table 4-5 below shows the two analytical curve that may be adequate to predict the experimental rain attenuation data points (based on the values of their regression coefficients) for each month, the chi-square statistic results, and the degrees of freedom for each month.

Table 4- 5: The χ^2 statistic of the monthly rain attenuation predicted curves

Calendar months	Degrees of freedom (n-1)	Analytical curves	Calculated χ^2 statistic	Hypothesis at 1% significance level
February	13	Exponential	3.49	Accepted
		Polynomial	0.82	Accepted
March	8	Polynomial	0.32	Accepted
		Power	0.37	Accepted
April	8	Polynomial	0.34	Accepted
		Power	0.55	Accepted
October	14	Polynomial	21	Accepted
		Power	42	Rejected
November	7	Exponential	6.39	Accepted
		Polynomial	2.34	Accepted
December	6	Polynomial	1.54	Accepted
		Power	0.67	Accepted

From the table (Table 4-5), it is seen that with the exception of the month of October, all the hypothesis of the curves are accepted at 1% significance or confidence level for each of the degrees of freedom in each month. The month of October has a calculated χ^2 statistic value of

21 for the polynomial fit and 42 for the power fit at 14 degree of freedom. From the threshold values of the chi-square test in Appendix C (see Appendix C-1), at this degree freedom, the chi-square value should not be more than 29.14 at 1% significance level. Therefore with the power fit given a 42 chi-square statistic value, the hypothesis is rejected and that of the polynomial accepted because of its chi-square statistical value of 21. This implies that the power fit cannot be used to predict the attenuation values for the month of October. Hence the power model is rejected. Other accepted hypothesis in each of the month can be reasonably used to predict the attenuation values for each month and can be accepted as the analytical models for each of the month.

To further justify and validate the model that will predict the experimental rain attenuation data points for each of the month under observation; the root mean square (rms) percentage error is used. Table 4-6 shows the rms percentage error for each of the monthly empirical model. Since the polynomial curve for the month of October is rejected, the rms percentage error is not calculated. Based on the rms percentage error for the curves, curve with the lower percentage error is adopted as the model to predict the rain attenuation for each of the month. For the month of February, March, April, October and November, the polynomial fit is adopted, and for December the power fit is adopted as the model. Table 4-7 shows the rain attenuation models for the rainy months in the year 2004 in Durban for a 6.73 km path at 19.5 GHz.

Table 4- 6: The root mean square percentage error between the measured rain attenuation and predicted curves

Calendar months	Analytical curves	Δ_{rms} (%)
February	Exponential	1.67
	Polynomial	0.79
March	Polynomial	1.37
	Power	1.52
April	Polynomial	1.36
	Power	1.54
October	polynomial	4.06
November	Exponential	3.40
	Polynomial	1.45
December	Polynomial	1.79
	Power	1.55

Table 4- 7: Rain attenuation models for the rainy months in the year 2004 in Durban, for a 6.73 km path

Calendar months	Empirical models
February	$A=0.0004R^3-0.012R^2+0.1642R+2.6184$
March	$A=0.0027R^3-0.0661R^2+0.8102R+0.1009$
April	$A=-0.0019R^3+0.0536R^2-0.0704R+0.9264$
October	$A=0.0002R^3-0.0149R^2+0.6024R-0.9477$
November	$A=0.1201R^2-0.1764R+1.3416$
December	$A=0.484R^{1.0992}$

These monthly empirical models have shown the monthly variability and the statistical behaviour associated with rain attenuation in Durban. This model can be used to give an initial working estimate for a short propagation path length. However, as the path length increases, the effective length become more pronounced, hence the accuracy reduces. At this point, it is important to state that longer measurement period with different path length links would have given a more robust model for each month. This can be extended to other geographical locations that have similar rain climatic nature as Durban to estimate the rain attenuation along terrestrial path lengths.

4.7 Behaviour of Point Rainfall along Propagation Path

The behaviour of point rainfall along radio propagation paths may not be the focus of this research, but in a situation where this behaviour seems to affect the efficient prediction of rain attenuation models, especially for path attenuation estimates; there is a need to be familiar with this concept because of the nature of rain. Rain is simply a natural phenomenon that displays significant variability in both time and space. This leads to its non-uniformity along radio propagation paths. Many researchers have developed various concepts to incorporate this effect in their rain attenuation models.

Many researchers have used the concept of equivalent rain cell [*da Silva Mello,* 2007] with uniform rain that is assumed to give the same path attenuation as the random clusters [*Pawlina-Bonati,* 1999]; Some have used the concept of equivalent path averaged or integrated rain rate [Lin, 1975; *Crane,* 1980; 1996], which is determined by multiplying the point rain rate by a

reduction factor [*Moupfouma*, 1984]; And others have used the concept of an effective path length d_{eff} which is determined by multiplying the actual path length d of the link by a reduction factor r. (Most of the rain attenuation models that employed some of these concepts have been discussed in the third chapter of this thesis).

The effective path length is a hypothetical length of which rain intensity over this path length is assumed to be constant [*Moupfouma*, 1984]. This effective path length reflects the spatial inhomogeneity present in a rain cell, because it is unlikely that reference rain rate will extend uniformly over the length of transmission path unless this propagation path length is very short [*Hall et al.*, 1996]. The longer the path, the less likely it is that rain will extend the full length of the propagation path. The spatial distribution of rain along propagation path lengths has been verified in the work of *Rogers* [1976], and experimentally determined by Bonati [*Pawlina and Binaghi*, 1998; *Pawlina-Bonati*, 1999].

From the experimental measurements analyzed for each month in Fig. 4-20 to 4-25, it is observed that the rain rates for each month resulted into rain attenuation that may be different from the rain attenuation in other months, though the rain rates are of the same values. At this point, it is important to mention that the propagation path length of 6.73 km employed in this experimental analysis might not have caused this anomalous behaviour, because the link path is relatively short. With this, most of the path length might have been covered by the same rain cell during a rain event for a particular month. Also, the experiment is at a fixed path length of 6.73 km. An increasing or longer propagation path length might have reflects this anomalous behaviour, but during the time this experimental work was observed, and up till now, no such link is available for this research.

Therefore, this monthly variation in rain rates and rain attenuation displayed in Fig. 4-20-4-25 might have resulted from different factors such as; the nature of rain in which the raindrop size distribution that constitutes the rain rate is bimodal, which results in different values of rain attenuation. The climatic season in which the rain occurs is another factor. In the summer months, convective rains are expected and these rains are usually associated with wind and thunder lightning with early rains and stratiform rains are common during the winter. In the summer during the lightning and thundering process, the transmitter and the receiver antenna will not aim at each other at this point; therefore, the receiver antenna will not be in direct sight with the transmitter for few minutes. With this, the signal at the reception may be altered. Another factor

is the clear-air effects which may either be pronounced in one month than the other (see section 4.6).

4.8 Rain Attenuation Modeling Per Rain Rate

From the analysis of the signal level measurements recorded for each rainy month in Durban along the 6.73 km link at 19.5 GHz for the year 2004, it was observed that these measurements varied with the same rain-rate intensity along the propagation path. For this reason, the measured maximum, average, and minimum rain attenuation values per rain rate for the entire year along the link is determined. This is shown in Fig. 4-26 below. The maximum and minimum curves in Fig. 4-26 define an attenuation bound for the given rain rates [see *Fashuyi and Afullo*, 2007]. These attenuation bounds were further analysed by employing a logarithmic and power fit on the maximum, average, and the minimum attenuation curves to estimate a suitable fit for these bounds. Fig 4-27 and Fig 4-28 shows the logarithmic and power regression curves on the measured attenuation bounds respectively.

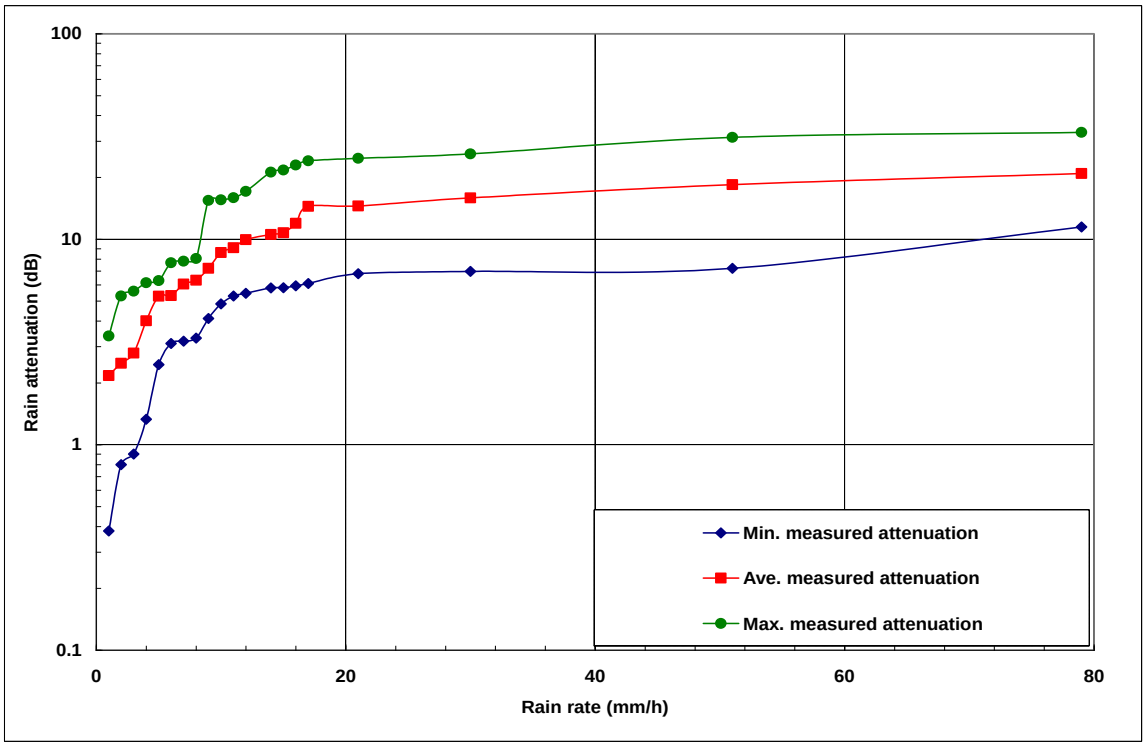

Fig. 4- 26: Rain attenuation for Durban along the 6.73 km link at 19.5 GHz for the year 2004: Maximum, minimum and average measured values

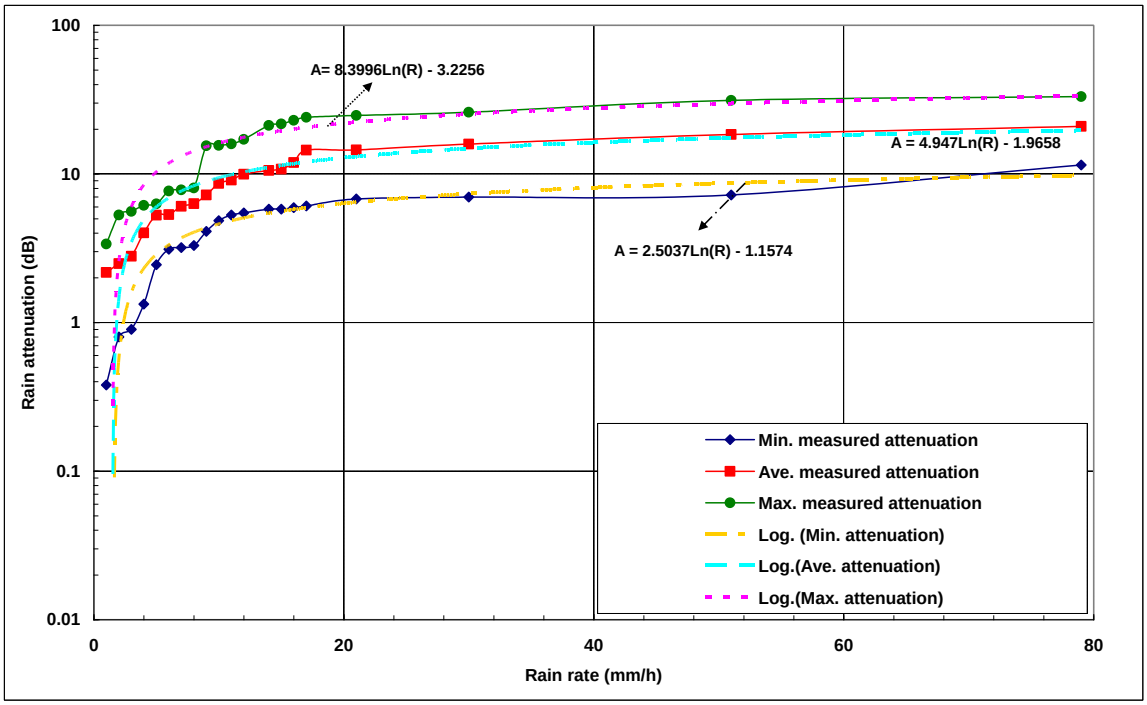

Fig. 4- 27: Measured minimum, average and maximum rain attenuation values and logarithmic regression estimates

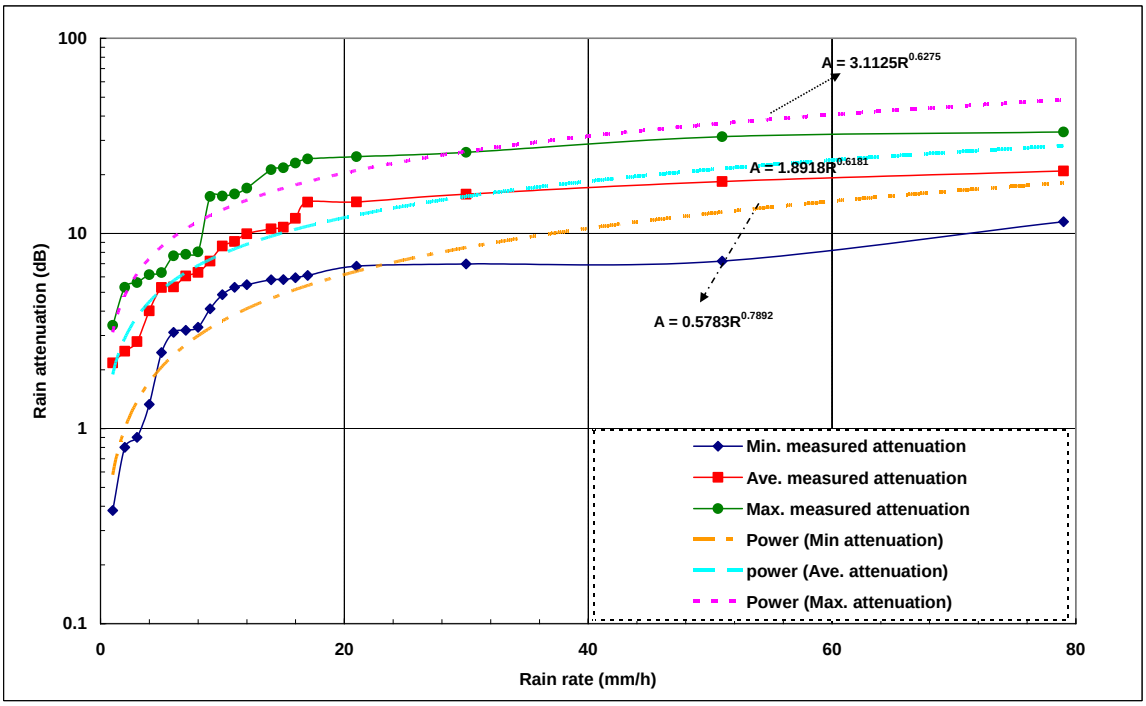

Fig. 4- 28: Measured minimum, average and maximum rain attenuation values and power regression estimates

Table 4-8 gives the equations and the regression coefficients of the curves for the measured minimum, average and maximum rain attenuation. The regression coefficients describe the extent at which the power or the logarithmic curves define the minimum, average and the maximum attenuation bound. From this table it can be seen that both the logarithmic and power regression coefficients are approximately 0.9 for all the rain attenuation bounds (though there limited data points). This implies that both of the logarithmic and the power estimates can be adopted to model the rain attenuation for the 6.73 km link at 19.5 GHz in Durban.

To validate the above sentence, the root mean square (rms) percentage error for both the logarithmic and the power regression estimates are calculated (using equation 4.4) so as to define the best empirical model that describe the each rain attenuation bound. Table 4-9 shows the rms percentage error for the logarithmic and power estimates. The values of the percentage root means square error shows that the power regression estimate gives the lowest percentage root mean square error for the minimum, average and maximum attenuation bounds. With this observation, the power regression estimation curve can be adopted to model the rain attenuation for the 6.73 km terrestrial link at 19.5 GHz in Durban. A longer measurement period would have resulted into more attenuation data points and a more robust and well-defined empirical rain attenuation model. These models can be employed to estimate the rain attenuation for short propagation path length in Durban and in regions that have similar climatic rain characteristics.

Table 4- 8: Analysis of the logarithmic and power regression estimates for the measured minimum, average and maximum attenuation values

Measured attenuation bound	Logarithmic equation	Regression coefficient (Logarithmic)	Power equation	Regression coefficient (Power)
Minimum	A = 2.503Ln(R)-1.157	0.922	$A = 0.578R^{0.789}$	0.886
Average	A = 4.947Ln(R)-1.966	0.917	$A = 1.892R^{0.618}$	0.948
Maximum	A = 8.399Ln(R)-3.226	0.887	$A = 3.112R^{0.6275}$	0.891

Table 4- 9: The root mean square percentage error for the logarithmic and power regression estimates

Measured attenuation bound	Δ_{rms} (%) for logarithmic estimate	Δ_{rms} (%) for power estimate
Minimum	8.43	3.25
Average	4.64	1.52
Maximum	5.49	2.32

4.9 Comparison of the Rain Attenuation Results with Existing Models

The measured maximum, average, and minimum rain attenuation values per rain rate along the 6.73 km at 19.5 GHz which defined the attenuation bounds for the given rain rates as shown in Fig. 4-26 is adopted as the empirical rain attenuation model for the terrestrial link in Durban. In this section, this model is compared with other established rain attenuation models developed for terrestrial line-of-sight links in other regions across the globe for the purpose of validating the empirical rain attenuation model predicted for this region. These established terrestrial rain attenuation models include:

i. ITU-R long term statistics of rain attenuation, [*ITU-R 530*, 2007]
ii. Global Crane attenuation model, [*Crane*, 1980; 1996]
iii. Lin attenuation model, [*Lin*, 1977]
iv. Moupfouma attenuation model, [*Moupfouma*, 1984]
v. New Moupfouma attenuation model, [*Moupfouma*, 2009]
vi. Garcia and Peiro attenuation model, [*Garcia-Lopez and Peiro*, 1983]
vii. CETUC rain attenuation model, [*Perez Garcia and da Silva Mello*, 2004]
viii. New CETUC rain attenuation model, [*da Silva Mello et al.*, 2007]

All these attenuation models have been formulated based on the available local propagation data and have been extended to other parts of the world. The theories and the guiding equations for all these models have been clearly stated and shown in third chapter of this report.

The measured 1-minute rain rates recorded along the 6.73 km link are used with the established terrestrial rain attenuation models to calculate the rain attenuation along the 6.73 km link. The attenuation results of each model are then compared with the maximum, average, and minimum attenuation bounds developed from the signal level measurements recorded on the terrestrial line-of-sight set up in Durban. Fig. 4-29 shows the attenuation results from the established rain attenuation models with the minimum, average, and maximum measured attenuation values in Durban.

It should be noted that the results from the new Moupfouma rain attenuation prediction model for terrestrial line-of-sight links [*Moupfouma*, 2009] are not shown on Fig. 4-29. This is because the

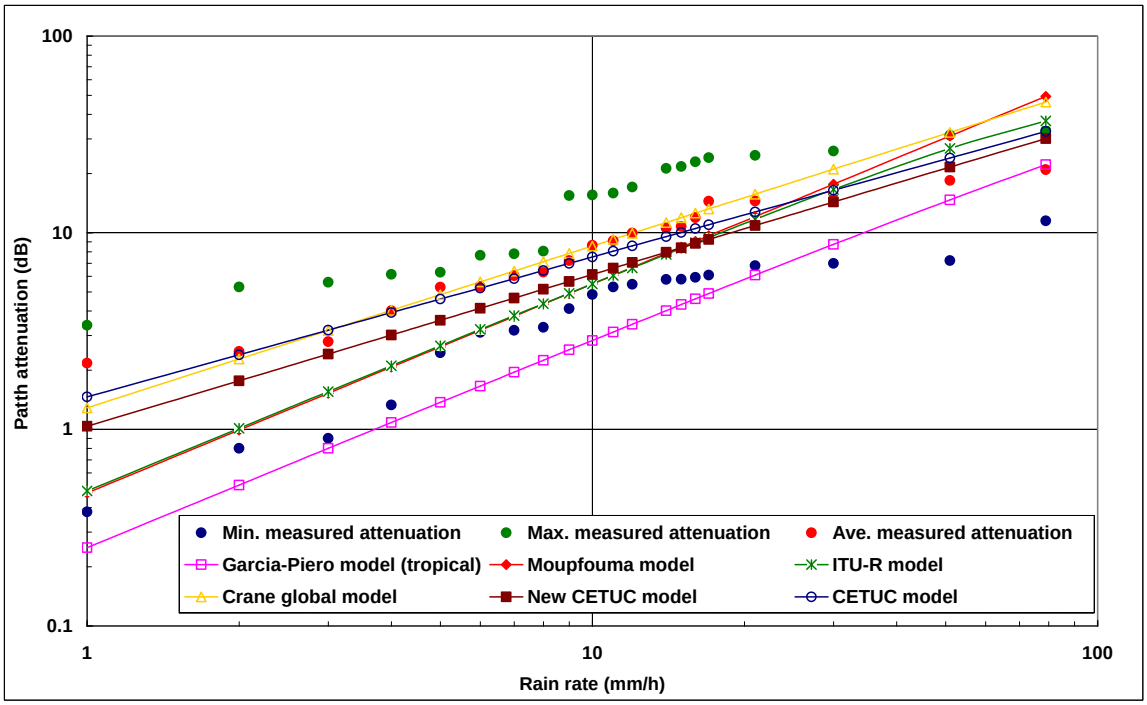

Fig. 4- 29: Rain attenuation for Durban along 6.73 km link at 19.5 GHz: Maximum, minimum, and average measured values with other rain attenuation models

rain attenuation results from this model tend to increase exponentially due to the exponential function and the estimated value for the parameter ξ in the model equivalent path length, L_{eq} (see equations 3.50 and 3.53a). And this resulted in a very large attenuation values that cannot be compared with the measured attenuation values along the link at any bounds. The Lin attenuation results [*Lin*, 1977] are also neglected in the plot, because the proposed reduction factor for the calculation of the rain attenuation in the Lin attenuation model is given for rain rate $R > 10$ mm/h [*Lin*, 1977] . Since the 1-minute rain rate recorded along the 6.73 km link in Durban that gave significant attenuation values along the path spanned between 1–79 mm/h, then the Lin attenuation results are not shown on the figure for comparative purposes.

Fashuyi and Afullo [2007] presented the measured attenuation bounds of this terrestrial link with the Crane global [*Crane*, 1980; 1996], Moupfouma [*Moupfouma*, 1984], and ITU-R rain attenuation model [ITU-R 530-10, 2001]. In the work, the power law coefficients given in *ITU-R 838-2* [2003] was utilized for the calculation of the specific attenuation. The rain attenuation result shows that, the Crane global, Moupfouma, and the ITU-R attenuation curves fall within the maximum and minimum bounds up to a rain rate of 50 mm/h [see *Fashuyi and Afullo*, 2007]. Beyond this rain rate, only the ITU-R prediction stays within the bound up to 65 mm/h, while the

Crane global Moupfouma plots exit and over-predict the expected attenuation along the paths [*Fashuyi and Afullo*, 200].

The rain attenuation results presented in Fig 4-29 from the established rain attenuation models are calculated from the new power law coefficients given in *ITU-R 838-3* [2005] which is shown in Appendix A-2. The k and α power-law coefficients at 19.5 GHz is calculated from the interpolation technique stated in equation (2.14) for the calculation of the specific attenuation. From Fig 4-29 above, the attenuation curve from Garcia-Peiro model [*Garcia-Lopez and Peiro*, 1983] gave the lowest attenuation values for the rain rate recorded along the 6.73 km path. The *Moupfouma* [1984] and the ITU-R [*ITU-R 530-12*, 2007] attenuation curves overlap up to a rain rate of about 30 mm/h. The Crane global [*Crane*, 1980; 1996], *Moupfouma* [1984] and the ITU-R attenuation curves stay within the maximum and minimum attenuation bounds up to a rain rate of 55 mm/h, beyond this, only the ITU-R prediction stays within the bound up to 70 mm/h. That is, the Crane global [*Crane*, 1980; 1996], and the *Moupfouma* [1984] curves exit and over-predict the expected attenuation along the 6.73 km path for rain rate above 55 mm/h.

It can also be observed from Fig. 4-29 that the Garcia and Peiro model [*Garcia-Lopez and Peiro*, 1983] which give the lowest attenuation values, only cut across the minimum attenuation bound. That is, the model may not be suitable for higher attenuation values recorded along the path. The CETUC model of 2004 and the new CETUC model of 2007 crosses mainly on the average and the maximum attenuation bounds, which may not be well suited for lower attenuation values recorded along the path. But it should be noted that the Garcia and Peiro [*Garcia-Lopez and Peiro*, 1983], CETUC [*Perez Garcia and da Silva Mello*, 2004] and new CETUC [*da Silva Mello et al.*, 2007] attenuation curves fall within the attenuation bound. The ITU-R [*ITU-R 530*, 2007] and the *Moupfouma* [1984] attenuation curves seem to be the two models that cut across the minimum, average, and the maximum bounds.

The root mean square percentage error is calculated between the measured attenuation bounds and the established empirical rain attenuation models to give a more detailed and quantitative comparison of the models. Table 4-10 below shows the root mean square percentage errors between the measurements and the models. From the table, the Garcia and Peiro [*Garcia-Lopez and Peiro*, 1983] has the lowest rms percentage error for the minimum measured attenuation bound then followed by the ITU-R model. For the average measured attenuation bound, the CETUC models give the lowest rms percentage error, and then followed by the ITU-R model. For

the maximum measured attenuation bound, the global Crane model [*Crane*, 1980; 1996] gives the lowest rms percentage error, and then followed by the ITU-R model.

Table 4- 10: The root mean square percentage error between the measured attenuation bounds and the established empirical models

Empirical attenuation models	Root mean square percentage error, Δ_{rms} (%)		
	Minimum measured attenuation	Average measured attenuation	Maximum measured attenuation
Garcia and Peiro (tropical) model	4.38	6.41	7.75
Moupfouma model	11.58	5.08	6.03
Global Crane model	17.02	3.46	3.96
New CETUC model	9.73	2.81	5.38
CETUC model	14.17	1.88	4.98
ITU-R model	8.19	3.25	4.85

All in all, none of the models have completely predicted the measured rain attenuation or the rain attenuation bound values along the 6.73 km terrestrial link. But it is observe that the ITU-R model has averagely estimates the attenuation values based on the calculated rms percentage error values across the three bounds. The ITU-R model has given the lowest rms percentage error when calculated for all the measured rain attenuation bounds. With these observations, the ITU-R model [*ITU-R 530*, 2007] can reasonably be adopted to predict the rain attenuation in Durban. More measurements campaigns in Durban and its environs with different propagation path lengths and longer measurement period are needed to further buttress and justify this conclusion

4.10 Chapter Summary

This chapter has utilized the signal level measurements from the 19.5 GHz, 6.73 km terrestrial radio link set up for a period of one year, and a 1-minute rain rate recorded alongside with the signal level for the same period in Durban. These measurements have been used to develop empirical monthly rain attenuation and rain attenuation model for the year 2004 along the terrestrial link. This chapter looked into the experimental set-up of the link and determined the average non-rain faded signal level for each month. The contributing factors to the non-rain faded signal level were also explained. The time series for different features of rain rates (light, moderate, and heavy rains) and their received signal levels are also analysed in this chapter. With

the average non-rain faded signal level, the rain attenuation of the different features of rains are estimated.

The rain attenuation models developed from the signal level measurements in Durban over the entire year were compared with other established rain attenuation models. The results indicate that all the six attenuation models stay within the measured attenuation bounds, except for the Crane global, Moupfouma and ITU-R model which exit the attenuation bound at some certain rain rates.. Other models which fall within the bounds without exiting them either reflect the minimum attenuation values and not the maximum or average values, and some may reflect the average and maximum but not the minimum attenuation values. From the error analysis, the ITU-R model tends to give a better prediction of the rain attenuation values along the 6.73 km in Durban.

With longer propagation measurements, these observations and conclusions can further be buttressed, and an improved empirical rain attenuation model can be predicted. The next chapter deals with the theoretical formulations of rain attenuation models. These involve the scattering effects of electromagnetic waves on raindrops and the raindrop size distributions.

Chapter Five

Theoretical Formulations of Rain Attenuation Models

5.1 Introduction

In Chapter four empirical rain attenuation models were developed from the signal level measurements recorded along a horizontally polarized 6.73 km terrestrial radio link. This is a direct method of estimating the behaviour of rain and rain attenuation along a terrestrial radio link [*Ajayi et al*., 1996; *Myers*, 1999]. The indirect method involves the knowledge of the microphysical structure of the raindrop, the interaction between an individual raindrop particle and the propagating electromagnetic wave, and the drop size distribution describing the raindrop spectra [*Green*, 2004].

In this chapter, theoretical rain attenuation models are developed based on the interaction between a raindrop particle, which is assumed to be of a spherical shape, and the propagating incident electromagnetic wave. The interaction between this raindrop and the incident electromagnetic wave results in a scattering problem [*Medeiros Filho et al.,* 1986]. Therefore, the scattering properties of the spherical raindrop are calculated for a wide range of frequencies for 14 different sizes of raindrops. From the scattering properties, the extinction cross-sections for the spherical raindrops are determined and the real parts of the extinction cross-sections for the raindrop sizes

are fitted to generate power-law models for different frequencies. These are integrated over different established raindrop-size distribution models to formulate rain attenuation models.

5.2 Fundamentals and Theoretical Considerations

Raindrops are formed by materials considered to be homogeneous but lossy dielectric [*Medeiros Filho et al.,* 1986; *Cermak et al.,* 2005] as shown in Section 2.9.1 of this work. The dielectric properties of the rain (water) drop, which is one of the key factors needed to calculate the electromagnetic scattering of the raindrop, can be described by a complex refractive index m and it is given as a function of frequency f, and temperature T, as shown in equation (3.54). The complex refractive index m initially developed by *Ray* [1972] has been utilized by many researchers to determine the scattering properties of the raindrop needed to calculate the propagation characteristics along radio paths [*Morrison and Cross* 1974; *Uzunoglu et al.,* 1977].

However, in this work the dielectric properties given by *Liebe et al.* [1991], which is a newer and more accurate model, are adopted to compute for the refractive index of rain drop. This model has also been employed by *Mätzler* [2002a] and more recently by *Mulangu and Afullo* [2009] to compute for the complex refractive indices of the rain drops. The Mie theory for electromagnetic scattering by dielectric spheres is used in this study under the assumption that each raindrop is of spherical shape and not oblate spheroids. The scattering approximations of oblate spheroids of raindrop shapes which have been subject of various investigators like *Oguchi* [1973], *Morrison and Cross* [1974], and *Uzunoglu et al.* [1977] and others were adopted because of the free-fall nature of rain that distorts the shape of the drop. This distortion effect of raindrop becomes pronounced as the drop-size increases [*Pruppacher and Beard,* 1970; *Pruppacher and Pitter,* 1971].

Investigations have shown that the spherical approximations of raindrops improve with increasing microwave frequencies. This is because the smaller raindrops, which are more numerous than the larger ones, contribute most to rain attenuation in the higher frequency range [*Adimula and Ajayi,* 1996]. Also, the smaller raindrops deviate very little from the spherical shape [*Medeiros Filho et al.,* 1986]. This has been observed in the dual polarized radar measurements reported by *Hall* [1981] and more recently in the work of *Moupfouma et al*. [1990]. Typically, attenuation calculated for spherical raindrops represent approximate "average" value between attenuations for horizontally and vertically polarized waves scattered from distorted drops [*Rogers and Olsen,* 1976]. *Rogers and Olsen* [1976] also observed that at higher frequencies, the differential

attenuation for the two polarizations decreased with increasing frequency – this was also noted by *Oguchi* [1964]. Therefore in their work, the specific attenuation curves from spherical raindrops are assumed to be the approximate values of the specific attenuation for waves of any polarization at all frequencies.

For the scattering approximations needed for calculation of the specific attenuation in this work, the Mie theory for electromagnetic scattering for a dielectric sphere is applied to the spherical raindrop under the assumption that each raindrop illuminated by a plane wave in a rain-filled medium, and the distance between drops sufficiently large to avoid any interaction between them that might result in multiple scattering. The effect of multiple scattering for propagation through a rain-filled medium has been investigated by [*Van de Hulst,* 1957; *Uzunoglu and Evans,* 1978]. It has been shown that, provided the density of the scatterers (rain drops) per unit volume is small, the multiple scattering effects are negligible for all likely rain rates and for frequencies up to 30 GHz (see Section 3.9.3) [*Van de Hulst,* 1957; *Uzunoglu et al.*, 1977; *Uzunoglu and Evans,* 1978].

5.2.1 Scattering by Dielectric Sphere (Spherical Raindrop)

Consider a dielectric sphere illuminated by an incident plane electromagnetic wave propagating in the positive z direction, with k_0 as the free space propagation constant and E_0 and H_0 as the wave amplitudes is described by [*Moupfouma,* 1997; *Sadiku,* 2000]:

$$E_{inc} = E_0 \exp\, j(\omega t - k_0 z)\hat{a}_x \tag{5.1a}$$

$$H_{inc} = H_0 \exp\, j(\omega t - k_0 z)\hat{a}_y \tag{5.1b}$$

where $\hat{a}_x$ and $\hat{a}_y$ are the unit vector specifying the polarization state of the incident wave.

When the incident electromagnetic plane wave hits the spherical raindrop (or a dielectric sphere), a scattered wave is generated and the corresponding scattered electric field in the far-field region for the spherical raindrop is given as [*Oguchi,* 1973]:

$$E_{sca}(r,\phi,\theta) = \frac{f(\hat{K}_i, \hat{K}_s)}{r}\exp(-jk_0 r) \tag{5.2}$$

(the $\exp(+j\omega t)$ time convention is assumed and suppressed), where (r,ϕ,θ) are the spherical coordinates of the observer, $\hat{K}_i$ is the unit vector directed toward the propagation direction of the incident wave, $\hat{K}_s$ is a unit vector directed from the origin to the observation point, r is the distance from the origin to the observation point, and $f(\hat{K}_i,\hat{K}_s)$ is a function denoting vector scattering amplitude [*Oguchi,* 1973]. The symbol θ is the field incidence angle and ϕ is the angle between the direction of the wave propagation and the drop axis, which is the observation angle. The scattering amplitude polarized in the same direction as the incident wave at observation angle $\phi = 0$ corresponds to the forward scattering and $\phi = \pi$ corresponds to the backward scattering [*Van de Hulst,* 1957; *Uzunoglu et al.,* 1977; *Moupfouma,* 1997; *Sadiku,* 2000]. The geometry for the incident electromagnetic plane wave on dielectric sphere is shown in Fig. 5-1 below.

5.3 Scattering Amplitudes of Spherical Raindrops

As mentioned above, the Mie scattering theory will be applied to the raindrops, under the assumption that the raindrop is of a spherical shape. With this, computations are made for the scattering functions in the incident wave propagation direction. Thus, the complex forward scattering amplitudes of the spherical raindrops for a wide range of frequencies are determined.

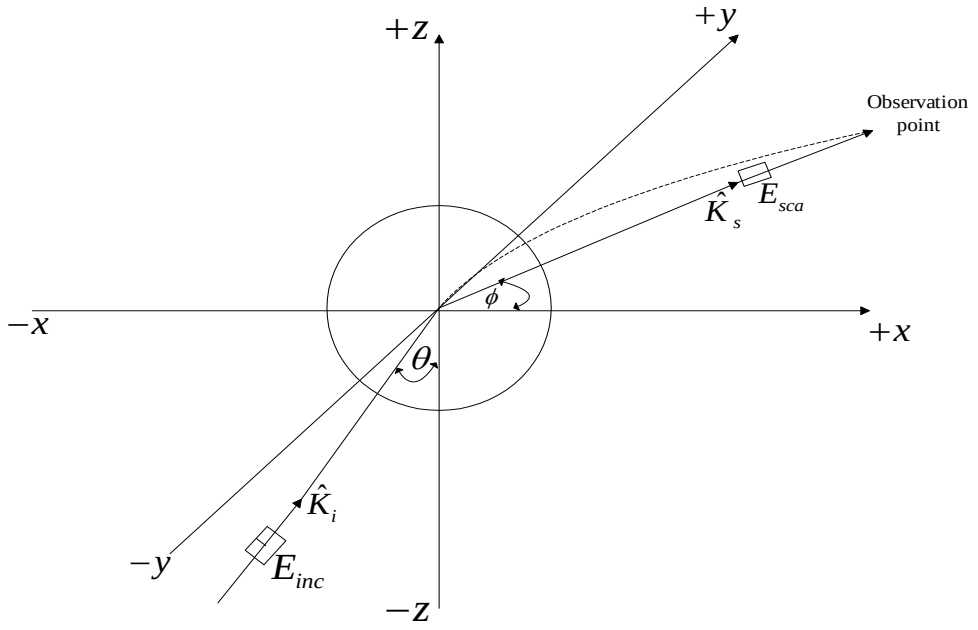

Fig. 5- 1: Incident electromagnetic plane wave on a dielectric sphere (spherical raindrop)

The complex forward scattering amplitude for spherical rain drop function can be written as [*Van de Hulst*, 1957; *Sadiku*, 2000]:

$$S(0)=\frac{1}{2}\sum_{n=1}^{\infty}(2n+1)(a_n+b_n) \tag{5.3}$$

for $\phi=0$, where a_n and b_n are the Mie coefficients which are depend on frequency (operating frequency of the microwave link), radius of raindrop, and the complex refractive index of water. The Mie coefficients can be given as [*Sadiku*, 2000; *Bohren and Huffman*, 2004]:

$$a_n(m,\alpha)=\frac{m^2 j_n(m\alpha)[\alpha j_n(\alpha)]' - j_n(\alpha)[m\alpha j_n(m\alpha)]'}{m^2 j_n(m\alpha)[\alpha h_n^{(1)}(\alpha)]' - h_n^{(1)}(\alpha)[m\alpha j_n(m\alpha)]'} \tag{5.4a}$$

$$b_n(m,\alpha)=\frac{j_n(\alpha)[m\alpha j_n(m\alpha)]' - j_n(m\alpha)[\alpha j_n(\alpha)]'}{h_n^{(1)}(\alpha)[m\alpha j_n(m\alpha)]' - j_n(m\alpha)[\alpha h_n^{(1)}(\alpha)]'} \tag{5.4b}$$

where m is the complex refractive index of the spherical raindrop (water drop) which is given by *Liebe et al.* [1991], $\alpha=k\bar{a}$ is the particle size (raindrop), $\bar{a}$ the radius of the spherical particle (raindrop) and $k=2\pi/\lambda$ is the wave number and λ the wavelength. The function $j_n(x)$ is the spherical Bessel function of the first kind and $h_n^{(1)}(x)$ is the spherical Bessel function of the third kind (or Hankel function of the first kind) which are of order n $(n=1,2,\ldots)$. The primes at the square brackets indicate differentiation with respect to the argument of the spherical Bessel function inside the brackets.

The first kind of the spherical Hankel function, $h_n^{(1)}(x)$ are represented by the linear combinations of j_n and n_n. This is given by [*Arfken and Weber*, 2005]:

$$h_n^{(1)}(x) = j_n(x) + in_n(x) \tag{5.5}$$

where

$$j_n(x) = \sqrt{\frac{\pi}{2x}}J_{n+1/2}(x) \tag{5.6}$$

and

$$n_n(x) = \sqrt{\frac{\pi}{2x}} N_{n+1/2}(x) \tag{5.7}$$

Here, $J_n(x)$ and $N_n(x)$ are Bessel functions of the first and second kind. Equations (5.6) and (5.7) give the relationships between Bessel and spherical Bessel functions [Mätzler, 2002a; *Arfken and Weber*, 2005].

For $n = 0$ and 1, the spherical Bessel functions are given by [*Bohren and Huffman*, 2004]:

$$j_0(x) = \frac{\sin x}{x}; \qquad j_1(x) = \frac{\sin x}{x^2} - \frac{\cos x}{x} \tag{5.8a}$$

$$n_0(x) = -\frac{\cos x}{x}; \qquad n_1(x) = -\frac{\cos x}{x^2} - \frac{\sin x}{x} \tag{5.8b}$$

In this calculation, the limit of the infinite series of the summation in equation (5.3) was limited to the $n_{\max}$ term given by [*Mätzler*, 2002a; *Bohren and Huffman*, 2004; *Mulangu et al.*, 2009] as:

$$n_{\max} = \alpha + 4\alpha^{1/3} + 2 \tag{5.9}$$

where; $\alpha = 2\pi a/\lambda$

The complex refractive index of the spherical water drops which is a function of temperature and frequency $m(f,T)$ is estimated by the dielectric function of *Liebe et al.*, [1993] at a temperature of 20°C (293K) for all frequencies used in this work. The 20°C (293K) is adopted in this work because most of the researchers that have calculated the scattering amplitudes needed for the estimation of the specific rain attenuation have used refractive indices of water at 20°C [*Oguchi*, 1973; *Uzunoglu et al.*, 1977]. Also, from the propagation measurements recorded in Durban along the 6.73 km terrestrial links at an operating frequency of 19.5 GHz in 2004, the average temperature recorded over link for the entire year was 20.18°C (which almost close to 20°C see Table 5-1 below).

Table 5- 1: Average temperature recorded for Durban in 2004 at 19.5 GHz along the 6.73 km terrestrial path

Months	Temperature (^{o}C)
February	21.78
March	22.48
April	23.12
May	19.03
June	18.79
July	17.07
August	18.10
September	19.13
October	17.82
November	18.79
December	25.84
Average	**20.18**

With the help of the MATLAB's built-in double precision Bessel functions, the Mie coefficients a_n and b_n are computed. This is then used to calculate the forward scattering amplitudes for 14 different spherical drop radii at different frequencies. The results of the scattering amplitudes are of real and imaginary parts. Tables 5-2 and 5-3 below give typical examples of the scattering amplitude results computed for frequencies 2 GHz and 15 GHz for the spherical raindrop radii. The Tables (5-2 and 5-3) show the radius of each raindrop, $\overline{a}$, the size of the spherical drop, $\alpha = k\overline{a},$ and the real and the imaginary part of the scattering amplitude of each drop radius. More results on the forward scattering amplitudes for frequencies ranging from 1-40 GHz are shown in Appendix D.

5.4 Calculation and Modeling of the Extinction Cross-section of Spherical Raindrops

Most particles have a geometrical cross-section G. For example a sphere of radius a has its geometrical cross section $G = \pi a^2$. According to *Van de Hulst* [1957], the dimensionless constants,

$$Q_{ext} = C_{ext}/G, \tag{5.10a}$$

$$Q_{sca} = C_{sca}/G, \tag{5.10b}$$

$$Q_{abs} = C_{abs}/G \tag{5.10c}$$

are referred to as the efficiency factors for extinction, scattering, and absorption cross-sections of a sphere, respectively [*Van de Hulst,* 1957*; Bohren and Huffman,* 2004]. For energy conservation, it requires the extinction cross-section, $Q_{ext} = Q_{sca} + Q_{abs}$ [*Bohren and Huffman,* 2004].

Extinction cross-section which may be defined in terms of the total power removed from an incident wave [*Ajewole, et al.,* 1999a] is a major parameter required in the calculation of rain attenuation. From equation (5.10a), the value of the extinction cross-section Q_{ext} can then be written as [*Van de Hulst,* 1957; *Sadiku,* 2000]:

$$Q_{ext} = \frac{4\pi}{k^2}\mathrm{Re}\{S(0)\} \tag{5.11}$$

where $k = 2\pi/\lambda$ and $\mathrm{Re}\{S(0)\}$ is the real part of the forward scattering amplitude.

Table 5- 2: The forward scattering amplitudes at f=2 GHz , T=293 K , m=8.90697+0.490563i , λ=15cm

Radius of the sphere $\bar{a}$ (cm)	Size of the spherical drop $\alpha = k\bar{a}$	Scattering amplitude of the spherical raindrop	
		Real Part	Imaginary part
0.025	0.01047619	0.000000004532549860	- 0.000001107790596i
0.050	0.02095238	0.000000036322350760	- 0.000008863990705i
0.075	0.03142857	0.000000123099793443	- 0.000029925347712i
0.100	0.04190476	0.000000294043288329	- 0.000070965325443i
0.125	0.05238095	0.00000058136035129	-0.000138682568619i
0.150	0.06285714	0.00000102249260343	- 0.000239809501670i
0.175	0.07333333	0.00000166296621718	- 0.000381121114356i
0.200	0.08380952	0.00000255991551283	- 0.00069443992321i
0.225	0.09428571	0.00000378631450672	- 0.000811665658347i
0.250	0.10476190	0.00000543595952	-0.00111474429996i
0.275	0.11523809	0.00000762925583	- 0.00148571897238i
0.300	0.12571428	0.00001051987340	- 0.00193172038208i
0.325	0.13619047	0.00001430235132	- 0.00245998237825i
0.350	0.14666667	0.00001922074931	- 0.00307785430658i

Table 5- 3: The forward scattering amplitudes at f=15 GHz, T=293 K, m=7.3206+2.53811i, λ=2cm

Radius of the sphere $\bar{a}$ (cm)	Size of the spherical drop $\alpha = k\bar{a}$	Scattering amplitude of the spherical raindrop	
		Real part	Imaginary part
0.025	0.07855	0.00001449968990376	- 0.000467470828578i
0.050	0.1571	0.00012788531180	- 0.00377935214657i
0.075	0.23565	0.00054055953158	- 0.01298375335361i
0.100	0.3142	0.00184281897299	- 0.03155600636920i
0.125	0.39275	0.00579292599253	- 0.06352962235470i
0.150	0.4713	0.01695708952164	- 0.11249060327696i
0.175	0.54985	0.04217142374164	- 0.17726025132892i
0.200	0.6284	0.08332265470309	- 0.25319149268816i
0.225	0.7029	0.13949688583590	- 0.33476373084196i
0.250	0.7855	0.22846657921871	- 0.42721238613631i
0.275	0.86405	0.33558859928812	- 0.49955866967605i
0.300	0.9426	0.44642433617927	- 0.54614047836989i
0.325	1.02115	0.54286629419557	- 0.57285613774297i
0.350	1.0997	0.61864449645075	- 0.59101349607839i

Thus, the extinction cross-section can be written as [*Van de Hulst,* 1957; *Sekine et al.,* 1987; *Sadiku,* 2000]:

$$Q_{ext} = \frac{\lambda^2}{\pi} \mathrm{Re}\{S(0)\} \tag{5.12a}$$

or

$$Q_{ext} = \frac{\lambda^2}{2\pi} \mathrm{Re} \sum_{n=1}^{\infty} (2n+1)(a_n + b_n) \tag{5.12b}$$

where $S(0) = \frac{1}{2}\sum_{n=1}^{\infty}(2n+1)(a_n + b_n)$ is the forward scattering amplitude from equation (5.3)

Using equation (5.12) on the real part of the forward scattering amplitudes computed at different frequencies, the extinction cross-section is calculated for the entire drop radius. Fig. 5-2 – 5-4 below shows the calculated extinction cross-sections for 14 raindrop radii at different frequencies.

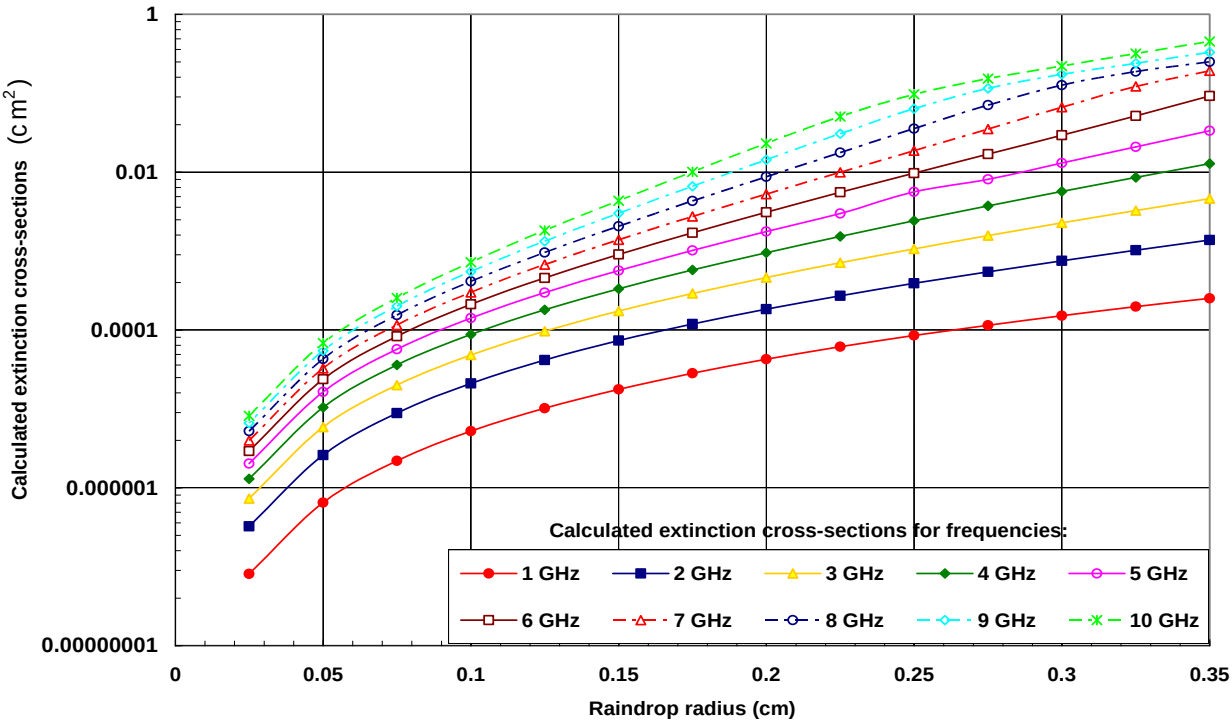

Fig. 5- 2: Calculated extinction cross-section of spherical raindrops for frequencies, f = 1 – 10 GHz

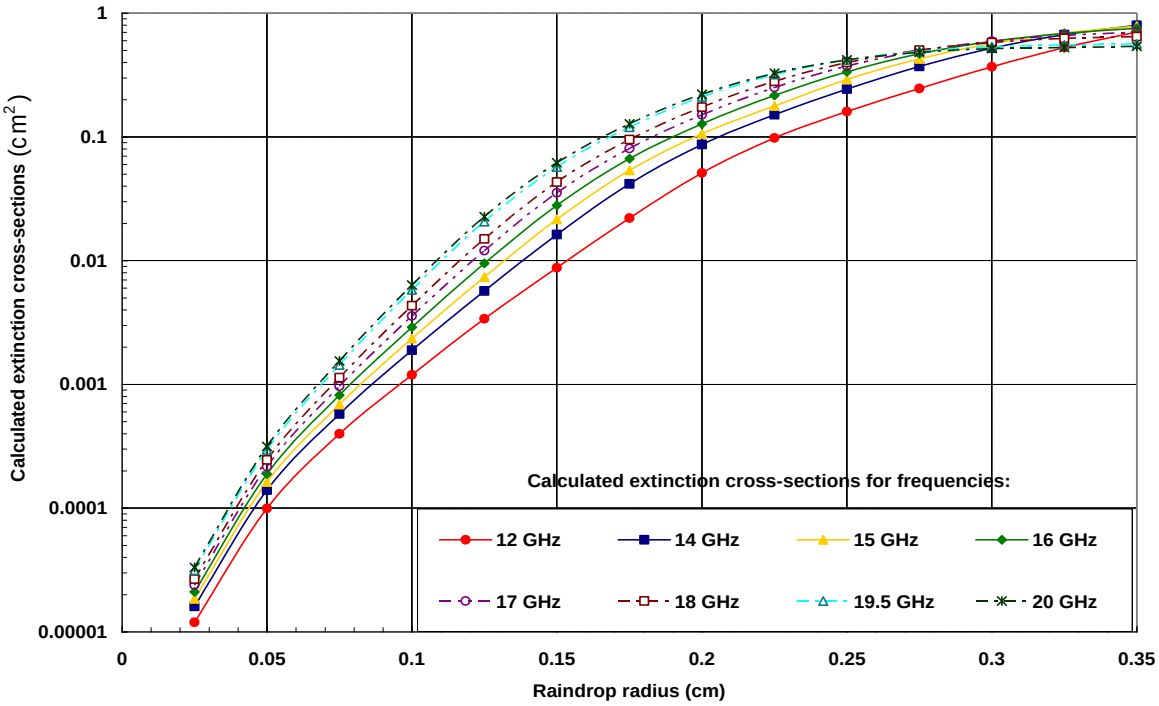

Fig. 5- 3: Calculated extinction cross-section of spherical raindrops for frequencies, f = 12, 14, 15, 16, 17, 18, 19.5, and 20 GHz

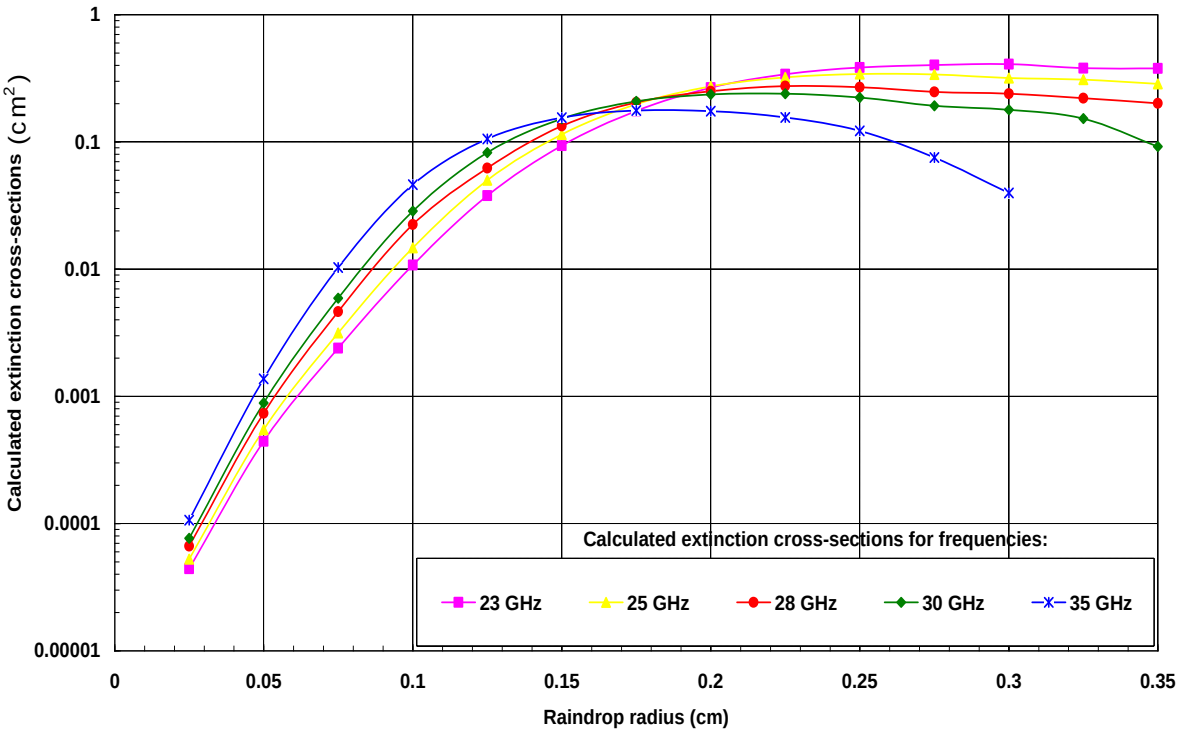

Fig. 5- 4: Calculated extinction cross-section of spherical raindrops for frequencies, f = 23, 25, 28, 30, 35 GHz

Applying power-law regression to fit the extinction cross-section calculated from the real part of the scattering amplitudes, it is observed that the extinction cross-section can be well modeled by a power law. From this, power law coefficients are determined for all the extinction cross-section calculated for frequencies up to about 35 GHz. Fig. 5-5 below shows an example of power law curve of the extinction cross-section for some frequencies that have been modeled by power law. Higher frequencies above 35 GHz are also fitted, but due to the negative scattering amplitudes produced by bigger raindrop size radius at the real part (see Appendix D), the power law model may not be suitable beyond 35 GHz.

From Fig. 5-5, the extinction cross-section can be described by this equation

$$\mathrm{Re}\,Q_{ext}(\phi=0,\bar{a},\lambda,T)=\kappa\bar{a}^{\varsigma} \tag{5.13}$$

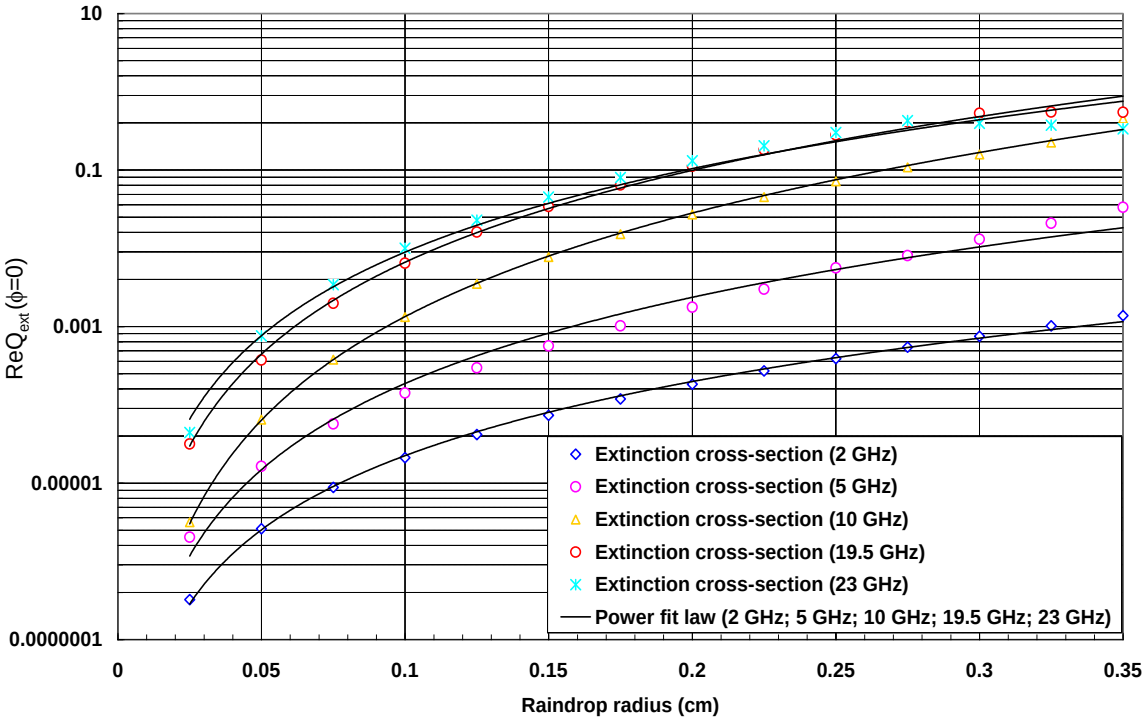

Fig. 5- 5: Modeling the extinction cross-section real part at different frequencies

where $\mathrm{Re}\,Q_{ext}$ is the real part of the extinction cross-section calculated which is dependent on the real part of the forward scattering amplitude with $\phi = 0$, radius of the spherical raindrop $\overline{a}$, wavelength λ,and the water (raindrop) temperature T. κ and ς are the extinction cross-sections power law coefficients. Table 5-4 below shows the extinction cross-section power-law coefficients determined for frequencies 1-35 GHz.

5.5 Formulation of the Rain Attenuation Models

The power in an electromagnetic wave that has passed a distance d through a homogeneous medium decreases in amplitude by a factor $e^{-\gamma d}$, where γ is the attenuation factor or attenuation coefficient ([*Hogg*, 1968; *Sadiku*, 2000; 2009]) which is given in [*Van de Hulst*, 1957; *Sadiku*, 2000] as:

$$\gamma = nQ_{ext} \tag{5.14}$$

Table 5- 4: The extinction cross-section power-law coefficients κ and ς for $ReQ_{ext}=\kappa\bar{a}^{\varsigma}$ at T=20°C

Frequencies (GHz)	κ_{ext}	ς_{ext}
1	0.0058	3.0408
2	0.0315	3.1478
3	0.107	3.2934
4	0.3086	3.4613
5	0.8542	3.6594
6	2.3114	3.8787
7	5.9654	4.0972
8	11.71	4.228
9	19.431	4.2975
10	30.043	4.3555
12	51.378	4.3217
14	87.188	4.4109
15	95.823	4.3751
16	100.89	4.3265
17	99.89	4.263
18	97.091	4.2223
19.5	83.956	4.1142
20	81.36	4.0887
23	51.931	3.7151
25	36.769	3.489
28	15.566	3.0001
30	10.2283	2.6873
35	8.7185	2.5773

The symbol n is assumed to be identical to spherical drops per unit volume. Therefore, the wave is attenuated by [*Crane*, 1996; *Sadiku*, 2000];

$$A(dB) = 10\log_{10}\frac{1}{e^{-\gamma d}} \text{ (ratio of power to reference power [}\textit{Crane}\text{, 1996])} \quad (5.15a)$$

$$A(dB) = \gamma d 10\log_{10} e \quad (5.15b)$$

where $e = 2.718$, and thus;

$$A(dB) = 4.343\gamma d \quad (5.16a)$$

or

$$A(dB/km) = 4.343\gamma \quad (5.16b)$$

Equations (5.16a) and (5.16b) are path attenuation and specific rain attenuation respectively.

Thus, using equation (5.14) and (5.16b), the specific attenuation can be given as

$$A = 4.343 \times n \times Q_{ext} \tag{5.17}$$

or

$$A = 4.343 \frac{\lambda^2 n}{\pi} \mathrm{Re}\{S(0)\} \tag{5.18}$$

for n identical drops.

For the formulation of rain attenuation models, a more realistic rainfall must be used rather than identical spherical drops, because rainfall comprises of drops of various sizes. It is therefore necessary to know the drop-size distribution of a given rain intensity for the theoretical modeling of the rain attenuation [*Hogg*, 1968; *Sadiku*, 2000]. Several raindrop-size distribution models have been proposed by different authors, but for the formulation of rain attenuation models in this study, negative exponential, lognormal, Weibull, and gamma raindrop-size distributions are used. These models have been tested by many researchers [*Rogers and Olsen*, 1976; *Ajayi and Olsen*, 1985; *Sekine et al.*, 1987; *de Wolf*, 2001] and they appear to adequately approximate most observed drop-size spectra fairly well [*Rogers and Olsen*, 1976]. Thus, the specific rain attenuation can then be estimated by integrating the extinction cross-section power law over all the spherical raindrop sizes [*Hogg*, 1968].

5.5.1 Negative Exponential Attenuation Model

The negative exponential attenuation model is formulated based on the negative exponential raindrop-size distribution model. The negative exponential drop-size distributions used in this work are the ones given by *Marshall and Palmer* [1948] (MP) for all rain types and that of *Joss et al* (J) [1968] for drizzle and thunderstorm type of rains (see Table 2-1). The negative exponential raindrop-size distribution as shown in equation (2.19) as a function of drop diameter can be represented by [*Marshall and Palmer*, 1948*; Joss et al.*, 1968]:

$$n(\bar{a}) = N_0 e^{-\Lambda \bar{a}} \tag{5.19}$$

as a function of drop radius, where $\bar{a}$ is the radius of the drop, N_0 is the number of concentration of drops $n(\bar{a})$ for radius $\bar{a} = 0$ on the exponential approximation and Λ is its slope per unit volume of space (defined in equation 5.19) [*Marshall and Palmer*, 1948].

From equation (5.13) the extinction cross-section power law model can be written as:

$$Q_{ext} = \kappa \bar{a}^{\varsigma} \tag{5.20}$$

To determine the attenuation coefficient, γ the extinction cross-section power law coefficients was integrated over exponential raindrop-size distribution models, to have

$$\gamma = \int_0^{\infty} \kappa \bar{a}^{\varsigma} \times n(\bar{a}) d\bar{a} = \int_0^{\infty} \kappa \bar{a}^{\varsigma} \times N_0 e^{-\Lambda \bar{a}} d\bar{a} \tag{5.21}$$

where $n(\bar{a})d\bar{a}$ is the number of drops of radius between $\bar{a}$ and $\bar{a} + d\bar{a}$ in a unit volume of space.

Applying integral gamma function in solving the integral in equation (5.21) [*Stroud and Booth*, 2003]:

$$\kappa N_0 \int_0^{\infty} \bar{a}^{\varsigma} \times e^{-\Lambda \bar{a}} d\bar{a} = \kappa N_0 \Gamma(\varsigma + 1) \int_0^{\infty} e^{-\Lambda \bar{a}} d\bar{a}$$

$$\gamma = \kappa N_0 \frac{\Gamma(\varsigma + 1)}{\Lambda^{\varsigma + 1}} \tag{5.22}$$

with Γ as the integral gamma function.

Substituting equation (5.22) into (5.16b), the specific rain attenuation can be written as:

$$A(dB/km) = 4.343 \times 10^5 \times \kappa \times N_0 \frac{\Gamma(\varsigma + 1)}{\Lambda^{\varsigma + 1}} \tag{5.23}$$

Substituting equation (5.22) into (5.16a), the path attenuation becomes:

$$A(dB) = 4.343 \times 10^5 \times \kappa \times N_0 \frac{\Gamma(\varsigma + 1)}{\Lambda^{\varsigma + 1}} \times d \tag{5.24}$$

where d is the propagation path length.

But because of the non-homogeneity of rain along propagation path length [*Crane,* 1980; 1996; *Moupfouma,* 1984; 2009; *Hall et al.,* 1996; *ITU-R 530-12,* 2007; *Forknall et al.,* 2008], as discussed in the previous chapters, the concept of effective path length d_{eff} was introduced into the path attenuation model formulated in equation (5.24). The ITU-R effective path length model is used in this work. This is because it seems to be the only model that cut across the three measured attenuation bounds (minimum, average, and maximum measured attenuation)and the model that has the minimum root mean square percentage error across the attenuation bounds predicted in Chapter four of this work. The effective path length is achieved by multiplying the actual path length of the propagation path by a distance factor r known as the reduction factor [*Moupfouma,* 1984; *ITU-R 530-12,* 2007]. The guiding equations for the effective path length are shown in Section 3.2.1.

Therefore equation (5. 24) for the path attenuation can be written as:

$$A(dB) = 4.343\times10^{5} \times d_{eff} \times \kappa \times N_0 \frac{\Gamma(\varsigma+1)}{\Lambda^{\varsigma+1}} \tag{5.25}$$

where d_{eff} is the effective path length of the terrestrial radio link, κ and ς is the extinction cross-section power-law coefficient, Γ is the integral gamma function, N_0 is the number of concentration of drops $n(\bar{a})$ for radius $\bar{a}=0$, and Λ is the slope (the rain dependent parameter), and is given as $\Lambda=\alpha\, \mathrm{R}^{-\beta}$ where R is the rain rate in $\mathrm{mmh}^{-1,}$ and α and β are the power law coefficients for the slope Λ [*Marshall and Palmer,* 1948; *Konwar,* 2006]

Equation (5.23) and (5.25) are the theoretical attenuation model formulated from the negative exponential rain distribution model for specific and path attenuation estimations, respectively.

5.5.2 Lognormal Attenuation Model

The lognormal attenuation model is formulated from the lognormal raindrop-size distribution. In this attenuation formulation, the general tropical lognormal raindrop-size distribution models given by Ajayi-Olsen (AO) [*Ajayi and Olsen,* 1985] for all rain types and that of Adimula-Ajayi

(AA) [*Adimula and Ajayi*, 1996] for drizzle, widespread, shower, thunderstorm and tropical thunderstorm rain are used in this work. The tropical lognormal models were chosen as against the continental lognormal models because of the similarities that the rain type in the South Africa has with the tropical environment [*Fashuyi et al.*, 2006]. The lognormal raindrop-size distribution model as given in equation (2.23) can be written as:

$$n(D) = \frac{N_t}{\sigma D\sqrt{2\pi}} \exp\left[-\frac{1}{2}\left(\frac{\ln(D) - \mu}{\sigma} \right)^2 \right] \tag{5.26}$$

where D is the raindrop diameter, $n(D)$ is the number of raindrops in a unit volume of air, σ is the standard deviation, μ is the mean of $\ln D$ and N_t is the total number of drops of all sizes. With σ, μ and N_t depending on the geographical characteristics of the location concerned [*Ajayi and Olsen*, 1985; *Adimula and Ajayi*, 1996].

Integrating the extinction cross-section power law coefficients over lognormal raindrop-size distribution models, we have:

$$\gamma = \int_0^\infty \kappa \left(\frac{D}{2} \right)^\varsigma \times n(D) dD = \int_0^\infty \kappa \left(\frac{D}{2} \right)^\varsigma \times \frac{N_t}{\sigma D\sqrt{2\pi}} \exp\left[-\frac{1}{2}\left(\frac{\ln(D) - \mu}{\sigma} \right)^2 \right] dD$$

$$\therefore \quad \gamma = \kappa N_t \left(\frac{1}{2} \right)^\varsigma \frac{1}{\sigma\sqrt{2\pi}} \int_0^\infty D^{\varsigma - 1} \exp\left(-\frac{(\ln D - \mu)^2}{2\sigma^2} \right) dD \tag{5.27}$$

Integrating by parts and applying the integration bounds, the attenuation coefficient γ for lognormal models can be given as [*Moupfouma*, 1997]:

$$\gamma = \int_0^\infty \kappa \left(\frac{D}{2} \right)^\varsigma \times n(D) dD = \frac{\kappa N_t}{2^\varsigma} \exp\left[\varsigma\mu + \left(\frac{\varsigma\sigma}{\sqrt{2}} \right)^2 \right] \tag{5.28}$$

Substituting equation (5.28) into (5.16b) the specific attenuation with a lognormal distribution model can be written as:

$$A(dB/km) = 4.343\times10^{5}\times N_t \times \frac{\kappa}{2^{\varsigma}} \times \exp\left[\varsigma\times\mu + \left(\frac{\varsigma\times\sigma}{\sqrt{2}}\right)^2\right] \tag{5.29}$$

and path attenuation can be written as:

$$A(dB) = 4.343\times10^{5}\times d_{eff} \times N_t \times \frac{\kappa}{2^{\varsigma}} \times \exp\left[\varsigma\times\mu + \left(\frac{\varsigma\times\sigma}{\sqrt{2}}\right)^2\right] \tag{5.30}$$

where N_t, μ, and σ are the rain dependent parameters

Equations (5.29) and (5.30) are the theoretical rain attenuation model developed from a lognormal rain distribution model for specific and path attenuation, respectively.

5.5.3 Weibull Attenuation Model

The Weibull attenuation model is formulated from the Weibull drop-size distribution models. The Weibull distribution model for drizzle, widespread and shower rains given by *Sekine et al.* [1987] are used in this work. The Weibull raindrop-size distribution model given in equation (2.25) can be represented by:

$$n(D) = N_0 \frac{c}{b}\left(\frac{D}{b}\right)^{c-1} \mathrm{e}^{-(D/b)^c} \tag{5.31}$$

where b and c are parameters depending on the geographical characteristics of the location concerned.

Integrating the extinction cross-section power law over equation (5.31), we have:

$$\begin{aligned}\gamma &= \int_0^{\infty} \kappa\left(\frac{D}{2}\right)^{\varsigma} \times n(D)dD = \int_0^{\infty} \kappa\left(\frac{D}{2}\right)^{\varsigma} \times N_0 \frac{c}{b}\left(\frac{D}{b}\right)^{c-1} \mathrm{e}^{-(D/b)^c} dD \\ &= \frac{c}{b}\kappa N_0 \int_0^{\infty}\left(\frac{D}{2}\right)\left(\frac{D}{b}\right)^{c-1} \mathrm{e}^{-(D/b)^c} dD\end{aligned} \tag{5.32}$$

Integrating equation (5.32) by parts and applying the integral gamma functions [*Stroud and Booth*, 2003], the attenuation coefficient γ can be given as:

$$\gamma = \int_0^\infty \kappa \left(\frac{D}{2}\right)^{\varsigma} \times n(D) dD = \kappa N_0 \left(\frac{b}{2}\right)^{\varsigma} \left(\frac{\varsigma}{c}\right) \Gamma\left(\frac{\varsigma}{c}\right) \tag{5.33}$$

with Γ as the integral gamma function. Therefore the specific attenuation from a Weibull distribution model can be written as:

$$A(dB/km) = 4.343 \times 10^5 \times N_0 \times \kappa \times \left(\frac{b}{2}\right)^{\varsigma} \times \left(\frac{\varsigma}{c}\right) \times \Gamma\left(\frac{\varsigma}{c}\right) \tag{5.34}$$

and the corresponding path attenuation is given as:

$$A(dB) = 4.343 \times 10^5 \times d_{eff} \times N_0 \times \kappa \times \left(\frac{b}{2}\right)^{\varsigma} \times \left(\frac{\varsigma}{c}\right) \times \Gamma\left(\frac{\varsigma}{c}\right) \tag{5.35}$$

Equation (5.34) and (5.35) are the theoretical attenuation model formulated from the Weibull rain distribution model for specific and path attenuation, respectively.

5.5.4 Gamma Attenuation Model

The gamma attenuation model is formulated based on the gamma drop-size distribution model discussed in section 2.12.2 of this thesis. The gamma drop-size distribution given in equation (2.20) can also be expressed as:

$$n(D) = N_0 D^{\mu} \exp(-\Lambda D) \tag{5.36}$$

Integrating the extinction cross-section power law model over the gamma drop-size distribution in equation (5.36), to obtain the attenuation coefficient γ

$$\gamma = \int_0^\infty \kappa \left(\frac{D}{2}\right)^{\varsigma} \times n(D) dD = \int_0^\infty \kappa \left(\frac{D}{2}\right)^{\varsigma} \times N_0 D^{\mu} \exp(-\Lambda D) dD$$

$$\gamma = \kappa\left(\frac{1}{2}\right)^{\varsigma} N_0 \int_0^{\infty} D^{\varsigma+\mu} e^{-\Lambda D} dD \tag{5.37}$$

Solving equation (5.37) by parts and applying the gamma integral function rule [*Stroud and Booth,* 2003], the attenuation coefficient γ can be written as;

$$\gamma = \kappa\left(\frac{1}{2}\right)^{\varsigma} N_0 \left(\frac{1}{\Lambda}\right)^{\varsigma+\mu+1} \Gamma(\varsigma+\mu+1) \tag{5.38}$$

Substituting equation (5.38) into (5.16b) the specific attenuation with a gamma distribution model can be written as:

$$A(dB/km) = 4.343\times10^5 \times \kappa \times \left(\frac{1}{2}\right)^{\varsigma} \times N_0 \left(\frac{1}{\Lambda}\right)^{\varsigma+\mu+1} \times \Gamma(\varsigma+\mu+1) \tag{5.39}$$

and substituting (5.38) into (5.16a), the path attenuation can be written as:

$$A(dB) = 4.343\times10^5 \times d_{eff} \times \kappa \left(\frac{1}{2}\right)^{\varsigma} \times N_0 \left(\frac{1}{\Lambda}\right)^{\varsigma+\mu+1} \times \Gamma(\varsigma+\mu+1) \tag{5.40}$$

Equation (5.39) and (5.40) are the theoretical attenuation model formulated from the gamma rain distribution model for specific and path attenuation estimations, respectively.

5.6 Computation of Specific Rain Attenuation

The specific rain attenuation is a fundamental quantity in the calculation of rain attenuation statistics [*Olsen et al.,* 1978]. Until now, the kR^{α} expression has been widely used for the computation of the specific rain attenuation due to its simplicity [*Olsen et al.,* 1978; *ITU-R,* 2005]. However, the values of k and α are often given for discrete frequencies [*ITU-R 838,* 2005]. In many times cases where the required frequencies lie between the corresponding values of k and α, these values are determined by interpolation [*Ajayi et al.,* 1996; *Moupfouma,* 1997]. Such an interpolation may sometimes bias the attenuation results [*Moupfouma,* 1997].

However, the attenuation models presented in Section 5.5 of this work for different raindrop size distribution enables us to calculate the specific rain attenuation even at some intermediate

frequencies such as 5.3 GHz, 21.3 GHz, 11.7 GHz, 19.5 GHz, and … etc without need for interpolation. This is because once the scattering amplitudes are determined for the spherical raindrops at the desired frequencies; the extinction cross section can be calculated. This can then be fitted and used to estimate the specific rain attenuation. The major parameter that will need to be known in the above proposed theoretical models, when applied to various geographical locations is the rain rate statistics of the location or the raindrop-size distribution governing the location in question.

The results from these models have been applied to the propagation measurements recorded in Durban along the 6.73 km to ascertain the best theoretical model that defines the Durban climate in section 5.7 of this chapter. But firstly, using a 5-year rain rate (mm/h) exceeded for 0.01% of the average year as determined by *Fashuyi* [2006], *Fashuyi et al.* [2006] for four different locations in South Africa, with the developed theoretical rain attenuation models, the respective specific attenuations are computed these locations. Each of this location is situated in four different climatic regions with each having different climatic rain zone. These four locations are Durban, Cape Town, Pretoria and Brandvlei with the locations having P, N, Q, and M climatic rain zones, respectively [*Fashuyi et al.*, 2006] (see Tables 3-3 and 3-4). Durban is located in the eastern coastal area of South Africa, Cape town in the western mediterranean side, Pretoria in the temperate inland, and Brandvlei in the desert area of South Africa [from South Africa weather Services (SAWS)]. Table 5-5 below shows the annual $R_{0.01}$, average $R_{0.01}$, and the geographical location of the four cities.

The theoretical rain attenuation models developed in section 5.5 above are used to calculate the specific rain attenuation. For the calculation of the negative exponential attenuation, the raindrop

Table 5- 5: Annual and averaged $R_{0.01}$ statistics for the four geographical locations [Fashuyi, 2006; Fashuyi et al., 2006; Fashuyi and Afullo, 2007]

Location	Latitude south	Longitude east	2000, (mm/h)	2001, (mm/h)	2002, (mm/h)	2003, (mm/h)	2004, (mm/h)	Average (2000-2004), mm/h
Durban	29°.97'	30°.95'	108.75	88.82	138.83	139.66	121.84	119.58
Cape Town	33°.97'	18°.60'	47.70	69.96	57.03	44.50	87.04	61.25
Pretoria	25°.73'	28°.18'	159.45	114.90	100.73	106.09	113.15	118.86
Brandvlei	30°.47'	20°.48'	41.25	105.2	67.02	13.67	42.34	53.90

size distribution coefficients proposed by *Marshall Palmer* [1948] for different rain types (MP) and the *Joss et al*. [1968] coefficients for drizzle (D) and thunderstorm (T) rain types are used (see Section 2.12.1). For the lognormal attenuation calculation, the drop-size coefficients given by *Ajayi and Olsen* [1985] for all tropical rains, and that of *Ajayi and Adimula* [1996] for tropical widespread (TW), topical shower (TS) and tropical thunderstorm (TT) are used (see Table 2-3). For Weibull attenuation calculation, the drop-size distribution coefficients given by *Sekine at al*. [1987] for drizzle, widespread and shower rains are used (see Section 2.12.4). Finally, for the gamma attenuation calculation, the coefficients given by *de Wolf* [2001] for the gamma distribution fit to the measurements of *Laws and Parsons* [1943] are used.

Figures 5-6 to 5-9 below show the specific rain attenuation models calculated from the various developed theoretical models, and the ITU-R model, for Durban, Cape Town, Pretoria and Brandvlei. In Fig. 5-6 and 5-8 where the rain rate exceeded for 0.01% of the average year $R_{0.01}$ is 119.58 mm/h and 118.86 mm/h for Durban and Pretoria, respectively, at about 4 GHz, the ITU-R model gives the highest attenuation values for the frequencies up to 15 GHz in Durban and 16 GHz in Pretoria. At 16 and 17 GHz for Durban, the ITU-R attenuation results overlaps with the Weibull attenuation model, after which the Weibull attenuation model takes the lead up to 35 GHz. For Pretoria, the overlap between the ITU-R and Weibull model occurred at 17 GHz after which the Weibull model also takes the lead up to 35 GHz.

The Weibull model is seen to give lower attenuation values at lower frequencies, but increases rapidly at frequencies above 5 GHz. This behaviour tends to be pronounced for lower rain rate environments, like Brandvlei with $R_{0.01} = 53.90\ mm/h$, and Cape Town with $R_{0.01} = 61.25\ mm/h$. With this, in the high rain rates environment, of figures 5-6 and 5-8, the Weibull model gives the lowest attenuation values at 1 GHz and the highest attenuation values at 35 GHz when compared to other models. The lognormal model of AA-tropical widespread (TW) also gives lower attenuation results in these figures (Fig. 5-6 and 5-8), but the attenuation results do not increase rapidly like that of the Gamma or Weibull model. Thus, the lognormal model of AA-tropical widespread (TW) gives the lowest attenuation results at 35 GHz for the two locations (Durban and Pretoria).

For figures 5-7 and 5-9 below, at frequency above 5 GHz, the gamma model is seen to give to lowest attenuation values up to 25 GHz, after which it also rises rapidly up to 35 GHz. Also in the same figures, the lognormal model of AA-tropical shower (TS) gives a higher attenuation from 7

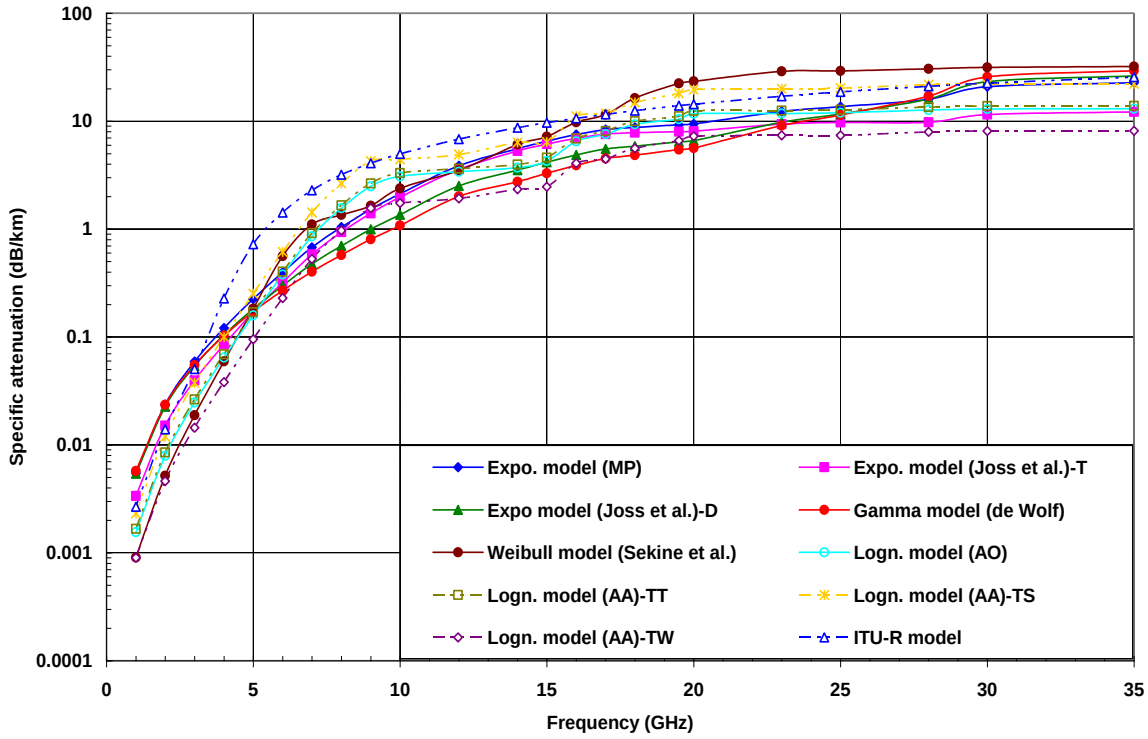

Fig. 5- 6: Specific rain attenuation from theoretical models for Durban

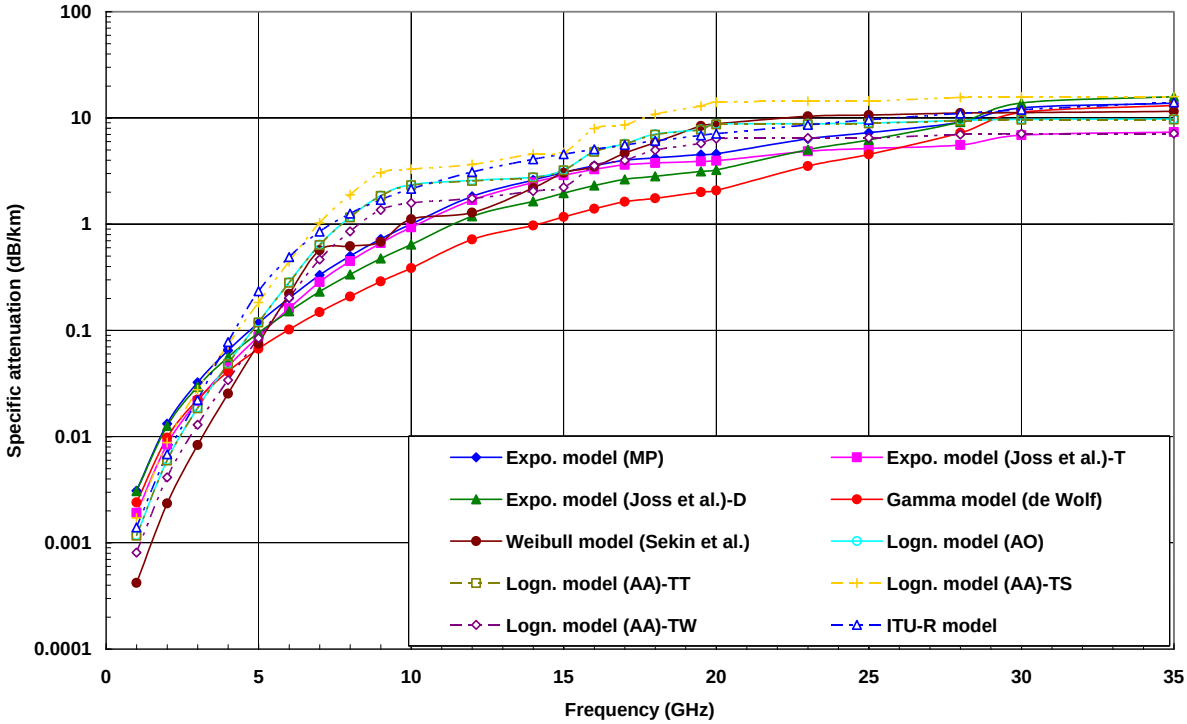

Fig. 5- 7: Specific rain attenuation from theoretical models for Cape Town

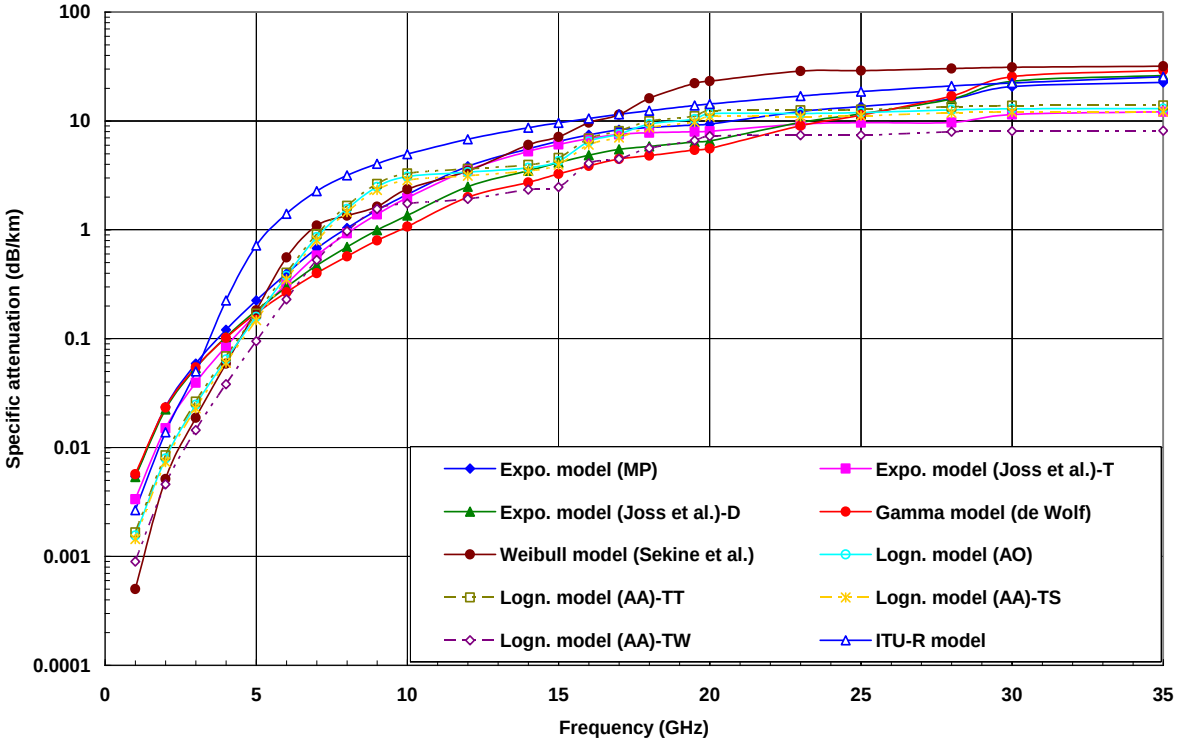

Fig. 5- 8: Specific rain attenuation from theoretical models for Pretoria

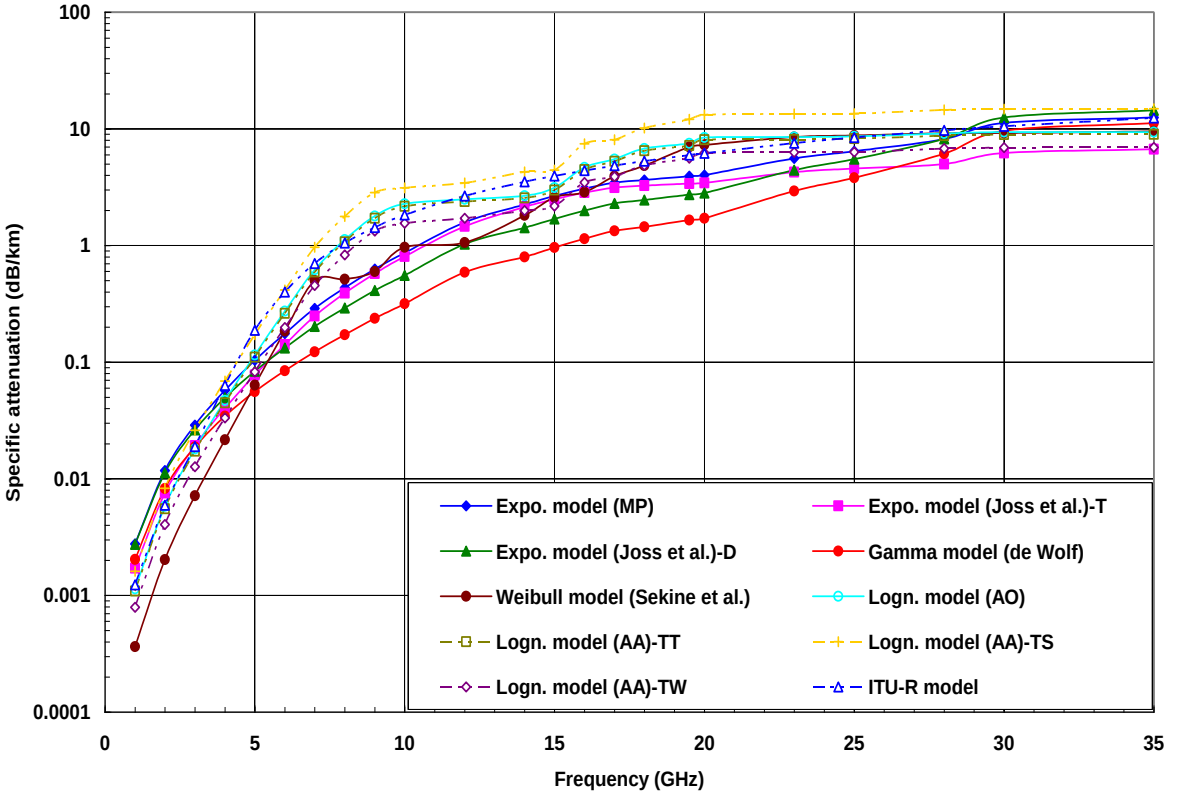

Fig. 5- 9: Specific rain attenuation from theoretical models for Brandvlei

GHz up to 35 GHz. At 6 GHz, the attenuation results of the ITU-R and the lognormal model overlap with a specific attenuation of about 0.45 dB/km in Cape Town. Beyond this point, the lognormal model of AA-tropical shower (TS) takes the lead. For Brandvlei, the attenuation results of the ITU-R and the lognormal model of AA-tropical shower (TS) also overlap, but in this location it is at 4 – 6 GHz. Above this, the lognormal attenuation values lead.

5.7 Theoretical and Experimental Rain Attenuation

The maximum, average, and minimum measured rain attenuation values per rain rate determined in the fourth chapter (Section 4.8) of this report from the experimental results are compared with the results obtained from the theoretical rain attenuation models. The theoretical rain attenuation models formulated for different raindrop-size distribution are used in conjunction with the 1-minute rain rates recorded at two points under the 6.73 km path length link. The 1-minute rain rate is collected with one rain gauge at the transmitter end and the other at the receiver end along the path to calculate the theoretical rain attenuation at 19.5 GHz.

These theoretical attenuation results are compared with the experimental results at each bound; the maximum, average and minimum measured attenuation. The chi-square (χ^2) statistics [*Freedman et al.,* 1978] is then employed to determine the theoretical attenuation models that best fit into these measured attenuation bounds. Figures 5-10a and 5-10b below show the measured rain attenuation values as well as the theoretical rain attenuation values for Durban at 19.5 GHz along the 6.73-km line-of-sight path. Fig. 5-10a shows the measured rain attenuation values at the 3 bounds (maximum, minimum and average attenuation values per rain rate), rain attenuation calculated from the ITU-R model, and theoretical attenuation models developed from the negative exponential, Weibull, and the gamma raindrop-size distribution model. Fig. 5-10b also shows the measured rain attenuation at the 3 bounds, the theoretical attenuation models developed from the lognormal raindrop-size distribution model of Ajayi-Olsen (AO) and Adimula-Ajayi (AA).

From Fig 5-10a, it is observed that the attenuation results from these models fall largely on the minimum measured attenuation. At this point it is important to state again that South Africa being a sub-tropical climate incorporates the climatic characteristics of the tropics and temperate climates in its seasonal varaibility. For example, Cape Town exhibits a mediterranean climate,

inlands areas such as Pretoria and Johannesburg have a temperate climate, and coastal areas such as Durban, Pietermaritzburg, and Richards Bay exhibit sub-tropical climate. Rains in the latter part of this climatic region, especially in the summer exhibit some tropical characteristics and in the winter, the rains may show some temperate characteristics. This is because the rains in such environment are usually heavy and come with larger raindrops (but sometimes alternate with light rains). In the spring/winter rains are usually light with smaller raindrops that can occur for longer periods of time. Examples of such rains are drizzle and widespread rains.

Therefore, Fig. 5-10a which shows that most of the theoretical attenuation results fall on the minimum measured attenuation in Durban might have reflected the effect of light rains with smaller raindrop sizes. Since the raindrop-size distribution models employed in formulating these theoretical attenuation models are developed from research works in the temperate zones, [*Green,* 2004], the minimum measured attenuation which is as a result of lower rain rates (smaller raindrop-sizes) tend to be reasonably described by these theoretical models in this figure.

It is also observed from this figure (Fig. 5-10a) that the *ITU-R model* [2007] gives attenuation values that fall within the measured minimum, average and increases rapidly towards the measured maximum attenuation. Though it has been confirmed by some researchers in the tropics and equatorial climates that there are large disparities between measured attenuation results and the ITU-R predictions, but for the locality of study in this work (South Africa), the attenuation disparities from the ITU-R model may not be as large as those for the tropical or equatorial climates. This is because of the location and the climatic characteristics of South Africa which is quite different from the tropical or equatorial climate.

From Fig 5-10b, it is observed that theoretical attenuation results falls within the average and the maximum attenuation bounds which are produced by rain-rates with bigger drop-sizes. Knowing the limitation of the former raindrop-size distributions developed in the northern temperate regions, which are mostly suitable for lower rain rates, authors like *Ajayi and Olsen,* [1985]; *Feingold et al.,* [1986]; *Zainal et al.,* [1993]; *Ajayi and Adimula,* [1996]; etc, developed alternative raindrop-size distribution models that can best describe drop-sizes in the tropics and lower latitudes regions with higher rain rates. That is why the higher rain-rates produced by bigger raindrops seems to be reasonably described with the lognormal attenuation model developed in this work.

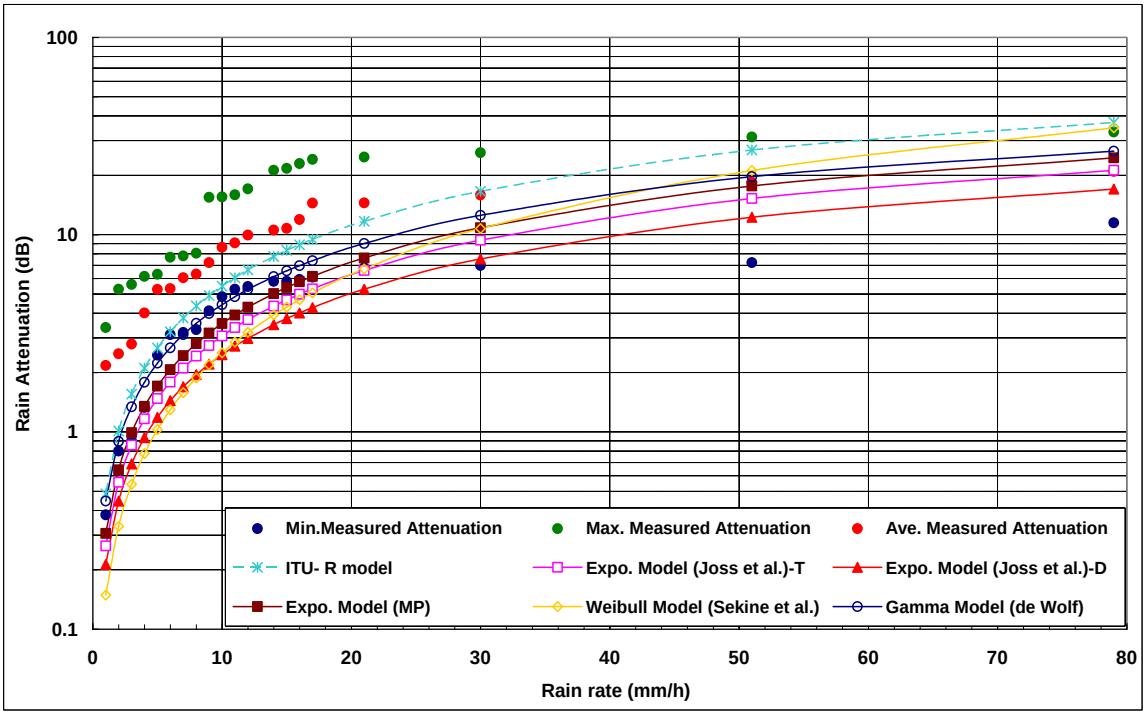

Fig. 5- 10a: Measured and theoretical rain attenuation along the 6.73 km path length at 19.5 GHz in Durban

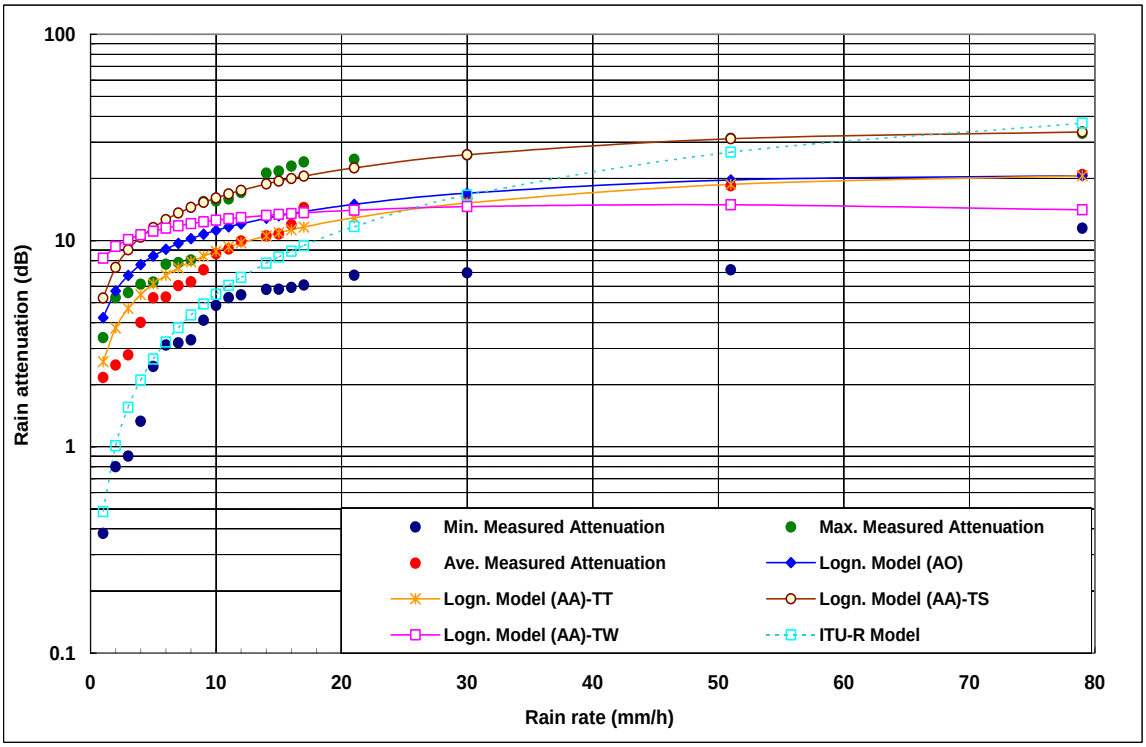

Fig. 5-10b: Measured and theoretical rain attenuation along the 6.73 km path length at 19.5 GHz in Durban

5.7.1 Statistical Analysis of the Rain Attenuation Results

From Fig. 5-10a and 5-10b, the theoretical attenuation models that best fit into the measured attenuation values for the minimum, average and the maximum bounds were determined by using the chi-square (χ^2) statistics. The χ^2 statistics which has been given in equation (4.3) as [*Freedman et al*., 1978];

$$\chi^2 = \sum_{i=1}^{N} \frac{\left(X_{mea,i} - X_{pre,i}\right)^2}{X_{pre,i}} \tag{5.41}$$

in this context, X_{mea} is the measured rain attenuation at the 3 bounds (minimum, average and maximum attenuation values), X_{pre} is the predicted theoretical rain attenuation values at 19. 5 GHz and N is the number of measured or predicted attenuation points ranging from $i = 1, 2...N$.

Table 5-6 shows the χ^2 results of all the theoretical attenuation models as compared to the

Table 5- 6: The χ^2 statistic (1% significance level) for the theoretical attenuation models as compared to the maximum, average and minimum measured attenuation at 19.5 GHz on 6.73 km path length [Odedina and Afullo, 2010]

Theoretical attenuation models	**Degrees of freedom is 20; χ^2 statistic threshold = 37.57**		
	Minimum measured attenuation	**Average measured attenuation**	**Maximum measured attenuation**
Negative exponential model (MP)	17.496	112.741	596.298
Negative exponential model (Joss et al.)-T	**16.656	156.69	753.963
Negative exponential model (Joss et al.)-D	23.308	243.898	1051.059
Gamma model	20.416	61.761	403.978
Weibull model	44.530	238.740	963.557
Lognormal model (AO)	88.811	16.347	60.432
Lognormal model (AA)-TT	55.534	**3.819	103.606
Lognormal model (AA)-TS	185.181	73.55	**15.935
Lognormal model (AA)-TW	105.245	41.455	103.558
*ITU-R model	44.559	38.774	256.386

*For the purpose of comparison
**Lowest χ^2 values of the theoretical attenuation model that best fit the measured rain attenuation

maximum, average and minimum measured attenuation. From this Table, the theoretical attenuation models developed from the negative exponential model of Joss et al. for thunderstorm (T) rain type, lognormal model of Adimula-Ajayi (AA) for tropical thunderstorm (TT), and the lognormal model of Adimula-Ajayi (AA) for tropical shower (TS) rains, give the lowest chi-square values for the minimum, average and maximum attenuation measurements, respectively. Hence these three theoretical models are accepted to give the best fit that describes the minimum, average and maximum rain attenuation values for the path. Fig. 5-11 below shows the measured and the best fit theoretical rain attenuation for Durban at 19.5 GHz on the 6.73 km link.

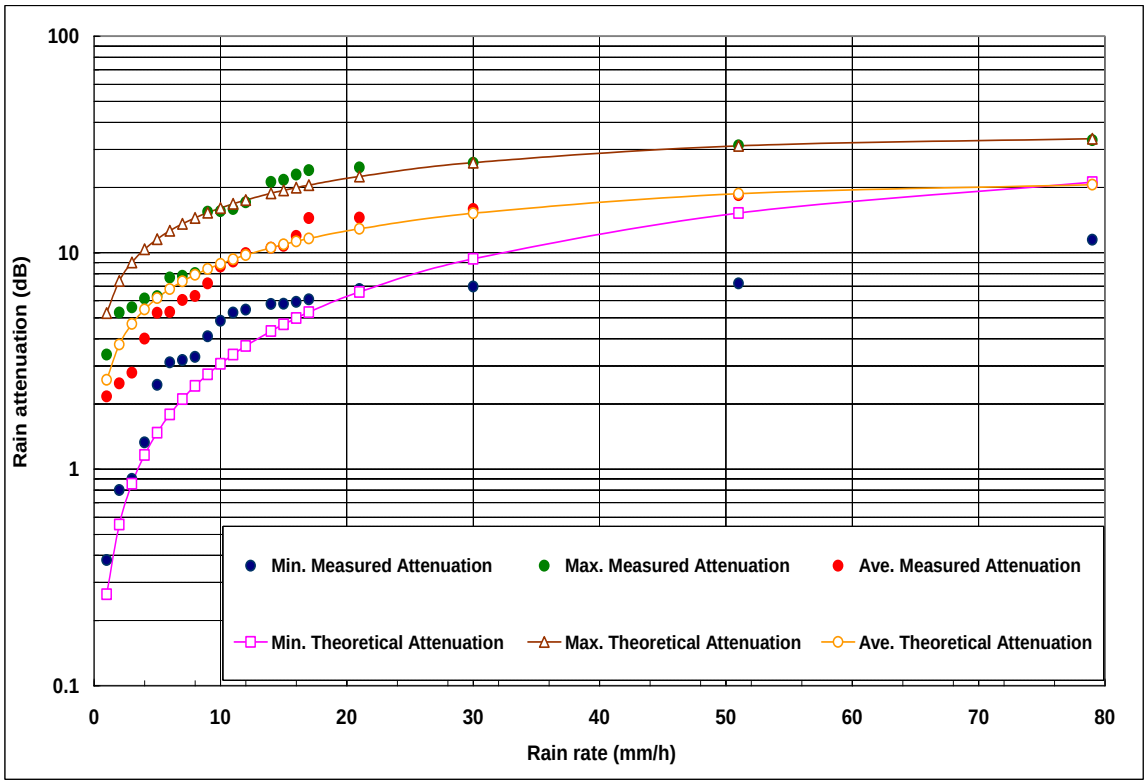

Fig. 5- 11: Best fit theoretical rain attenuation in Durban at 19.5 GHz along the 6.73 km link for the maximum, average and minimum measured attenuation [Odedina and Afullo, 2010]

5.8 Comparison of Theoretical Attenuation Results with Moupfouma Theoretical Model

From Fig. 5-11 above, the best fit theoretical attenuation models were predicted for the minimum, average and the maximum measured attenuation. In this section, the theoretical model that

describes the average measured rain attenuation at 19.5 GHz is compared with theoretical attenuation model formulated by *Moupfouma* [1997]. The *Moupfouma* [1997] approach as discussed in section 3.9.4 is similar to the approach employed in this work but differs in two or three specific ways.

Firstly, while Moupfouma obtains his power law model from the scattering amplitudes calculated from oblate spheroidal raindrops of *Uzunoglu et al* [1977], this work computed its scattering amplitudes from spherical raindrops. Secondly, the *Ray* [1972] complex refractive index was used by *Uzunoglu et al.* [1977] for the calculation of its scattering amplitudes for oblate spheroidal drops (which *Moupfouma* [1977)] used), but in this work, the refractive index of the spherical rain (water) drop are calculated by using the Liebe model [*Liebe et al.*, 1991] – a method also employed by *Mätzler* [2002a] and more recently by *Mulangu and Afullo* [2009]. Thirdly, while *Moupfouma* [1997] develops his rain attenuation coefficients from the imaginary part of the scattering amplitudes from the oblate spheroidal raindrop, in this work, the rain attenuation coefficients are determined from the real part of the extinction cross-sections of the spherical raindrops, which is calculated from the real part of the spherical scattering amplitudes.

For reasons stated above, the average attenuation values predicted by the theoretical model describing the average measured attenuation are compared with the attenuation values predicted by the Moupfouma theoretical model. Though some researchers like *Oguchi* [1973] and *Morrison and Cross* [1974] have also computed scattering amplitudes for oblate spheroidal drops, however their scattering amplitudes have not been really modeled out like *Moupfouma* [1997] did to the scattering amplitudes obtained by *Uzunoglu et al.* [1977]. Fig. 5-12 below shows the measured average rain attenuation at 19.5 GHz along the 6.73 km link, attenuation values from the *Moupfouma* [1997] theoretical model and predicted theoretical average attenuation from the lognormal model of *Adimula-Ajayi* [1996] (AA) for tropical thunderstorm (TT) at 19.5 GHz.

It can be observed from the figure (Fig. 5-12) that both *Moupfouma* [1997] theoretical attenuation and the predicted theoretical average attenuation model reasonably describe the measured average attenuation. The most conspicuous observation in this figure is that both models predicted almost the same path attenuation values, despite the differences in the formulation of each theoretical model. Knowing that the *Adimula-Ajayi* [1996] lognormal distribution for tropical thunderstorm is the most suitable drop-size distribution for this environment, the coefficients of this distribution

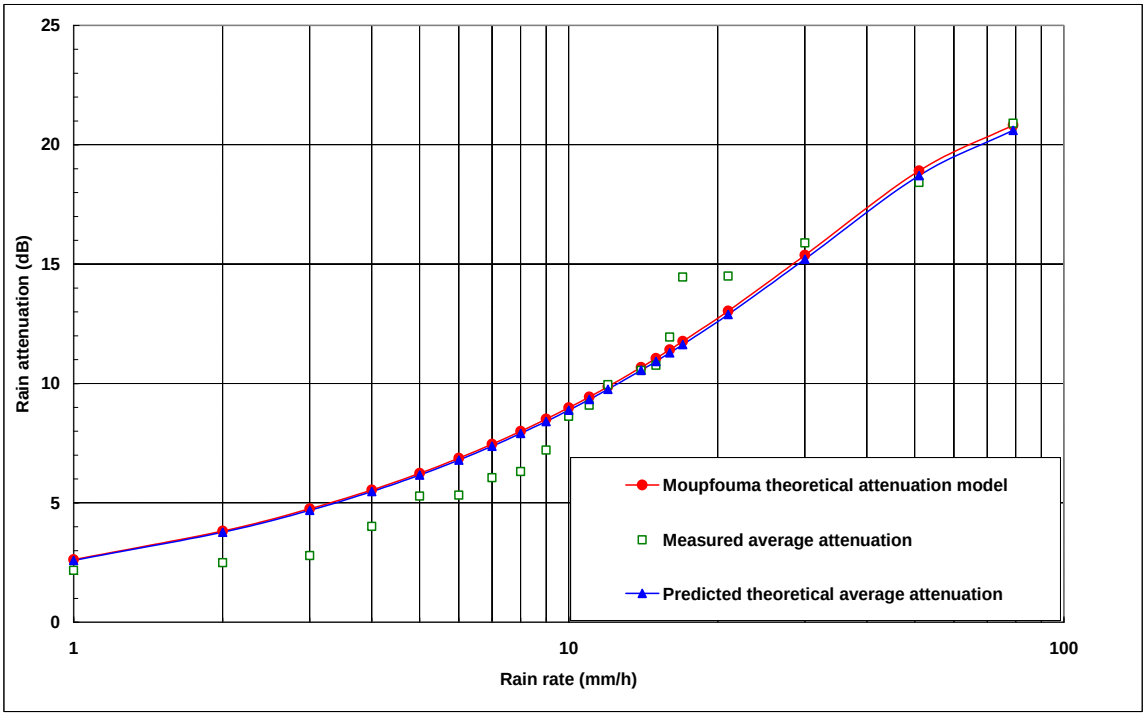

Fig. 5- 12: Comparison between the theoretical attenuation results and the Moupfouma theoretical model along the 6.73 km radio path

was incorporated into the *Moupfouma* [1997] theoretical model to obtain the Moupfouma theoretical attenuation curve shown in Fig 5-12

The major thing that should be noted in the formulation of these theoretical models is that, the *Moupfouma* [1997] model is developed from the scattering amplitudes of an oblate spheroidal drop calculated by *Uzunoglu et al.* [1977], while the average theoretical model predicted in this work is developed from the scattering amplitudes calculated from a spherical drop. Then, it can easily be said that whether rain attenuation is modeled with a spherical or an oblate spheroidal drop, the same rain attenuation might be expected along a terrestrial link if the approach employed in this thesis is used, though the results may be influenced by the drop-size distribution used in the calculation of the path attenuation. Therefore, the major parameter that needs to be known if this approach is to be applied to various locations around the world to estimate the path attenuation is to know the raindrop size distribution that describes the geographical location of interest. Since the attenuation models proposed in this chapter has been formulated from different raindrop-size distributions, therefore these proposed models can be used directly to determine the attenuation caused by rain.

5.9 Preliminary Studies on Raindrop Size Distribution

As mentioned above, the drop-size distribution model is one of the major parameter that is needed for accurate prediction of rain attenuation on a terrestrial radio link. The proposed theoretical rain attenuation models have used some established drop-size distribution models on the signal level measurements recorded in Durban to estimate the drop-size distribution for this location. But in the course of writing this thesis, a direct drop-size measurement and 1-minute rain rate is being recorded with a RD-80 distrometer in Durban.

These measurements have just been done for six months in the course of writing this thesis, and with the few months data gathered, the probability density functions (pdf) of the raindrop size measurements for these months are determined. Also, the rain events recorded over these months are classified into drizzle, widespread, shower and thunderstorm rain types and the mean rain rate statistics determined for each of the rain classes. This section simply gives the preliminary studies on the raindrop-size distribution in Durban. A valid drop-size distribution for Durban has not been confirmed.

5.9.1 Description of the Raindrop size Measurement and Distribution

Raindrop size measurement was collected with a Joss and Waldvogel distrometer (JWD), specifically RD-80 as shown in Fig. 5-13. The figure comprises: a sensor, which is the outdoor unit that is exposed to rain, the processor, a 10 meters long cable which is used to connect the sensor to the processor, and a computer unit which is indoor. The RD-80 consists of electromechanical sensors which convert mechanical momentum of falling drops into electrical pulses. The processor contains circuitry to eliminate unwanted signals, mainly due to acoustic noise and produces a 7-bit code at the output for every drop hitting the sensitive surface of the sensor [*Distrometer RD-80 Operating Instructions, Feb, 2007*].

The distrometer has 50 cm^2 of sampling area with an accuracy of +/-5% and a resolution of 127 drop-size classes. It collects raindrop sizes ranging between 0.359 mm to 5.373 mm in diameter with 20 bins or channels of diameter classes [*User's Guide for Distrodata V. 17, Aug. 2004; Distrometer RD-80 Operating Instructions, Feb, 2007*].

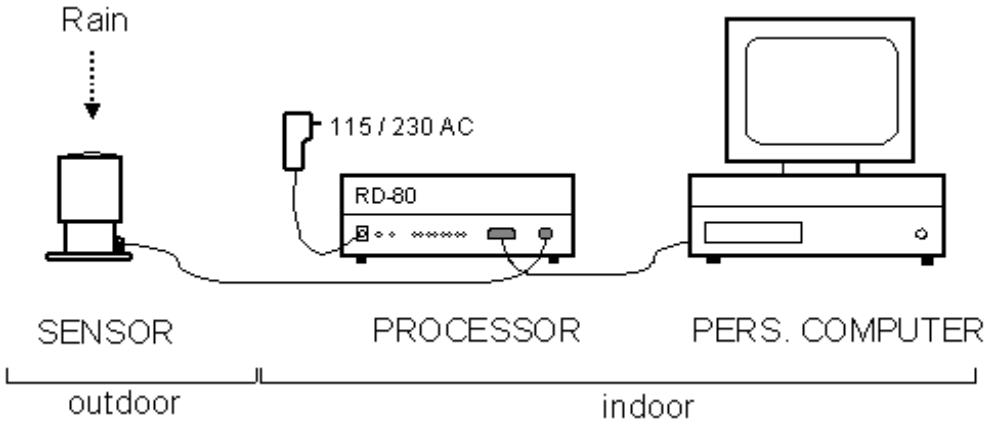

Fig. 5- 13a: Schematics diagram of configuration of distrometer with other accessories -RD-80 [*Distrometer RD-80 Operating Instructions, Feb 2007*]

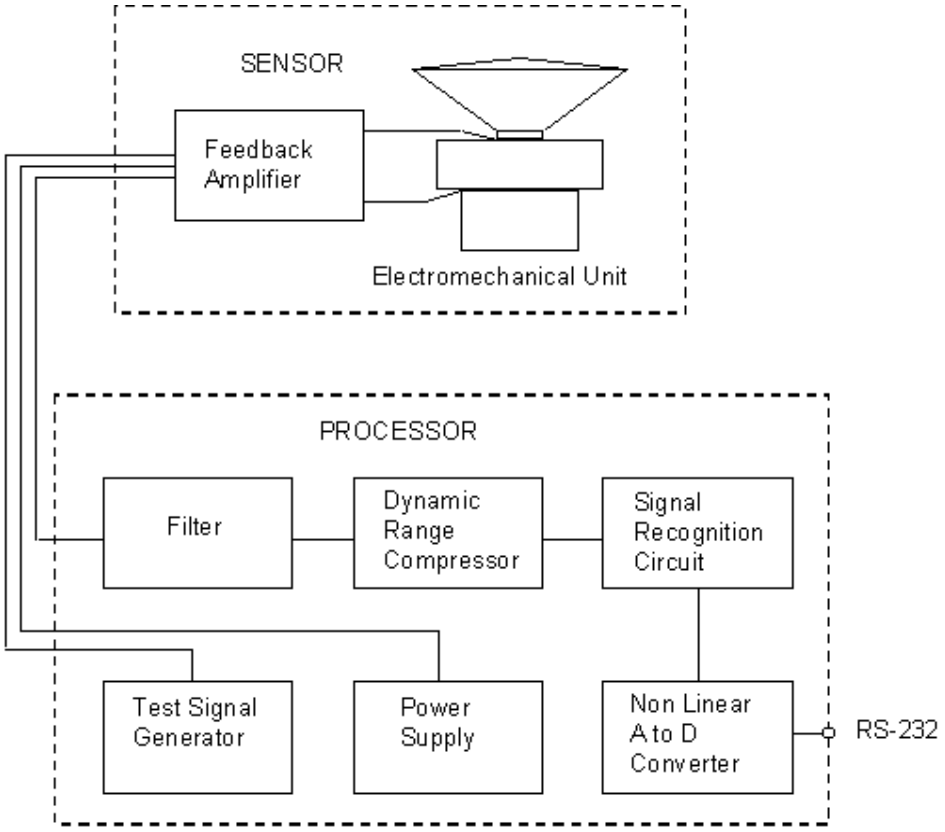

Fig. 5-13b: Block diagram of the distrometer RD-80 [*Distrometer RD-80 Operating Instruction, Feb, 2007*]

Fig. 5-14 below shows the distribution of the probability density function for the measured drop-sizes in Durban for six months (October 2008 – April, 2009). In this figure, the probability density function distribution for each month shows a negative exponential distribution. These distributions confirm the statement of *Feingold et al.* [1986] that says *"the inherent assumption of drop-size distribution is that they are exponential"* and also that of *Joss and Gori* [1978] that says *"drop size distribution tends to be exponential when the sampling time is sufficiently long"*. This monthly probability distribution function can be said to be long-term.

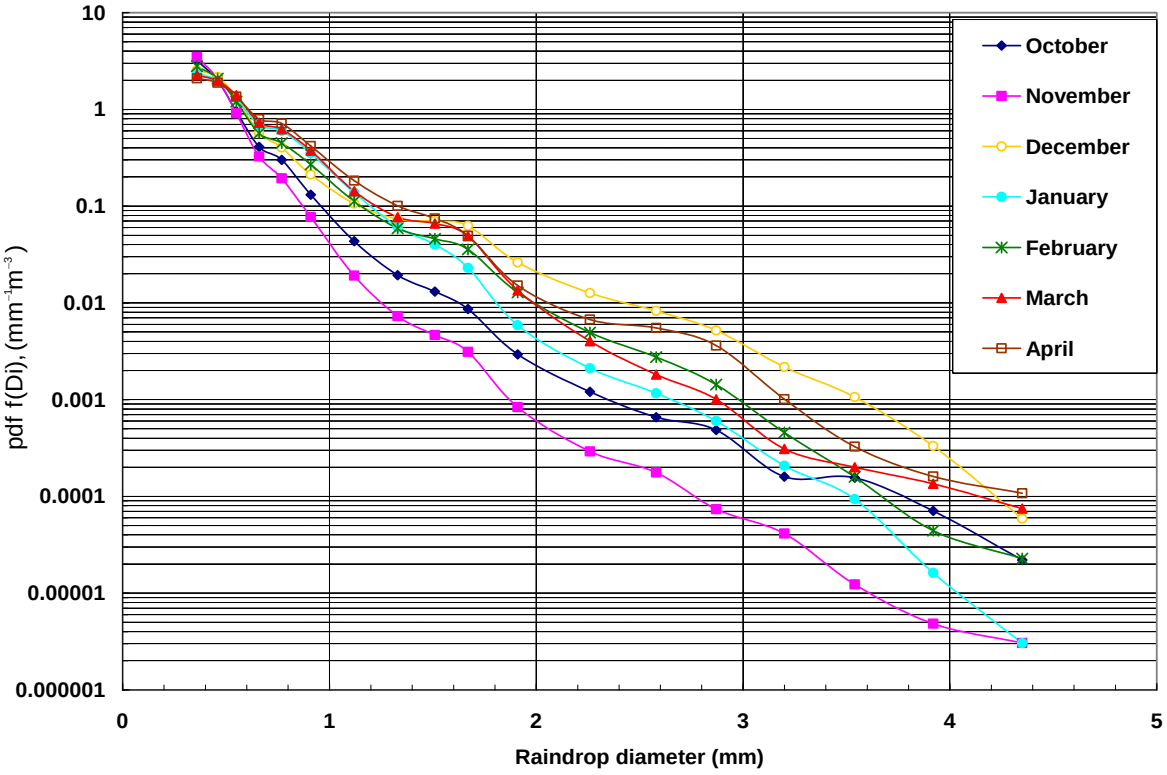

Fig. 5- 14: Probability density function for the measured drop-sizes in Durban

The rain events recorded in these six months are classified into drizzle, widespread, shower and thunderstorm rains for efficient propagation prediction and modeling. Though there are no defined ways of classifying these rain types, but various researchers such as *Joss et al.* [1968], *Fang and Chen* [1982], *Ajayi and Adimula* [1996], *Tokay and Short* [1996], etc. have classified the rain based on the climatic characteristics, drop diameter, and the rain rate recorded in their location (see Chapter 2).

The 1-minute rain rates for all the rain events are then grouped into ten classes of rain and classified into the drizzle widespread, shower and thunderstorm. These rain types are classified based on the nature and the characteristics of rain, the drop diameters and the rain rates recorded in Durban. These rains are then categorized into the stratiform and convective rains using 10 mm/h rain rate as the boundary between the two categories of rain as used by *Matricciani et al.,* [2000] and *Konwar, et al.,* [2006]. Table 5-7 below shows the groups, descriptions of the rain types, and the mean rain rate values for each the rain rate group. Fig. 5-15 – 5-18 below shows the drop-size distributions that describe the measured rain drops spectra for the different rain types.

Table 5- 7: Groups and description of the rain types in Durban

Rain rate, R (mm/h) groups	Mean rain rate (mm/h)	Description	Types of rain	Categories of rain
$R < 0.5$	0.24	Extremely light rain	Drizzle	Stratiform rain
$0.5 < R \leq 1$	0.73	Light rain		
$1 < R \leq 3$	1.71			
$3 < R \leq 5$	3.84			
$5 < R \leq 10$	6.90	Moderate rain	Tropical widespread	
$10 < R \leq 20$	13.70	Heavy rain	Tropical shower	Convective rain
$20 < R \leq 40$	27.04			
$40 < R \leq 60$	48.78	Very heavy rain	Tropical thunderstorm	
$60 < R \leq 100$	68.15	Extreme rain		
$R > 100$	117.15			

From these figures (Fig. 5-15 – 5-18) the drizzle and widespread rains which have small mean rain rate values have larger numbers of smaller drop-size diameters. As the values of the rain rate increases, the number of the smaller drops diameters also decreases, especially with the shower and thunderstorm rains. To determine the suitable distribution for these rain types, quantitative analysis is done between the measured raindrop sizes and the distribution models. A measure of the error between the distributions and raindrop size measurement is conducted. Table 5-8 shows the root mean square percentage error between the lognormal, gamma, exponential distribution and the measured drop-size distribution

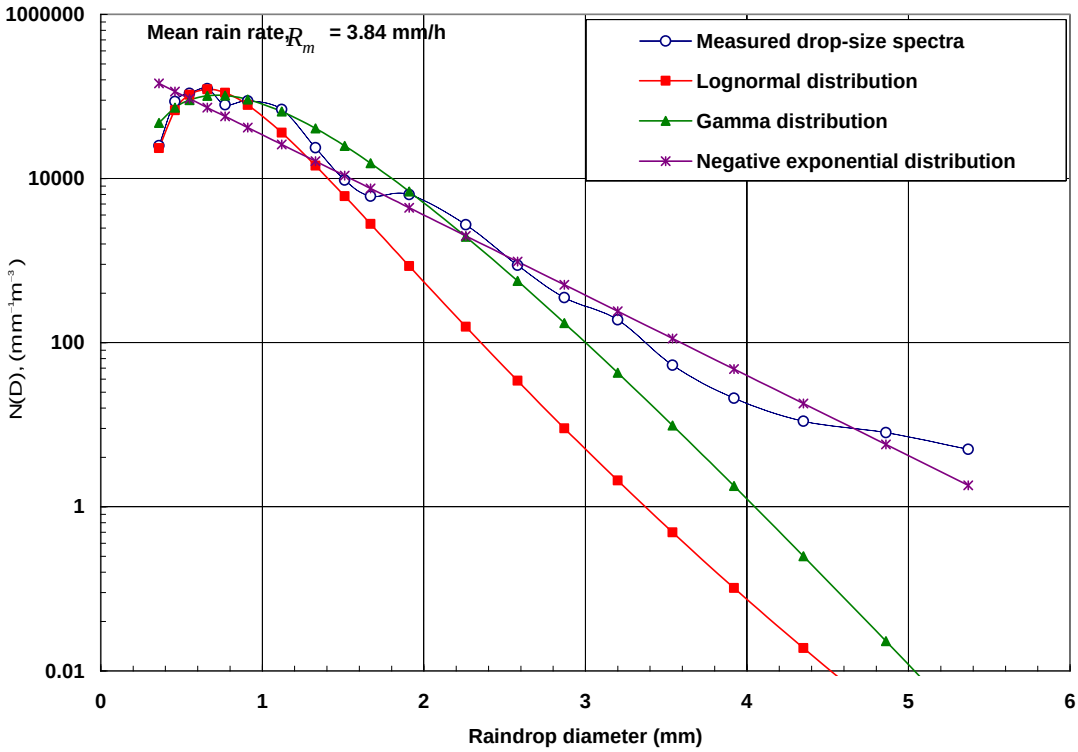

Fig. 5- 15: Raindrop size distribution for drizzle rains

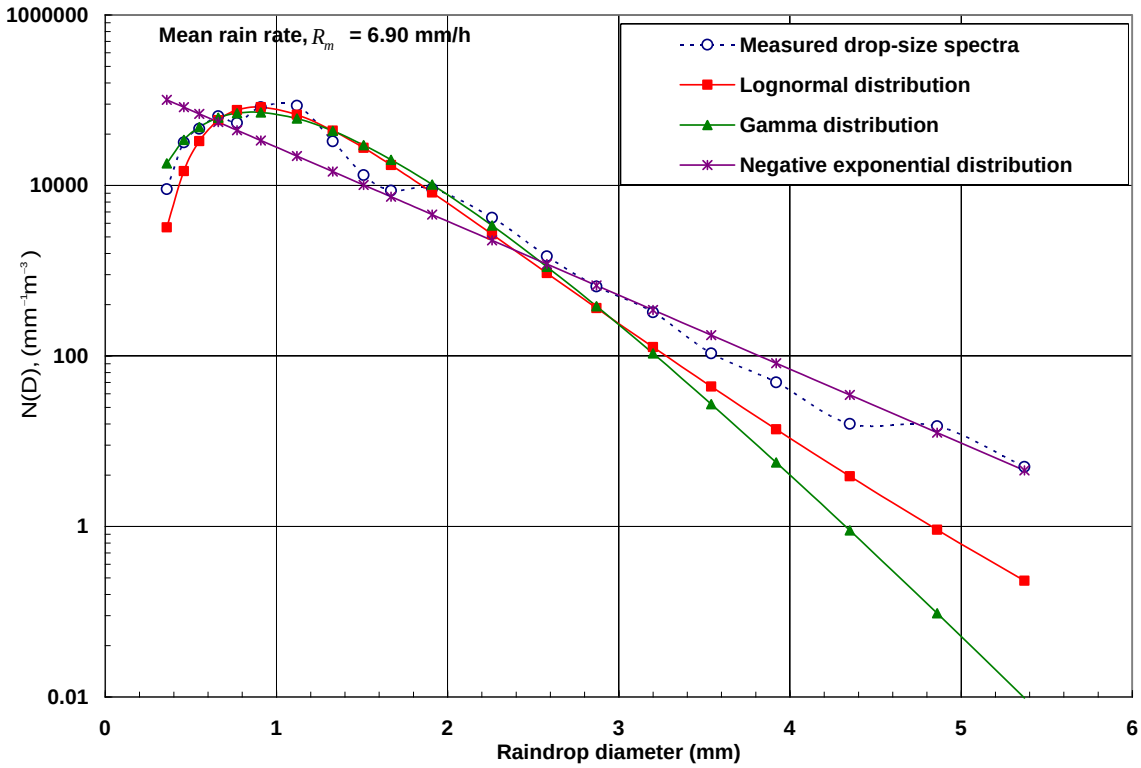

Fig. 5- 16: Raindrop size distribution for widespread rains

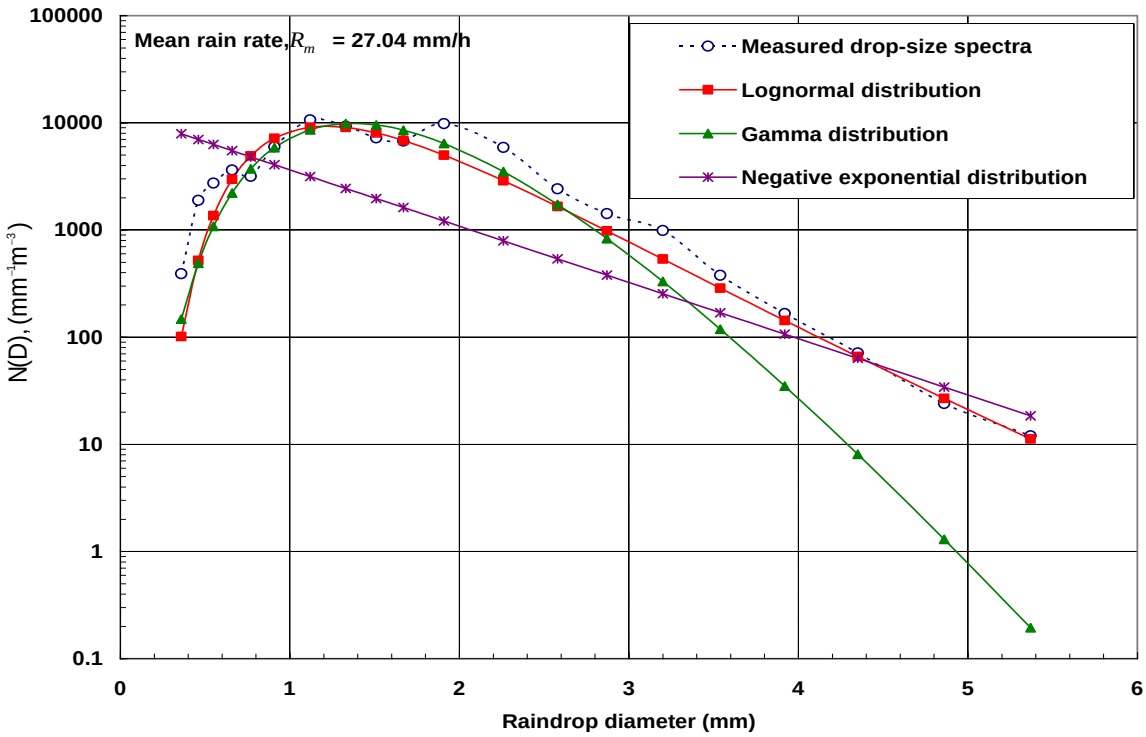

Fig. 5- 17: Raindrop size distribution for shower rains

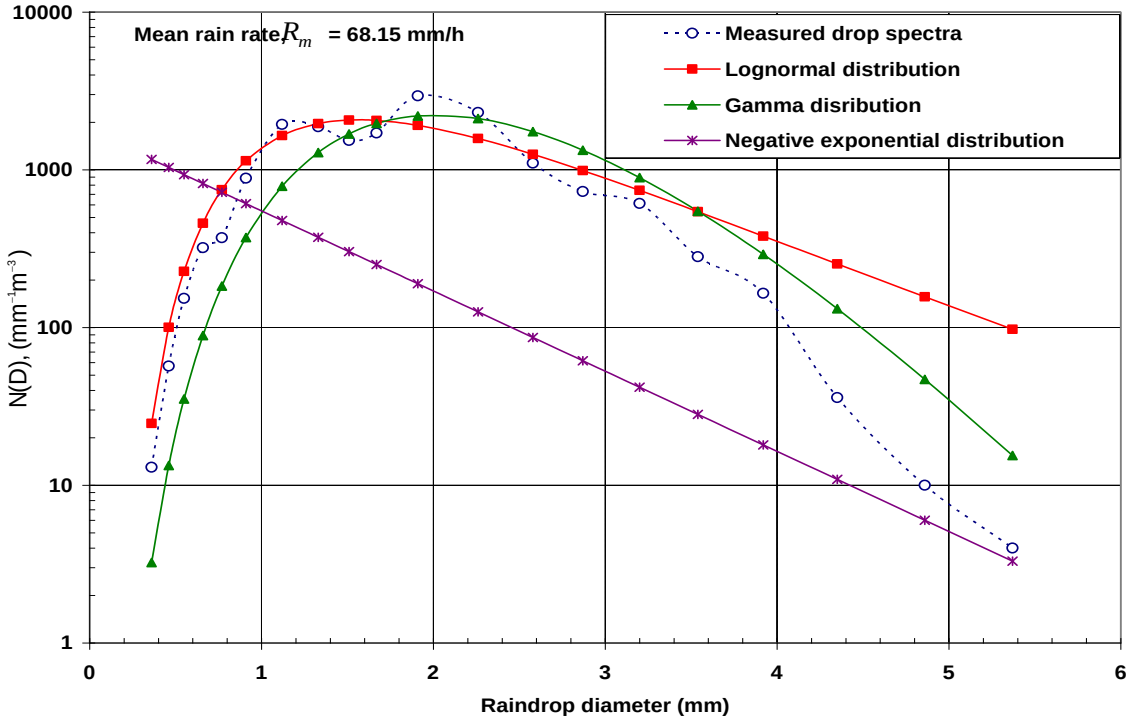

Fig. 5- 18: Raindrop size distribution for thunderstorm rains

Table 5- 8: The root mean square percentage error between the measured rain drop distribution and other distributions

Rain types	Root mean square percentage error, Δ_{rms} (%)		
	Lognormal distribution	Gamma distribution	Negative exponential distribution
Drizzle	7.24	7.72	11.79
Widespread	6.06	6.89	23.41
Shower	3.71	5.66	43.96
Thunderstorm	63.31	13.23	201.87

From the above table (Table 5-8), the negative exponential distribution gives the highest percentage of error for all the rain types, therefore it is not suitable to predict the distribution for the rain types. The lognormal drop-size gives the lowest percentage error for drizzle, widespread, and shower rain types, and the gamma drop-size distribution gives the lowest percentage error for thunderstorm rains. Therefore the lognormal drop-size distribution can be employed to predict the drizzle, widespread, and shower rain types, while the gamma drop-size distribution is better suited for the thunderstorm rain types.

It should be noted that the measured raindrop-sizes are recorded for just six months in Durban, between October-April, which basically are the summer and autumn seasons. A longer period of the raindrop size measurements and 1-minute rain rates taken throughout the year may be required for accurate drop-size distribution models.

5.10 Chapter Summary

This chapter gives a theoretical approach for the calculation of rain attenuation along a terrestrial communication radio link based on the assumption that the raindrops are of a spherical shape. The theoretical rain attenuation model is formulated by integrating the extinction cross-section power law models developed from the scattering amplitudes of the spherical raindrops over different established raindrop-size distribution models. This is then used to compute the specific rain attenuation for four locations situated in different rain climatic zones in South Africa. To validate these theoretical models, it is compared with the experimental signal level measurement

recorded in Durban. And for the purpose of cross referencing, it is also compared with the ITU-R rain attenuation model.

The results show that the theoretical attenuation model developed from the negative exponential drop-size distribution of *Joss et al.* [1968] thunderstorm rain type, lognormal model of *Adimula-Ajayi* [1996] for tropical thunderstorm rains, and tropical shower types of rains give the best fits for the minimum, average and maximum measured attenuation, respectively. Hence the rain attenuation values predicted by the average theoretical attenuation model are then compared with the attenuation values predicted from the *Moupfouma* [1997] theoretical model. The comparative results showed that either raindrop is spherical or oblate spheroidal, the shape of the raindrop is not the dominant factor in the estimation of rain attenuation along terrestrial paths.

These proposed theoretical attenuation models can be applied to various geographical locations around the world to estimate the rain attenuation along a terrestrial radio link, especially when either the rain rate statistics or the raindrop-size distribution governing the target locality is known. This chapter also gives a preliminary study on raindrop size distributions for different rain types in Durban based on the measurements carried out in the location.

However, a lot of work needs to be done to expand the power law coefficients of the extinction cross-section beyond 35 GHz. Also longer period of propagation measurements such as signal level, drop-size, and lower integration time rain rate measurements should be taken not only in Durban, but other geographical locations in South Africa. This is to ascertain the propagation models developed in this chapter and its applicability to other tropical and subtropical climates. The next chapter focuses on the characteristics and variations associated with rain attenuation distributions in South Africa.

Chapter Six

Characterization of Rain Attenuation Statistics and Its Impact on System Design

6.1 Introduction

In the previous chapters, rain attenuation has been modeled empirically and theoretically. These models were cross-referenced with different established rain attenuation models and validated by the ITU-R model. All the newly developed models and the already established ones can be used extensively in any part of the world to describe the behaviour of radio link performance in the presence of rain. Among many factors contributing to a reliable radio communication system, the link availability is an important parameter [*Schnell et al.,* 2002]. This is because it strongly influences the required fade margin needed on a line-of-sight link to accommodate any impairment that may occur due to rain [*COST 255,* 2002; *Odedina and Afullo,* 2009a]. For a given link, which is free from obstruction, the size of the fade margin depends on the amount of time the radio link is available during an average year [*Forknall et al.,* 2008].

Appropriate values for fade margin can be derived from the rain attenuation cumulative distribution. Not only does this distribution give the percentage of time for which a certain attenuation level is exceeded, it also gives the outage period of the radio link and reflects the characteristics associated with different attenuation distributions. This can contribute significantly

to propagation behavioural patterns and fading predictions on line-of-sight links [*Schnell et al.*, 2002; *Odedina and Afullo*, 2008b; 2009a]. Some of these distributions can reflect annual, seasonal, monthly, daily, and diurnal variations of the attenuation. The version that is needed to support a radio communication service depends on what is required on the radio link to guarantee availability over an average year, month or season. Obviously, the requirements of these availabilities yield different fade margins [*Schnell et al.*, 2002].

This chapter looks into the characteristics of seasonal, monthly, and average year attenuation distributions and their implications on radio system designs in four different geographical locations in South Africa. These four geographical locations are chosen for study because of their unique climatic features which contribute significantly to their propagation behavioural patterns and predictions. These locations are Durban which lies in the coastal region, Cape Town in the mediterranean, Brandvlei in the desert, and Pretoria in the temperate climatic region of South Africa [*Information from South Africa Weather Services (SAWS)*]. The attenuation distributions are estimated from a 5-year locally observed rain rate data (2000-2004) in these four geographical locations. From these distributions, appropriate figures of fade margins are derived for various percentages of link availability on monthly and seasonal basis [*Odedina and Afullo*, 2009a].

6.2 Calculation of Rain Attenuation Statistics

A 5-year point rain rate data measured by the South African Weather Service (SAWS) in the year 2000-2004 in the four geographical locations (Durban, Cape Town, Pretoria, and Brandvlei) are utilized to compute the rain attenuation statistics. The rain data which was in one-hour integration time have been converted to the recommended 1-minute integration time in the previous works of *Fashuyi et al.*, [2006] and *Fashuyi* [2006] (see Section 3.8 and equation 3.38) . This is because longer integration times have been observed to hide the probable rain peaks, during which the highest outage take place. Therefore, outage probabilities and fade margins would be inaccurately determined if the 1-hour integration data are used [*Fashuyi*, 2006].

Equation (3.38) is then employed as the conversion factor to convert the 1-hour rain rate data to the recommended 1-minute integration time rain rate. The ITU-R rain attenuation model [*ITU-R 838-3, 2005; 530-12*, 2007], is adopted in this chapter to calculate the rain attenuation. This because of its computational simplicity for radio system designers; thus, ITU-R rain attenuation

model is used with the converted 1-minute integration time rain rate in the four geographical locations to calculate the rain attenuation statistics.

6.3 Seasonal Variation of Rain Attenuation Statistics

The seasonal cumulative distributions of rain attenuation are determined for the four geographical locations. As mentioned above, these four geographical locations are situated in different climatic region and different rain zones in South Africa. Durban, Cape Town, Pretoria and Brandvlei are located in the P, N, Q, and M climatic rain zones respectively [*Fashuyi et al.,* 2006*; Odedina and Afullo,* 2007]. For the estimation of these distributions, the five years locally observed rain rates which have been converted to rain rates of 1-minute integration time are used in conjunction with the ITU-R model at 20 GHz. South Africa which is located in the most southern tip of the Africa continent can be classified into four seasons and they are: summer (mid-October to mid-February), autumn (mid-February to April), winter (May to July) and spring (August to mid-October) [see Section 2.14.1].

The seasonal cumulative distributions give a good insight into the propagation characteristics in the four climatic rain zones. Figures 6-1 to 6-4 below show the seasonal attenuation distributions averaged over a period of five years for the four geographical locations. From these distributions, it is seen that the attenuation distributions in each of the geographical location are strongly influenced by the South African seasons. The summer and autumn seasons give the highest attenuation figures in each of the climatic region, except at the mediterranean region in which Cape Town is located that behaves otherwise. As explained in Section 2.14.1, South Africa records most of its highest rain rates in the summer and autumn season. Therefore, the attenuation distribution produced in the summer and autumn seasons reflect this high degree of the precipitation rate in these seasons.

Cape Town, because of its location and mediterranean nature of climate, has lower rain in the summer and autumn seasons, but records most of its high rain rates in the spring and winter seasons. Due to these climatic characteristics, the highest attenuation distributions occur during the spring and winter seasons as shown in Fig. 6-2. From this figure, the winter is seen to lie close to spring and overlaps at 3.76 dB/km. The lowest attenuation is recorded during summer season. Pretoria which has a temperate climate, also shows similar characteristics as that of Durban because of its high rain rates. From its attenuation distributions in Fig 6-3, it is observed that

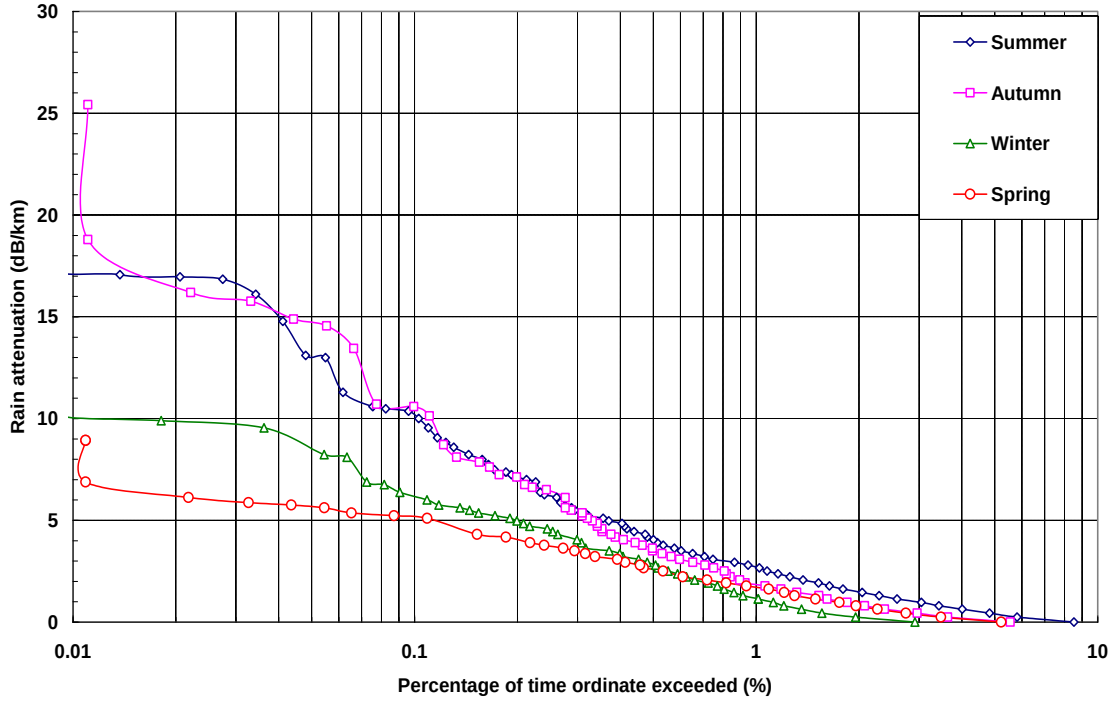

Fig. 6- 1: Seasonal distribution of rain attenuation of the average year in Durban

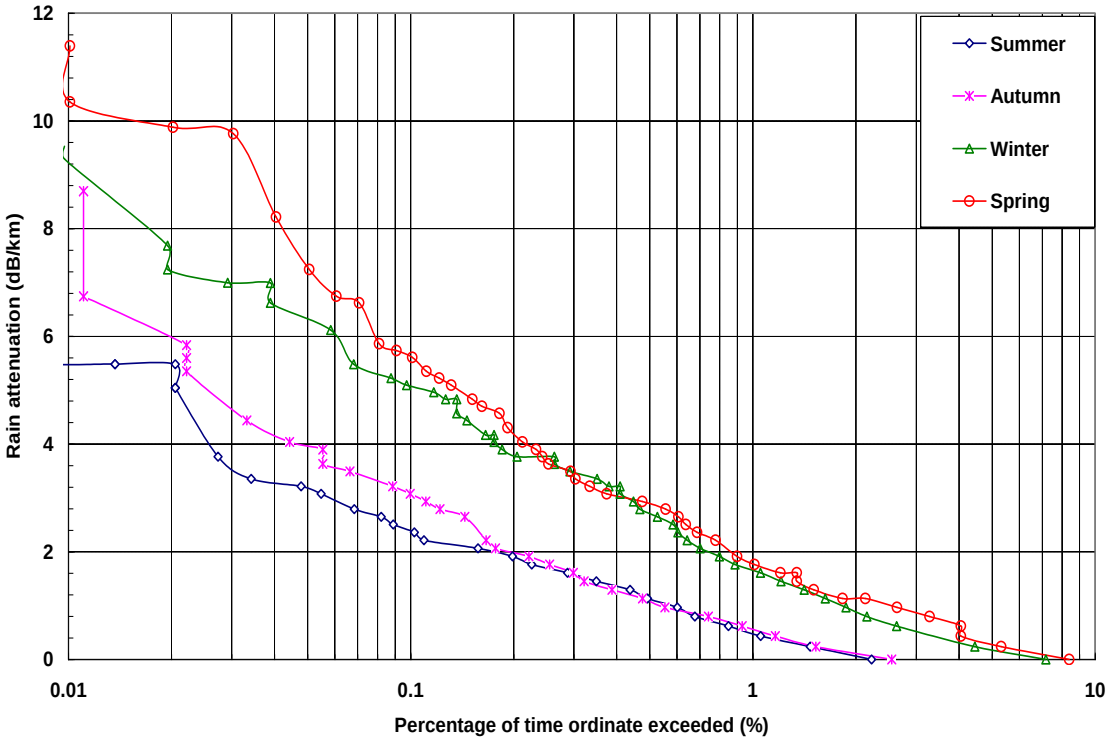

Fig. 6- 2: Seasonal distribution of rain attenuation of the average year in Cape Town

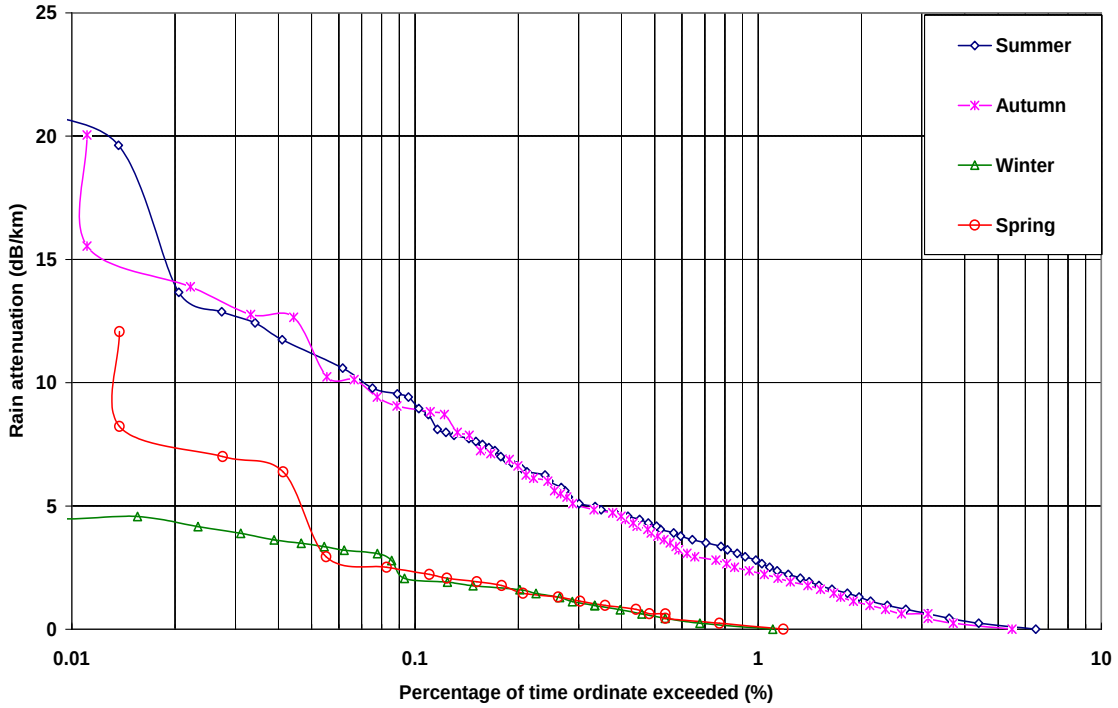

Fig. 6- 3: Seasonal distribution of rain attenuation of the average year in Pretoria

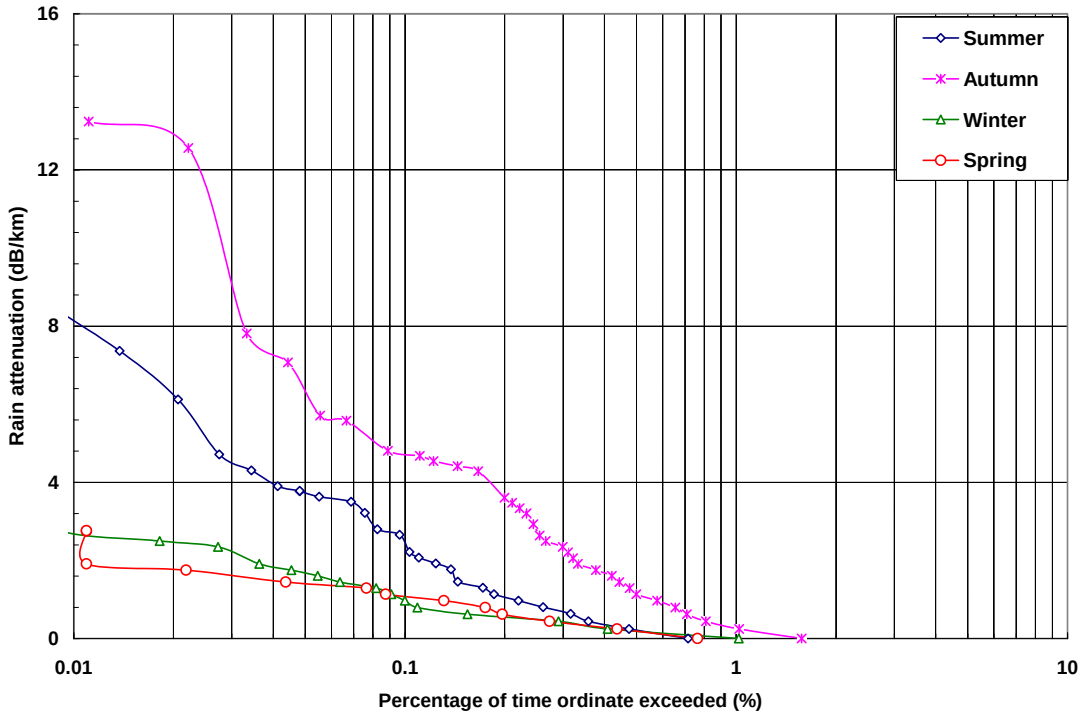

Fig. 6- 4: Seasonal distribution of rain attenuation of the average year in Brandvlei

Pretoria just divides the season into two; summer/autumn and the winter/spring. These distribution features are seen to overlap to a certain extent as the attenuation exceedance probabilities decrease. Brandvlei which is found in the desert, records its highest attenuation in the autumn season and the lowest in the winter and spring. At 1.28 dB/km, the spring tends to give the lower attenuation distribution than winter for the average year.

6.4 Seasonal Fade Margin and Link Availability

One of the major applications of cumulative distribution of rain attenuation is the derivation of fade margin figures at that percentage of time for which a certain attenuation level is exceeded [*Schnell et al.,* 2002]. These fade margin figures give the necessary allowance needed on a radio communication system to guarantee a reliable radio communication system. With this, the link availability and outage period on a radiocommmunication system can be estimated for an averaged year [*Schnell et al.,* 2002; *Odedina and Afullo,* 2009a].

From the attenuation distribution plots shown in Figures 6-1 to 6- 4 above, fade margin figures are determined at different percentage of time for the four geographical locations. Tables 6-1 – 6-4 below gives the required seasonal fade margin figures in dB at 20 GHz for a unit length radio link for the four geographical locations. The tables display the fade margins that can guarantee different levels of link availability for each season in each geographical location. The levels of the link availability, as shown in the tables (Table 6-1 – 6-4), are 99%, 99.5%, 99.9%, 99.95%, and 99.99%. The estimation of the outage period for an average year is shown in table 5-5 below. For example, for an availability of 99.99%, the outage time is 0.88 hour/year. This is simply calculated from the illustrations shown below:

One year has 8,760 hours or $8{,}760 \times 60$ *minutes.*

Considering a link availability of 99.99%:

The unavailability will be $1 - 0.999 = 0.0001$ *(outage); thus, outage (%) probability can be written as* ***1-availability.***

Then for 0.0001 outage (99.99% availability),

$\boldsymbol{0.0001 \times 8{,}760 \times 60}$ ***minutes = 52.56 minutes***

Table 6- 1: Required fade margin at 20 GHz for coastal climatic region: Durban

Availability (%)	99%	99.5%	99.9%	99.95%	99.99%
Fade margin in dB (Summer)	2.79	4.17	10.18	13.10	22.73
Fade margin in dB (Autumn)	1.92	3.62	10.12	14.54	22.10
Fade margin in dB (Winter)	1.30	2.14	6.38	8.88	11.04
Fade margin in dB (Spring)	1.77	2.65	5.23	5.74	8.93

Table 6- 2: Required fade margin at 20 GHz for mediterranean climatic region: Cape Town

Availability (%)	99%	99.5%	99.9%	99.95%	99.99%
Fade margin in dB (Summer)	0.52	1.13	2.43	3.13	5.54
Fade margin in dB (Autumn)	0.62	1.05	3.00	3.85	7.72
Fade margin in dB (Winter)	1.76	2.79	5.09	6.36	9.52
Fade margin in dB (Spring)	1.83	2.86	5.60	7.24	11.39

Table 6- 3: Required fade margin at 20 GHz for temperate climatic region: Pretoria

Availability (%)	99%	99.5%	99.9%	99.95%	99.99%
Fade margin in dB (Summer)	2.66	4.17	8.94	11.16	20.66
Fade margin in dB (Autumn)	2.22	3.77	8.82	10.24	17.79
Fade margin in dB (Winter)	0.15	0.61	2.06	3.48	6.08
Fade margin in dB (Spring)	0.24	0.63	2.51	6.37	12.07

Table 6- 4: Required fade margin at 20 GHz for desert climatic region: Brandvlei

Availability (%)	99%	99.5%	99.9%	99.95%	99.99%
Fade margin in dB (Summer)	0.09	0.24	2.43	3.78	8.21
Fade margin in dB (Autumn)	0.44	1.13	4.67	6.85	13.63
Fade margin in dB (Winter)	0.07	0.24	0.97	1.68	3.73
Fade margin in dB (Spring)	0.05	0.24	1.05	1.37	2.76

Table 6- 5: Relationship between system availability and outage period for an averaged year

Availability	99%	99.5%	99.9%	99.95%	99.99%
Outage/year	87.7 hours	43.8 hours	8.77 hours	4.38 hours	0.88 hours

From Table 6-5 above, it should be noted that the outage periods calculated for each level of the link availability does not necessarily imply a complete loss of signal, but the signal may be at a reduced quality [*Marcus and Pattan,* 2005]. The ITU-R [*530-12,* 2007] recommends the 0.01% exceedance attenuation value which gives the 99.99% availability on a radio link. Fig.6-5 below gives the fade margin at 20 GHz for 99.99% availability for the four locations. From Fig. 6-5, it is seen clearly that Durban which lies in the coastal region of South Africa needs a large fade margin of up to 23 dB in the summer or autumn season to guarantee 99.99% availability. Pretoria which lies in the temperate climate, also needs a large fade margin in these seasons (autumn and summer), but may not be as high as that of the coastal area. This is because the summer and the autumn seasons are predominantly characterized with high rain rates in South Africa.

Brandvlei which lies in the desert also needs a large fade margin for the 99.99% availability relative to the figures needed in the winter or spring season where there are lesser rains. It is obvious from this figure Cape Town is the only location that has a different variation pattern in that it requires required a large fade margin in the spring and the lowest in the summer season.

It should be noted that according to the South Africa seasonal weather and climate characteristics,

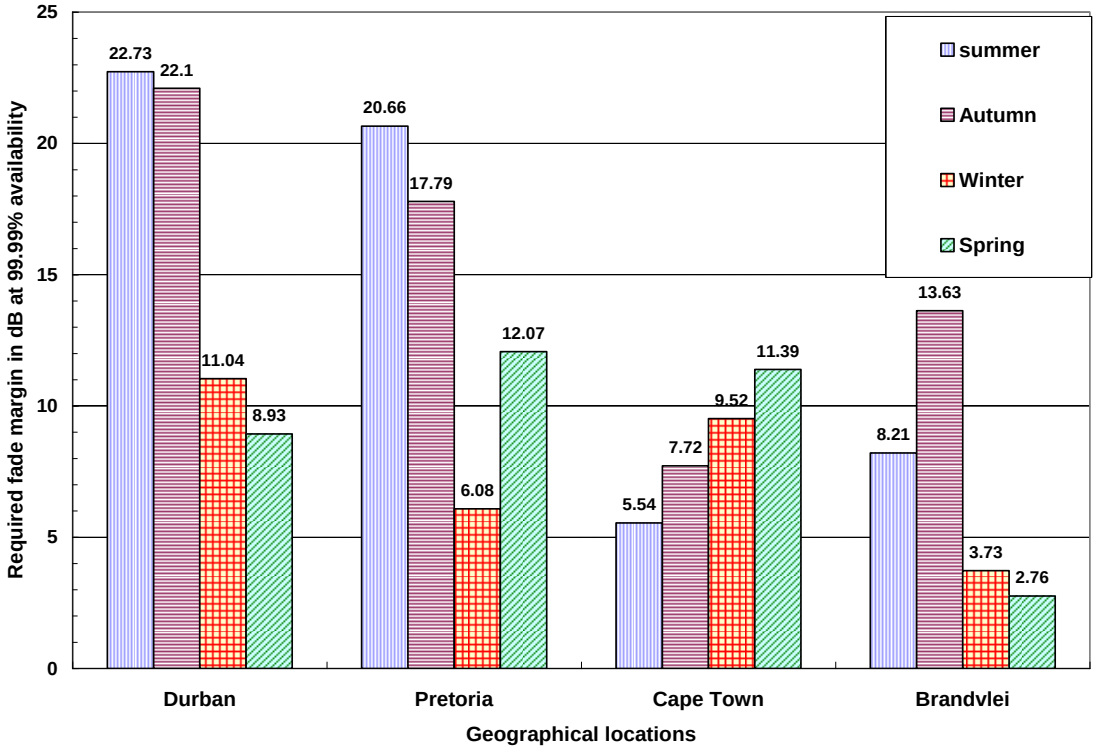

Fig. 6- 5: Required fade margin for 99.99% availability for the geographical locations

a high fade margin should be implemented in the summer seasons, and followed by the autumn seasons, because these are actually the rainy seasons, with lower fade margin in the spring and the lowest in the winter seasons, because these seasons have the lower rain rates. From the above figure (Fig. 6-5), Pretoria is the only geographical location that follows these characteristics. Durban needs the lowest fade margins in the spring and not in the winter, as does Brandvlei, which requires the highest fade margins in the autumn and not in the summer.

6.5 Monthly Variation of Rain Attenuation Statistics

The monthly variation of the rain attenuation statistics gives a detailed analysis of the attenuation distribution on a monthly basis. This provides a better insight into the characteristics and propagation patterns for each of the four locations. From this, a distinct and a better fade margin figures can be predicted. The monthly cumulative distributions of rain attenuation for each of the four geographical locations are determined, with each monthly distribution referring to the respective five months of the period 2000-2004. Furthermore, the cumulative distribution of rain attenuation for the averaged year is shown for the whole period 2000-2004.

Figures 6-6 to 6-9 below give the monthly and average variations of the cumulative distribution of rain attenuation for Durban, Cape Town, Pretoria, and Brandvlei from January to December for a period of 5 years. These distributions give a very good insight into the variational behaviour of the rain attenuation in each month for each location. It also gives the percentage of time for which a certain attenuation level is exceeded on monthly basis. These distributions show distinctively that each month has its own unique characteristics.

From these figures, Durban and Pretoria are seen to exact the highest attenuation distributions when compared with the other two locations. In Fig. 6-6, which shows the monthly distribution of Durban, the highest attenuation distribution occurs in the month of January up to an exceedance level of about 0.07%, after which the distribution of April supersedes. Also in Fig. 6-8, the highest attenuation distribution occurs in the month of February up to an exceedance level of about 0.065%, after which the distribution of October takes over. It should be noted here that the February and October are summer months, and April falls within the autumn season. Interestingly for Durban, the month of October gives the lowest attenuation distribution, with 3.75 dB/km, 3.48

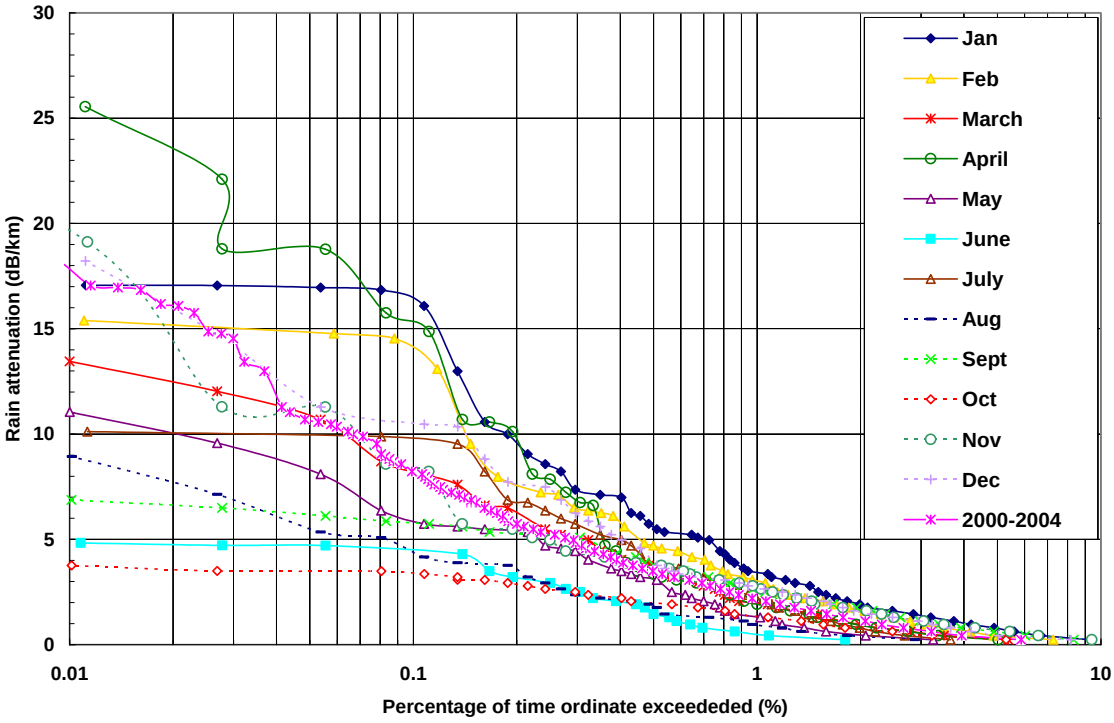

Fig. 6- 6: Monthly distribution of rain attenuation of the average year in Durban

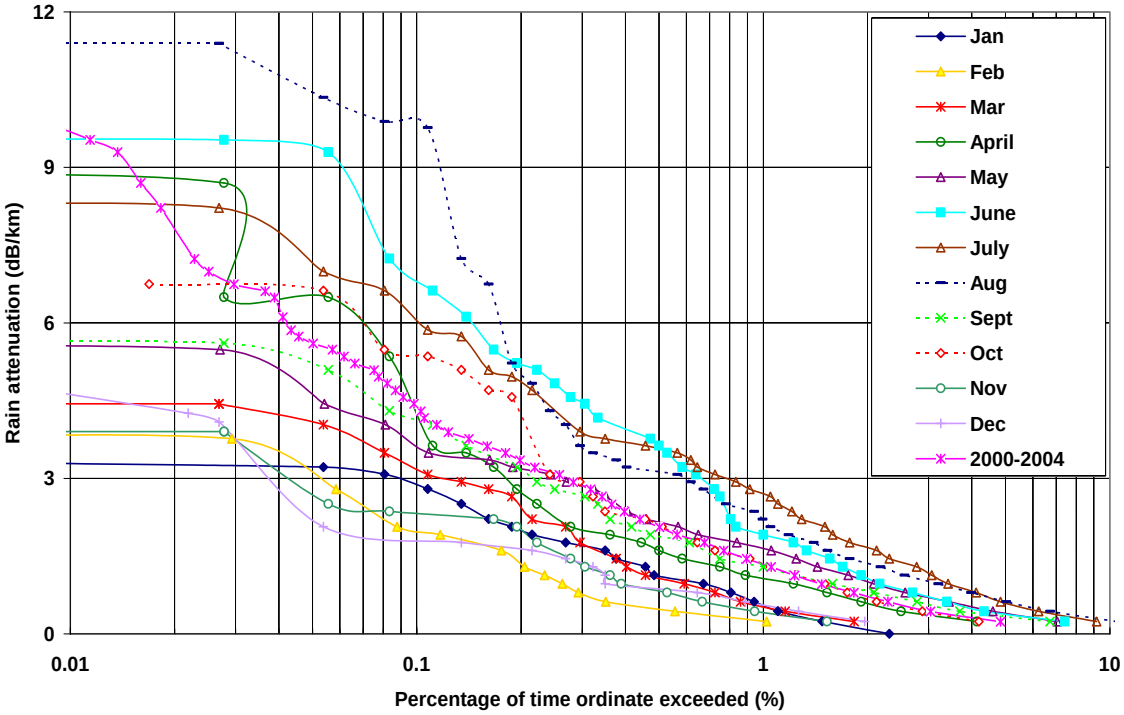

Fig. 6- 7: Monthly distribution of rain attenuation of the average year in Cape Town

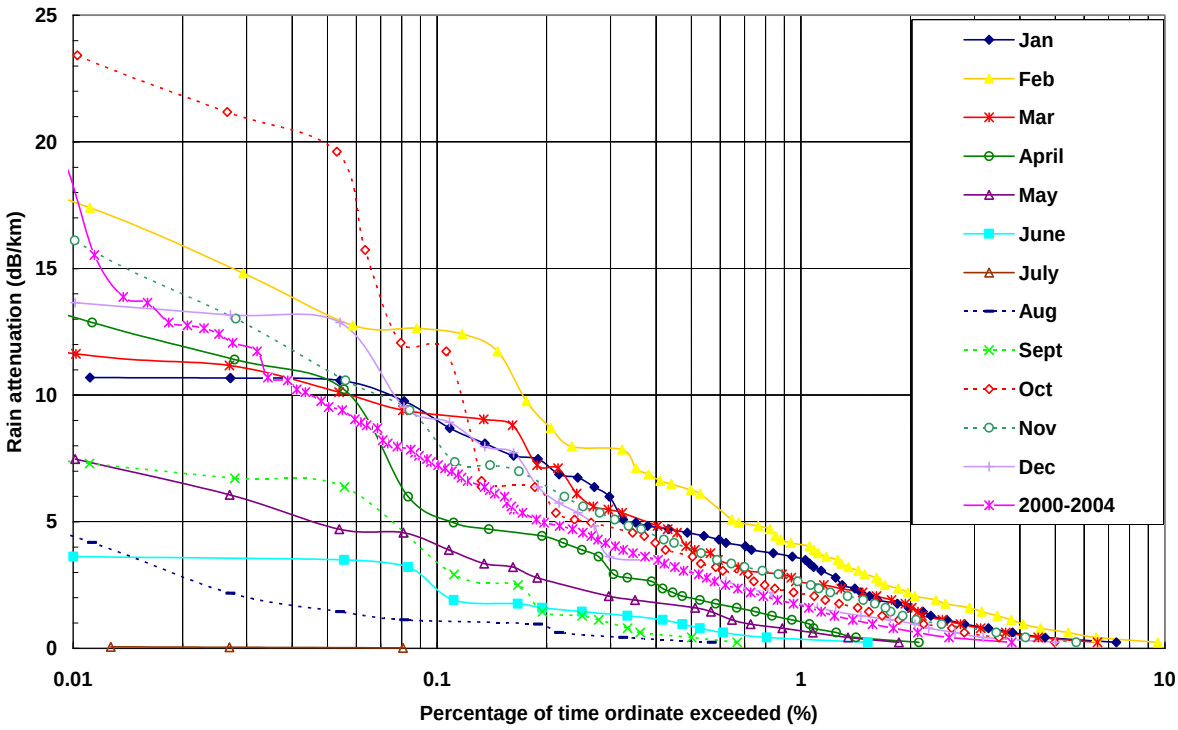

Fig. 6- 8: Monthly distribution of rain attenuation of the average year in Pretoria

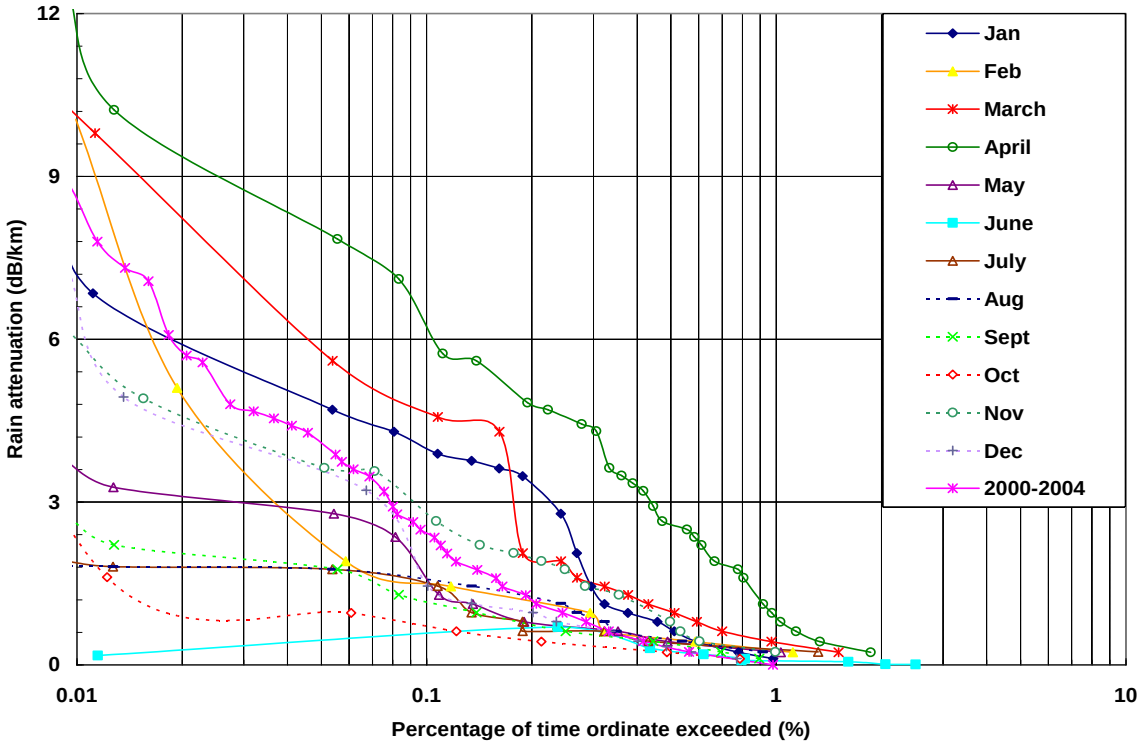

Fig. 6- 9: Monthly distribution of rain attenuation of the average year in Brandvlei

dB/km and 3.34 dB/km at 0.01%, 0.05% and 0.1% exceedance level respectively. The month of June in Durban is also seen to have a very low attenuation distribution. The distribution for the whole 5 year period, 2000-2004 is seen to average the whole distribution with attenuation of 17.05 dB/km at 0.01% attenuation exceedance level.

The Cape Town monthly distribution gives the lowest attenuation distribution when compared to that of Pretoria and Durban. The highest attenuation distribution starts in the month of July up to 0.52% attenuation exceedance level, after which the month of June takes over up to 0.19 % with an attenuation value of 5.22 dB/km. From this point, the month of August supersedes with attenuation values of 11.39 dB/km, 10.34 dB/km and 9.76 dB/km at 0.01%, 0.05% and 0.1% exceedance level respectively. January gives the lowest attenuation value of 3.35 dB at 0.01% exceedance level. November, December and February also give low attenuation values and they are seen to overlap each other at 0.02% exceedance level. The distribution for the whole 5 year period gives an attenuation of 9.54 dB at 0.01% exceedance level. In Brandvlei (Fig. 6-9) the highest attenuation distribution occurs in the month of April, without any overlaps with other monthly attenuation distributions in the location. Lowest attenuation occurs in June with the average year attenuation of 8.5 dB at 0.01%exceedance level.

6.6 Monthly Fade Margin and Link Availability

The applicability of the monthly rain attenuation cumulative distributions estimated for different percentages of time result to different values of fade margin figures for different percentages of link availability. Figures 6-10 to 6-13 below give the monthly required fade margin in dB for a unit length of radio link at 20 GHz to guarantee the various level of availability from 95% to 99.99% for an average of 5 years in each month.

From Fig. 6-10, the highest fade margin is required in April and the lowest in October to guarantee 99.99% availability. It should be noted that these two months are both characterized as rainy months in South Africa, hence high fade margins are expected to be implemented on the line-of-sight links. If the high fade margin figures implemented in the month of April is applied to the month October, this will just amount to over-estimating the link budget. This can result in a very costly over-design, because the link for that month does not really need it. This propagation effect can not be seen with the seasonal attenuation variation, because the distribution averages

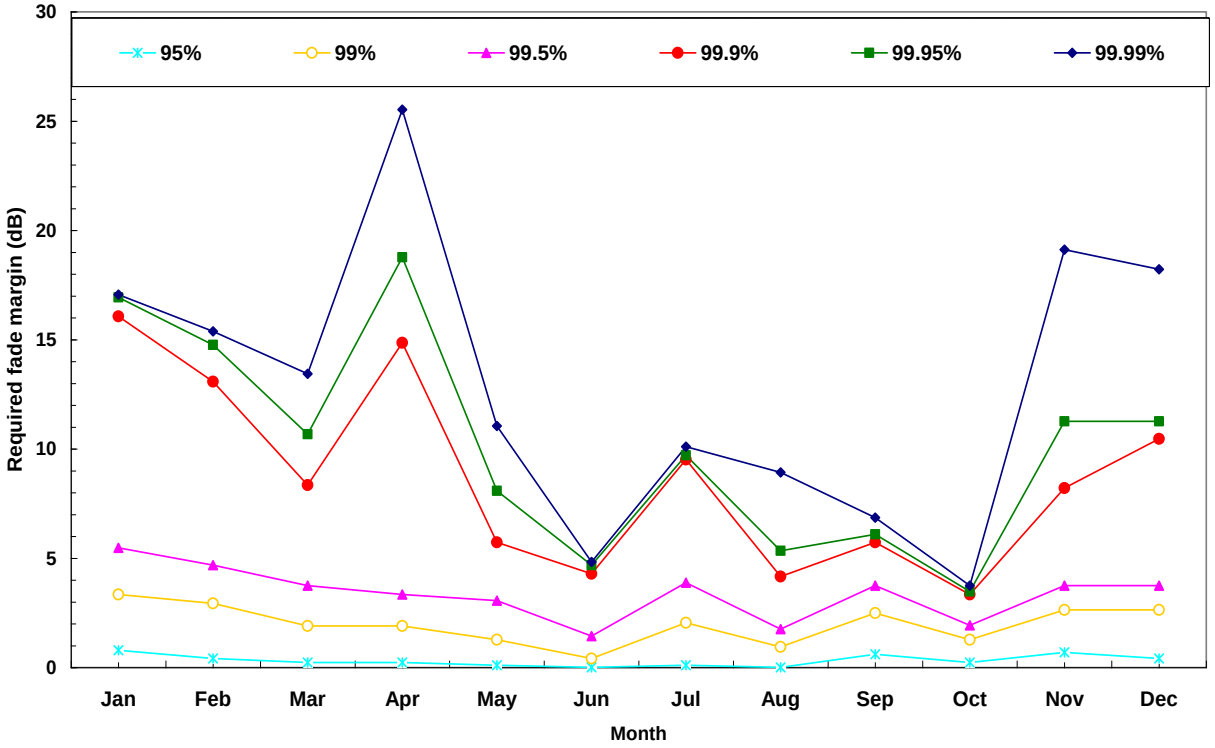

Fig. 6- 10: Fade margin in Durban at various level of availability as a function of month

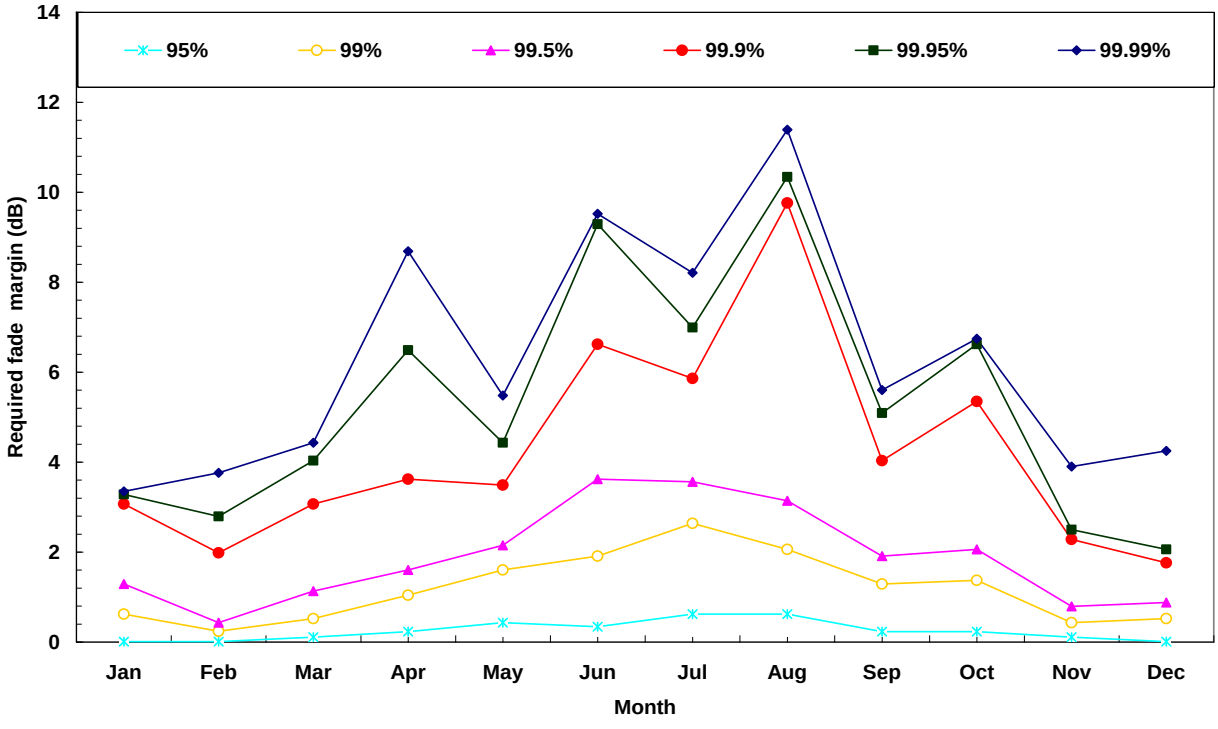

Fig. 6- 11: Fade margin in Cape Town at various level of availability as a function of month

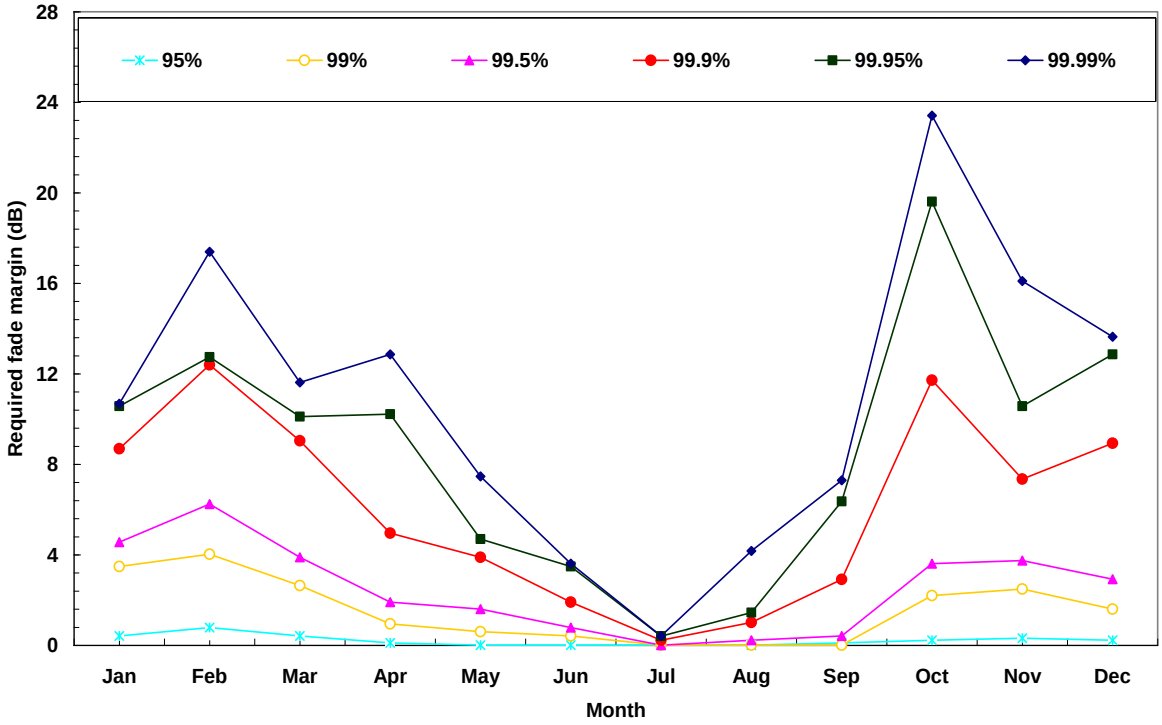

Fig. 6- 12: Fade margin in Pretoria at various level of availability as a function of month

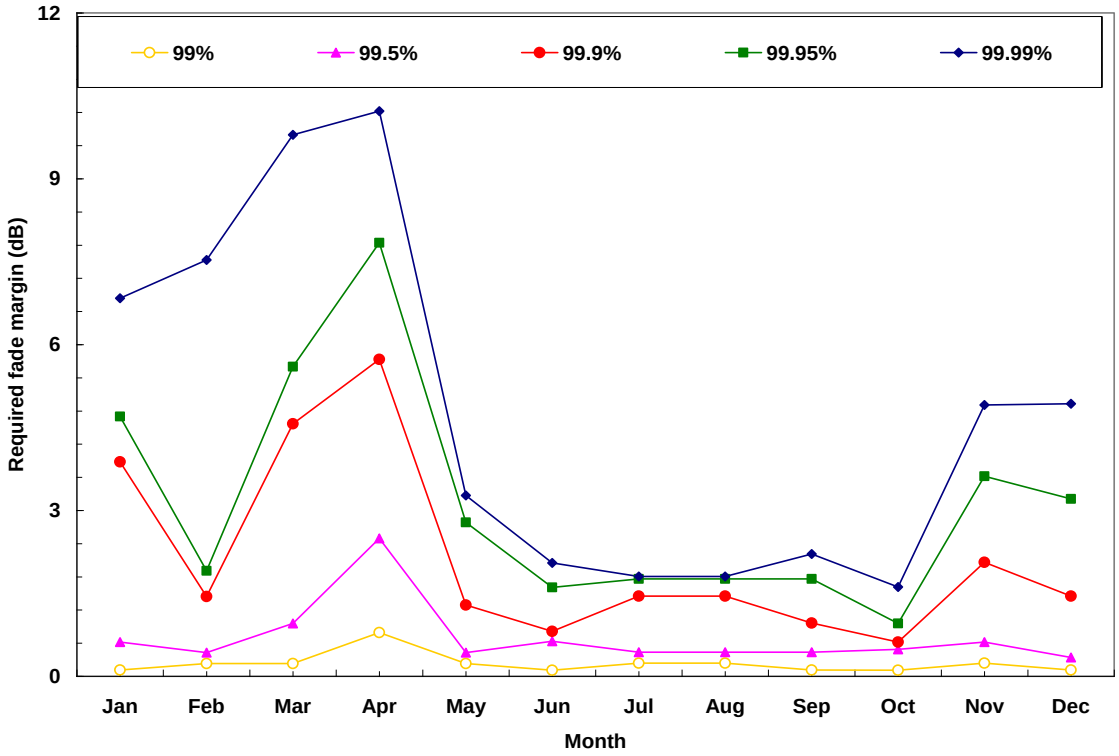

Fig. 6- 13: Fade margin in Brandvlei at various level of availability as a function of month

the fade margin for each season. In Fig. 6-11, it is observed that at the different levels of link availability, the highest fade margins are required for the months of August and June. The two months form part of the spring and winter seasons in South Africa, where lesser rains are expected in other geographical locations.

At higher link availabilities of 99.9%, 99.95% and 99.99%, a zigzag pattern of fade margin is observed. Fig. 6-12 records its highest fade margin figures in October for all the link availability percentages. Low fade margins are required between the months of June and August, but July requires the lowest fade margin at all the levels of link availability. In Brandvlei, the highest fade margin is needed in the month of April and the lowest in the month of October at the various levels of link availability. This propagation behaviour is similar to that of Durban, given that both months (April and October) fall within the autumn and the summer season. From the monthly analysis in Durban and Brandvlei, the month of October needs the lowest fade margin, compared to the other months in the season.

In conclusion, the monthly, seasonal, and the averaged year attenuation distributions give the values of fade margin that may be required on a radio link, depending on the type of service to be fulfilled. If a radio service requires link availability over an average year, the fade margin figures will definitely be different for services that require availability over an averaged month. The cumulative distribution of rain attenuation is indeed a valuable tool for system designers.

It should be noted here that, the noise impact of rain attenuation on terrestrial communication system has not been assessed in this chapter and it is not included in the seasonal or monthly fade margins presented in this work. Nevertheless, this impact is a significant factor in both terrestrial and satellite communication systems that employ directional antennas. Hence, a reasonable allowance may be introduced by a communication system designer to account for this effect.

6.7 Chapter Summary

This chapter has delved into the analysis and the characteristics associated with rain attenuation statistics in South Africa. This analysis has taken four geographical locations situated in different climatic rain zones in South Africa as a case study. For the estimation of these attenuation distributions, a 5-year point rain rate data collected in these geographical locations are used with the ITU-R model at 20 GHz. The analysis of the seasonal attenuation distribution in each of the

four geographical locations is observed to be linked to their climatic characteristics. High attenuation distributions are observed in the coastal (Durban) and the temperate (Pretoria) climates as well as the summer and the autumn seasons. This results in large fade margins for different levels of link availability. Cape Town is an exception to this pattern due to its mediterranean nature of climate and its location. Cape Town has most of its rains in the winter and spring seasons, which leads to higher fade margin figures in these seasons. Therefore, lower fade margins are required in the summer and autumn seasons in Cape Town.

In a more detailed analysis, the monthly attenuation distributions tend to highlight the propagation characteristics of each month distinctively without averaging them over the seasons. From these distributions, it is seen that some summer or autumn months may not require as large a fade margin as other months in the seasons (as shown in Durban and Brandvlei monthly distributions) because the rain rates recorded in these months over the five years period are relatively low. It is also observed that the average attenuation distributions over the entire five years in each of the four locations may not be adequate for fade margin design as it underestimates the peak months fade margin. Thus, this may not be able to accommodate the fades that may occur in months of high rain rates – hence it may not be appropriate for systems employed seasonally or monthly.

All in all, large fade margins may be implemented on a line-of-sight link when a high degree of availability is required in months of high rain rates, so as to achieve a satisfactory and a reliable service. However, relatively small fade margins may be required when availability needed to be guaranteed in months of low rains, so as to avoid costly over-design of communication systems.

Chapter Seven

Conclusion

7.1 Summary

The effect of rain on radio signals and the importance of an accurate prediction of rain attenuation models on terrestrial radio links cannot be overemphasized in radio communication studies. For these reasons, this study has employed a semi-empirical approach for the formulation of the rain attenuation prediction models. This approach has involved knowledge of the scattering properties of raindrops, raindrop size distributions, rain rates, and signal level measurements recorded at 19.5 GHz on a horizontally polarized terrestrial radio link. The impact of the rain attenuation statistics on terrestrial radio links has also been investigated.

Firstly, empirical rain attenuation models were predicted based on the signal level measurements from the 19.5 GHz horizontally polarized 6.73 km terrestrial radio link in Durban. The link was set up for a period of one year, and 1-minute rain rates recorded alongside with the signal level measurements. From the link, non-rain faded average signal levels for each month was determined and the time series for different features of rains (light, moderate, and heavy rains) and their received signal levels are also analysed. With the average non-rain faded signal level, the rain attenuation of the different features of rains are estimated and the monthly rain attenuation models depicting the month-to-month attenuation variability were estimated statistically.

The rain attenuation models depicting the measured upper and lower attenuation bounds for the average year along the 6.73 km line-of-sight link were predicted. These empirical rain attenuation models were compared with six different established rain attenuation models: The ITU-R model [*ITU-R 530,* 2007]; the global Crane [*Crane,* 1980: 1996]; the Moupfouma model [*Moupfouma,* 1984]; Garcia and Peiro model [*Garcia-Lopez and Peiro,* 1983]; the CETUC [*Perez Garcia and da Silva Mello,* 2004]; and new CETUC model [*da Silva Mello et al.,* 2007]. This comparison are analysed quantitatively by calculating the root mean square (rms) percentage error between these six different established rain attenuation models and the measured attenuation bounds.

From the rms percentage error analysis, it was seen that, the Garcia and Peiro model has the lowest rms percentage error for the minimum measured attenuation bound then followed by the ITU-R model. For the average measured attenuation bound, the CETUC models give the lowest rms percentage error, and then followed by the ITU-R model. For the maximum measured attenuation bound, the global Crane model [*Crane,* 1980; 1996] gives the lowest rms percentage error, and then followed by the ITU-R model. The ITU-R model has given the lowest rms percentage error when calculated for all the measured rain attenuation bounds. With these observations, the ITU-R model [*ITU-R 530,* 2007] can reasonably be adopted to predict the rain attenuation in Durban and its environs.

The theoretical rain attenuation models for different drop-size distribution models proposed in this study were based on the interaction between raindrop particles, and the propagating incident electromagnetic wave. The scattering amplitudes for 14 different raindrop sizes were calculated by using the Mie scattering theory for dielectric spheres with the assumption that the shape of the raindrop is spherical. The extinction cross-section of the spherical raindrops were calculated from the forward scattering amplitudes, and modeled with a power-law relationship. The power law model from the extinction cross-section was integrated mathematically over different established drop-size distributions to propose different rain attenuation models for specific attenuation and path attenuation estimations on terrestrial radio links.

These models were used to compute the specific rain attenuation for four locations situated in different climatic rain zones in South Africa. To validate these theoretical models, they were compared with the experimental signal level measurement recorded in Durban. For the purpose of cross referencing, they were also compared with the ITU-R rain attenuation model. The results showed that the theoretical attenuation model developed from the negative exponential drop-size

distribution of Joss et al. thunderstorm rain type [*Joss et al.* 1968] , lognormal drop-size distribution of Adimula-Ajayi tropical thunderstorm rains, and tropical shower rains [*Adimula and Ajayi,* 1996] gave the best fits for the minimum, average and maximum measured attenuation, respectively with the use of the chi-square statistic. The attenuation values predicted by the average theoretical attenuation model were also compared with the attenuation values predicted from the *Moupfouma* [1997] theoretical model.

It was observed that the Moupfouma theoretical attenuation model developed from oblate spheroidal raindrops [*Moupfouma,* 1997] and the predicted theoretical average attenuation model formulated from spherical raindrops reasonably describe the measured average attenuation. It was also observed that both models predicted almost the same rain attenuation values, despite the differences in the formulation of each theoretical model. Thus, it can be stated that, whether rain attenuation is modeled with a spherical or an oblate spheroidal drop, the same rain attenuation might be expected along a terrestrial link if the approach employed in this work is used; though the results may be influenced by the drop-size distribution used in the calculation of the path attenuation. Thus, the major parameter that needs to be known if this approach is to be applied to various geographical locations around the world for the estimation of rain attenuation is to know the raindrop size distribution governing the location. Since the attenuation models proposed in this work have been formulated from different raindrop-size distributions, these proposed models can be used directly to determine the attenuation caused by rain.

In this regard, preliminary raindrop size distributions for different rain types based on measurements carried out in Durban have been estimated. These distributions are estimated for the different rain types by measuring the percentage error between the distributions and the raindrop size measurement. From the error analysis, negative exponential distribution gives the highest percentage of error for all the rain types, lognormal drop-size gives the lowest percentage error for drizzle, widespread, and shower rain types, and gamma drop-size distribution gives the lowest percentage error for thunderstorm rains. Therefore, with this analysis the lognormal drop-size distribution can be employed to predict the drizzle, widespread, and shower rain types, while the gamma drop-size distribution is better suited for the thunderstorm rain types.

As a result of the rapidly varying nature of rain, the characteristics and the variations associated with rain attenuation statistics in South Africa were analyzed. This analysis took four geographical locations situated in four different climatic rain zones in South Africa as case

studies. The analysis employed the ITU-R rain attenuation model on a 5-year rain rate data obtained from the four geographical locations to estimate the cumulative distributions of the rain attenuation. These attenuation distributions are estimated on a monthly, seasonal, and an average year basis. From these distributions, fade margin values are derived for various percentages of link availability. The fade margins give the necessary allowance needed on a terrestrial link to accommodate any impairment that may occur due to rain, and also estimate the outage probability of a radio link.

The analysis of the seasonal attenuation distributions in each of the four geographical locations are observed to be linked to their climatic characteristics. High attenuation distributions were observed in the coastal (Durban) and the temperate (Pretoria) climates as well as the summer and the autumn seasons. This resulted in large fade margins for different level of link availability. Cape Town is an exception to this pattern due to its mediterranean nature of climate and its location. The monthly attenuation distributions tend to highlight the propagation characteristics of each month distinctively without averaging them over the seasons. From these distributions, it is seen that some summer or autumn months may not require a large fade margins as other months in the seasons (as shown in Durban and Brandvlei monthly distributions). It is also observed that the average attenuation distributions over the entire 5 years in each of the four locations may not be adequate for fade margin design as it underestimates the peak month's fade margin. Thus, this may not be able to accommodate the fades that may occur in months of high rain rates.

7.2 Suggestion for Future Work

- As it has been stated in this study, propagation measurements such as signal level measurements for radio links at different frequencies, raindrop-size measurements, and lower integration time rain rates (e.g. 1-minute rain rates or less) are highly needed for accurate propagation prediction and rain attenuation modeling. With this, it a longer measurement campaign is highly recommended that longer period in South Africa (not Durban alone). This will in turn give a better precision and accuracy to the rain attenuation prediction models and ascertain its applicability to tropical and sub-tropical climates around the world.

- *Joss and Gori* [1978] stated that *"drop size distribution tends to be exponential when the sampling time is sufficiently long".* The monthly probability density function (pdf) of the drop-size measurements shown in Chapter five (Fig. 5-14), which exhibits a negative exponential distribution can be said to be a long-term measurement. This long-term distributions have been described to be inadequate for short-term or event-by-event precipitation assessments which are needed for modeling of a reliable radio communication link [*Fang and Chen*, 1982]. For this reason, it is suggested that the raindrop size distribution may need to be modeled for each of the rain events or for a very short occurrence of rainy period. With this, suitable drop-size distribution models may be estimated for the drop-size spectra in a rainy event. It should be noted that the rain event can exhibit a drizzle, a tropical widespread, a tropical shower, or a tropical thunderstorm rain type.

- As a result of the non-uniformity of rain rate distribution along radio propagation path, the concept of effective path length or an equivalent rain cell has been very useful in overcoming this problem. Though in this work, empirical parameters stated by the ITU-R were employed, it is recommended that an effective path length factor should be determined for the distribution of rain rate along terrestrial radio links. This is to improve the prediction of rain attenuation along radio links.

- Further studies need to be carried out on the scattering properties of raindrops, as a spherical or an oblate spheroidal drop. It is recommended that the scattering properties should be calculated for higher frequencies and the extinction cross-section power law models extended for these frequencies.

- In Chapter six, seasons and months of high rain rates require large fade margins to accommodate the rain impairments during these periods. For instance, Durban requires 23 dB fade margins during these periods. This margin will be uneconomical and unrealistically large to be implemented all through the year to accommodate this effect. In order to decrease the fade margins, it is recommended that some adaptive fade mitigation techniques such as adaptive data rate switching, adaptive modulation or adaptive coding should be implemented on the link. These techniques enable the reduction of the required fade margins to manageable values.

- The outage probability of a radio link for an average year at different percentages of time has been calculated in Chapter six. For example a link availability of 99.9% indicates a loss of service of about 8.77 hours for an average year. However, this outage period does not show how long and how often the service is expected to be interrupted. For instance a link could be interrupted about 50 times a year for 10 consecutive minutes; this situation may not be acceptable for service providers and even the consumers. With this effect, it is recommended that the fade (outage) durations of the link either for an average year, season, or months needed to be known.

References

Adimula, I. A., and G. O. Ajayi (1996), Variation in raindrop size distribution and specific attenuation due to rain in Nigeria, *Ann. of Telecomms., 51*(1-2), 87 – 93.

Afullo, T. J., and P. K. Odedina (2006), On the k-factor distribution and diffraction fading for Southern Africa, *SAIEE Res. J., 97*(2), 172 – 181

Ajayi, G. O., and E. B. C. Ofoche (1983), Some tropical rainfall rate characteristics at Ile-Ife for microwave and millimeter Wave Application, *J. Climate and Appl. Meteor., 23*(4), 562 – 567

Ajayi, G. O., and R. L. Olsen (1985), Modeling of a tropical raindrop size distribution for microwave and millimeter wave applications, *Radio Sci. J., 20*(20), 193 –202.

Ajayi, G. O., and S. U. B.Ezekpo (1988), Development of climatic maps of rainfall rate and attenuation for microwave application in Nigeria, *The Nigerian Engineer 23*(4), 13 – 30

Ajayi, G. O. (1989), Physics of the Tropospheric Radiopropagation, *Internal Rep. IC/89/23*, Int. Centre for Theo. Phy., Trieste, Italy, Feb.

Ajayi, G. O. (1990), Some aspects of tropical rainfall and their effect on microwave propagation, *Int. J. Sat. Commun., 8*, 163 – 172.

Ajayi, G. O., S. Feng, S. M. Radicella, and B. M. Reddy (Eds.) (1996), *Handbook on Radiopropagation Related to Satellite Communications in Tropical and Subtropical C*ountries, pp. 2–14, ICTP Press, Trieste

Ajewole, M. O. (1997), Scattering and attenuation of centimeter and millimeter radio signals by tropical rainfall, Ph.D Thesis, Dept. of Physics, Fed. Uni. of Tech., Akure, Nigeria, Sept

Ajewole, M. O., L. B. Kolawole, and G. O. Ajayi (1999a), Theoretical study of the effect of different types of tropical rainfall on microwave and millimeter-wave propagation, *Radio Sci. J., 34*(5), 1103 – 1124

Ajewole, M. O., L. B. Kolawole, and G. O. Ajayi (1999b), Cross polarization on line-of-sight links in tropical location: effects of variation of canting angle and rain dropsize distributions, *IEEE Trans. Antennas Propag. 47*(8), 1254 – 1259

Al-Nuaimi, M. O., and R. B. L. Stephens (1998), Measurements and prediction model optimization for signal attenuation in vegetation media at centimeter frequencies, *IEE Proc., Microwave Antennas Propag., 145*(6), 201 – 206

Altshuler, E. E. (1984), A simple expression for estimating attenuation by fog at millimeter wavelengths, *IEEE Trans. Antennas Propag. 32*(7), 757– 758

Asen, W., and T. Tjelta (2003), A novel method for predicting site dependent specific attenuation rain attenuation of millimeter radio waves, *IEEE Trans. Commun., 51*(10), 2987 – 2999

Assis, M. S. (1992), Rain attenuation in terrestrial paths, *ISRP 92, Sapporo,* Japan

Assis, M. S., and M. H. C. Dias (1998), Modified ITU-R rain attenuation model for low latitude areas, In *Proceedings of URSI Commission F Open Symposium on Climatic Parameters in Radiowave Propagation Prediction, CLIMPARA '98*, pp. 137 – 139, Ottawa, Canada

Atlas, D., C. W. Ulbrich, F. D. Marks Jr., E. Amitai, and C. R. Williams (1999), Systematic variation of drop size and radar-rainfall relations, *J. Geophys. Research Atmos., 104*(), 6155 –6169

Awang, M. A., and J. Din (2004), Comparison of the rain drop size distribution model in tropical region, *In Proc. RF and Microwave Conf.*, pp. 20 – 22, Selangor, Malaysia

Barclay, P. A. (1975), Raindrop-size distributions in Melbourne area, *Institute of Engineering*, Armidale, New South Wales, Australia.

Barclay, P. A., J. A. Bennett, and R. C. Boston (1978), Properties of rain for microwave propagation studies, *Rep. MEE 78-1,* pp.35 – 68, Electr. Eng. Dep., Monash Univ., Melbourne

Battan, L. J. (1973), *Radar Observation of the Atmosphere*, Uni. Chicago Press, Chicago, Illinois

Beard, K. V., and C. Chuang, (1987), A new model for the equilibrium shape of raindrops. *J. Atmos. Sci*., 44, 1509 – 1524

Bennarroch, A., P. Garcia del Pino, V. Kvicera (2002), Comparison of rain rate statistics measured in Spain and Prague, *Cost Action 280 on Propagation Impairment Mitigation for Millimeter Wave Radio Systems, Doc. PM3003S*, 1st International Workshop , July

Bohren, C. F., and D. R. Huffman (2004), *Absorption and Scattering of Light by Small Particles*, Wiley-VCH press, Weinheim

Burrows, C. R. (1966), Ultra-short-wave propagation in the jungle, *IEEE Trans. Antennas Propag. 14*(5), 386 – 388

Bradley, S. G., and C. D. Stow (1974), The measurement of charge and size of raindrops: part II. results and analysis at ground level, *J.Appl. Meteor,* 13(1), 131 – 147

Brasseur, G. P., J. J. Orlondo, and G.S Tyndall (1999), *Atmospheric Chemistry and Global Change,* Oxford University Press, New York

CCIR (1982), Volume V: Propagation in non-ionized media, *Rep. 338-4: Propagation data required for line-of-sight radio relay systems*, ITU, Geneva, Switzerland

CCIR (1986), Influence of terrain irregularities and vegetation on troposphere propagation, pp. 235 – 236, *CCIR 236-2 Rep.,* Geneva, Switzerland

Cermak, D., O. Fiser, and V. Schejbal (2005), Electromagnetic scattering by rain drops, *Cost 280, PM-9-109*, Czech Republic, June

Cerro, C., B. Codina, J. Bech, and J. Lorente (1997), Modeling raindrop size distribution and Z(R) relations in the western mediterranean area, *J. Appl. Meteor., 36*(11),1470 – 1479

Crane, R. K. (1971), Propagation phenomena affecting satellite communication systems, operating in the centimeter and millimeter wavelength bands, *Proc. IEEE, 59*(2), 173 – 188

Crane, R. K. (1974), The rain range experiment-propagation through a simulated rain environment, *IEEE Trans. Antennas and Propag. 22*(2), 321–328

Crane, R. K. (1977), Prediction of the effects of rain on satellite communication systems, *Proc. IEEE, 65*(3), 456 – 474

Crane, R. K. (1980), Prediction of attenuation by rain, *IEEE Trans. Commun., 28*(9), 1717 – 1733

Crane, R. K., and H-C Shieh (1989), A two-component ran attenuation model for prediction of site diversity improvement performance, *Radio Sci ., 24*(6), 641 – 655

Crane, R. K. (1996), *Electromagnetic Wave Propagation Through Rain,* John Wiley, New York.

Crane, R. K. (2003), *Propagation Handbook for Wireless Communication System Design*, CRC Press, New York.

COST 235 (1996), Radio propagation effects on next generation fixed service terrestrial telecommunication systems, *Final Rep.*, Luxembourg.

COST 255 (2002), Radiowave propagation modelling for SatCom services at Ku-band and above, *Final Rep., SP-1252,* ESA Publications Division, Noordwijk, Netherlands, March

COST 280 (2005), Propagation impairment mitigation for millimetre wave radio systems, *Final Worksop Rep*. *PM-9-109*, Prague, June

Cox, A. J., A. J. DeWeerd, and J. Linden (2002), An experiment to measure Mie and Rayleigh total scattering cross sections, *Am. J. Phys. 70*(6), 620 – 625

da Costa, A. T., and M. S. Assis (2002), The concept of path length factor in the prediction of rain attenuation in terrestrial links, *in Proceedings of XXVIIth General Assembly of URSI*, Maastricht, Netherlands

da Silva Mello, L. A. R., M. S. Pontes and, R. S. L. de Souza (2007), New method for prediction of rain attenuation in terrestrial links using concept of effective rainfall rate, *In Proc. Microwave Opt. Conf.*, pp. 899 – 901, Brazil

de Miranda, E. C., M.S. Pontes and L.A.R. da silva Mello (1998a), Rainfall induced satellite beacon attenuation on three 12 GHz links in equatorial and tropical Brazil, *IEEE Int. Sym. Antennas, Propag. Digest, 4*, 1892 – 1895

de Miranda, E. C., M. S. Pontes, and L.A.R. da silva Mello (1998b), Statistical modelling of the cumulative probability distribution function of rainfall rate in Brazil, *Proceedings of URSI Commission F Open Symposium on Climatic Parameters in Radiowave Propag. Prediction*, Ottawa, Canada, pp.77 – 80, April

de Wolf, D. A. (2001), On the Laws-Parsons distribution of raindrop sizes, *Radio Sci. J.,36*(4), 639 – 642

Diermendjian, D. (1969), *Electromagnetic Scattering on Spherical Polydispersions*, American Elsevier Publisher & Co. New York

Downie, N. M., and R. W. Heath (1965), *Basic Statistical Methods*, 2nd ed., Harper and Row, New York.

Dutton, E. J. (1979), Precipitation variability in the USA for microwave terrestrial system design, *Office of Telecommun, (OT) Rep. 77-134*, Dept. of Commerce, Boulder, CO

Fang, D. J., and C. H Chen (1982), Propagation of centimeter/millimeter waves along a slant path through precipitation, *Radio Sci ., 17*(5), 989 – 1005

Fashuyi, M. O. (2006), A Study of Rain Attenuation on Terrestrial Paths at Millimetric Wavelengths in South Africa, MSc thesis, School of Electrical, Electronic and Computer Engineering, Uni. of KwaZulu-Natal, S. Africa, Feb.

Fashuyi, M. O., P. A. Owolawi, and T. J. O. Afullo (2006), Rainfall rate modelling for LOS radio systems in South Africa, *SAIEE Res. J.*, *97*(1), 74–81.

Fashuyi, M. O., and T.J. Afullo (2007), Modeling of attenuation due to rain at 19.5 GHz for line-of sight radio systems in South Africa*" in Proceedings of the North American Radio Science Meeting, URSI 2007,* Ottawa, ON, Canada.

Fashuyi, M. O., and T.J Afullo (2007), Rain attenuation prediction and modeling for line-of-sight Links on terrestrial paths in South Africa, *Radio Sci., 42,* RS5006, doi: 10.1029/2007RS003618.

Fedi, F. (1979), Attenuation due to rain on terrestrial paths, *Alta Frequenza, 66,* 167 – 184

Feingold, G., and Z. Levin (1985), The lognormal fit to raindrop spectra from frontal convective clouds in Israel, *J. Climate Appl. Meteor.*, *25*(10), 1346 – 1363

Flavin, R. K. (1980), Earth-Space path rain margins above 10 GHz in Australia, *Rep. 7358* Telecom Australia Res. Lab.

Flavin, R. K. (1981), Rain attenuation considerations for satellite paths, *Rep. 7505* Telecom Australia Res. Lab.

Flavin, R. K. (1982), Rain attenuation considerations for satellite paths in Australia, *Australian Telelecommu Res., 16,* 11 –24

Flavin, R. K. (1996), Satellite link rain attenuation in Brisbane and a proposed new model for Australia, *Rep. no. 8375,* Telstra Res. Lab.

Freeman R. L. (1997), Radio *System Design for Telecommunications*, 2nd Edition, John Wiley & Sons Inc.

Freedman, D., R. Pisani, and R. Purves (1978), *Statistics*, W.W. Norton & Company, New York

Forknall, N., R. Cole, and D. webb (2008), Cumulative fading and rainfall distribution for a 2.1 km, 38 GHz, vertically polarized, line-of-sight link, *IEEE Trans. Antennas Propag. 56*(4), 1085–1093

Garcia-Lopez, J. A., J. Peiro (1983), Simple rain-attenuation-prediction technique for terrestrial radio links, *Electron Lett., 19*(21), 879 – 880

Garcia-Lopez, J. A., J. M. Hernando, and J. M. Selga (1988), Simple rain-attenuation-prediction technique for satellite radio links, , *IEEE Trans. Antennas Propag. 36*(3), 444 – 448

Goldhrish, J., and W. J. Vogel (1998), Handbook of propagation effects for vehicular and personal mobile satellite systems, *Rep. A2A-98-U-0-021*, Applied Phy. Lab., John Hopkins Uni., Laurel, M.D

Green, H.E. (2004), Propagation impairment on Ka-band SATCOM links in tropical and equatorial regions, *IEEE Antennas Propag. Mag. 46*(2), 31 – 44.

Govindarajan, P. (1987), Rain attenuation measurements in India, *CCIR IWP 5/3 Doc. 87/18*, Sept.

Gunn, R. and G. D. Kinzer (1949), The terminal velocity of fall for water droplets in stagnant air, *J. Meteor, 6* (4), 243 – 248

Hall, M. (1981), Dual polarization radar helps gauge rainfall rate, *Microwaves, 20*(9), 93 – 101

Hall, M. P. H., L. W. Barclay, and M.T. Hewitt (1996), *Propagation of Radiowaves*, IEE Press, London

Harden, B. N., J. R. Norbury, and W. J. K. White (1978), Use of lognormal distribution of raindrop sizes in millimetric radio attenuation studies, *in Proceedings of the Int. Conf. Antennas propag*, IEE, Part 2, pp. 87 – 91 London, England, 28-30 November.

Hogg, D. C. (1968), Millimeter-wave communication through the atmosphere, *Am. Ass. for the advancement of Sci., 159*(3810), 39 – 46

Holt, A. R., N. K. Uzunoglu, and B. G. Evans (1978), An integral solution to the scattering of electromagnetic radiation by dielectric spheroids and ellipsoids, *IEEE Trans. on Antennas Propag, 26*(5), 706–712

Houze, R. A. Jr. (1993), *Cloud dynamics*. Academic Press

Houze, R. A. Jr. (1997), Stratiform precipitation in regions of convection: A meteorological Paradox? *Bulletin of the Amer. Meteor. Soc. 78*(10), 2179 – 2196.

Ihara, T., Y. Furuhama, and T. Manabe (1984), Interference of raindrop size distribution from rain attenuation statistics at 12, 35, and 82 GHz, *Trans. IECE, E67,* 211 – 217, Japan.

ITU-R (1999), Propagation data required for the design of broadcasting-satellite systems, *Recommend. 679-2, ITU-R P Ser.,* Int. Telecommun. Union, Geneva

ITU-R (2003), The radio refractive index: Its formula and refractivity data, *Recommend. 453-7, 11, ITU-R P Ser.,* Int. Telecommun. Union, Geneva

ITU-R (2003), Characteristics of Precipitation for Propagation modelling, *Recommend. 837-1, 2, 3, 4, ITU-R P Ser.,* Int. Telecommun. Union, Geneva.

ITU-R (2005), Specific rain attenuation model for use in prediction models, *Recommend. 838-3 ITU-R P Ser.,* Int. Telecommun. Union, Geneva.

ITU-R (2007), Propagation data and prediction methods required for the design of terrestrial line-of-sight systems, *Recommend. 530-12 ITU-R P Ser.,* Int. Telecommun. Union, Geneva.

ITU-R (2007), Characteristics of Precipitation for Propagation modelling, *Revision of Recommend. 837-4, Doc. 3/111(Rev.1)-E, ITU-R P Ser.,* May.

Jassal, B. S., G. Gupta, A. K. Verma, M. P. Singh, and L. Singh (1994), 20/30 GHz radiometric

propagation measurements in India, *IEEE Int. Sym. Antennas Propag. Digest*, *2*, 1340 – 1343, Seattle , USA

Jiang, H., M. Sano, and M. Sekine (1997), Weibull raindrop-size distribution and its application to rain attenuation, *IEE Proc. Microwave, Antennas Propag. 144* (3), 197 – 200

Joss, J., J. C. Thams, and A. Waldvogel (1968), The variation of raindrop size distribution at Locarno, in *Proc. Int. Conf. Cloud Physics*, pp. 369 – 373, Toronto, Canada,

Joss, J., and E. G. Gori (1978), Shapes of raindrop size distributions, *J.Appl. Meteor.*, *17*(7), 1054 –1061

Juy, M., R. Maurel, M. Rooryck, I. A. Nugroho, and T.Hariman (1990), Rain Rate Measurements In Indonesia, *Electron Lett.*, *26*(9), 596 – 598

Kerr, D. E. (1951), *Propagation of Short Radio Waves,* MIT Radiation laboratories Series, McGraw-Hill Book Company, inc.

Konwar, M., D. K. Sarma, J. Das, and S. Sharma (2006), Shape of the raindrop size distributions and classification of rain type at Gadanki, *Indian J. Radio and Space phys.*, *35*, 360 – 367.

Kvicera, V., M. Grabner, M. Hlavaty (2003), Results of statistical processing of rain intensities in Prague from period 1992-2002, *Cost Action 280 on Propagation Impairment Mitigation for Millimeter Wave Radio Systems , MC#5 Meeting and Joint Workshop with Cost 272,* ESTEC, May

Kvicera, V., M. Grabner (2006), Rain attenuation at 58 GHz: prediction versus long-term trial results, *EURASIP J. Wireless Commun. Networking, 2007*, doi:10.1155/2007/46083

Laws, J. O., and D. A. Parsons (1943), The relationship of raindrop-size to intensity, *Am. Geophys. Union Trans. 24*, 452-460

Levin, Z. (1971), Charges Separation by splashing of naturally falling raindrops, *J.Atmos.Sci.28*

(4), 543 – 548

Li, L. W., P. S. Kooi, M. S. Leong, and T. S. Yeo (1994a), A gamma distribution of raindrop sizes and its application to Singapore's tropical environment, *Microwave Opt. Tech. Lett.*, *7*(5), 253 – 257

Li, L. W., T. S. Yeo, P. S. Kooi, and M. S. Leong (1994b), Comment on raindrop size distribution model, *IEEE Trans. Antennas Propag. 42*(9), 1360

Li, L. W., M. S. Leong, T. S. Yeo, and M. Z. Gao (1995), Microwave attenuation by realistically distorted raindrops: Part II – Predictions, *IEEE Trans. Antennas Propag. 43*(8), 823 – 828

Liebe, H. J. (1989), An atmospheric millimeter wave propagation model, *Int. J. Infrared milli. Waves*, *10*(6), 631 – 650

Liebe, H. J., G. A. Hufford and T. Manabe (1991), A model for the complex permittivity of water at frequencies below 1 THz, *Int. J. Infrared and mm Waves*, *12*(7), 659 – 675

Lin, S. H. (1975), A method for calculating rain attenuation distributions on microwave paths, Bell *Syst. Tech. J.*, *54*(6), 1051 –1086

Lin, S. H. (1977), Nationwide long-term rain rate statistics and empirical calculation of 11-GHz microwave rain attenuation, *Bell Syst. Tech. J.*, *56*(9), 1581 –1604

Lin, D. P., and H. Y. Chen (2002), An empirical formula for the prediction of rain attenuation in frequency range 0.6–100 GHz, *IEEE Trans. Antennas and Propag. 50*(4), 545–551

Maagt, P. J. I, S. I. E. Touw, J. Dijk, G. Brussard, and J. A. Allnut (1993), Results of 1.2 GHz propagation experiments in Indonesia, *Electron Lett.*, *29*(22), 1988 – 1990

Maciel, L. R. and M. S. Assis (1990), Tropical rainfall drop-size distribution, *Int. J. Sat. Commun.*, *8*, 181 – 186

Maggiori, D. (1981), Computed transmission through rain in 1-400 GHz frequency range for spherical and elliptical raindrops and any polarization, *Alta Frequenza, 50*, 262-273

Maitra, A. (2000), Three parameter raindrop size distribution modeling at a tropical location, *Electron. Lett., 36,* 906 – 907

Maitra, A. (2004), Rain attenuation modeling from measurements of raindrop size distribution in the Indian region, *IEEE Antennas Wireless propag. Lett., 3,* 180 – 181.

Maitra, A., and K. Chakravarty (2005), Raindrop size distribution measurements and associated rain parameters at a tropical location in the Indian Region, in *Proceedings of the URSI General Assembly*, 2005.

Manabe, T., T. Ihara, J. Awaka, Y. Furuhama (1987), The relationship of raindrop-size distribution to attenuation experienced at 50, 80, 140 and 240 GHz, *IEEE Trans. on Antennas Propag, 35*(11), 1326–1330

Marcus, M., and B. Pattan (2005), Millimeter wave propagation: spectrum management implications, *IEEE Microwave Mag., 6*(2), 54 – 61

Markowitz, A. H. (1976), Raindrop size distribution expressions, *J.Appl. Meteor,* 15(), 1029 – 1031

Marshall, J. S., and W. M. Palmer (1948), The distribution of raindrops with size, *J. Meteor.,5*, 165 – 166

Massambani, O, and C. A, M. Rodriquez (1990), Specific attenuation as inferred from drop size distribution measurements in the tropics, in *Proceedings of URSI Commission F symposium,* pp. 25 – 28, Rio de Janeiro, Brazil, 3-7 December

Matricciani, E., and A. Pawlina-Bonati (2000), Statistical characterization of rainfall structure and occurrence for convective and stratiform rain inferred from long-term point rain rate data,*AP-2000 Millennium Conf. Antennas Propag*. Davos, Switzerland, 9-14 April

Mätzler, C. (2002a), MATLAB functions for Mie scattering and absorption, *IAP Research Report No 2002-08*, Uni. Bern, Switzerland, June.

Mätzler, C. (2002b), Drop-size distributions and Mie computations for rain, *IAP Research Report No. 2002-16*, Uni. Bern, Switzerland, November.

Medeiros Filho, F. C., R. S. Cole, and A. D. Sarma (1986), Millimeter-wave rain induced attenuation: Theory and Experiment, *IEE Proc. Part H, Microwave Antennas Propag., 133*(4), 308 –314

Medhurst, R. G. (1965), Rainfall attenuation of centimeter waves: Comparison of theory and measurements, *IEEE Trans. on Antennas Propag, 13*(4), 550–564

Mello Silva, L. A .R., M. A. G. M. Maia, M. B. P Jimenez, and M. S. Pontes (1990), Conversion to one-minute rainfall rate distributions for different integration time Statistics, *Preprint of URSI Comm. F Open Symposium on regional Factors in Predicting Radiowave Attenuation Due to Rain*, Rio de Janeiro, Brazil

Meng, Y. S., Y. H. Lee and, B. C. Ng (2009), Empirical near ground path loss modeling in a forest at VHF and UHF bands, , *IEEE Trans. Antennas Propag. 57*(5), 1461–1468

Mie, G. (1908), Beiträge zur optik trüber medien, speziell kollodaler metallösungen, *Ann. Physics, 25*, 377 – 445.

Migliora, C. G. S., M.S. Pontes, and L. A. R. Silva Mello (1990), Rain rate and attenuation measurements in Brazil, *Preprint of URSI Commission. F Open Symposium on regional Factors in Predicting Radiowave Attenuation Due to Rain*, Rio de Janeiro, Brazil, pp.8 – 13

Mondal, N. C., A. B. Bhattacharya, and S. K. Sarkar (1999), Attenuation of centimetre, millimetre and sub-millimetre waves due to rain over tropical Indian stations, *Int. J. Infrared Milli. Waves, 20*(4), 699 – 724

Morrison, J. A., and M. J. Cross (1974), Scattering of a plane electromagnetic wave by axisymmetric raindrops, *Bell Syst. Tech. J. 53*(6), 955 –1019.

Moupfouma, F., and J. Tiffon (1982), Raindrop size distribution from microwave scattering measurements in equatorial and tropical climates, *Electron Lett., 18,* 1982, 1012 –1014

Moupfouma, F. (1984), Improvement of a rain attenuation prediction method for terrestrial microwave links, *IEEE Trans. Antennas and Propag, 32*(12), 1368 –1372

Moupfouma, F.(1987),More about rainfall rates and their prediction for radio systems engineering *IEE Proc., 134* (6), 527 – 537

Moupfouma F., L. Martin, N. Spanjaard, and K. Hughes (1990), Rainfall rate characteristics for microwave systems in tropical and equatorial area, *, Int. J. Sat. Commun, 8,* 151 – 161

Moupfouma, F. (1997), A new theoretical formulation for calculation of the specific attenuation due to precipitation particles on terrestrial and satellite radio link, *Int. J. Sat. Commun., 15,* 89 – 99.

Moupfouma, F. (2009), Electromagnetic waves attenuation due to rain: A prediction model for terrestrial or L.O.S SHF and EHF radio communication links, *J. Infra, Milli., Tetrahertz Waves, 3*0(6), 622 – 632

Mueller, E. A., and A. L. Sims (1966), Investigation of the quantitative determination of point areal precipitation by radar echo measurements, *Tech Rep.* No. 9, Ill. State Water Surv., Urbana.

Mulangu, C. T., and T. J. O. Afullo (2009), Variability of the propagation coefficients due to rain for microwave links in Southern Africa, *Radio Sci. 44*(3): RS3006 doi: 10.1029/2008RS003912,

Myers, W. (1999), Comparison of propagation Models, *IEEE 802.16 Broadband Wireless Access Working Group, IEEE 802.16cc-99/13,* Aug

Naicker, K., and S. H. Mneney (2006), Propagation of measurements and multipath channel modeling for line-of-sight links at 19.5 GHz, *SAIEE Res. J., 97*(2), 162 – 171.

Naicker, K (2006), Rain attenuation modeling for line-of-sight terrestrial links, MSc thesis, School of Electrical, Electronic and Computer Engineering, Uni. of KwaZulu-Natal, S. Africa, Sept.

Odedina, P. K., and T.J. Afullo (2005), Effective earth radius factor determination and its application in Southern Africa, in *Proceedings of IASTED Intl. Conf. Antennas, Radar, and Wave Propag.*, pp. 222 – 225, Banff, Canada , July

Odedina, M. O., and T.J. Afullo (2007a), Modeling of rain attenuation for terrestrial LOS radio systems in South Africa" *in Proceedings of Southern Africa Telecommunications Networks Applications conference (SATNAC),* Mauritius

Odedina, M. O., and T. J. Afullo (2007b), Rain Attenuation Prediction on Terrestrial Paths in South Africa Using Existing Attenuation Models, *In IEEE AFRICON 2007 Conference*, ISBN: 0-7803-8606-X, Namibia, September

Odedina, M. O., and T.J. Afullo (2008a), Seasonal variation of rain attenuation on radio propagation paths in South Africa, In *Proceedings of the XXIX General Assembly of the International Union of Radio Science (URSIGA 2008),* Chicago, Illinois, USA, August

Odedina, M. O., and T. J. Afullo (2008b), Characteristics of seasonal attenuation and fading for line-of-sight links in South Africa, in *Proceedings of Southern Africa Telecommunication Network Application (SATNAC),* pp. 203 – 208, Eastern-Cape, South Africa, September

Odedina, M. O., and T. J. Afullo (2009a), Characterization of rain attenuation and Its application to terrestrial communication systems in South Africa, *In the 6th IASTED Intl. Conf. on Antennas, Radar and Wave Propag.,* Banff, Alberta, Canada, ISBN: 978-0-88986-795 - 6. July

Odedina, M. O., and T. J. Afullo (2009b), Analytical modeling of rain attenuation and its application to terrestrial LOS Links, *In Proceedings of Southern Africa Telecommunications Networks Applications conference (SATNAC),* Swaziland, Sept.

Odedina, M. O., and T. J. Afullo (2009c), Determination of rain attenuation from electromagnetic scattering by spherical raindrops: Theory and experiment *Radio Sci., doi:10.1029/2009RS004192, in press*, October

Oguchi, T. (1960), Attenuation of electromagnetic wave due to rain with distorted raindrops, *J. Radio Res. Lab. (Jap.), 7*(33), 467 – 485

Oguchi, T. (1964), Attenuation of electromagnetic wave due to rain with distorted raindrops, **2** *J. Radio Res. Lab. (Jap.), 11*(53), 19 – 44

Oguchi, T. (1973), Attenuation and phase rotation of radio waves due to Rain: Calculation at 19.3 and 34.8 GHz, *Radio Sci. J., 8*(1), 31 – 38

Ojo, J. S., M. O. Ajewole, and S. K. Sarkar (2008), Rain rate and rain attenuation prediction for satellite communication in Ku and Ka bands over Nigeria, *Progress in Electromag. Res.B 5*, 207 –223

Olsen, R. L., D.V. Rogers, and D. B. Hodge (1978), The aR^b relation in the calculation of rain attenuation, *IEEE Trans. Antennas Propag., 26*(2), 547 – 556.

Olsen, R. L. (1999), Radioclimatological modeling of propagation effects in clear-air and precipitation conditions: Recent advances and future directions, *in Proceedings of Radio Africa "99 Conference,* pp. 92 – 106, Gaborone, Botswana

Owolawi, P. A., and T. J. Afullo (2007), Rainfall rate modeling and worst month statistics for millimetric line-of-sight radio links in South Africa, *Radio Sci. J., 42, RS6004, doi:10.1029/2006*

Ong, J. T., and Y. Y. Shan (1997), Rain drop size distribution models for Singapore-Comparison with results from different regions, *10th Int. Conf. on Antennas Propag., 2*(436), 281 – 285

Pawlina- Bonati, A., M. Binaghi (1998), Rain distribution along the Path: new statistics of cells and cells separations from radar data, *Proceedings of URSI Commission F Open Symposium on Climatic Parameters in Radiowave Propagation Prediction,* CLIMPARA '98, pp. 81 –84, Ottawa, Canada

Pawlina- Bonati, A. (1999), Essential knowledge of rain structure for radio applications based on available data and models, *Proceedings of the 3rd Regional Workshop on Radio communication, Radio Africa '99,* pp.96-106, Gaborone- Botswana

Perez Garcia, N. A., and L. A. R. da Silva Mello, (2004), Improved method for prediction of rain attenuation in terrestrial links. *Electron. Lett.*, *40*(11), 683 – 684

Pozar, D. M. (1988), *Microwave Engineering,* Second Edition, John Wiley and Sons, Inc.

Pruppacher, H. R., and K. V. Beard (1970), A wind tunnel investigation of the internal circulation and shape of water drops falling at terminal velocity, *Quart. J. Royal. Meteor. Soc. 96*(408), 247 – 256

Pruppacher, H. R., and R. L. Pitter (1971), A semi-empirical determination of the shape of cloud and raindrops, *J. of the Atmos. Sci.*, *28,* 86 – 94.

Ray, P. S. (1972), Broadband complex refractive indices of ice and water, *Appl. optics*, *11*(8), 1836 –1844

Republic of South Africa 2005-2006: *Official Year Book of the Republic of South Africa*, 29th Edition, Bureau for information.

Rice, P. L., and N. R. Holmberg (1973), Cumulative time statistics of surface-point rainfall rates, *IEEE Trans. Commun., 21*(10), 1131 – 1136

Rogers, D. V., and R. L. Olsen (1976), Calculation of radiowave attenuation due to rain at frequencies up to 1000 GHz, *Commun. Res. Centre Rep. No. 1299*, Ottawa, Canada, November

Rogers, D. V. (1981), Diversity and single-site radiometric measurements at 12 GHz rain attenuation in different climates, *IEE Conf. Publ., 195,* 118 – 123

Rogers, R. R. (1976), Statistical rainstorm models: their theoretical and physical foundations, *IEEE Trans. Antennas Propag.*, *24*(4), 547 – 566

Ruffner, J. A., and F. E. Blair (1977), The *Weather Almanac, Gale Research Company*, Detroit

Ryde, J. W., and D. Ryde (1944), Attenuation of centimeter waves by rain, hail and clods, *Rep. 8516, General electric Co. Res. Labs.*, Wembley, England, Aug.

Sadiku, M. N. O. (2001), *Numerical Techniques in Electromagnetics*, 2nd Edition, CRC Press, LLC.

Sadiku, M. N. O. (2007), Elements *of Electromagnetics*, 4th Edition, Oxford University Press

Salema, C (2003), *Microwave Radio Links from Theory to Design*, John Wiley & Sons, New Jersey

Sanders, J. (1975), Rain attenuation of millimeter waves at $\lambda = 5.77$, 3.3, and 2 mm, *IEEE Trans. Antennas Propag. 23*(2), 213 –220

Sarkar, S. K., I. Ahmed, M. V. S. M. Prasad, H. M. Dutta, and B. M. Reddy (1992), Rain rate distributions over the Indian Subcontinent- *Reference Data manual*.

Saxton, J. A., and J. a. Lane (1952), Electrical properties of sea water, *Wireless Eng.*, *29*(349), 269 –275

Schnell, M., U-C. Fiebig, E. Vilar, and C. Catalan (2002), Propagation impairments and impact on system design, *Cost Action 255 Final Rep.*, March

Seeber, R. J. (1985a), A method for the prediction of earth –space rain attenuation distribution in the USA, using a Southern African rain-rate model, *Trans. SAIEE,* 76 – 84.

Seeber, R. J. (1985b), An extreme value model of surface-point-rain-rate distribution for the prediction of microwave rain attenuation in Southern Africa, Thesis, Uni. of Pretoria

Segal, B. (1979), High intensity rainfall statistics for Canada, *Commun. Res. Centre(CRC) Rep, No. 1329-E,* , Canada.

Segal, B. (1980), A new procedure for the determination and classification of rainfall rate climatic zones, *Ann. Télécommun*., *35*(11-12), 411 – 417

Segal, B. (1986), The influence of raingage integration time on measured rainfall-intensity distribution functions, *J. Atmospheric and Oceanic Tech*, *3*(4), 662 – 667

Sekine, M., and C. D. Chen (1985), Rain attenuation in terrestrial and satellite communication links, in *Proceedings of the 15th European Microwave Conference*, pp. 985 – 990, Paris, France, September

Sekine, M., C. Chen, and T. Musha (1987), Rain attenuation from log-normal and Weibull raindrop-size distributions, *IEEE Trans. Antennas Propag., 35* (3), 358 – 359

Srivastava, R. C. (1967), on the role of coalescence between raindrops in shaping their size distribution, *J. Atmos. Sci. 24* (3), 287 – 292

Steiner, M., and R. A. Houze Jr. (1997), Sensitivity of estimated monthly convective rain fraction to the choice of Z-R relation, *J. Appl. Meteor*., 36(5), 452 – 462

Stroud, K. A., and D. J. Booth (2003), *Advanced Engineering Mathematics*, 4th Edition, Palgrave Macmillan, New York.

Suryana, J., S. Utoro, K. Tanaka, K. Igarashi, and M. Iida (2005), Study of prediction models compared with the measurement results of rainfall rate and KU-band rain attenuation at Indonesian tropical cities, *In Proc. 5th Int. Conf. Information, Communication and Signal Processing,* pp. 1570 – 1574

Takeuchi, D. M. (1978), Characterization of raindrop size distributions, *Preprints Conf. on Cloud Physics and Atmospheric Electricity,* Issaquah, *Amer. Meteor. Soc*., 154 – 161

Tharek, A. R., and J. Din (1992), Rainfall drop size distribution measurements in Malaysia, *URSI, General Assembly*, North Yorkshire, UK

Timothy, K. I., J. T. Ong, and E. B. L. Choo (2002), Raindrop size distribution using method of moments for terrestrial and satellite communication applications in Singapore, *IEEE Trans. Antennas Propag. 50*(10), 1420 –1424

Tseng, C.-H, K.-S. Chen, J. C. Shi, and C. H. Chu (2005), Prediction of Ka-band terrestrial rain attenuation using 2-year rain drop size distribution measurements in northern Taiwan, *J. Electromagn.. Waves and Appl. 19*(13), 1833-1841

Tokay, A., and D. A. Short (1996), Evidence from tropical raindrop spectra of the origin of rain from stratiform versus convective clouds, *J. Appl. Meteor. 35*(3), 355 – 371

Tyson, P. D., R. A. Preston-Whyte, and R.E. Schulze (1976), *The Climate of the Drakensberg,* Natal Town and Regional Planning Commission

Tyson, P. D. (1986), *Climatic Change and Variability in Southern Africa, Oxford* University Press, Cape Town

Ulbrich, C. W. (1983), Natural variations in the analytical form of raindrop size distribution, *J. Climate Appl. Meteor, 22*(10), 1764-1775

Ulbrich, C. W., and D. Atlas (1984), Assessment of the contribution of differential polarization to improved rainfall measurements, *Radio Sci. J. 19*(1), 49 – 57

Uzunoglu, N. K., B. G Evans, and A. R. Holt (1977), Scattering of electromagnetic radiation by precipitation particles and propagation characteristics of terrestrial and space communication systems, *IEE Proc, 124*(5), 417 – 424

Uzunoglu, N. K., and Evans (1978), Multiple scattering effects in electromagnetic wave propagation through a medium containing precipitation, *J. Phys, A: Math.Gen.,11*(4), 767 – 776

Van de Hulst, H. C (1957), *Light scattering by Small Particles*, John Wiley & Sons, New York.

Waldvogel, A. (1974), The N_0 jump of raindrop spectra, *J .Atmos. Sci.,31*(4), 1067 – 1078

Watson, P. A., V. Sathiaseelan, and B. Potter (1981), Development of a Climatic Map of Rainfall Attenuation for Europe, Post Graduate School of Electrical and Electronic Engineering, *Rep. No.300*, Uni. of Bradford, U.K.

Watson, P. A., M. J. Leito, V. Sathiaseelan, M. Gunes, J. P. V. Poires Baptista, B. A. Potter, N. Sengupta, O. Turney, and G. Brussaard (1987), Prediction of attenuation on satellite-earth links in European region, *IEE Proc., 134*(6), 583 – 596

Widodo, P. S., (2005), It is time to use the Ku-band in Indonesia, *Int. Electronic. J., Issue 8*

Willis, P. T. (1984), Functional fits to some observed drop size distributions and parametization of rain, *J. Atmos. Sci., 41*(9), 1648 – 1661

Yeo, T. S., P. S. Kooi, and M. S. Leong, and S. S. Ng (1990), Microwave attenuation due to rainfall at 21.255 GHz in the Singapore Environment, *Electron. Lett., 26*(14), 1021 – 1022

Yeo, T. S., P. S. Kooi, and M. S. Leong (1993), A two-year measurement of rainfall attenuation of CW microwaves in Singapore, *IEEE Trans. Antennas Propag. 41*(6), 709 –712

Yeo, T. S., P. S. Kooi, M. S. Leong, and L. W. Li (2001), Tropical raindrop size distribution for the prediction of rain attenuation of microwaves in the 10-40 GHz band, *IEEE Trans. Antennas Propag,. 49*(1), 80 – 83

Young, K. C. (1975), The evolution of drop spectra due to condensation coalescence, and breakup, *J. Atmos. Sci. 32*(5), 965-973

Zainal, A. R., I. A. Glover, and P. A. Watson (1993), Rain rate and drop size distribution measurements in Malaysia, *in Proceedings of IEEE International Geoscience and Remote Sensing Symposium* pp. 309 – 311

Zhang, M. G., and D. Z. Hu (1995), Investigation of rain attenuation and rates statistics in China and its neighbouring area, *Paper Submitted for* [*Ajayi, et al,* 1996]

Zhang, W., and N. Moayeri (1999), Power-law parameters of rain specific attenuation, *IEEE 802.16 Broadband Wireless Access Working Group, IEEE 802.16cc-99/41*, Dec

Zhou, Z. X., L. W. Li, T. S. Yeo, and M. S. Leong (2000), Cumulative distributions of rainfall rate and microwave attenuation in Singapore's tropical region, *Radio Science, 35*(3), 751 – 756

Internet References

[1]. *http://en.wikipedia. org/wiki/Subtropics*

[2]. *http://www.southafrica.info/plantrip/travel_tips/questions/ climate.htm*

[3]. *www-das.uwyo.edu/~geerts/cwx/notes/chap10/con_str.html*

[4]. *http://en.wikipedia.org/wiki/ precipitation types _ (meteorology)*

[5]. *http://en.wikipedia.org/wiki/precipitation types*

[6]. *http://en.wikipedia.org/wiki/equatorial_climate*

[7]. *http://www.mapofworld.com/ lat long/south-africa-lat-long.html*

[8]. *http://en.wikipedia.org/wiki/Tropics*

[9]. *http://places.co.za/maps/south africa map.html*

[10]. *http://www.southafrica.info/travel/advice/climate.htm*

[11]. *http://en.wikipedia.org/wiki/Radome*

[12]. *http://www.home.agilent.com/USeng/nav/-536900735.536879154/pd.html*

[13]. *http://www.sa-venues.com/no/weather.htm;*

Appendices

Appendix A

Appendix A-1 gives the descriptive summary of frequency bands spectrum used by the ITU-R.

Appendix A-1: Nomenclature of frequency bands [Hall, 1996]

Frequency range	**Wavelength**	**Descriptive designation**	
Below 3 KHz	Above 100 km		ELF
3-30 KHz	10-100 km	Myriametric waves	VLF
30-300 KHz	1-10 km	Kilometric waves	LF
300-3000 KHz	100-1000m	Hectometric waves	MF
3-30 MHz	10-100m	Decametric waves	HF
30-300 MHz	1-10 m	Metric waves	VHF
300-3000 MHz	10-100 cm	Decimetric waves	UHF
3-30 GHz	1-10 cm	Centimetric waves	SHF
30-300 GHz	1-10 mm	Millimetric waves	EHF
300-3000 GHz	0.1-1 mm	Sub-millimetric waves	
3-30 THz	10-100 μm	Far-infrared waves	
30-430 THz	0.7-10 μm	Near-infrared waves	
430-860 THz	0.35-0.7 μm	Optical waves	

Appendix A-2: ITU-R Frequency Dependent Power Law Values for Estimation of Specific Attenuation [ITU-R 838-3, 2005]

Frequency (GHz)	k_H	α_H	k_V	α_V
1	0.0000259	0.9691	0.0000308	0.8592
1.5	0.0000443	1.0185	0.0000574	0.8957
2	0.0000847	1.0664	0.0000998	0.9490
2.5	0.0001321	1.1209	0.0001464	1.0085
3	0.0001390	1.2322	0.0001942	1.0688
3.5	0.0001155	1.4189	0.0002346	1.1387
4	0.0001071	1.6009	0.0002461	1.2476
4.5	0.0001340	1.6948	0.0002347	1.3987
5	0.0002162	1.6969	0.0002428	1.5317
5.5	0.0003909	1.6499	0.0003115	1.5882
6	0.0007056	1.5900	0.0004878	1.5728
7	0.001915	1.4810	0.001425	1.4745
8	0.004115	1.3905	0.003450	1.3797
9	0.007535	1.3155	0.006691	1.2895
10	0.01217	1.2571	0.01129	1.2156
11	0.01772	1.2140	0.01731	1.1617
12	0.02386	1.1825	0.02455	1.1216
13	0.03041	1.1586	0.03266	1.0901
14	0.03738	1.1396	0.04126	1.0646
15	0.04481	1.1233	0.05008	1.0440
16	0.05282	1.1086	0.05899	1.0273
17	0.06146	1.0949	0.06797	1.0137
18	0.07078	1.0818	0.07708	1.0025
19	0.08084	1.0691	0.08642	0.9930
20	0.09164	1.0568	0.09611	0.9847
21	0.1032	1.0447	0.1063	0.9771
22	0.1155	1.0329	0.1170	0.9700
23	0.1286	1.0214	0.1284	0.9630
24	0.1425	1.0101	0.1404	0.9561
25	0.1571	0.9991	0.1533	0.9491
26	0.1724	0.9884	0.1669	0.9421
27	0.1884	0.9780	0.1813	0.9349

28	0.2051	0.9679	0.1964	0.9277
29	0.2224	0.9580	0.2124	0.9203
30	0.2403	0.9485	0.2291	0.9129
31	0.2588	0.9392	0.2465	0.9055
32	0.2778	0.9302	0.2646	0.8981
33	0.2972	0.9214	0.2833	0.8907
34	0.3171	0.9129	0.3026	0.8834
35	0.3374	0.9047	0.3224	0.8761
36	0.3580	0.8967	0.3427	0.8690
37	0.3789	0.8890	0.3633	0.8621
38	0.4001	0.8816	0.3844	0.8552
39	0.4215	0.8743	0.4058	0.8486
40	0.4431	0.8673	0.4274	0.8421
41	0.4647	0.8605	0.4492	0.8357
42	0.4865	0.8539	0.4712	0.8296
43	0.5084	0.8476	0.4932	0.8236
44	0.5302	0.8414	0.5153	0.8179
45	0.5521	0.8355	0.5375	0.8123
46	0.5738	0.8297	0.5596	0.8069
47	0.5956	0.8241	0.5817	0.8017
48	0.6172	0.8187	0.6037	0.7967
49	0.6386	0.8134	0.6255	0.7918
50	0.6600	0.8084	0.6472	0.7871
51	0.6811	0.8034	0.6687	0.7826
52	0.7020	0.7987	0.6901	0.7783
53	0.7228	0.7941	0.7112	0.7741
54	0.7433	0.7896	0.7321	0.7700
55	0.7635	0.7853	0.7527	0.7661
56	0.7835	0.7811	0.7730	0.7623
57	0.8032	0.7771	0.7931	0.7587
58	0.8226	0.7731	0.8129	0.7552
59	0.8418	0.7693	0.8324	0.7518
60	0.8606	0.7656	0.8515	0.7486
61	0.8791	0.7621	0.8704	0.7454
62	0.8974	0.7586	0.8889	0.7424
63	0.9153	0.7552	0.9071	0.7395
64	0.9328	0.7520	0.9250	0.7366
65	0.9501	0.7488	0.9425	0.7339
66	0.9670	0.7458	0.9598	0.7313

67	0.9836	0.7428	0.9767	0.7287
68	0.9999	0.7400	0.9932	0.7262
69	1.0159	0.7372	1.0094	0.7238
70	1.0315	0.7345	1.0253	0.7215
71	1.0468	0.7318	1.0409	0.7193
72	1.0618	0.7293	1.0561	0.7171
73	1.0764	0.7268	1.0711	0.7150
74	1.0908	0.7244	1.0857	0.7130
75	1.1048	0.7221	1.1000	0.7110
76	1.1185	0.7199	1.1139	0.7091
77	1.1320	0.7177	1.1276	0.7073
78	1.1451	0.7156	1.1410	0.7055
79	1.1579	0.7135	1.1541	0.7038
80	1.1704	0.7115	1.1668	0.7021
81	1.1827	0.7096	1.1793	0.7004
82	1.1946	0.7077	1.1915	0.6988
83	1.2063	0.7058	1.2034	0.6973
84	1.2177	0.7040	1.2151	0.6958
85	1.2289	0.7023	1.2265	0.6943
86	1.2398	0.7006	1.2376	0.6929
87	1.2504	0.6990	1.2484	0.6915
88	1.2607	0.6974	1.2590	0.6902
89	1.2708	0.6959	1.2694	0.6889
90	1.2807	0.6944	1.2795	0.6876
91	1.2903	0.6929	1.2893	0.6864
92	1.2997	0.6915	1.2989	0.6852
93	1.3089	0.6901	1.3083	0.6840
94	1.3179	0.6888	1.3175	0.6828
95	1.3266	0.6875	1.3265	0.6817
96	1.3351	0.6862	1.3352	0.6806
97	1.3434	0.6850	1.3437	0.6796
98	1.3515	0.6838	1.3520	0.6785
99	1.3594	0.6826	1.3601	0.6775
100	1.3671	0.6815	1.3680	0.6765
120	1.4866	0.6640	1.4911	0.6609
150	1.5823	0.6494	1.5896	0.6466
200	1.6378	0.6382	1.6443	0.6343
300	1.6286	0.6296	1.6286	0.6262
400	1.5860	0.6262	1.5820	0.6256

500	1.5418	0.6253	1.5366	0.6272
600	1.5013	0.6262	1.4967	0.6293
700	1.4654	0.6284	1.4622	0.6315
800	1.4335	0.6315	1.4321	0.6334
900	1.4050	0.6353	1.4056	0.6351
1 000	1.3795	0.6396	1.3822	0.6365

Appendix B

Appendices B-1, B-2, and B-3 gives the ITU-R rain intensity exceeded at different percentages of time, the ITU-R rain climatic region, and the ITU-R rain contour map for rain intensity exceeded for 0.01% for an average year for different part of the globe.

Table B-1:1 Rainfall intensity (mm/h) exceeded at different percentages of time for ITU-R rain climatic zones [*ITU-R 837-1*, 1994]

Percentage of time (%)	A	B	C	D	E	F	G	H	J	K	L	M	N	P	Q
1.0	<0.1	0.5	0.7	2.1	0.6	1.7	3	2	8	1.5	2	4	5	12	24
0.3	0.8	2	2.8	4.5	2.4	4.5	7	4	13	4.2	7	11	15	34	49
0.1	2	3	5	8	6	8	12	10	20	12	15	22	35	65	72
0.03	5	6	9	13	12	15	20	11	21	23	33	40	65	105	96
0.01	8	12	15	19	22	28	30	32	35	42	60	63	95	145	115
0.003	14	21	26	29	41	54	45	55	45	70	105	95	140	200	142
0.001	22	32	42	42	70	71	65	53	55	100	150	120	180	250	170

Appendix B-2: ITU-R rain climatic region: Map

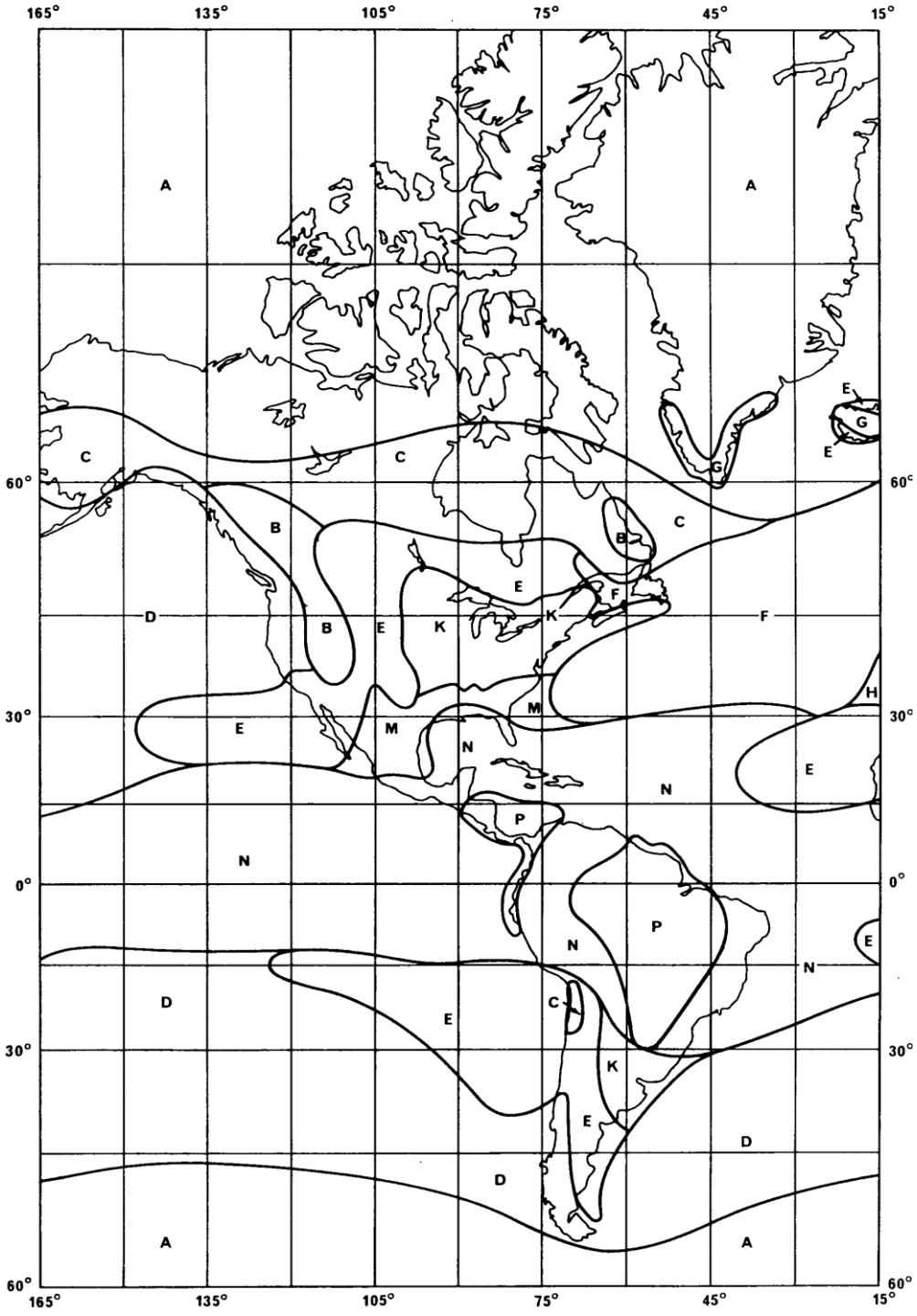

Fig B-2:1 Rain climatic zone boundaries in America [*ITU-R 837-1*, 1994]

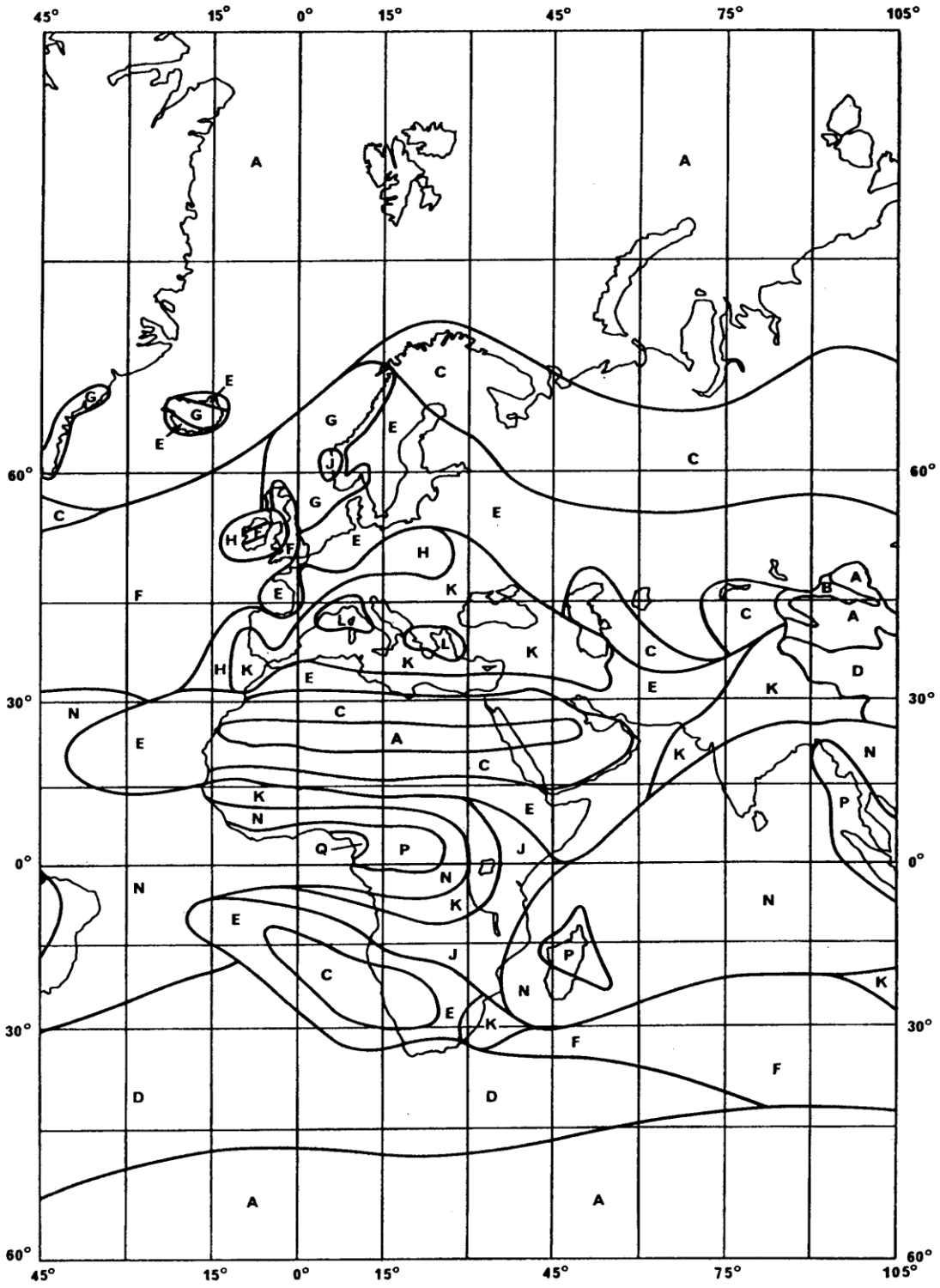

Fig B-2:2 Rain climatic zone boundaries in Europe and Africa [*ITU-R 837-1*, 1994]

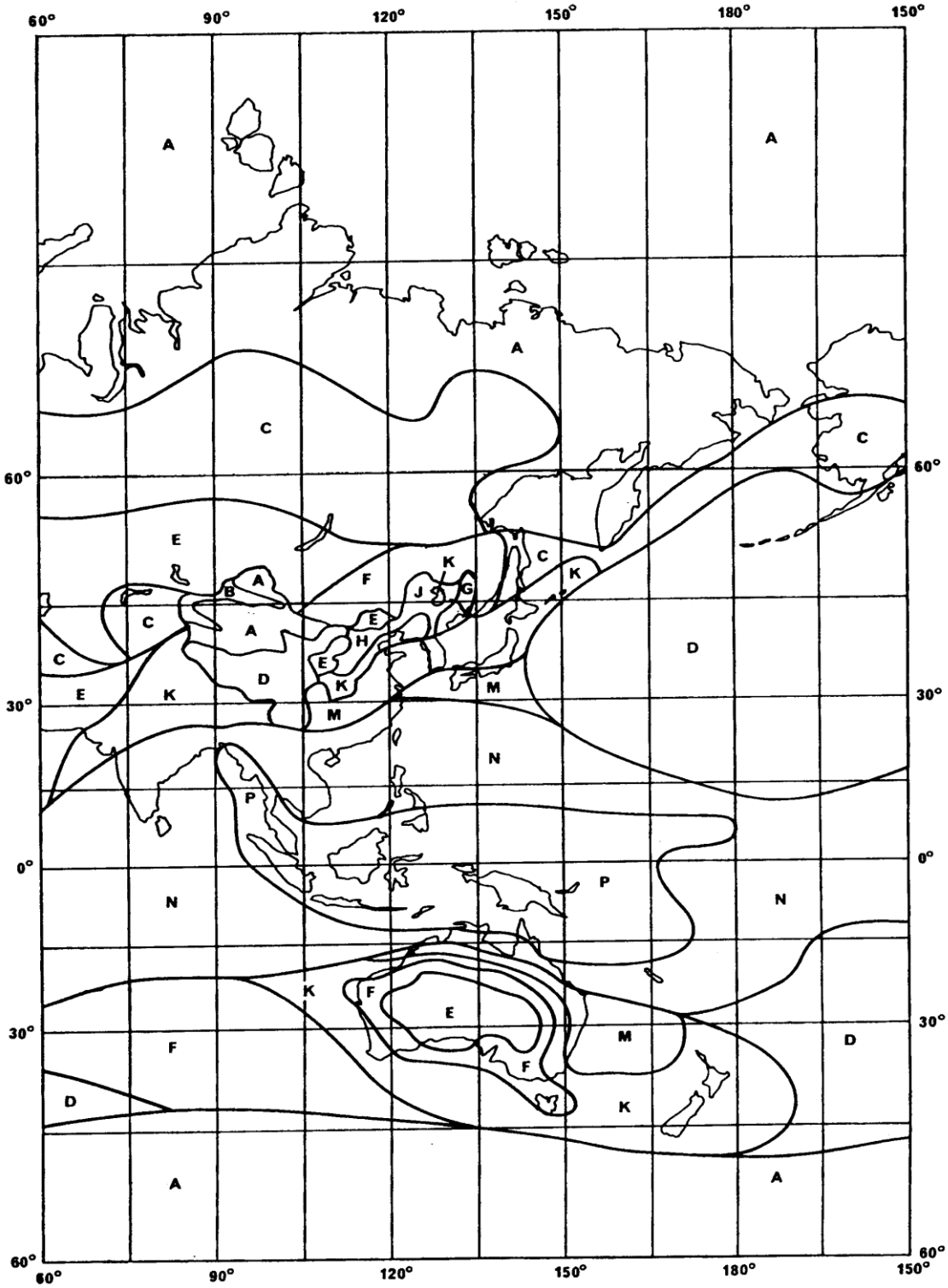

Fig B-2:3 Rain climatic zone boundaries in Asia [*ITU-R 837-1,* 1994]

Appendix B-3: ITU-R rain rate exceeded for 0.01% of the average year: Contour Map

FIGURE 1, 2, 3, 4, 5, and 6 of Appendix B-3 shows the contours for rain rate exceeded for 0.01% of the average year for all the latitudes and longitudes on the globe.

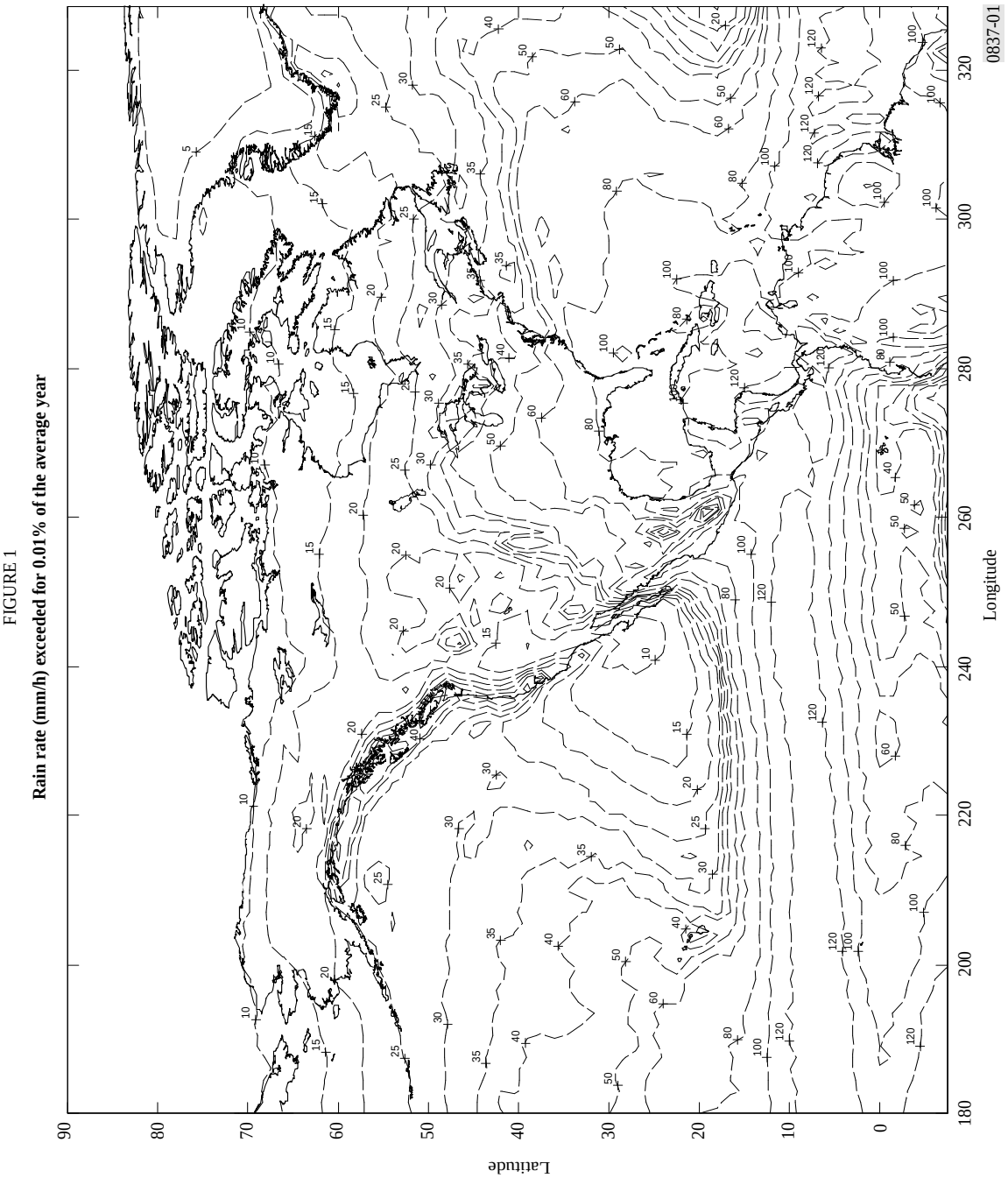

FIGURE 2

Rain rate (mm/h) exceeded for 0.01% of the average year

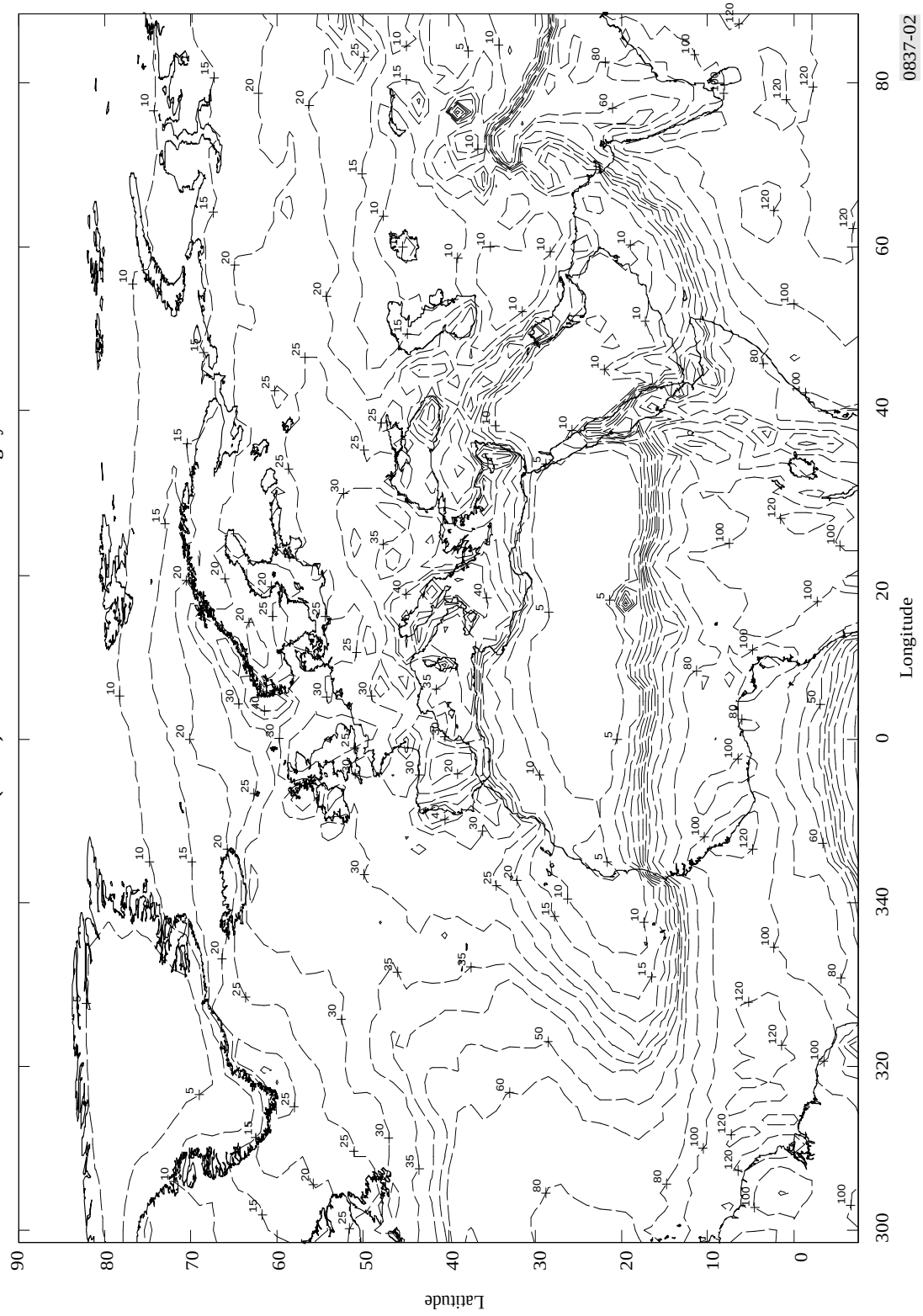

FIGURE 3

Rain rate (mm/h) exceeded for 0.01% of the average year

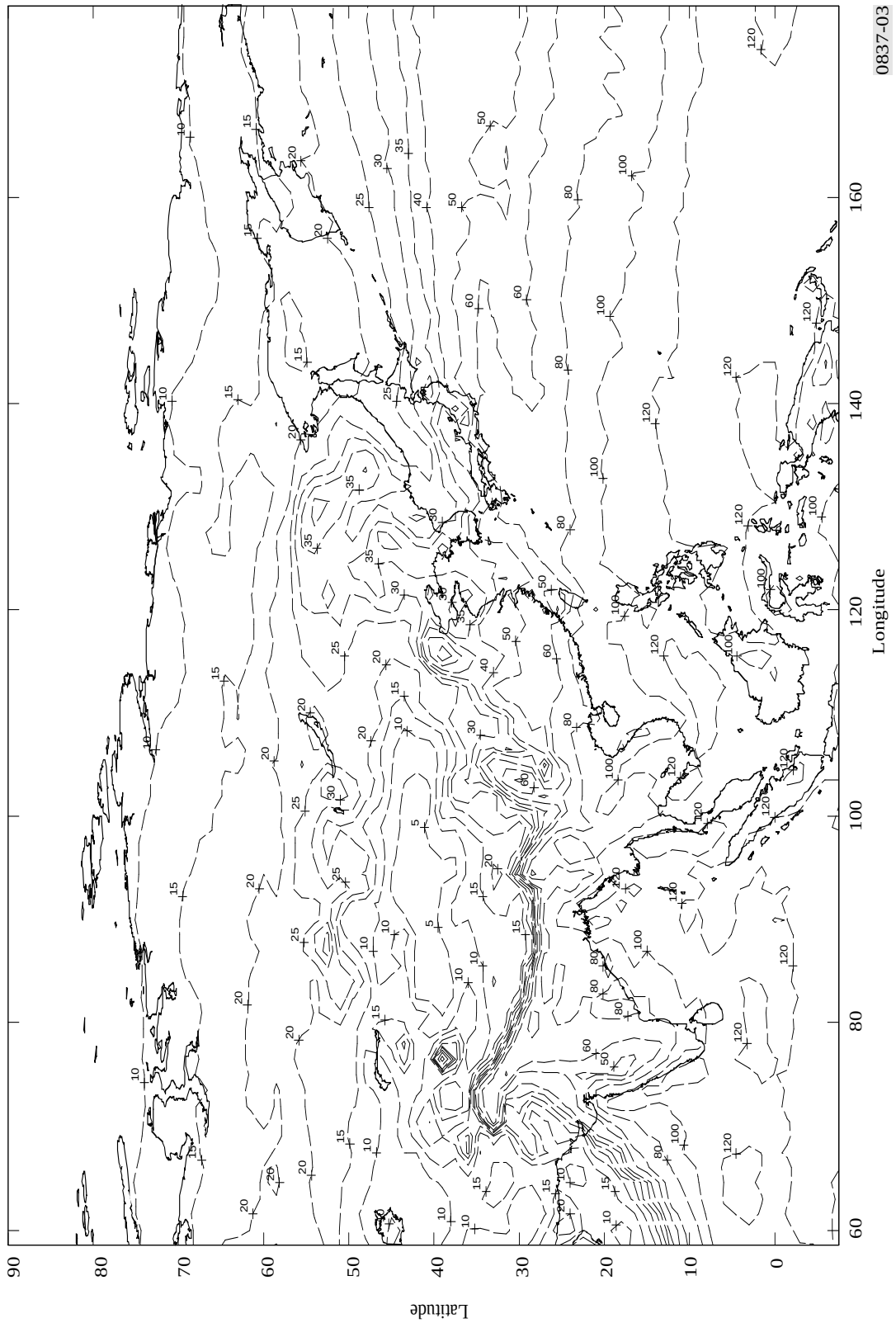

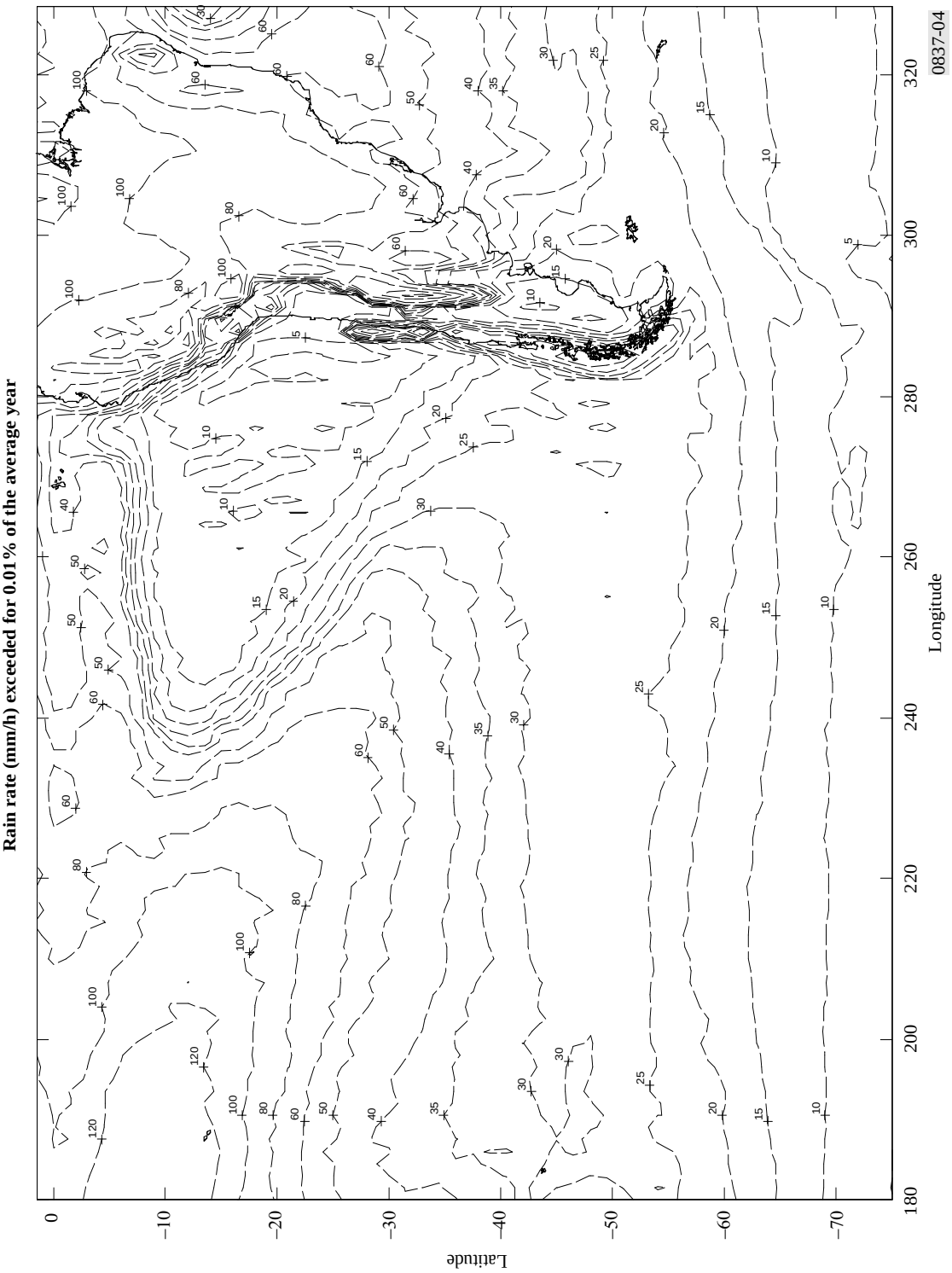

FIGURE 4
Rain rate (mm/h) exceeded for 0.01% of the average year

FIGURE 5

Rain rate mm/h) exceeded for 0.01% of the average year

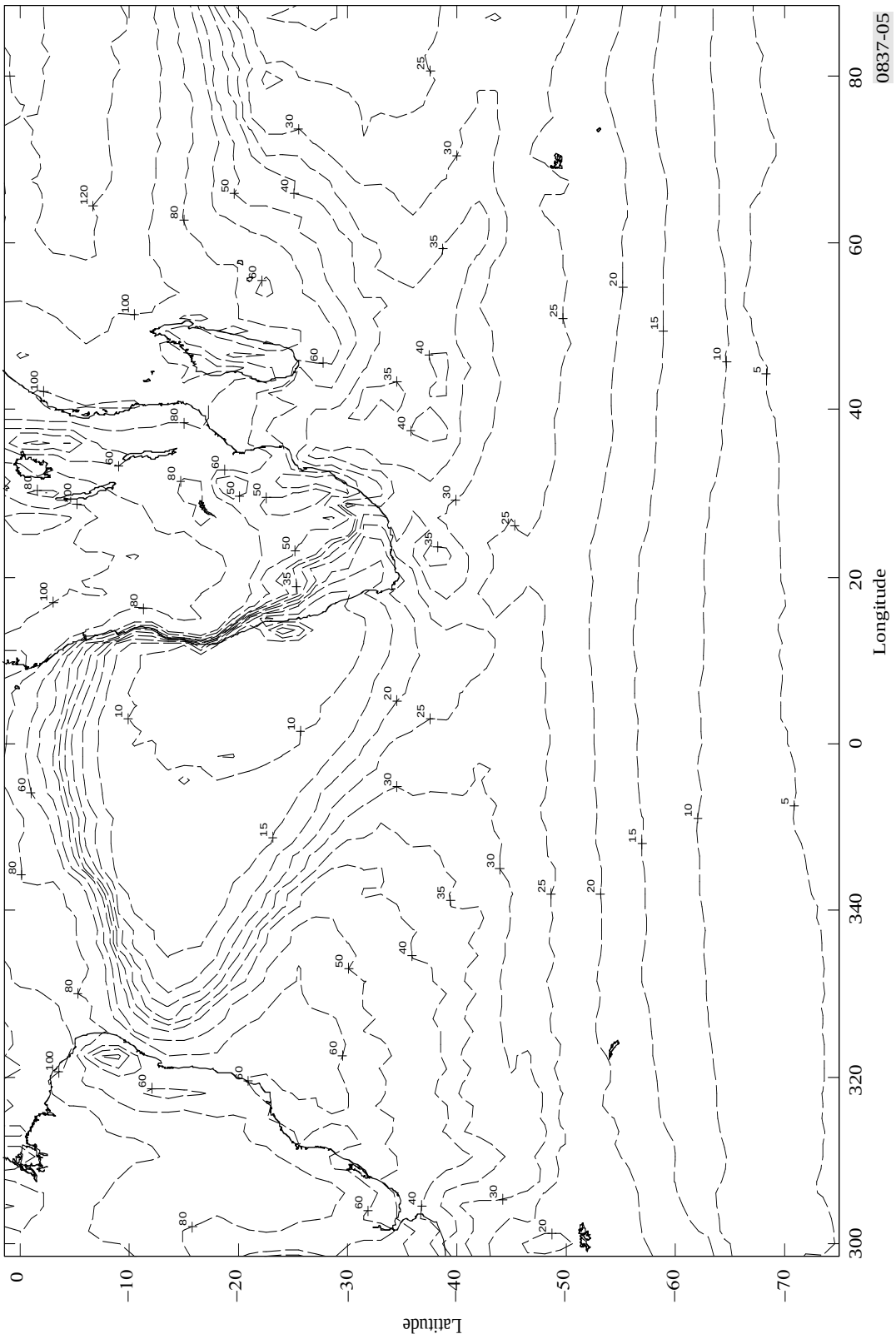

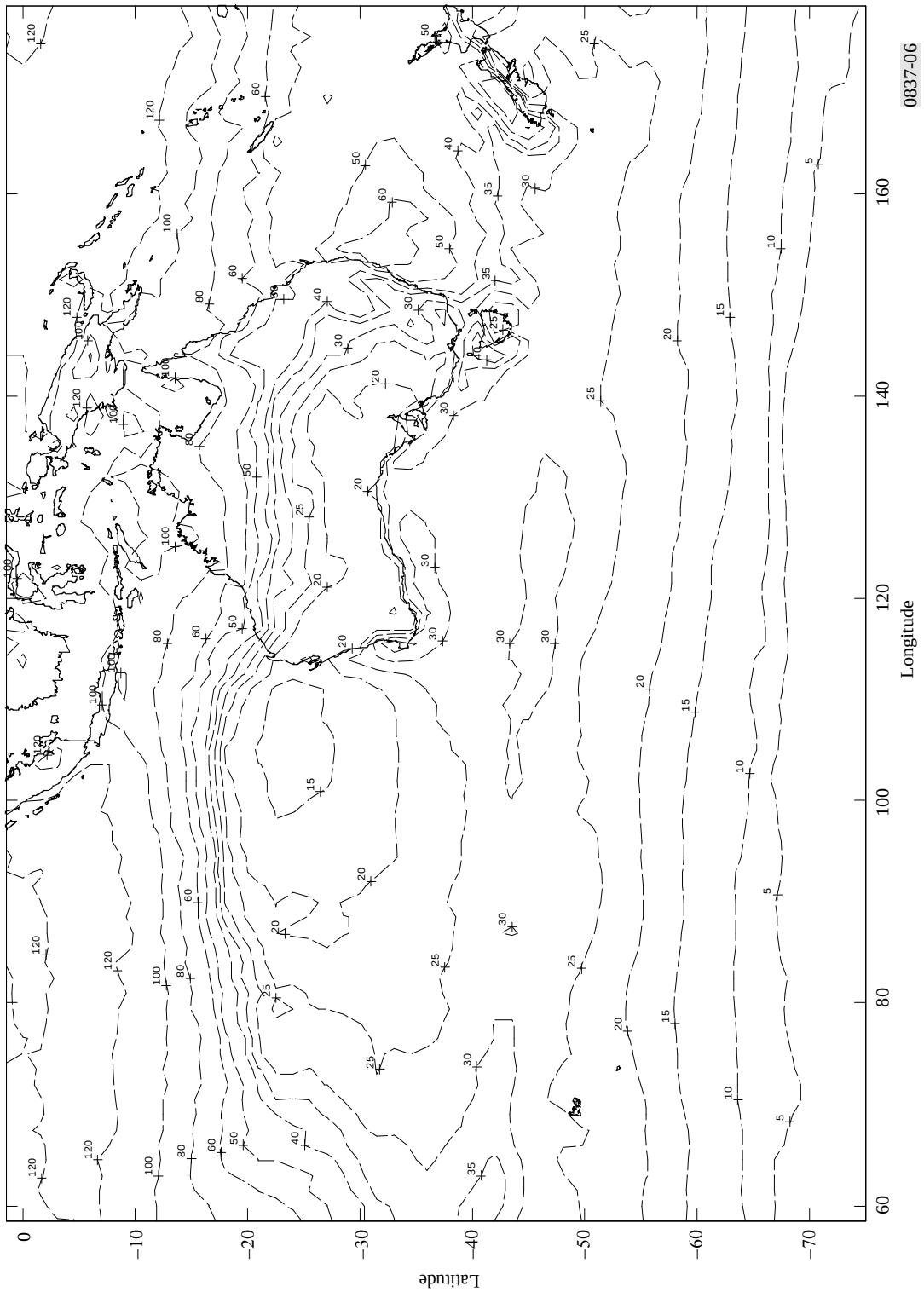

FIGURE 6

Rain rate (mm/h) exceeded for 0.01 % of the average year

Appendix B-4: Description of Crane's Global Rain Climatic Zone

Crane [1980] divided the world into eight rainfall climates labeled A-H. Region A and B corresponds to the driest regions (polar) and G and H are for the wettest climates (tropical). Sub-tropical regions are designated by E and F and temperate climates by C and D. Region D was further sub-divided into D1, D2 and D3, with D1 driest and D3 wettest. Region B was also sub-divided to B1 and B2 [*Crane,* 1996]. Fig. B-4:1 shows the global rain climatic zone by *Crane* [1980]. From this figure, South Africa climate is divided into F, C, and D, where the D is D1, D2, and D3 [*Crane,* 1996].

The rain rate exceeded for different percentages of the year for each climatic rain zone is given in Table B-4:1

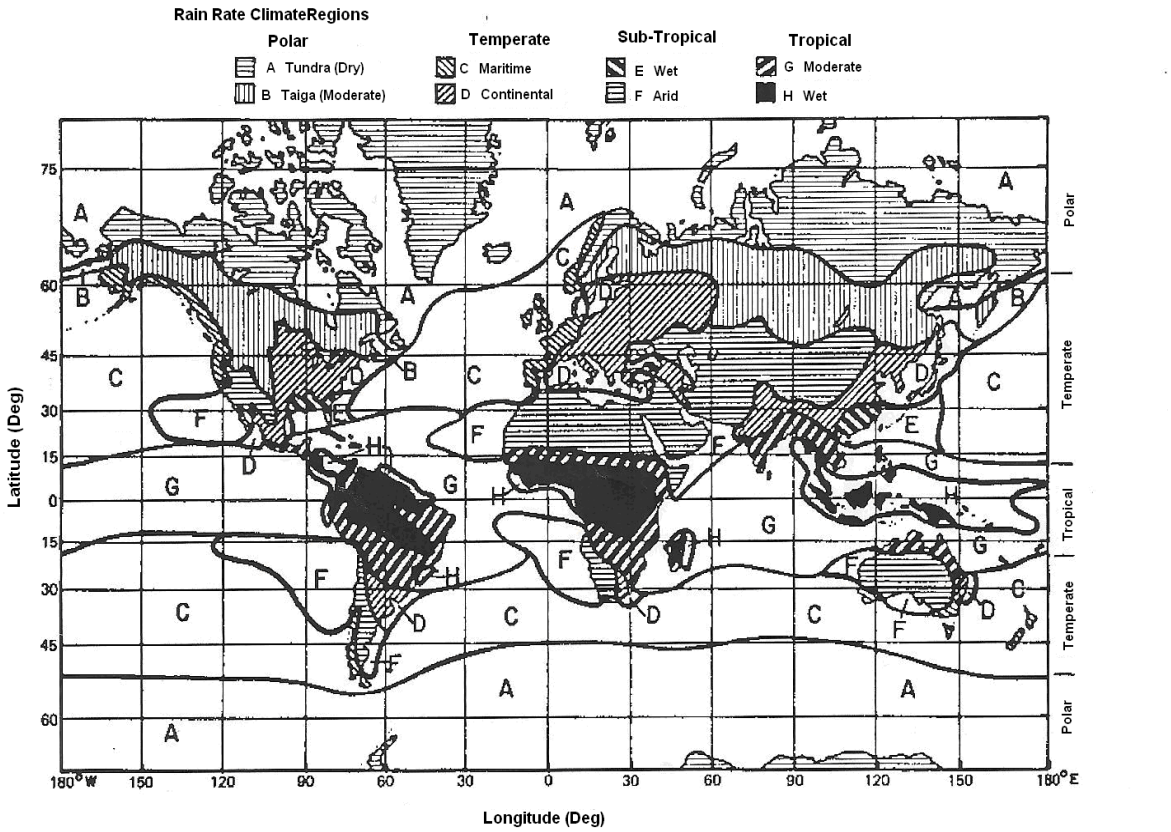

Fig. B-4:1 Crane global climatic zone [*Crane,* 1980]

Table B-4:1: Rain rate (mm/h) exceeded for different percentages of the year [*Crane*, 1996]

Global Percent Of the year	A	B	B1	B2	C	D1	D2	D3	E	F	G	H
1.0	0.2	1.2	0.8	1.4	1.8	2.2	3.0	4.6	7.0	0.6	8.4	12.4
0.5	0.5	2.0	1.5	2.4	2.9	3.8	5.3	8.2	12.6	1.4	13.2	22.6
0.3	1.1	2.9	2.2	3.4	4.1	5.3	7.6	11.8	18.4	2.2	17.7	33.1
0.2	1.5	3.8	2.9	4.4	5.2	6.8	9.9	15.2	24.1	3.1	22.0	43.5
0.1	2.5	5.7	4.5	6.8	7.7	10.3	15.1	22.4	36.2	5.3	31.3	66.5
0.05	4.0	8.6	6.8	10.3	11.5	15.3	22.2	31.6	50.4	8.5	43.8	97.2
0.03	5.5	11.6	9.0	13.9	15.6	20.3	28.6	39.9	62.4	11.8	55.8	125.9
0.02	6.9	14.6	11.3	17.6	19.9	25.4	34.7	47.0	72.2	15.0	66.8	152.4
0.01	9.9	21.1	16.1	25.8	29.5	36.2	46.8	61.6	91.5	22.2	90.2	209.3
0.05	13.8	29.2	22.3	35.7	4`.4	49.2	62.1	78.7	112.0	31.9	118.0	283.4
0.003	17.5	36.1	27.8	43.8	50.6	60.4	75.6	93.5	130.0	41.4	140.8	350.3
0.002	20.9	41.7	32.7	50.9	58.9	69.0	88.3	106.6	145.4	50.4	159.6	413.9
0.001	28.1	52.1	42.6	63.8	71.6	86.6	114.1	133.2	176.0	70.7	197.0	542.6

Appendix B-5: Köppen classification system for South Africa

According to *Seeber* [1985b], South Africa can be classified into 12 climatic rain zones by using the Köppen system as shown in Fig. B-5. A description of each zone is given in Table B-6 from *Seeber* [1985b]

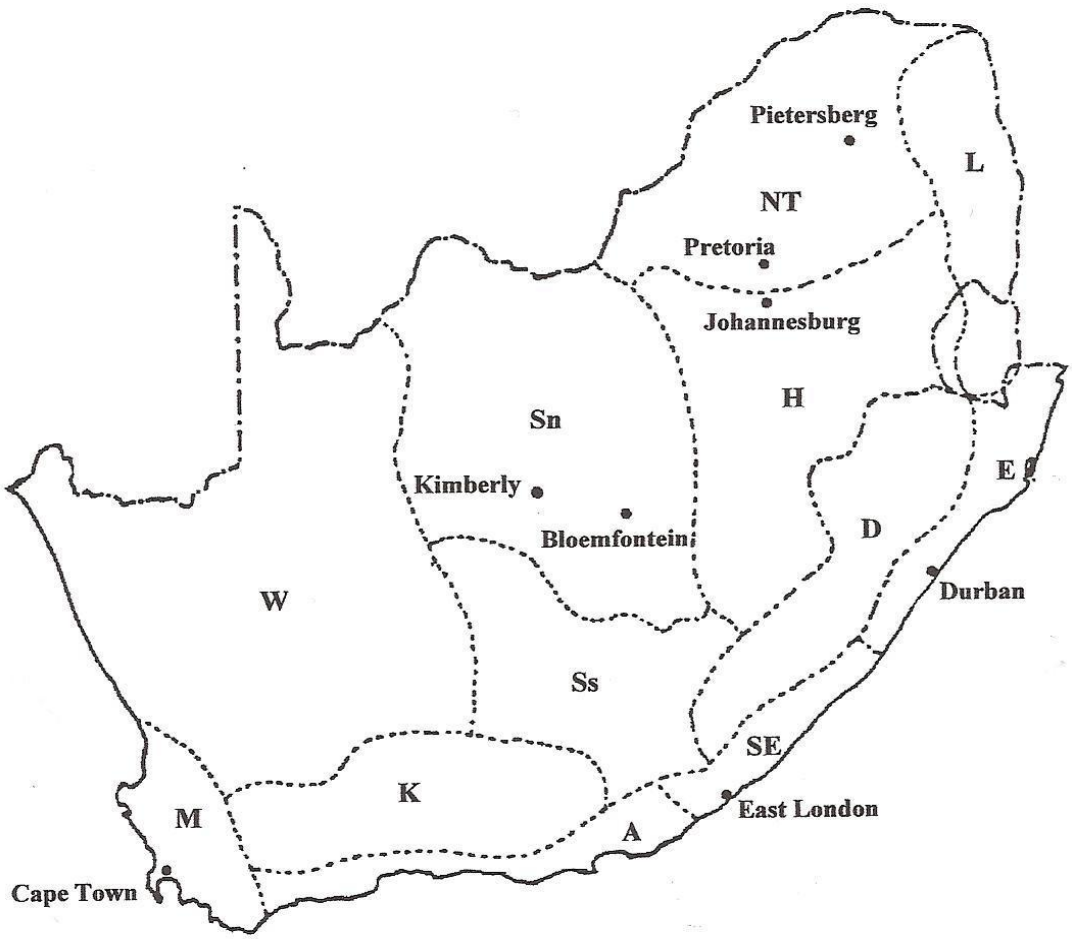

Fig. B-5 Map of South Africa climatic regions [From *Seeber,* 1985b]

Appendix B-6: Description of South Africa climate: Köppen system

Table B-6: Description of South Africa climatic rain zones [*Seeber,* 1985b]

Climatic classification for South Africa (Köppen system)	
W	*Northern Cape:* Dessert climate **(BW)**
M	*South-Western Cape:* Mediterranean climate with winter rains **(Cs)**
K	*Karoo:* Dessert climate **(BW and BSk)**
A	*Southern coastal belt:* Rain during all seasons **(Cf)**
SE	*South –eastern coastal belt*: Warm temperate with summer rain **(Cfw)**
E	*Eastern coast and Zululand:* Subtropical with summer rain **(Cfw and Cfa)**
D	*Drakensberg and interior KwaZulu-Natal:* Warm temperate with summer rain **(Cwb)**
L	*Lowveld (Northern Province):* Hot steppe with summer rain **(BShw)**
NT	*Northern Province:* Hot steppe with summer rain **(BShw)**
H	*Highveld (Mpumalanga, Gauteng, and Free State):* Warm temperate with summer rain **(Cwb)**
Sn	*Northern Steppe (Free state and North-West):* Steppe summer and autumn rain **(BSw)**
Ss	*Southern Steppe (Eastern Cape and Free State):* Cold steppe with autumn rains **(BSkw)**

Appendix C:

Appendix C-1: The Threshold values of the Chi-Square Test

[*Downie and Heath, 1965*]

Degrees of Freedom	Threshold at α =1%	Threshold at α =5%	Degrees of Freedom	Threshold at α =1%	Threshold at α =5%
1	6.6349	3.8415	18	34.8053	28.8693
2	9.2103	5.9915	20	37.5662	31.4104
3	11.3449	7.8147	25	44.3141	37.6525
4	13.2767	9.4877	30	50.8922	43.7730
5	15.0863	11.0705	35	56.0609	49.8018
6	16.8119	12.5916	40	63.6907	55.7585
7	18.4753	14.0671	50	76.1539	67.5048
8	20.0902	15.5073	60	88.3794	79.0819
9	21.6660	16.9190	70	100.4252	90.5312
10	23.2092	18.3070	80	112.3288	101.8795
12	26.2170	21.0261	90	124.1163	113.1453
14	29.1412	23.6848	100	135.8067	124.3421
16	31.9999	26.2962	1000	1106.9690	1074.6794

Appendix D:

Forward Scattering Amplitudes for Spherical Raindrops

This section gives the scattering amplitudes calculated for spherical raindrops from equation (4.3) for frequencies 1-40 GHz using the refractive indices of water given by *Liebe et al* [1991] at 20^{O}C (293K). Tables D-1 to D- 24 shows the radius of each raindrop $\bar{a}$, the size of the spherical drop, $\alpha = k\bar{a}$, and the real and the imaginary part of the scattering amplitude of each drop radius.

Table D-1: The forward scattering amplitudes at f=1 GHz, T=293 K, m=8.94022+0.24693i, λ=30cm

Radius of the spherical drop $\bar{a}$ (cm)	**Size of the spherical drop $\alpha = k\bar{a}$**	**Scattering amplitude of the spherical raindrop**	
		Real Part	**Imaginary part**
0.025	0.005237	0.00000000028300	-0.0000001383585i
0.050	0.010473	0.00000000226503	- 0.000001106919i
0.075	0.015710	0.00000000765244	- 0.0000037361474i
0.100	0.020947	0.00000001817406	- 0.0000088570240i
0.125	0.026183	0.00000003560550	- 0.0000173013140i
0.150	0.031420	0.000000061802810	- 0.0000299018250`i
0.175	0.036657	0.000000098745488	- 0.0000474926709i
0.200	0.041893	0.000000148589072	- 0.0000709095372i
0.225	0.047130	0.0000002137272448	- 0.0001009899481i
0.250	0.052367	0.0000002968637140	- 0.0001385735366i
0.275	0.057603	0.0000004010939759	- 0.0001845023168i
0.300	0.062840	0.0000005299971367	- 0.0002396209606i
0.325	0.068077	0.00000068773799262	- 0.00030477707720i
0.350	0.073313	0.00000087917958529	- 0.00038082149785i

Table D-2: The forward scattering amplitudes at f=2 GHz , T=293 K, m=8.90697+0.490563i , λ=15cm

Radius of the spherical drop $\bar{a}$ (cm)	Size of the spherical drop $\alpha = k\bar{a}$	Scattering amplitude of the spherical raindrop	
		Real Part	Imaginary part
0.025	0.01047619	0.000000004532549860	- 0.000001107790596i
0.050	0.02095238	0.000000036322350760	- 0.000008863990705i
0.075	0.03142857	0.000000123099793443	- 0.000029925347712i
0.100	0.04190476	0.000000294043288329	- 0.000070965325443i
0.125	0.05238095	0.00000058136035129	-0.000138682568619i
0.150	0.06285714	0.00000102249260343	- 0.000239809501670i
0.175	0.07333333	0.00000166296621718	- 0.000381121114356i
0.200	0.08380952	0.00000255991551283	- 0.00069443992321i
0.225	0.09428571	0.00000378631450672	- 0.000811665658347i
0.250	0.10476190	0.00000543595952	-0.00111474429996i
0.275	0.11523809	0.00000762925583	- 0.00148571897238i
0.300	0.12571428	0.00001051987340	- 0.00193172038208i
0.325	0.13619047	0.00001430235132	- 0.00245998237825i
0.350	0.14666667	0.00001922074931	- 0.00307785430658i

Table D-3: The forward scattering amplitudes at f=3 GHz , T=293 K m=8.85265+0.727778i , λ=10cm

Radius of spherical drop $\bar{a}$ (cm)	Size of the spherical drop $\alpha = k\bar{a}$	Scattering amplitude of the spherical raindrop	
		Real Part	Imaginary part
0.025	0.01571	0.000000022933303170	- 0.00000373582677i
0.050	0.03142	0.000000184172736358	0.000029899251899i
0.075	0.04713	0.000000627433779170	- 0.00010098120084i
0.100	0.06284	0.000001513066781996	- 0.00023959994617i
0.125	0.07855	0.000003036459589499	- 0.00046856661483i
0.150	0.09426	0.000005454088021617	- 0.00081095308745i
0.175	0.10997	0.000009117857348	- 0.00129016335575i
0.200	0.12568	0.000014518624950	- 0.00193000964795i

0.225	0.14139	0.000022340125429	- 0.00275479498808i
0.250	0.1571	0.000033524978367	0.003789404368487i
0.275	0.17281	0.000049355115849	- 0.00505940745300i
0.300	0.18852	0.000071549935376	- 0.00659117679270i
0.325	0.20423	0.000102386951943	- 0.00841202707874i
0.350	0.21994	0.000144852007824	- 0.01055038320929i

Table D-4: The forward scattering amplitudes at f=4 GHz , T=293 K m=8.77885+0.95579i , λ=7.5cm

Radius of spherical drop $\bar{a}$ (cm)	**Size of the spherical drop** $\alpha = k\bar{a}$	**Scattering amplitude of the spherical raindrop**	
		Real Part	**Imaginary part**
0.025	0.020952	0.00000007256658	- 0.00000886284905i
0.050	0.0419047	0.00000058452086	- 0.00007095614397i
0.075	0.0628571	0.00000200591578	- 0.00023977811384i
0.100	0.0838095	0.0000049017618	- 0.00056936773771i
0.125	0.1047619	0.00001003912023	- 0.00111458908529i
0.150	0.1257142	0.00001854225247	- 0.00193143461931i
0.175	0.1466666	0.00003210379760	- 0.00307735732022i
0.200	0.1676190	0.00005326422358	- 0.00461164518472i
0.225	0.18857142	0.00008577865212	- 0.00659585750878i
0.250	0.20952380	0.00013510165186	- 0.00909435160505i
0.275	0.230476190	0.00020904075167	- 0.01217494313810i
0.300	0.251428571	0.00031866622017	- 0.01590976598070i
0.325	0.272380952	0.00047963449149	- 0.02037643232214i
0.350	0.293333333	0.00071422035694	- 0.02565964431008i

Table D-5: The forward scattering amplitudes at f=5 GHz , T=293 K m=8.68759+1.17227i , λ=6cm

Radius of spherical drop $\bar{a}$ (cm)	Size of the spherical drop $\alpha = k\bar{a}$	Scattering amplitude of the spherical raindrop	
		Real Part	Imaginary part
0.025	0.026182	0.000000177086530	- 0.0000172952059i
0.050	0.052365	0.000001431943097	- 0.00013852429940i
0.075	0.0785475	0.000004960192923	- 0.000468439217729i
0.100	0.104730	0.000012325728768	- 0.001113452507013i
0.125	0.1309125	0.000025887024988	- 0.002182535024343i
0.150	0.1570950	0.000049435655310	- 0.003788209336291i
0.175	0.1832775	0.000089108663816	- 0.006047696714805i
0.200	0.209460	0.000154682724510	- 0.009084305327705i
0.225	0.2356425	0.000261446829481	- 0.013029196263890i
0.250	0.268350	0.000489768565091	- 0.019449548806607i
0.275	0.2880075	0.000705950548619	- 0.024222788789010i
0.300	0.314190	0.001137498074485	- 0.031799245047475i
0.325	0.3403725	0.001820586363704	- 0.040950105578701i
0.350	0.366555	0.002913839330013	- 0.051902100142608i

Table D-6: The forward scattering amplitudes at f=6 GHz , T=293 K m=8.58119+1.3754i , λ=5cm

Radius of spherical drop $\bar{a}$ (cm)	Size of the spherical drop $\alpha = k\bar{a}$	Scattering amplitude of the spherical raindrop	
		Real Part	Imaginary part
0.025	0.031428571	0.000000367755722578	- 0.000029915066229i
0.050	0.062857142	0.00000298788945085	-0.0002397261037435i
0.075	0.094285714	0.00001046923012156	- 0.000811373754496i
0.100	0.125714285	0.00002654727436	- 0.00193097508670i
0.125	0.157142857	0.00005743332877	- 0.00379115631751i
0.150	0.188571428	0.00011392955039	- 0.00659374795249i
0.175	0.22000000	0.00021466902501	- 0.01055308892426i

0.200	0.251428571	0.00039120720162	- 0.01590032577867i
0.225	0.282857142	0.00069652384208	- 0.02288927242765i
0.250	0.3142857142	0.00122048499981	- 0.03180440484624i
0.275	0.345714285	0.00212069772683	- 0.04297021151613i
0.300	0.377142857	0.00368868160065	- 0.05675267873704i
0.325	0.4085714285	0.00649076805096	- 0.07350316705725i
0.350	0.4400000000	0.01158698518455	- 0.09323960166867i

Table D-7: The forward scattering amplitudes at f=7 GHz , T=293 K m=8.46215+1.56392i , λ=4.2857cm

Radius of spherical drop $\bar{a}$ (cm)	**Size of the spherical drop $\alpha = k\bar{a}$**	**Scattering amplitude of the spherical raindrop**	
		Real Part	**Imaginary part**
0.025	0.0366575	0.0000006812649689326	- 0.00004747142100i
0.050	0.073315	0.000005566195036320	- 0.000380647367087i
0.075	0.1099725	0.000019767441417	- 0.001289660286097i
0.100	0.14663	0.000051310636652	- 0.003073749912241i
0.125	0.1832875	0.000114771791027	- 0.006046535493906i
0.150	0.219945	0.000237326183307	- 0.010542384956336i
0.175	0.2566025	0.000468902742490	- 0.016924642761724i
0.200	0.29326	0.000900376225936	- 0.025596676037478i
0.225	0.3299175	0.001699436452832	- 0.037015646707785i
0.250	0.366575	0.003187933449382	- 0.051700143464885i
0.275	0.4032325	0.006010442347311	- 0.070175662561843i
0.300	0.43989	0.011401687541399	- 0.092610980697017i
0.325	0.4765475	0.020839303283544	- 0.117648989982158i
0.350	0.513205	0.032988338410104	- 0.142388474295985i

Table D-8: The forward scattering amplitudes at f=8 GHz , T=293 K m=8.33296+1.73711i , λ=3.75cm

Radius of spherical drop $\bar{a}$ (cm)	**Size of the spherical drop $\alpha = k\bar{a}$**	**Scattering amplitude of the spherical raindrop**	
		Real Part	**Imaginary part**
0.025	0.0419047	0.000001164015012405	- 0.000070919564563i
0.050	0.08380952	0.00000957270853337	- 0.000569067462436i
0.075	0.12571428	0.00003452821371	- 0.00193034481185i
0.100	0.167619047	0.00009203435390	- 0.00460862357535i
0.125	0.209523809	0.00021359690422	- 0.00908653636721i
0.150	0.251428571	0.00046195585811	- 0.01588900714905i
0.175	0.293333333	0.00096053066363	- 0.02560094601464i
0.200	0.335238095	0.00195398687598	- 0.03888767058499i
0.225	0.3771428571	0.00394320549407	- 0.05649460399621i
0.250	0.4190476190	0.00796586114617	- 0.07908741646521i
0.275	0.46095238095	0.01581215532086	- 0.10643238474286i
0.300	0.50285714285	0.02830353776374	- 0.13602450063369i
0.325	0.54476190476	0.04205227197481	- 0.16659967708785i
0.350	0.58666666666	0.05569326527065	- 0.20243462402471i

Table D-9: The forward scattering amplitudes at f=9 GHz , T=293 K m=8.19605+1.89469i , λ=3.3333cm

Radius of spherical drop $\bar{a}$ (cm)	**Size of the spherical drop $\alpha = k\bar{a}$**	**Scattering amplitude of the spherical raindrop**	
		Real Part	**Imaginary part**
0.025	0.0419047	0.000001164015012405	- 0.000070919564563i
0.050	0.08380952	0.00000957270853337	- 0.000569067462436i
0.075	0.12571428	0.00003452821371	- 0.00193034481185i
0.100	0.167619047	0.00009203435390	- 0.00460862357535i
0.125	0.209523809	0.00021359690422	- 0.00908653636721i
0.150	0.251428571	0.00046195585811	- 0.01588900714905i
0.175	0.293333333	0.00096053066363	- 0.02560094601464i

0.200	0.335238095	0.00195398687598	- 0.03888767058499i
0.225	0.3771428571	0.00394320549407	- 0.05649460399621i
0.250	0.4190476190	0.00796586114617	- 0.07908741646521i
0.275	0.46095238095	0.01581215532086	- 0.10643238474286i
0.300	0.50285714285	0.02830353776374	- 0.13602450063369i
0.325	0.54476190476	0.04205227197481	- 0.16659967708785i
0.350	0.58666666666	0.05569326527065	- 0.20243462402471i

Table D-10: The forward scattering amplitudes at f=10 GHz , T=293 K m=8.05366+2.0368i , λ=3 cm

Radius of spherical drop $\bar{a}$ (cm)	**Size of the spherical drop $\alpha = k\bar{a}$**	**Scattering amplitude of the spherical raindrop**	
		Real Part	**Imaginary part**
0.025	0.05238095	0.00000284729383971	- 0.000138539266668i
0.050	0.10476190	0.00002378576389	- 0.00111353969500i
0.075	0.15714285	0.00008901346244	- 0.00378810398883i
0.100	0.20952380	0.00025219959061	- 0.00908134237807i
0.125	0.26190476	0.00063523837387	- 0.01800391364256i
0.150	0.31428571	0.00151433792178	- 0.03170120143758i
0.175	0.36666667	0.00351627915834	- 0.05147960090511i
0.200	0.419047619	0.00804756258776	- 0.07862679818430i
0.225	0.471428571	0.01766660604578	- 0.11328753437549i
0.250	0.5238095238	0.03375664311790	- 0.15277864136196i
0.275	0.5761904761	0.05342832477377	- 0.19634575044588i
0.300	0.6285714285	0.07732654480877	- 0.24798242465793i
0.325	0.6809523809	0.11081135723351	- 0.30799252982765i
0.350	0.7333333333	0.15819557433448	- 0.37194519424121i

Table D-11: The forward scattering amplitudes at f=12 GHz , T=293 K m=7.76021 + 2.27668i , λ=2.5 cm

Radius of spherical drop $\bar{a}$ (cm)	Size of the spherical drop $\alpha = k\bar{a}$	Scattering amplitude of the spherical raindrop	
		Real Part	Imaginary part
0.025	0.06286	0.000006	-0.0002395i
0.050	0.12571	0.00005	-0.0019i
0.075	0.18857	0.0002	-0.0066i
0.100	0.25143	0.0006	-0.0159i
0.125	0.31429	0.0017	-0.0317i
0.150	0.37714	0.0044	-0.0561i
0.175	0.44000	0.0111	-0.0912i
0.200	0.50286	0.0257	-0.13691i
0.225	0.56571	0.0493	-0.18971i
0.250	0.62857	0.0805	-0.2505i
0.275	0.691429	0.1239	-0.3208i
0.300	0.75429	0.1855	-0.3949i
0.325	0.81714	0.2652	-0.46201i
0.350	0.88000	0.3542	-0.5127i

Table D-12: The forward scattering amplitudes at f=14 GHz , T=293 K m=7.46553+2.46281, λ=2.143 cm

Radius of spherical drop $\bar{a}$ (cm)	Size of the spherical drop $\alpha = k\bar{a}$	Scattering amplitude of the spherical raindrop	
		Real Part	Imaginary part
0.025	0.073328	0.0000109925767	- 0.000380253441i
0.050	0.146656	0.00009574890761	- 0.0030701118518i
0.075	0.21998533	0.00039386483144	- 0.0105235982240i
0.100	0.29331377	0.00129129121288	- 0.0255004579504i
0.125	0.36664222	0.00389196383632	- 0.05120917015340i
0.150	0.439970668	0.01113136999489	- 0.09095614155519i
0.175	0.513299113	0.02857104460112	- 0.14546017084829i
0.200	0.5866275581	0.05931190097310	- 0.21067603893621i

0.225	0.6599560029	0.10327179707095	- 0.28595452479213i
0.250	0.733284447	0.16666257770415	- 0.36957275317923i
0.275	0.8066128924	0.25378547543979	- 0.44978940166981i
0.300	0.87994133724	0.35677999780078	- 0.51183265544968i
0.325	0.95326978201	0.45819946982314	- 0.55110905447936i
0.350	1.02659822678	0.54526626746282	- 0.57547527982032i

Table D-13: The forward scattering amplitudes at f=15 GHz , T=293 K , m=7.3206+2.53811i , λ=2cm

Radius of the sphere $\bar{a}$ (cm)	**Size of the spherical drop $\alpha = k\bar{a}$**	**Scattering amplitude of the spherical raindrop**	
		Real part	**Imaginary part**
0.025	0.07855	0.00001449968990376	- 0.000467470828578i
0.050	0.1571	0.00012788531180	- 0.00377935214657i
0.075	0.23565	0.00054055953158	- 0.01298375335361i
0.100	0.3142	0.00184281897299	- 0.03155600636920i
0.125	0.39275	0.00579292599253	- 0.06352962235470i
0.150	0.4713	0.01695708952164	- 0.11249060327696i
0.175	0.54985	0.04217142374164	- 0.17726025132892i
0.200	0.6284	0.08332265470309	- 0.25319149268816i
0.225	0.7029	0.13949688583590	- 0.33476373084196i
0.250	0.7855	0.22846657921871	- 0.42721238613631i
0.275	0.86405	0.33558859928812	- 0.49955866967605i
0.300	0.9426	0.44642433617927	- 0.54614047836989i
0.325	1.02115	0.54286629419557	- 0.57285613774297i
0.350	1.0997	0.61864449645075	- 0.59101349607839i

Table D-14: The forward scattering amplitudes at f=16 GHz , T=293 K , m=7.17855+2.60291i , λ=1.875cm

Radius of the sphere $\bar{a}$ (cm)	Size of the spherical drop $\alpha = k\bar{a}$	Scattering amplitude of the spherical raindrop	
		Real part	Imaginary part
0.025	0.0838095	0.00001881755562371	- 0.00056788660998i
0.050	0.16761904	0.00016821206117	- 0.00459777682635i
0.075	0.25142857	0.00073167591138	- 0.01583300674432i
0.100	0.335238095	0.00259511893098	- 0.03859703776787i
0.125	0.419047619	0.00847793633670	- 0.07783029779065i
0.150	0.5028571428	0.02502542793300	- 0.13690568952479i
0.175	0.5866666666	0.05966181531116	- 0.21221706402133i
0.200	0.67047619047	0.11397850932784	- 0.29904481545338i
0.225	0.75428571428	0.19350260470797	- 0.39284089591917i
0.250	0.83809523809	0.30054893646154	- 0.47734926034675i
0.275	0.9219047619	0.42004620597685	- 0.53551952930308i
0.300	1.0057142857	0.52851427346720	- 0.56756819225071i
0.325	1.089523809	0.61357930278903	- 0.58663238715261i
0.350	1.1733333333	0.67409667639149	- 0.60297439564394i

Table D-15: The forward scattering amplitudes at f=17 GHz , T=293 K m=7.03977+2.6582i , λ=1.765 cm

Radius of spherical drop $\bar{a}$ (cm)	Size of the spherical drop $\alpha = k\bar{a}$	Scattering amplitude of the spherical raindrop	
		Real Part	Imaginary part
0.025	0.089032780	0.00002401230003	- 0.00068092496981i
0.050	0.178065560	0.00021769199158	- 0.00552129080151i
0.075	0.267098340	0.00097512376186	- 0.01906017682484i
0.100	0.356131121	0.00359559393235	- 0.04659885959806i
0.125	0.445163901	0.01213535637151	- 0.09399087831177i
0.150	0.534196681	0.03559921629860	- 0.16369189886095i
0.175	0.623229461	0.08135371278236	- 0.24955403605656i
0.200	0.712262242	0.15184577498365	- 0.34600891528471i

0.225	0.801295022	0.25279056317856	- 0.44196708205740i
0.250	0.890327802	0.37702191300169	- 0.51611482658552i
0.275	0.979360582	0.49916940429094	- 0.5585498859921i
0.300	1.068393363	0.59778794497268	- 0.58046672933603i
0.325	1.157426143	0.66768559959168	- 0.59681108274458i
0.350	1.246458923	0.71045483878746	- 0.61554719672097i

Table D-16: The forward scattering amplitudes at f=18 GHz , T=293 K m= 6.90475+2.70492i , λ=1.67 cm

Radius of spherical drop $\bar{a}$ (cm)	**Size of the spherical drop $\alpha = k\bar{a}$**	**Scattering amplitude of the spherical raindrop**	
		Real Part	**Imaginary part**
0.025	0.09409751	0.00003006851507637	- 0.00080398562324i
0.050	0.188195038	0.00027649494987	- 0.00652916350037i
0.075	0.282292557	0.00127485063428	- 0.02259519369445i
0.100	0.376390076	0.00487462201879	- 0.05538505144553i
0.125	0.470487596	0.01686270426896	- 0.11155833986135i
0.150	0.564585115	0.04862077991298	- 0.19188397535008i
0.175	0.6586826347	0.10714257031581	- 0.28772123680372i
0.200	0.7527801539	0.19597737822132	- 0.39084171811944i
0.225	0.8468776732	0.31687364104888	- 0.48278589960561i
0.250	0.9409751924	0.45062647818807	- 0.54263057769908i
0.275	1.0350727117	0.56711170536936	- 0.57201473027177i
0.300	1.12917023096	0.65172280796180	- 0.58897212777588i
0.325	1.2232677502	0.70467382898745	- 0.60679889856436i
0.350	1.317365269461	0.72903168861420	- 0.63128487004319i

Table D-17: The forward scattering amplitudes at f=19.5 GHz , T=293 K m= 6.70992+2.76083i , λ=1.538 cm

Radius of spherical drop $\overline{a}$ (cm)	Size of the spherical drop $\alpha = k\overline{a}$	Scattering amplitude of the spherical raindrop	
		Real Part	Imaginary part
0.025	0.102173509	0.00004183589175	-0.00102956615290
0.050	0.2040816326	0.00039247068136	-0.00834979696648
0.075	0.3065205275	0.00190813784582	- 0.02912885446014
0.100	0.408694036782	0.00772007620377	-0.07164784916604
0.125	0.510867545978	0.02740969410522	-0.14340670469889
0.150	0.61304105517	0.07581456728698	-0.24064127046920
0.175	0.7152145643693	0.15895399777737	- 0.35019455351243
0.200	0.8173880735649	0.27945577892918	- 0.45551291803182
0.225	0.919561582	0.42379060579441	-0.53023455131557
0.250	1.0217350919562	0.55625984735721	- 0.56664375606289
0.275	1.123908601	0.65232268838710	-0.58425305634393
0.300	1.22608211034	0.70991851443617	- 0.60237450814628
0.325	1.32825561954300	0.73386412846509	- 0.62926726890026
0.350	1.430429128738	0.72857254116480	-0.66728188924486

Table D-18: The forward scattering amplitudes at f=20 GHz , T=293 K m= 6. 64712 + 2.77609i , λ=1.5 cm

Radius of spherical drop $\overline{a}$ (cm)	Size of the spherical drop $\alpha = k\overline{a}$	Scattering amplitude of the spherical raindrop	
		Real Part	Imaginary part
0.025	0.1047333	0.00004626230309	-0.00110899942439i
0.050	0.20946666	0.00043947899444	-0.00903746984050i
0.075	0.3142	0.00215971380601	-0.03144427255943i
0.100	0.4189333	0.00888321766811	-0.07740701514868i
0.125	0.523666	0.03166515660494	-0.15444364729073i
0.150	0.6284	0.08626266016963	- 0.25689093161163i
0.175	0.7331333	0.17827721285361	- 0.36978187238681i
0.200	0.8378666	0.30854046876688	- 0.47319754043658i

0.225	0.9426	0.45703077131492	- 0.54063524458408i
0.250	1.047333	0.58537983042381	- 0.57093134421558i
0.275	1.1520666	0.67324871351806	- 0.58727984721910i
0.300	1.2568	0.72171943376416	- 0.60762690541457i
0.325	1.36153333	0.73633239689940	- 0.63857897621466i
0.350	1.46626666	0.72175626933766	- 0.68133839949871i

Table D-19: The forward scattering amplitudes at f=23 GHz , T=293 K m= 6.29326+2.83852i , λ=1.304 cm

Radius of spherical drop $\bar{a}$ (cm)	**Size of the spherical drop $\alpha = k\bar{a}$**	**Scattering amplitude of the spherical raindrop**	
		Real Part	**Imaginary part**
0.025	0.12050832	8.16173E-05	- 0.00169040295823i
0.050	0.24101665	0.000817617	- 0.01385383807040i
0.075	0.36152497	0.004423637	- 0.04858818655285i
0.100	0.48203330	0.019873827	- 0.11970298815377i
0.125	0.602541630	0.069964224	- 0.23101899435865i
0.150	0.723049956	0.172276353	- 0.35988328662168i
0.175	0.843558282	0.323049662	- 0.47500504442415i
0.200	0.964066608	0.49233033	- 0.54421270285105i
0.225	1.084574934	0.628805581	- 0.57037335760912i
0.250	1.205083260	0.709873431	- 0.58705836896663i
0.275	1.325591586	0.741570474	- 0.61577504226873i
0.300	1.446099912	0.753217032	- 0.66109250677065i
0.325	1.5666082380	0.701164164	- 0.72044684206803i
0.350	1.6871165644	0.69806891	- 0.78803159092306i

Table D-20: The forward scattering amplitudes at f=25 GHz , T=293 K m= 6. 07895 + 2.85783i , λ=1.2 cm

Radius of spherical drop $\bar{a}$ (cm)	Size of the spherical drop $\alpha = k\bar{a}$	Scattering amplitude of the spherical raindrop	
		Real Part	Imaginary part
0.025	0.13095238	0.000114426	- 0.00217003252596i
0.050	0.26190476	0.001190637	- 0.01785694687601i
0.075	0.39285714	0.00686005	- 0.06293193047720i
0.100	0.523809523	0.032115276	- 0.15420892947768i
0.125	0.654761904	0.108881496	- 0.28726282580774i
0.150	0.7857142857	0.249497874	- 0.42325407071363i
0.175	0.91666666667	0.431190321	- 0.52024381254070i
0.200	1.04761904761	0.5967427	- 0.56056801733294i
0.225	1.178571428	0.701089229	- 0.57694707572460i
0.250	1.3095238095	0.743941026	- 0.60395153586849i
0.275	1.4404761904	0.738275449	- 0.65122309150372i
0.300	1.5714285714	0.692952412	- 0.71558720809142i
0.325	1.7023809523	0.673355615	- 0.78941604964719i
0.350	1.8333333333	0.622887495	- 0.86308732770753i

Table D-21: The forward scattering amplitudes at f=28 GHz , T=293 K m= 5.78786+2.86283i , λ=1.071 cm

Radius of spherical drop $\bar{a}$ (cm)	Size of the spherical drop $\alpha = k\bar{a}$	Scattering amplitude of the spherical raindrop	
		Real Part	Imaginary part
0.025	0.14672535	0.000181831	- 0.00305457228653i
0.050	0.293450713	0.002011456	- 0.02529891754033i
0.075	0.440176070	0.012697323	- 0.08966333349435i
0.100	0.586901427	0.061386754	- 0.21514056865418i
0.125	0.7336267840	0.170512676	- 0.37218660150285i
0.150	0.8803521408	0.365973302	- 0.49541636886052i
0.175	1.0270774976	0.55987862	- 0.55025918644237i

0.200	1.17380285447	0.684199403	- 0.56771804317233i
0.225	1.32052821128	0.750630273	- 0.59676163765795i
0.250	1.46725356809	0.73719373	- 0.65218525202952i
0.275	1.613978924903	0.676228438	- 0.72794460788288i
0.300	1.760704281712	0.654137565	- 0.81202757563201i
0.325	1.907429638522	0.60464864	- 0.89059593143666i
0.350	2.054154995331	0.550130218	- 0.95002661013150i

Table D-22: The forward scattering amplitudes at f=30 GHz , T=293 K m= 5.61242+2.85434i , λ=1.0 cm

Radius of spherical drop $\overline{a}$ (cm)	**Size of the spherical drop $\alpha = k\overline{a}$**	**Scattering amplitude of the spherical raindrop**	
		Real Part	**Imaginary part**
0.025	0.157142857	0.000240811	- 0.00375431360765i
0.050	0.314285714	0.002779169	- 0.03123219792132i
0.075	0.471428571	0.018549842	- 0.11089680006046i
0.100	0.628571428	0.08967129	- 0.25963820145335i
0.125	0.785714285	0.258238221	- 0.42229050829367i
0.150	0.942857142	0.477760105	- 0.52315004427508i
0.175	1.1000000000	0.655506015	- 0.55471811819310i
0.200	1.2571428571	0.742240284	- 0.57476971094222i
0.225	1.4142857142	0.751070211	- 0.62219887889894i
0.250	1.5714285716	0.701527787	- 0.69726911945045i
0.275	1.7285714285	0.603430419	- 0.78644154620297i
0.300	1.8857142857	0.561757328	- 0.87302027631259i
0.325	2.0428571428	0.479515672	- 0.94016490380028i
0.350	2.20000000000	0.289060923	- 0.97350564581011i

Table D-23: The forward scattering amplitudes at f=35 GHz , T=293 K m= 5.23037+2.80641i , λ=0.857 cm

Radius of spherical drop $\bar{a}$ (cm)	Size of the spherical drop $\alpha = k\bar{a}$	Scattering amplitude of the spherical raindrop	
		Real Part	Imaginary part
0.025	0.183363893	0.00045417258734	- 0.00597263620661i
0.050	0.366727787	0.00586430039937	- 0.05024448230240i
0.075	0.550091681	0.04403437890506	- 0.17718153055515i
0.100	0.733455575	0.19726719018573	- 0.37268267449570i
0.125	0.916819469	0.45157372635139	- 0.50426797262886i
0.150	1.100183363	0.66274717243088	- 0.54145885181099i
0.175	1.283547257	0.75511109086289	- 0.56478251440782i
0.200	1.4669111518	0.74675030105795	- 0.62738211123573i
0.225	1.6502750458	0.66509486757592	- 0.72363940795846i
0.250	1.8336389398	0.52195740888088	- 0.82864744087758i
0.275	2.0170028338	0.32246227253303	- 0.91544126720948i
0.300	2.2003667277	0.07002995161138	- 0.96031659808071i
0.325	2.3837306217	-0.13011124699610	- 0.94842677097185i
0.350	2.56709451575	-0.36387437078796	- 0.87703257192672i

Table D-24: The forward scattering amplitudes at f=40 GHz , T=293 K m= 4.91529+2.7364i , λ=0.75 cm

Radius of spherical drop $\bar{a}$ (cm)	Size of the spherical drop $\alpha = k\bar{a}$	Scattering amplitude of the spherical raindrop	
		Real Part	Imaginary part
0.025	0.2095238	0.00078980377755	- 0.00892338867326i
0.050	0.4190476	0.01145447348313	- 0.07582452091701i
0.075	0.6285714	0.09231716148629	- 0.25845231871317i
0.100	0.8380952	0.34693692849423	- 0.45838968234124i
0.125	1.04761904	0.62027261801745	- 0.52384580031382i
0.150	1.25714285	0.75359844933180	- 0.54461718794452i
0.175	1.46666666	0.75167800917083	- 0.61079553718818i

0.200	1.676190476	0.65411634807846	- 0.72171210142369i
0.225	1.885714285	0.47826228973951	- 0.84013179784351i
0.250	2.095238095	0.23019965355711	- 0.92643536682534i
0.275	2.304761904	-0.08521561801201	- 0.94982255765627i
0.300	2.5142857142	-0.45475512789879	- 0.89772281257995i
0.325			
0.350			